

THE INFLUENCE OF TEXTURE ON THE FATIGUE
BEHAVIOUR OF COPPER

by

Michael Anthony Burke, M.A. (Cantab.), M.S.

A Thesis submitted for the
degree of Doctor of Phil-
osophy in the University
of Sheffield,

December 1980

To my parents...

TABLE OF CONTENTS

	<u>Page</u>
ACKNOWLEDGEMENTS	
SUMMARY	
1.0 <u>INTRODUCTION</u>	1
2.0 <u>LITERATURE REVIEW</u>	4
2.1 <u>Introduction</u>	4
2.2 <u>Fatigue Parameters</u>	4
2.2.1 S-N Data	5
2.2.2 Cyclic Response Data	5
2.2.3 Phenomenological Aspects	6
2.2.4 Quantitative Aspects of Crack Propagation	7
2.3 <u>Fatigue of f.c.c. Single Crystals</u>	8
2.3.1 S-N Data	8
2.3.2 Cyclic Response	9
2.3.3 Phenomenological Aspects	12
2.3.4 Quantitative Aspects of Crack Growth	17
2.4 <u>Fatigue of b.c.c. Single Crystals</u>	20
2.4.1 S-N Data	20
2.4.2 Cyclic Response	23
2.4.3 Phenomenological Aspects	26
2.5 <u>Summary of Fatigue of Cubic Single Crystals</u>	30
2.5.1 S-N Data	30
2.5.2 Cyclic Response	30
2.5.3 Phenomenological Aspects	31
2.5.4 Quantitative Aspects of Crack Growth	32

2.6	<u>Fatigue Behaviour of Textured Polycrystals</u>	32
2.6.1	Interaction Between Textures and Fatigue in Cubic Metals	32
2.6.2	Influence of Texture on Fatigue Life of Cubic Metals	34
2.6.3	Phenomenological Aspects in Cubic Metals		35
2.6.4	Quantitative Aspects in Cubic Metals	..	39
2.6.5	Fatigue Anisotropy of Hexagonal Poly- crystals	40
3.0	<u>EXPERIMENTAL METHODS</u>	45
3.1	<u>Introduction</u>	45
3.2	<u>Material Preparation</u>	45
3.2.1	Thin Sheet	46
3.2.2	Plate	46
3.2.3	Rod	47
3.3	<u>Texture Measurement</u>	48
3.3.1	Introduction	48
3.3.2	Specimen Fabrication	49
	3.3.2.1 Thin Sheet	50
	3.3.2.2 Plate	50
	3.3.2.3 Rod	51
3.3.3	Specimen Preparation	52
3.3.4	Data Acquisition	52
3.4	<u>Preliminary Experiments</u>	53
3.5	<u>Mechanical Testing</u>	54
3.5.1	Strain Life Testing	54
	3.5.1.1 Specimen Preparation	54
	3.5.1.2 Fatigue Testing	55
	3.5.1.3 Elastic Modulus Measurement	..	56
3.5.2	Crack Propagation Testing	57
	3.5.2.1 Specimen Preparation	57

	3.5.2.2	Crack Propagation Testing	..	58
3.6		<u>Observations</u>	58
	3.6.1	Optical Techniques	58
	3.6.2	Scanning Electron Microscopy	58
4.0		<u>DATA MANAGEMENT</u>	49
4.1		<u>Introduction</u>	59
4.2		<u>Strain Life</u>	59
	4.2.1	Parametric Approach	59
	4.2.2	Computer Program	62
	4.2.3	Precision of Parameters	63
4.3		<u>Crack Propagation</u>	63
	4.3.1	Analysis of Data	63
	4.3.2	Computer Program	64
	4.3.3	Precision of Crack Propagation Data	..	65
4.4		<u>Texture Analysis</u>	67
	4.4.1	Analysis	67
	4.4.2	Pole Figures	67
	4.4.3	Crystallite Orientation Distribution Function	68
	4.4.3.1	Estimation of Errors in the c.o.d.f.	69
	4.4.4	Description of Textures by the c.o.d.f.		70
	4.4.5	Application of the c.o.d.f. to Cyclic Properties	71
	4.4.5.1	Mechanical Property Predictions	72
	4.4.5.2	Elastic Modulus Prediction	..	72
	4.4.5.3	Yield Stress Anisotropy Prediction	73
	4.4.6	Application of the c.o.d.f. to Texture Development	74
	4.4.6.1	Quantitative Assessment of Texture Development	74

	4.4.6.2	Simulation of Texture Development	74
	4.4.7	Texture Data Management	76
5.0	<u>RESULTS</u>	77
	5.1	<u>Microstructural Characterisation</u>	77
	5.1.1	Metallographic Observations	77
	5.1.2	Texture Data	77
	5.1.2.1	Thin Sheet Material	77
	5.1.2.2	Plate Material	78
	5.1.2.3	Rod Material	79
	5.1.3	Mechanical Property Reductions	79
	5.2	<u>Elastic Modulus Measurements</u>	80
	5.3	<u>Preliminary Experiments</u>	81
	5.3.1	Fractographic Observations	82
	5.3.2	Preliminary Conclusions	84
	5.4	<u>Cyclic Stress-Strain Investigation</u>	85
	5.5	<u>Fatigue Crack Propagation Investigation</u>	87
	5.6	<u>Scanning Electron Microscopy Observation</u>	89
	5.6.1	Strain-Life Specimens	89
	5.6.1.1	Specimen Sides	89
	5.6.1.2	Fracture Surfaces	90
	5.6.2	Crack Propagation Specimens	92
	5.7	<u>Texture Development During Fatigue</u>	93
	5.7.1	Simulation	93
	5.7.2	Experimental Measurement of Texture Development During Fatigue	93
6.0	<u>DISCUSSION</u>	95
	6.1	<u>Preliminary Experiments</u>	96
	6.2	<u>Strain-Life</u>	99
	6.3	<u>The Development of Texture During Fatigue</u>	117
	6.4	<u>Fatigue Fracture</u>	121

7.0	<u>SUMMARY, CONCLUSIONS AND SUGGESTIONS FOR FURTHER WORK</u>	132
7.1	<u>Summary and Conclusions</u>	132
7.2	<u>Suggestions for Further Work</u>	135

REFERENCES

APPENDICES

FIGURES

AUXILIARY FIGURES (relate to Appendices)

LIST OF MATERIAL CODES (fold out)

ACKNOWLEDGEMENTS

This thesis is original, except where due reference has been made, and pertains to work carried out between October, 1977 and August, 1978 in the Department of Metallurgy and Materials Science, University of Cambridge, and between September, 1978 and December, 1980 at the Department of Metallurgy, University of Sheffield and at G.K.N. Group Technology Centre, Wolverhampton. I should like to thank Professor R. W. K. Honeycombe, Professor G. W. Greenwood and Dr. P. Watson for permission to use laboratory facilities at the afore mentioned establishments, respectively.

I should like to express my sincere thanks to my supervisor, Professor G. J. Davies, for his helpful advice and encouragement throughout the duration of this project and for his ruthless eradication of the split infinitive from the manuscript of this thesis. I am also indebted to Dr. R. M. Bateman for his aid with the computing techniques involved in this work. Valuable technical assistance was rendered by Mr. V. Kumar of G.K.N. Group Technological Centre and helpful discussions with the staff of G.K.N., especially, Dr. P. E. Irving and Dr. P. Watson. Thanks are also due to Miss Linda Machin who typed the manuscript.

Finally, I am profoundly grateful to my wife, Grace, for her affectionate support throughout the course of this study.

Michael Anthony Burke
Sheffield1980

SUMMARY

This investigation attempts to assess the effect of preferred crystallographic orientation on the fatigue properties of a cubic metal. Quantitative texture analysis is performed using the crystal-lite orientation distribution function (c.o.d.f.) which enables quantitative predictions of mechanical properties to be made from texture measurements. Copper has been chosen as a model material since its single crystal properties exhibit values which are typical of cubic metals and also since the effects of thermomechanical processing are reasonably well documented.

The fatigue properties are evaluated by producing textured plates of different texture types and severities and machining specimens at specific orientations to the rolling direction of the plate. Fibre textures are also investigated by evaluating the fatigue properties parallel to the long axis of thermomechanically processed rod. Smooth sided cylindrical specimens were tested under fully reversed strain amplitude control to generate strain-life and cyclic stress-strain data. These data were analysed using the parametric approach of Morrow to develop a set of characteristic material parameters. Similarly, fatigue crack propagation studies were conducted on single edge notch specimens machined at specific angles from textured plate. Testing under constant load amplitude control produced data in the form of crack length vs. number of cycles which was analysed to produce crack propagation rate vs. stress intensity amplitude data which may be parametrically expressed by the constants C and m in the Paris equation.

It is shown that the anisotropy of fatigue behaviour may be predicted from texture measurements. The cyclic stress-strain data display anisotropy which is related to the type and severity of the texture. As the texture severity increases, the fatigue data displays greater anisotropy. The anisotropy of fatigue life data is shown to be a function of the product $\Delta\sigma \Delta\varepsilon$ per cycle which is directly dependent on the cyclic stress strain curve. The anisotropy of fatigue crack data has been shown to be a function of the ability of the texture to influence the crack orientation and hence the crack opening mode. It has been shown that this effect may be predicted from texture data by considering the plastic strain ratio "R".

CHAPTER 1

Introduction

Fatigue failure is not only the most common single cause of material failure but also, in conjunction with corrosion effects, failure under repeated loading accounts for the vast majority of engineering failures. Given the importance of such a failure mechanism surprisingly few data are available with regard to the effect of material anisotropy upon fatigue. This thesis examines the effect of one form of mechanical anisotropy, that due to preferred crystallographic orientation, or crystallographic texture as it is widely known, upon the fatigue failure of a single phase f.c.c. metal.

Although it is well known that thermomechanical processing induces preferred orientation effects commercially processed materials are frequently regarded as possessing mechanical isotropy. It has been recognised that many of the problems encountered during the forming processes of metals may be due to the influence of texture. In hexagonal metals the severe anisotropy has been shown to influence the fatigue properties of numerous metals and alloys. However, due to the greater isotropy of f.c.c. metals, the influence of crystallographic texture on the cyclic properties has not been widely investigated.

The aims of this investigation have been to examine the effects of texture on the fatigue properties of copper and by employing a quantitative technique for the determination of texture data to assess the quantitative predictability of the anisotropy so induced. The quantitative method of texture analysis employed makes use of the crystallite orientation distribution function (c.o.d.f.), which, when combined with

suitable models of the deformation mode may be used to predict the mechanical properties. This technique has become well established in recent years and consequently, only a brief description of the application of the technique is presented in Chapter 4.

Similarly, the nature of the fatigue failure process is well known and only a brief summary of the relevant factors is presented at the beginning of Chapter 2. The remainder of Chapter 2 presents a literature survey of the influence of crystallographic orientation upon the fatigue of metals. The effects are reviewed for cubic metals in both single crystal and polycrystal form and for polycrystalline hexagonal metals.

The fatigue properties are assessed using the cyclic stress-strain analysis and standard techniques of crack propagation measurements. The cyclic stress-strain analysis technique considers that the resistance of a material to cyclic deformation may be characterised by a set of material parameters which are not independent but are, in fact, related by the relationship between the cyclic stress amplitude and the cyclic strain amplitude developed by the loading conditions. Hence, endurance data is collected in the form of fatigue life as a function of the applied constant strain amplitude while monitoring the stress amplitude developed under such conditions. The fatigue crack propagation data were collected by standard optical measurements under constant load cycling. The experimental details are described in Chapter 3 and the analyses employed for the two techniques are outlined in Chapter 4.

Chapter 5 presents the experimental results. The results of the texture analysis are compared in Chapter 6 and the effect of crystallographic orientation upon the localised failure process and the macro-parametric characterisation of the cyclic properties is discussed. That section of Chapter 6 which considers the influence of texture on the

fatigue resistance also critically examines the cyclic stress-strain approach and its applicability to the quantitative investigation of influences such as texture. The findings of the investigation and the conclusions to be drawn from them are summarised in Chapter 7, which also includes suggestions for further work.

Three Appendices are provided which respectively reproduce the text of the cyclic stress-strain analysis program, outline the mathematical deviation of the c.o.d.f. from pole figure data and describe the influence of anisotropy on the fatigue properties of a C-Mn steel.

CHAPTER 2

Literature Review

2.1 Introduction

In engineering applications it is clearly established that a knowledge of fatigue behaviour is of paramount importance. In considering fatigue behaviour, it is normal to assume that metals and alloys are isotropic. This is despite the fact that it is well-established that, after processing to semi-finished or finished form, cubic metals possess texture (preferred orientation) and that the existence of texture normally leads to anisotropy of elastic and plastic properties. Initially, a brief summary of the various fatigue parameters of interest is presented. This is followed by an examination of data relating to the fatigue behaviour of f.c.c. and b.c.c. single crystals respectively. Attention is then turned to textured cubic polycrystals.

The intention throughout is to highlight the important ways in which metals and alloys can exhibit anisotropic behaviour under fatigue loading conditions and to indicate the extent to which assumptions of isotropy must be qualified.

2.2 Fatigue Parameters

The general nature of the fatigue failure process has been described frequently and for detailed accounts the reader is referred to a number of previous review articles⁽¹⁻⁵⁾. Since fatigue failure in metals and alloys normally involves the same processes, it is convenient, in order to examine the effects of crystallographic preferred orientation

in fatigue, to examine previous results by classifying them into four broad groups, namely,

- (i) S-N data
- (ii) Cyclic response data
- (iii) Phenomenological data relating to fatigue failure, and
- (iv) Quantitative data concerning crack propagation.

2.2.1 S-N Data

The simplest determination of the fatigue response of a material can be obtained by performing tests during which a cyclic amplitude parameter is maintained at a constant value for the duration of the test. The results from a series of such tests are presented in the form of a plot of the amplitude of the controlling parameter against the number of cycles to failure. Because many data were collected under conditions of constant stress amplitude testing, such plots are usually known as S-N curves, although the controlling parameter may also be strain, stress or strain intensity factor, etc.

2.2.2 Cyclic Response Data

Depending on the initial state of work hardening a pure metal or single phase alloy may cyclically harden or soften, before stabilising to produce a "saturation" response in which the cyclic strain produced is a function of the applied cyclic stress amplitude. In many materials this cyclic response is unique and unaffected by prior mechanical processing, although some alloys do exhibit a cyclic stress-strain response which is history dependant⁽⁶⁾. Many two-phase alloys do not, however, exhibit a "saturation" stage during fatigue, exhibiting

either continual softening or an initial hardening followed by gradual softening prior to failure.

The cyclic response of a material can be conveniently specified by its cyclic stress-strain curve⁽⁷⁾. This curve shows the corresponding stress and strain amplitudes during the "saturation" stage. Clearly the determination of this curve is time-consuming (many specimens are needed to produce one curve) and limited to materials which exhibit a saturation stage. In the absence of a saturation stage the problem may be handled by defining the cyclic stress-strain curve as the cyclic response after a given fraction of the life. A more practicable solution to both problems is to produce curves by methods⁽⁷⁾ such as the incremental step test or the multiple step test from which complete curves may be produced from a small number of specimens⁽⁸⁾.

Anisotropy of cyclic properties should, therefore, be apparent in changes in either the cyclic stress-strain curve or the rate of cyclic work hardening as a function of orientation.

2.2.3 Phenomenological Aspects of Fatigue Failure

Metallographic observations of fatigue failures indicate that prior to crack nucleation considerable modification of surface topography occurs and that fatigue crack propagation occurs in a step-wise manner with a step associated with each cycle⁽⁸⁾. Crack nucleation occurs at persistent slip bands or at cell⁽⁵⁾, grain⁽⁹⁾ or twin⁽¹⁰⁾ boundaries which may become "persistent". At these sites topographic development results from the local irreversibility of slip giving rise to inhomogeneities. The intrusions or notches which develop from these inhomogeneities become preferred sites for crack nucleation. It should be expected that crack nucleation from persistent slip bands should display

greater crystallographic anisotropy, in a manner consistent with slip symmetry, than nucleation from other sites and, therefore, it may be anticipated that surface feature development would be orientation dependent.

Fatigue fracture surfaces are often characterised by striations which are "tidemarks", delineating the position of the crack front at the end of each cycle⁽⁸⁾. Striations are most prominent at high rates of crack propagation at 90° to the stress axis. Observation of fracture surfaces can, therefore, show the position of the crack front and the local direction of propagation during any cycle and thus reveal the influence of crystallographic effects.

2.2.4 Quantitative Aspects of Crack Propagation

The resistance of a material to fatigue crack propagation may be regarded, in a similar manner to monotonic toughness, as a property specific to that material. Although a more accurate description would correlate crack advance per cycle with specified values of the applied stress amplitude and the crack length, it is usual to correlate the crack advance rate with the amplitude of the applied stress intensity factor ΔK . Crack propagation data may, therefore, be conveniently represented by plotting da/dN vs ΔK on logarithmic co-ordinates, where da/dN is the rate of crack extension per cycle. The similarity of form of $da/dN - \Delta K$ plots for many materials (Figure 1) has led to the development of a number of mathematical descriptions of fatigue crack propagation rates. While recognising that other descriptions do exist, the simplest description of crack propagation rates is that due to Paris⁽¹¹⁾,

$$\frac{da}{dN} = C(\Delta K)^m$$

where C and m are constants for a given material.

Hence, anisotropic fatigue properties should be displayed in terms of either C or m in the Paris equation. Other possible influences of anisotropy could control the range over which the Paris equation is operative i.e. by the influence on the threshold value of the stress intensity factor at one extreme and on the initiation of monotonic tearing at the other although no data are available to examine the effect of orientation on these properties.

2.3 Fatigue Behaviour of f.c.c. Single Crystals

2.3.1 S-N Data for f.c.c. Single Crystals

The simplest method of assessing fatigue properties is comparison of the number of cycles to failure at a given stress (or strain) level. The possible effect of orientation on the fatigue properties of single crystals should be revealed by this simple comparison. Unfortunately, very few data exist.

Broom and Ham⁽¹²⁾ attempted to assess orientation effects by fatiguing single crystals of copper of two orientations at similar stresses (Figure 2). Crystal A, oriented such that the applied stress axis lay well within the easy glide region of the stereographic triangle, failed after 4.9×10^5 cycles at a shear stress of $\pm 3.39 \text{ kg mm}^{-2}$ (as resolved onto the primary slip plane). Crystal B, oriented so that the stress axis lay on the $\langle 001 \rangle - \langle 111 \rangle$ symmetry line of the stereographic triangle, failed after 5.2×10^5 cycles at $\pm 3.46 \text{ kg mm}^{-2}$. Thus, while the crystals can be considered as weakly anisotropic in fatigue, in a similar way to their monotonic properties, it is surprising that the effect of possible duplex slip is so small.

On the other hand the experiments of Honeycombe and Roberts⁽¹³⁾ with single crystals of aluminium showed that large differences in life could be obtained from differently oriented crystals fatigued at the same shear stress as can be seen in Figure 3. Crystals of soft orientations, i.e. those deforming by easy glide, had much shorter fatigue lives than those crystals which lay with their stress axes near the $\langle 001 \rangle$ - $\langle 111 \rangle$ boundary of the stereographic triangle. These results were explained in terms of the cyclic hardening behaviour. (This is discussed in detail in the next section). It may be important to notice that these tests were stress controlled and, therefore, the cyclic plastic strain experienced by the crystals of the soft orientations was always greater than that experienced by the crystals of the hard orientations.

Kettunen^(14,15) has produced an S-N curve for fatigued copper single crystals by relating the resolved shear stress to number of cycles to failure, as shown in Figure 4. The experimental points appear to lie close to the curve for all orientations. It was observed that crystals which had orientations (and stress axes) close to boundaries of the stereographic triangle tended to have slightly shorter lives and at stresses relatively close to the endurance limit. More recently, Laird⁽⁶⁾ has confirmed this view by observing that the fatigue limit of copper single crystals occurs at a shear stress of 28.4 MN m^{-2} (2.90 kgmm^{-2}) below which level the cyclic strain can be accommodated without the formation of persistent slip bands (P.S.B.'s).

2.3.2 The Cyclic Response of f.c.c. Single Crystals

The first stage of the cyclic response in f.c.c. metals is the establishment of a stable stress-strain relation, occurring over the first tens of percent of life, in a manner similar to work hardening in monotonic

deformation. This cyclic work hardening can be a function of orientation. The work of Patterson and Kemsley^(17,18) demonstrated the anisotropic cyclic hardening of copper single crystals. The cyclic hardening rate under constant plastic strain amplitude cycling was found to be more rapid for crystals oriented so that the strain axis was close to the $\langle 100 \rangle$ - $\langle 111 \rangle$ boundary of the stereographic triangle (Figure 5). It is interesting to note that a crystal lying near the $\langle 110 \rangle$ strain axis did not display a very rapid hardening rate thus exhibiting the same behaviour as a corresponding crystal tested in simple tension. These results were subsequently confirmed by the work of Wadsworth⁽¹⁹⁾ who showed that crystals oriented for multiple slip showed a higher cyclic work hardening rate than those oriented for single slip.

Similar results were obtained in stress controlled cyclic testing of aluminium single crystals by Roberts and Honeycombe⁽¹³⁾. By monitoring the strain width of the cyclic hysteresis loop during the life of the fatigue test, they observed an anisotropy of fatigue hardening (Figure 3) similar to that found in copper by Patterson. The orientations which produced the most rapid cyclic hardening were close to the $\langle 100 \rangle$ - $\langle 111 \rangle$ boundary. The orientation dependence of the hardening rate could also be correlated with the fatigue life behaviour. Under stress control it was found that crystals of hard orientations exhibited greater lives than crystals of soft orientations tested under similar conditions. More recently, Sastry et al⁽²⁰⁾ showed that fatigue hardening in silver single crystals is orientation dependent. In this investigation tests were conducted under constant shear strain amplitude on two sets of crystals, the orientations of the crystals and the results are shown in Figure 6. Crystals of orientation B show higher hardening rates at the same shear strain amplitude than crystals of orientation A (for

example, compare crystals A4 and B2). This is in agreement with previous work. Orientation B is closer to the $\langle 100 \rangle$ - $\langle 111 \rangle$ boundary, and electron microscopy indicated that for this orientation deformation produces a greater forest dislocation density to which can be attributed the more rapid hardening rate. It was also noted that, not only was the saturation stress different in crystals of different orientation fatigued with the same shear strain amplitude, but also that the dislocation substructures developed at saturation in these crystals were also different. Despite these differences, the cyclic stress-strain curve of silver was plotted as being independent of orientation (Figure 7).

Following the evidence of Laird and Feltner⁽²¹⁾ that there are many similarities between monotonic and cyclic deformation, Bhat and Laird⁽²²⁾ have suggested that the cyclic stress-strain curve is independent of orientation and should be expressed in terms of shear stress and shear strain on the primary slip plane. They postulated that the cyclic stress-strain curve is composed of three portions (Figure 8),

- (a) a region below which P.S.B.'s cannot form;
- (b) an intermediate plateau where the saturation stress is independent of applied strain during which stage the reversible plastic strain is carried by the P.S.B.'s (which require a stress of 28.4 MPa to operate),
- and (c) a region where the saturation stress increases with the applied shear strain in which the whole of the specimen has the structure of a persistent slip band and the cell size within the P.S.B. can adjust to accommodate the applied strain.

The postulate that fatigue deformation and damage in the critical stages (b) and (c) are confined to persistent slip bands which lie parallel to

the primary slip plane was also applied to polycrystalline behaviour. Assuming a random aggregate, the longitudinal stress and strain data were converted to shear stress - shear strain data by assuming a Taylor factor of 3.06, i.e.,

$$\Delta\tau = \frac{\Delta\sigma}{3.06}$$
$$\Delta\gamma_p = 3.06 \Delta\epsilon_p$$

Data for both polycrystals and single crystals^(23,24) were then plotted together and Bhat and Laird, in the light of the results shown in Figure 8 concluded that the agreement between polycrystalline and single crystal cyclic shear stress - shear strain curves was quite good. In a similar manner Kettunen⁽¹⁴⁾ compared the S-N data of single crystal and polycrystal copper expressing the fatigue life as a function of the shear stress on {111} - <101> slip systems. Although the agreement between the two sets of data was not as good as was previously obtained⁽¹⁵⁾ for b.c.c. iron (see also Section 4) the correlation was regarded as reasonably satisfactory.

2.3.3 Phenomenological Aspects of the Nucleation and Growth of Fatigue Cracks in f.c.c. Single Crystals

Metallographic evidence concerning the crystallographic effects in the fatigue of f.c.c. single crystals has been obtained from studies of the topographic development of the sides of smoothly polished crystals and of the appearance of fracture surfaces. The nucleation of fatigue cracks has been associated with intrusion/extrusion pairs⁽²⁵⁾ found at P.S.B.'s (Figure 9). Specifically, it has been proposed that Stage I fatigue cracks develop, by growth along the primary slip plane, from the

intrusions adjacent to extrusions which are easily visible either optically or by scanning electron microscopy.

The importance of cross slip in the slip band extrusion process was established by Avery, Miller and Backofen⁽²⁶⁾. They fatigued single crystals of two orientations, both being oriented for single slip. Crystals of orientation A had a Schmid factor of 0.21 on the cross slip system while crystals of orientation B had a cross slip Schmid factor of only 0.026. By an electropolishing-and-taper sectioning technique it was shown that the slip band extrusion rate, after the crystal had cyclically hardened, was a function of the shear stress on the cross slip system (Figure 10).

The development of P.S.B.'s has been shown to be associated with a specific dislocation substructure in which the reversible cyclic strain is accommodated. The nucleation of fatigue cracks results from slip band-free surface interaction and the occurrence of non-reversed slip. While strain can be macroscopically reversed it is extremely unlikely that the slip occurring on each slip plane in each half cycle will be exactly reversed during the next half cycle. The role of cross slip in reducing reversibility of slip can be correlated with the superior resistance to slip band development⁽²⁷⁾ of planar slip materials over wavy slip materials. The differences in surface-developed features in single crystals of copper and copper-aluminium single crystals (wavy slip v. planar slip) are given in Table 1⁽²⁸⁾.

The tendency for cross slip to induce more rapid crack nucleation at P.S.B.'s has also been observed in single crystals. The early work of Patterson⁽¹⁷⁾ and Kemsley and Patterson⁽¹⁸⁾ showed that crystals oriented for easy glide displayed, after cyclic straining, a fine homogeneous distribution of slip lines while crystals oriented so that the axis of

cyclic strain lay near [111] developed slip bands in which the slip was coarser (Figure 11). The regions between the clustered slip bands were almost free of dislocation activity, an observation also noted by Woods⁽²⁸⁾. Although slip markings were predominantly due to slip on the primary system faint cross-slip markings were found on the surfaces of crystals strained in directions near [111].

The work of Roberts and Honeycombe⁽¹³⁾ on aluminium single crystals supports the work on slip band development in copper. The development of slip markings on the surface of aluminium single crystals does not appear as pronounced as in copper but the slip markings were of the primary slip system. Although the slip markings developed during the early stages may have contained some cross slip markings, these could be obliterated during the test. Certainly, subsequent electropolishing and testing showed that the slip markings produced later in life were due to slip on the primary slip system. The role of cross-slip in the nucleation of fatigue cracks in f.c.c. single crystals is to promote a more rapid development of the fatigue crack by reducing the microscopically reversed slip at the crystal surface.

Kemsley and Patterson⁽⁸⁾ attempted to extend their observations concerning the early stages of fatigue to cover crack propagation by postulating that the processes occurring at the crack tip are the same as those at a free surface, accelerated by the stress raising effect of the notch. This approach must be a considerable simplification since the interaction between slip bands and smooth specimen sides produces cracking on a primary slip plane which is inclined to the tensile axis and near to the plane of maximum shear stress, while crack propagation from a notch frequently occurs at 90° to the tensile axis. Laird⁽³⁾ has suggested that Stage I and Stage II crack propagation mechanisms are

variations of the same process, with the change in opening mode being controlled by the relative amplitudes of the tensile and shear components of the crack tip stress field.

Since Stage I crack propagation is usually slow, very little metallographic evidence is available to describe the effect of orientation on the process. However, if Stage I propagation is, as Laird⁽³⁾ suggests, a variation of the Stage II "sliding-off" model, then the ideas postulated concerning Stage II propagation should be applicable also to Stage I. Indeed, McEvily and Boettner⁽²⁹⁾ noted that ostensibly flat crack propagation in their aluminium single crystals could occur as the crack path alternated between two $\{111\}$ fracture planes.

The results of McEvily and Boettner showed slip band markings consistent with cross slip occurring in intersecting bands at the crack tip to produce increments of crack propagation. This idea has been extended by Neumann^(30,31) to describe Stage II propagation in terms of strain bursts along intersecting slip bands at the crack tip. This view is consistent with the plastic blunting mechanism postulated by Laird and Smith⁽³²⁾ which also involves shear in bands at the crack tip at 45° to the plane of crack propagation. Clearly both models involve the concept that Stage II propagation occurs via intersecting cross slip processes at an angle to the crack plane.

Neumann⁽³¹⁾ has recently published a systematic analysis of the effect of crack plane orientation on the fracture surface appearance of fatigued copper single crystals. By testing notched samples in 4-point bending the crack plane and crack propagation direction should be clearly defined. It was observed that the only crack planes which gave macroscopically flat fracture surfaces were the $\{100\}$ planes. Propagation on these planes in either the $\langle 100 \rangle$ direction, (notch root parallel to the

$\langle 010 \rangle$), or the $\langle 110 \rangle$ direction, (notch root parallel to the $\langle 110 \rangle$ direction), was found to give flat fracture surfaces with reasonably straight crack front striations (Figure 12). According to the coarse slip model, fatigue crack propagation occurs by slip in alternating coarse bands at the crack tip to cause separation. The crack front should therefore be determined by the intersection of $\{111\}$ planes, i.e., the microscopic crack front should be aligned along a $\langle 110 \rangle$ direction. For a crack to have a macroscopically straight front therefore it should consist of segments of two different $\langle 110 \rangle$ directions. Neumann observed that crack propagation in the $\langle 100 \rangle$ direction produces striations that are macroscopically parallel to $\langle 010 \rangle$ but consist of small segments parallel to the $\langle 110 \rangle$ directions (see Figure 13). Similar results were also obtained by Donch and Haasen⁽³³⁾ for copper single crystals.

Stage I propagation is often described as crystallographic crack propagation since it produces faceted fracture surfaces which can be shown to be approximately aligned with the $\{111\}$ primary slip plane. Leverant and Gell⁽³⁴⁾ showed that the mode of propagation in cube oriented nickel superalloy single crystals is a function of the strain rate and temperature of testing. Other work⁽³⁵⁾ on Ni-based superalloy single crystals tested at 30° to the $\langle 100 \rangle$ concluded that strain was accommodated in bands parallel to the primary slip plane and that propagation occurs due to the tensile stress at the crack tip.

The role of orientation in Stage I propagation has also been investigated in aluminium alloy single crystals⁽³⁶⁾, copper cobalt alloy⁽³⁷⁾ and copper single crystals⁽³⁸⁾. Nageswararao and Gerold⁽³⁶⁾ showed that smoother fracture surfaces were obtained when propagation occurred in the $\langle 101 \rangle$ direction on the $\{111\}$ plane. Propagation in other directions, induced by notching produced rougher fracture surfaces. The

influence of cross slip in Stage I propagation was emphasised by Meyer, Gerold and Wilhelm⁽³⁷⁾ who noted that propagation in slip bands is a thermally activated process, requiring an activation energy similar to that necessary for cross slip. The facets obtained on the Stage I fracture surfaces of copper single crystals⁽³⁸⁾ were found to be within $\pm 6^\circ$ of the $\{111\}$ primary slip plane. Propagation along the $\{111\}$ plane was attributed to cyclic softening process requiring to and fro motion in the slip bands ahead of the crack tip.

2.3.4 Quantitative Aspects of Fatigue Crack Growth in f.c.c. Single Crystals

Although very little evidence exists with regard to the quantitative effect of orientation on the fatigue of f.c.c. single crystals, the metallographic evidence discussed in Section 2.3.3 suggests that crack propagation should be accelerated by increasing cross-slip. The experimental evidence, however, does not completely confirm this and the situation is somewhat confused. A major problem in analysing fatigue crack propagation data arises from the statistical aspect of the failure process⁽³⁹⁾, such that statistical variations in propagation rates may obscure orientation effects.

McEvily and Boettner⁽²⁹⁾ correlated Stage I crack growth rates with the orientation dependence of cyclic hardening rates. Tension-compression testing of aluminium single crystals showed that crystals oriented so that the stress axis lay near the $\langle 100 \rangle$ - $\langle 111 \rangle$ boundary of the stereographic triangle had faster propagation rates than crystals of soft orientations. The growth rate in one crystal with the stress axis lying 5° away from the $\langle 100 \rangle$ - $\langle 111 \rangle$ boundary was an order of magnitude greater than in a crystal which had the stress axis over 10° away from the $\langle 100 \rangle$ - $\langle 111 \rangle$ boundary.

It has been postulated that crack growth at intermediate growth rates should follow the Paris⁽¹¹⁾ equation:

$$\frac{da}{dN} = C(\Delta K)^m$$

Orientation effects in single crystals should therefore cause variations in the parameters C or m. Donch and Haasen⁽³³⁾ analysed Stage I growth in copper single crystals of two orientations in this manner (Figure 14). Orientation E produces deformation by single slip while crystals of orientation D deform by duplex slip. The authors quote values of the exponent in the Paris equation as 3.8 for E-oriented crystals and 4.5 for crystals oriented for duplex slip from their results.

Crack propagation in notched copper single crystals deformed at room temperature and liquid nitrogen temperature was also examined by Ishii and Weertman⁽⁴⁰⁾. Their data showed that crystals having the same shear stress on the primary slip plane could display different rates of crack propagation as a function of the stress on the secondary slip systems (Figure 15). Analysing the crack propagation data in terms of the Paris equation, where the stress intensity range, ΔK , was calculated from the applied tensile load, showed that the exponent m varied from 3.5 to 6 as a function of orientation at room temperature but was a constant at liquid nitrogen temperature. The value of C was found to vary with respect to orientation at both temperatures. The larger m values were found in crystals oriented near the $\langle 100 \rangle$ - $\langle 111 \rangle$ boundary which agrees with the results of McEvily and Boettner⁽²⁹⁾.

Similar variations were not observed in single crystals of copper-aluminium, a planar slip material. The reduction in the orientation

effect by a decrease in stacking fault energy or by a decrease in temperature can be explained in terms of changes in the ease of cross slip. Ishii and Weertman⁽⁴⁰⁾ noted that the crack propagation rate was dependent on the shear stress on the cross slip plane. The variation of C is a little more difficult to explain. It would seem at first that the orientation effects could influence C through its dependence on the elastic modulus, E . Weertman⁽⁴¹⁾ has suggested

$$C = \left(\frac{\sigma_u + \sigma_y}{2} e_u \sigma_u^2 E \right)^{-1}$$

However, as Ishii and Weertman note, the temperature dependence of the elastic moduli is negligible and therefore the same variation of C should be observed at room temperature as at liquid nitrogen temperature. The reality is that C is more strongly dependent on orientation at the lower temperature.

The data of Santer and Fine⁽⁴²⁾ on single crystals of Al-3.6wt%Cu alloy suggest that crack propagation rates are independent of orientation. They did note, however, that crystals of orientations near $\langle 111 \rangle$ tensile axis required an order of magnitude longer to produce a crack of length 0.15 mm from a starter notch than crystals of softer orientations.

Yeske and Weertman^(38, 43) analysed crystallographic crack propagation in copper single crystals. Stage I crack propagation, they concluded, is only weakly dependent on orientation (Figure 16). They stated that the reproducibility of propagation rates in crystals of a given orientation was quite good with the data from each orientation being confined within a small scatter band. It would appear, therefore, that although Stage I growth in copper single crystals is orientation-

dependent it is not as strongly dependent as was suggested by Ishii and Weertman⁽⁴⁰⁾.

2.4 Fatigue of b.c.c. Single Crystals

Slip of dislocation in body centred cubic crystals is similar to slip in face centred single crystals. Before discussing the fatigue of b.c.c. single crystals it is necessary however, to draw attention to two prominent differences between slip in the two types of structures.

- (i) In b.c.c. crystals, slip is not confined solely to the closest-packed planes as it is in f.c.c. crystals.
- (ii) In b.c.c. crystals, there exists the possibility of asymmetric slip, such that for a given crystal orientation, slip of screw dislocations may occur on one plane in tension but on a different one if the crystal is under compression along the same axis⁽⁴⁶⁾.

Despite the relative ease of cross slip in b.c.c. crystals, a greater degree of anisotropy is exhibited in fatigue in comparison with f.c.c. single crystals. The major anisotropic effect is, therefore, caused by asymmetric slip and not, as in the case of f.c.c. crystals, by the confinement of slip to close-packed planes.

2.4.1 S-N Data for b.c.c. Single Crystals

In early experiments on fatigue of iron (.006%C) crystals in bending fatigue, Hempel⁽⁴⁴⁾ found little effect of orientation upon the

S-N curve. He plotted the macroscopic fatigue bending stress against the number of cycles to failure and suggested that the experimental data could be represented by a single curve (Figure 17). It was pointed out, however, that since slip in b.c.c. crystals is not confined to closest-packed planes the applied stress should be resolved onto the operative $\{112\}$, $\{101\}$ or $\{213\}$ slip plane with a $\langle 111 \rangle$ slip direction. If this was done for the crystals which were used, it was found that for the same applied bending stress the shear stress resolved onto the operative slip plane would be the same to within 10%. Hempel's data have been reanalysed by Kettunen⁽¹⁵⁾ and presented in terms of the resolved shear stress amplitude of the operating pencil glide or $\{101\}$ slip system, (Figure 18). Also shown in this Figure are the S-N curves for polycrystalline material (with the shear stress determined from the applied stress using the appropriate Taylor factor) which seem to agree quite closely with the single crystal data. Kettunen concluded that the fatigue behaviour of b.c.c. -iron and f.c.c. - copper single crystals is very similar. Such a comparison may be misleading for two reasons:

- (a) As already cited, only a limited range of orientation factor is involved in relating the macroscopic bending stress to the resolved shear stress. No data come from orientations of the stress axis near $\langle 110 \rangle$ where the Schmid factor is only 60% of that for the crystals tested.
- (b) The purity of Hempel's crystals is not directly specified but the polycrystalline iron prior to strain annealing contained 480 ppm oxygen plus other interstitial solutes. Nine⁽⁴⁵⁾ has recently shown that the

impurity content of b.c.c. Niobium single crystals is important in determining the slip characteristics in fatigue. In particular, oxygen was found to have the ability to inhibit asymmetry of slip and to produce persistent slip bands at the surface, similar to the P.S.B.'s observed on fatigued copper crystals.

Therefore, the results of Hempel must be treated with caution with regard to the orientation effects in the fatigue of b.c.c. single crystals. Work on single crystals of iron^(46, 47, 50), molybdenum⁽⁴⁸⁾ and niobium^(44, 49, 50, 51), has demonstrated the effect of asymmetric slip in the fatigue of b.c.c. metals. Mughrabi and Wuthrich⁽⁵¹⁾ suggested that the fatigue limit of iron single crystals may be ascribed to the to-and-fro motion of edge dislocations at low stresses. Increasing the stress range should produce motion of screw dislocations which would lead to asymmetric slip and failure.

Nine⁽⁴⁵⁾ proposed that the sole cause of anisotropic fatigue properties in b.c.c. crystals is the asymmetry of slip in this structure, since the greater ease of cross slip in b.c.c. crystals should render them relatively more isotropic than f.c.c. single crystals. Asymmetric slip produces rapid development of localised fatigue damage and hence accelerates failure. Asymmetry of slip occurs when crystals are oriented such that the resolved shear stress on the operative slip plane is far greater than on any other slip plane. The asymmetry derives from the asymmetry in the critical resolved shear stress necessary for screw dislocation glide on the various systems. The relationship between the critical resolved shear stress was described as:

$\langle 111 \rangle (112)$ (soft direction) \ll $\langle 111 \rangle (011)$ \ll $\langle 111 \rangle (112)$ (hard direction)

The degree of asymmetry of slip displayed by a single crystal in fatigue can be correlated with a decrease in fatigue life. Nine^(46,47) showed that crystals of iron fatigued in torsion display asymmetric slip behaviour if the stress axis is near $\langle 123 \rangle$ but not if the stress axis is near $\langle 112 \rangle$. The corresponding fatigue lives at a surface shear strain of ± 0.002 were 3.0×10^5 for the specimen deforming by asymmetric slip and 3.7×10^6 for the $\langle 112 \rangle$ oriented crystal deforming with symmetric slip. This applied strain is only slightly greater than the lowest strain which was found to cause fatigue failure (± 0.0018).

Results from fatigue tests of iron, molybdenum and niobium single crystals^(50,51) have shown that accelerated failure occurs due to rapid localised damage and that large unreversed strains (~ 1) may be produced prior to crack nucleation. This process of accelerated nucleation may be inhibited by suppressing asymmetric slip. In niobium, it was found⁽⁴⁵⁾ that asymmetry of slip could be suppressed by the concentration of interstitial solute elements and that the resulting surface deformation (Figure 19) resembled the persistent slip band features found on the surface of fatigued copper crystals. The S-N data from Nine's work are reproduced in Figure 20. It is immediately obvious that while no distinct S-N curve can be drawn through any set of points the data can be divided into two quite separate distributions with the crystals which had deformed by asymmetric slip consistently show poorer fatigue lives.

2.4.2 The Cyclic Response of b.c.c. Single Crystals

The effect of asymmetric slip upon cyclic hardening has also been investigated in iron⁽⁵¹⁾ molybdenum⁽⁴⁸⁾ and niobium⁽⁵⁰⁾ single crystals. Mughrabi and Wuthrich⁽⁵¹⁾ examined the cyclic stress-strain curve of

iron single crystals and recorded a three-part curve (Figure 21). A small amount of cyclic plastic strain may be accommodated by the to-and-fro motion of edge dislocations in the same plane. At intermediate levels of cyclic plastic strain, slip over greater distances is required. This results in the immobilisation of edge dislocations by dislocation reactions, a greater dependence on the motion of screw dislocations and the necessity for an increased rate of dislocation multiplication. This behaviour is reflected in the cyclic stress-strain curve by a large increase in the rate of cyclic work hardening and in an increasing asymmetry of slip. In Figure 21(b) the way in which the degree of slip asymmetry is dependent upon the applied cyclic plastic strain is shown. The measure of asymmetry is derived from the changes in cross-sectional shape which develop when crystals of originally circular cross-section are fatigued. In the region of higher applied strain the cyclic hardening rate levels off, even though the degree of slip asymmetry is quite high, it no longer increases with the applied cyclic strain range. Mughrabi and Wuthrich⁽⁵¹⁾ described the deformation mechanism in region C as irreversible cyclic macrostrain. It was suggested that region A, described as quasi reversible microstrain, describes fatigue deformation below the fatigue limit. The transition from region A to region B should, therefore, define the fatigue limit. This agrees with the work of Nine⁽⁴⁵⁾ who found that fatigue failures in iron single crystals did not occur if the applied surface shear (in torsion) was below ± 0.0018 .

Etemand and Guiu⁽⁴⁸⁾ performed cyclic hardening experiments between constant total strain limits on molybdenum single crystals of two orientations with $\langle 100 \rangle$ and $\langle 110 \rangle$ tensile axes, respectively. Their results showed that flow stress asymmetry existed in crystals

oriented in either direction whenever cyclic plastic straining occurred. The cyclic stress-strain curves which were derived from the saturation values of the stress-strain hysteresis loop, are shown in Figure 22. At lower plastic strain amplitudes the hardening rates of crystals of both orientations were very similar but at stresses greater than 300 MNm^{-2} crystals of the $\langle 100 \rangle$ orientation exhibited a work hardening rate which was significantly greater than that of $\langle 110 \rangle$ oriented crystals. It is at this stress that the monotonic deformation curve exhibits a proportional limit. As the cyclic plastic strain amplitude increased the asymmetry of the saturation stress also increased, with the crystals of $\langle 100 \rangle$ orientation showing a greater effect than those of $\langle 110 \rangle$ orientation. It should be remembered, however, that the Schmid factor for the $\langle 110 \rangle$ stress axis orientation is approximately 60% of that for $\langle 100 \rangle$ stress axis orientation. Due to the coincidence of the monotonic proportional limit, the cyclic stress level at which rapid cyclic hardening begins and the appearance of saturation stress asymmetry it may be concluded that the asymmetric cyclic behaviour of molybdenum single crystals is very similar to that described by Mughrabi and Wutrich⁽⁵¹⁾ for iron single crystals.

Doner et al⁽⁴⁹⁾ investigated the cyclic hardening response of niobium single crystals of three orientations, (Figure 23). They suggested that a unique cyclic stress strain curve exists for niobium of the form

$$\frac{\Delta\tau}{2} = k \left(\frac{\Delta\gamma_p}{2} \right)^n$$

where the stresses are resolved onto the $\{101\} \langle 111 \rangle$ slip systems since

metallographic evidence indicated that the crystals deformed by these systems only. This is in contrast to other results^(45,51) and it is possible that the purity of the crystals was such as to inhibit asymmetric deformation. It should be noted, however, that this does not make the fatigue properties independent of orientation since, in a similar manner to the behaviour of f.c.c. crystals, the restriction of slip to well defined crystallographic planes renders the fatigue properties anisotropic in a manner consistent with the symmetry of the cubic system. Despite the symmetrical slip observed in this investigation, the hardening rate of the niobium crystals was reported to be lower than that in copper crystals and this was attributed to the ease of cross slip of screw dislocations in the b.c.c. structure.

2.4.3 Phenomenological Aspects of the Nucleation and Growth of Fatigue Cracks in b.c.c. Single Crystals

The most easily identifiable difference between f.c.c. crystals and b.c.c. crystals in fatigue is the shape change induced in the cross section of b.c.c. crystals oriented for asymmetric slip. Such shape changes have been observed in iron, niobium and molybdenum^(46,51,52). Nine⁽⁴⁶⁾ showed that iron single crystals oriented along {123} and fatigued in torsion exhibited heavy localised deformation at two positions, 180° apart over the cross section of the crystal. The effect of such asymmetric slip has been explained in the work of Mughrabi and Wuthrich⁽⁵¹⁾ and Neumann⁽⁵²⁾ for iron and niobium, respectively. Mughrabi and Wuthrich showed that as long as asymmetric deformation is occurring the degree of ellipticity increases with each reversal, the positions of the major and minor axes of the ellipses are determined by the projection of the Burgers Vector of the screw dislocations on to the cross section of the crystal. The change in shape of the crystals, as a function of

accumulated plastic strain is shown in Figure 24. At larger strain amplitudes the crystals also deformed into an S-shape, a feature observed by Neumann⁽⁵²⁾ after push-pull cycling of niobium single crystals. This effect is due to the interaction of asymmetric slip and the constraints can only be relieved by deformation on systems other than the one activated by the cyclic stress⁽⁵¹⁾.

The movement of material during fatigue of b.c.c. single crystals has been observed by Nine⁽⁴⁵⁾ using a technique which employed fiducial marks parallel to the long axis of crystals fatigued in torsion.

Figure 24 shows the motion of material around the circumference of torsional fatigue specimens as a function of azimuthal angles. The positions of asymmetric slip can be determined by plotting the relative resolved shear stress for the possible slip systems as a function of the azimuthal angle about the crystal. When this was done it was found that the heavy asymmetric slip lines were located at positions corresponding to the maxima of the relative resolved shear stresses. The number and positions of such maxima are functions of the orientation of the crystals. For the torsional fatigue experiments of Nine⁽⁵⁰⁾ it was reported that crystals oriented near the $\langle 123 \rangle$ axis displayed two very strong azimuthals, crystals oriented near the $\langle 110 \rangle$ display four, somewhat weaker azimuthals, while crystals oriented near $\langle 112 \rangle$ showed no signs of asymmetric slip.

The large localised strains accumulated during asymmetric slip provide sites suitable for fatigue crack nucleation. The slip marking of crystals oriented along $\langle 001 \rangle$ have been reported^(50,53) to be much less severe and less localised than those on the surface of a crystal oriented along $\langle 123 \rangle$. The rapid development of slip markings due to asymmetric slip accelerates fatigue crack nucleation and is reflected

in the shorter fatigue lives of crystals which deform by asymmetric slip.

Mughrabi and Wuthrich⁽⁵¹⁾ pointed out the possible technological significance of accelerated nucleation due to asymmetric slip in polycrystals. In the interior of a polycrystal the deformation undergone by any given grain is determined by the applied stress or strain state and the requirements of stress/strain compatibility across grain boundaries. However, at the specimen surface, these constraints are relaxed and significant surface rumpling can occur. In polycrystalline α -iron after fatigue, micro-cracks were found to nucleate at grain boundaries. The strain rate dependence of the susceptibility to grain boundary cracking suggests that it is related to the asymmetric properties of b.c.c. metals.

It is always difficult to extend the evidence from work on pure single crystals to polycrystalline materials of technological importance. It will certainly be important to determine if asymmetric slip plays a role in the fatigue cracking of technologically useful b.c.c. metals. Nine⁽⁴⁵⁾ and Doner et al⁽⁵⁰⁾ fatigued niobium single crystals which did not show asymmetric slip and both found the surface markings to be similar to those found on copper crystals, giving rise to fatigue crack nucleation in persistent slip bands. It is possible, therefore, that asymmetric slip would be suppressed in less pure b.c.c. metals and hence produce a weaker orientation dependence of fatigue properties than observed in pure single crystals.

Very little evidence exists in relation to fatigue crack growth in b.c.c. single crystals. Recently it was demonstrated⁽⁵⁴⁾ that fatigue cracks in Fe-3%Si grew in accordance with the "coarse-slip" mechanism. Previously, it had been shown⁽³¹⁾ that this mechanism operated during fatigue of copper single crystals. The conditions

required to produce flat fracture surfaces with straight crack fronts are not as severe in Fe-3%Si as in copper and it is postulated that a number of configurations are possible. In the later work however, another feature of fatigue fracture that is not observed in f.c.c. metals was observed, fatigue cracks in Fe-3%Si were found to propagate at larger crack opening displacements by a cyclic cleavage mechanism, which produces {100} brittle facets on the fracture surface.

Rieux, Driver and Rieu⁽⁵⁵⁾ using a technique similar to that of Neumann, have examined the rate of crack propagation in single crystals of austenitic and ferritic stainless steel single crystals. By testing the crystals in 3-point load controlled bending they were able to control the macroscopic fracture plane and the macroscopic direction of crack propagation. In accordance with the results of Neumann⁽³¹⁾ it was found that macroscopically flat fracture surfaces were obtained for {100} fracture planes in the austenitic alloy. However, it was also noted that flat fractures could be obtained by fatigue crack propagation on {100} planes in the $\langle 011 \rangle$ direction and also on {110} $\langle 111 \rangle$ and {112} $\langle 110 \rangle$, combinations of crack plane and direction of propagation which according to the 'sliding-off' theory of Neumann, should not produce macroscopically flat fractures. It was also noted that in both the f.c.c. and the b.c.c. crystals the orientations which produced the most rapid crack propagation also developed macroscopically flat fracture surfaces. Rieux et al consider that the process of fatigue crack growth is due to the accommodation of strain at the crack tip by shear in two bands which are inclined to the stress axis. The theory is similar to that of Neumann except that the strain is accommodated not by slip on single planes but by multiple slip in narrow bands. Analysis of the slip processes in the two bands in terms of the allowable slip

modes seem to produce reasonable agreement between the crack orientations which should produce plane strain conditions at the crack tip and those orientations which were observed to produce macroscopically flat fracture surfaces.

2.5 Summary of Fatigue of Cubic Single Crystals

2.5.1 S-N Data

Although it is not possible to quantify the effect of crystal orientation upon S-N curves it is clear that the stress amplitude life relationship is orientation dependent for both face centred and body centred cubic metals. In b.c.c. crystals asymmetric slip produces more rapid failure while ⁱⁿ f.c.c. single crystals and b.c.c. crystals in which asymmetric slip is inhibited, S-N relationships are exhibited which can be reduced as a first approximation to an S-N curve in which the stress parameter is the resolved shear stress amplitude on the primary slip plane. In a similar manner the fatigue limit of metal single crystals of both structures has been shown to be orientation dependent.

2.5.2 The Cyclic Response of Cubic Single Crystals

The rates of cyclic hardening in cubic single crystals have been shown to be orientation dependent. The cyclic work hardening rate of b.c.c. single crystals in which asymmetric slip is possible can be correlated with the degree of asymmetry of slip. In face centred structures the cyclic work hardening rate increases with slip activity on secondary slip systems and crystals oriented with the stress axis near to the $\langle 100 \rangle$ - $\langle 111 \rangle$ boundary harden more rapidly than those crystals oriented initially for easy glide. The amplitude of the resolved shear

stress at saturation appears to be a function of the applied shear strain amplitude only for f.c.c. crystals. For b.c.c. crystals the possibility of asymmetric slip produces an orientation dependence of the saturation shear stress amplitude, and hence, also of the cyclic shear stress-strain curve. Since most of the data pertaining to the cyclic response of single crystals have been obtained using orientations which deform initially in single slip the effect of multiple slip on the cyclic stress-strain curves of single crystals and polycrystals is difficult *to analyse*. Although such comparisons have been made it would be better possibly to compare the cyclic stress-strain curves of polycrystals of different textures and to produce the cyclic shear stress-shear strain curves using the appropriate Taylor factors. These may be calculated directly from texture measurements⁽⁵⁶⁾.

2.5.3 Phenomenological Aspects of Nucleation and Growth of Fatigue Cracks in Cubic Single Crystals

The nucleation of fatigue cracks in cubic single crystals is accelerated by local irreversibility of plastic strain, this produces a notch-peak topography of a form which can provide sites for fatigue crack initiation. In some orientations of b.c.c. single crystals highly localised surface damage is rapidly accumulated as a result of asymmetric slip. In f.c.c. single crystals fatigue cracks nucleate in persistent slip bands at free surfaces and more rapid nucleation occurs with increasing amounts of cross slip. The rate of development of a notch-peak topography within a slip band has been shown to be orientation dependent in that surface damage accumulates more rapidly as the shear stress on the cross slip system increases.

Metallographic evidence indicates that fatigue crack propagation in cubic single crystals is a crystallographically-controlled process.

Stage I crack propagation occurs along slip bands, which in f.c.c. crystals form parallel to the $\langle 111 \rangle$ primary slip planes. Stage II crack propagation in cubic single crystals appear to be satisfactorily described by the "plastic-blunting" or "coarse-slip" models which require the activation of two intersecting slip systems at the crack tip. The influence of crystallographic orientation on Stage II fatigue crack propagation in single crystals is highlighted by the stringent conditions required to produce macroscopically flat fracture surfaces and straight crack fronts in single crystals of copper and iron-silicon. The appearance of facets on fatigue fracture surfaces has been recognised as a product of crystal orientation although such facets may not necessarily be produced by a true cleavage mechanism.

2.5.4 Quantitative Aspects of Fatigue Crack Growth in Cubic Single Crystals

Due to the lack of available data to correlate fatigue crack growth rates with crystal orientation in b.c.c. single crystals the following remarks apply to crack growth in f.c.c. single crystals. Stage I fatigue crack growth rates are more rapid in single crystals in which the stress axis lies close to the $\langle 100 \rangle$ - $\langle 111 \rangle$ boundary of the stereographic triangle. This is reflected in the value of the "m" parameter in the Paris equation. It has been suggested, however, that although fatigue crack propagation rates in f.c.c. single crystals are orientation dependent, this dependence is rather weak.

2.6 Fatigue Behaviour of Textured Polycrystals

2.6.1 The Interaction of Texture and Fatigue in Cubic Metals

Very little attention has been paid to the effects of preferred

orientation (crystallographic texture) on the behaviour of cubic polycrystals under cyclic loading. It is usual to analyse polycrystalline properties in terms of a random aggregate of crystals. While this approach has met with some success, it must be recognised that thermo-mechanical processing can induce significant anisotropy due to the development of textures⁽⁵⁶⁾. Bhat and Laird⁽²²⁾ analysed polycrystalline data in terms of the resolved shear stress and shear strain by using a Taylor factor of 3.06 and showed that the cyclic stress-strain curve which they obtained agreed quite well with the curve obtained from a single crystal oriented for slip on one system only. It is obvious, therefore, that if the Taylor factor M is not an isotropic property, which will be the case for textured materials, the macroscopic cyclic stress strain curve (applied longitudinal stress - longitudinal strain) will be determined by the relative orientation of the stress-strain axes to the principal components of the texture.

Some reports have indicated that, in a manner analogous to metal working, not only does texture affect the bulk properties in fatigue but that the fatigue process itself may induce some degree of preferred orientation^(57,58), (it has also been reported that the development of texture could be used to monitor fatigue damage although this approach does not appear to be very successful⁽⁵⁹⁾). Hayashi and Suzuki⁽⁵⁷⁾ monitored texture changes in polycrystalline copper under fully reversed loading and concluded that fatigue tends to randomise the texture. In contrast Inakozu and Yamamoto⁽⁵⁸⁾ found that under torsional fatigue the most stable orientations were $\{110\}\langle 111 \rangle$ and that grains of other orientations tended to rotate towards $\{110\}\langle 111 \rangle$. They suggested that the endurance limit was controlled by the texture with the stable orientation resulting in a higher endurance limit. Inakazu and Yamamoto⁽⁵⁸⁾

correlated the instability of texture with the more rapid crack nucleation in those specimens by postulating that grain rotations require increasing components of cross slip, which, once activated, produce the topography required for crack nucleation.

There exists, therefore, confusion with regard to the development of texture during fatigue of f.c.c. metals. The work of Hayashi and Suzuki⁽⁵⁷⁾ can be criticised on several points, despite the apparent agreement between their experimental data and theoretical calculations. Axisymmetric textures were assumed and on this basis texture measurements were made on composite specimens cut at 45° to the axis of the fatigue specimen. The pole figures shown for initial material do not entirely support this view. The computed and experimental textures were compared after 10, 50 and 100 cycles at 0.7% strain. These are quite small fractions of life at this strain and are probably not sufficient to allow the detection of the development of a particular preferred orientation. However, it would be possible to observe material rotating away from an unstable orientation. Thus it is possible that the randomisation observed by Hayashi and Suzuki⁽⁵⁸⁾ is the flow of material towards more stable orientations. It is obvious that many more data are needed to clarify the development of preferred orientation during fatigue.

2.6.2 The Effect of Texture on the Fatigue Lives of Cubic Metals

A most comprehensive investigation of textured effects was reported by LeMay and Nair^(60,61,62). Three f.c.c. materials were tested, namely, aluminium-2.5% magnesium, tough pitch copper and super pure aluminium, in fully reversed bending. By cutting specimens parallel to either the rolling direction or the transverse direction of the sheet

specimens were tested which were identical in all aspects save orientation. Typical results are shown in Figure 25. The cold rolled sheet materials displayed $\{110\}\langle 112 \rangle$ textures, the annealed aluminium alloy exhibited a random texture while annealing of the copper produced $\{100\}\langle 001 \rangle$ ("cube" texture). The transverse proportions of the cold rolled material are seen to be consistently better than these in the rolling direction, while the S-N curves for the annealed materials are found to be coincident. On the basis of these findings, LeMay and Nair postulated that the effect was due to texture and not some form of microstructural inhomogeneity. While it is probable that this is correct it is important to point out that these experiments did not rule out effects of microstructural anisotropy arising from variations in grain shape. In the cold rolled specimens the structures at 0° and 90° differ, not only in texture, but also in grain size (intercept parallel to the stress axis), in the annealed materials the structures are identical in terms of texture and grain size intercept.

2.6.3 Phenomenological Aspects of Fatigue Failure in Textured Cubic Materials

The work of Nair and LeMay established that the modes of crack initiation and propagation are determined by the crystallographic texture. In cold rolled materials, cracks initiated by the link up of many surface micro cracks, presumably along substructure cell boundaries as described by the "H-mechanism" of Wood⁽⁵⁾. In the annealed cube-texture copper crack nucleation occurred by the development of persistent slip bands in the randomly-textured alloy surface damage consisted of both types, the "H-mechanism" being more prominent at higher stress levels⁽⁶¹⁾. It was also found that the mode of crack propagation can be

influenced by texture, in particular the transition from Stage I to Stage II propagation. This is presumably due to the constraints imposed on the crack tip stress field by the texture. Thus in cube textured specimens tested along the cube directions shear is easily accommodated on the $\{111\}$ planes and, hence, Stage I crack growth is preferred to Stage II growth. This is, of course, an oversimplification of the problem as in even very severe textures only a small fraction of the material is suitably oriented, (e.g. for a very severe cube-texture copper less than 25% of material is oriented within 10° of the $\{001\}$ $\langle 100 \rangle$ orientation⁽⁶³⁾). It does, however, indicate the mechanism by which preferred orientation may control crack initiation.

Nair and LeMay came to the apparently erroneous conclusion that texture affects the fatigue behaviour of f.c.c. metals by its influence on ductility. They proposed that the mechanism of fatigue crack propagation contains "a ductile component...and a brittle fracture component"⁽⁶²⁾. They suggested that the orientation of each grain with respect to the stress axis encourages one mode or the other. Grains oriented to promote shear fail by cyclic slip while grains of other orientations may adopt a tensile cracking mode. It was also pointed out, however, that textural influences could be greater than the effect of stress magnitude, which suggests that the constraints imposed by preferred orientation serve to modify the conditions imposed by the applied stresses, possibly on a scale greater than the grain size. (Such a modification of the cyclic plastic zone at a crack tip has been observed in a titanium alloy by Tchorzewski and Hutchinson⁽⁶⁴⁾).

While it may not be possible to consider crack propagation in terms of localised events, the nucleation and very early growth of fatigue cracks have been correlated with the orientation of individual grains.

Amell and Teer⁽⁶⁵⁾, using an X-ray microbeam technique, showed that topographic development at surface grains was consistent with the slip systems that would be activated in a single crystal of that orientation under the same applied stress, except in grains in which the stress axis lay near the $\langle 100 \rangle$ - $\langle 110 \rangle$ boundary of the triangle. Then the secondary slip system which was activated appeared to be the conjugate rather than the critical slip plane. It was noted that cracks could be initiated in grains of almost any orientation (nucleation is difficult near $\langle 111 \rangle$), but that microcracks which nucleate in grains oriented for multiple slip do not propagate due to the greater ability of these grains to harden. The more rapid propagation of cracks nucleated in grains oriented such that the stress axis lies in the centre of the stereographic triangle suggests that these grains are effectively fatigued under higher strain amplitudes than those grains of harder orientations.

Nair and LeMay observed that the fracture surfaces of cube-oriented specimens were featureless in comparison to the fracture surfaces of specimens in which propagation occurred by Stage II propagation. This is consistent with the usual lack of features on the fracture surfaces of Stage I failures. Indeed Laird⁽³⁾ has commented that it is precisely this lack of evidence that makes analysis of stage I failure so speculative. It is recognised that Stage I failure occurs on slip planes, probably by a variation of the sliding-off mechanism. However, the appearances of a crystallographically faceted fracture surface does not necessarily imply failure in the Stage I mode. Flat crystallographic facets have been observed on fatigue fracture surfaces of aged aluminium alloys. Etch pitting⁽⁶⁶⁾ and X-ray diffraction⁽⁶⁷⁾ techniques confirm that the facets are parallel to the $\{100\}$ crystal planes. Forsyth et al⁽⁶⁶⁾ in 1962 suggested that crack propagation occurred by a

mechanism which involved two competing processes, producing a zone of ductile fracture and a zone of brittle cleavage within each fatigue striation. Garrett and Knott⁽⁶⁷⁾ found facets on the fatigue fracture surface of another aluminium alloy. Although their micro-diffraction data indicated that the facets were produced by a fracture mechanism which involved very little plastic deformation, crack propagation by cleavage was discounted on the basis of environmental effects. It was postulated that cube-oriented facets are produced under conditions of restricted slip, requiring dislocation interactions on two intersecting $\{111\}$ planes at the crack tip to produce a crack advance on a $\{100\}$ plane.

Similar crystallographically dependent mechanism have been shown to operate in b.c.c. materials. Fukui et al⁽⁶⁸⁾ observed that fatigue crack propagation in iron-3% silicon tended to occur on $\{110\}$ or $\{100\}$ planes. Crack propagation which is initially inclined to these planes tended to produce a curved surface so that the crack plane bent around until it became parallel to the crystallographically specified plane. Because of this tendency the striation pattern was somewhat complex but the striation direction was identified as being parallel to the line of intersection of the macroscopic fracture plane and the $\{110\}$ or $\{100\}$ planes. It was not possible to ascribe any particular mechanism to this crystallographic mode of failure but it was suggested that the phenomenon could be generally accounted for by a modified version of the sliding-off mechanism. Richards⁽⁶⁹⁾, who also investigated the fatigue of iron-silicon, found that the fracture surface topography was a function of the orientation of the stress axis with respect to the texture. Using sheet specimens, Richards noted that flat, 90° fracture was obtained only in specimens parallel to the $\langle 001 \rangle$ components of the *Cross*-textured material and that fatigue striation spacing could

vary widely from grain to grain. (The grain size of the Fe3%Si was reported as 3.85 mm.).

2.6.4 Quantitative Aspects of Fatigue Crack Propagation in Textured Cubic Metals

The fractographic observations of Richards⁽⁶⁸⁾ mentioned in the previous section, suggest that crack propagation rates in iron-silicon may be texturally controlled. The crack propagation data *are* reproduced in Figure 26. Correlating the experimental data to a Paris type equation Richards noted that the m parameter varied between 2.4 and 4.6 although this variation cannot be systematically correlated with the texture.

Slip line studies indicated that flat fracture surfaces were produced under conditions of plane strain. The ability of the texture to limit the in-plane deformation, for certain orientations of the stress axis, produces slant crack growth. Growth of fatigue cracks oriented at an acute angle to both the through thickness direction and the stress axis require slip in the through-thickness direction and produce crack opening displacements that are not parallel to the stress axis⁽⁷⁰⁾. It has been shown that mixed-mode opening results in more rapid crack propagation⁽⁷¹⁾, although the data of Richards do not agree with this simplification, i.e. flat, 90° fractures were produced by fatiguing specimens at 0° to the rolling direction and yet these specimens displayed the highest crack propagation rates. Similar effects have also been observed in thin copper sheet fatigued in cyclic tension⁽⁷²⁾, it is clear that fatigue crack growth in cubic metals, at least in thin sheet, can be significantly affected by texture.

2.6.5 Fatigue Anisotropy in Hexagonal Polycrystals

The anisotropy of mechanical properties which result from the preferred crystallographic orientation in hexagonal metals is much more marked than that in cubic metals and has been much more widely noted. The anisotropy of hexagonal metals derives from the restriction of slip to the basal plane. The activation of slip on other planes is often difficult and twinning is often preferred as a secondary mode of deformation. The presence of such severe mechanical anisotropy in the single crystal properties causes thermomechanical processing to induce exceptionally sharp textures in polycrystalline samples and thus, in turn, to produce severe mechanical anisotropy. Although the investigation reported in this thesis is concerned with the influence of texture on the fatigue properties of a cubic metal the available data pertaining to the influence of texture in hexagonal metals will be reviewed in order to emphasize that the combination of anisotropic single crystal properties and the existence of crystallographic preferred orientation in polycrystals does lead to anisotropic fatigue properties in polycrystalline materials.

2.6.5.1 Zinc

Extruded zinc rod shows an unconventionally flat S-N curve⁽⁷³⁾. The fibre texture which exists after extrusion ($\{0001\}$ fibre with $\{1010\}$ lying in the transverse direction) is thought to contribute to this by encouraging the twinning mode of deformation. Surface-twin boundaries facilitate fatigue crack nucleation, and this results in early nucleation and thus accelerated failures at lower stress.

2.6.5.2 Titanium Alloys

Accelerated fatigue crack nucleation associated with surface twins

has also been reported in Ti-4Al-4V⁽⁷⁴⁾. Figure 27 is taken from this work and it clearly shows the inferior properties of specimens taken from the transverse directions of rolled plate as compared with specimens taken from the longitudinal direction. The reported texture data indicate that the stress imposed on the longitudinal specimens would suppress twin formation while testing specimens parallel to the plate direction would encourage deformation by twinning. The reported surface observations confirmed the view that surface twins accelerate fatigue crack nucleation since in the specimens oriented to suppress twinning fatigue crack nucleation occurred by the development of intrusions in persistent slip bands while crack nucleation in the other group of specimens resulted from twin-matrix interactions.

Fatigue crack propagation has also been shown to be influenced by texture in Ti-6Al-4V⁽⁷⁵⁾. Single edge notch specimens were produced from a cold rolled and annealed plate (of almost single crystal texture). The specimens were machined such that the crack plane normal and the direction of crack growth were parallel to two of the three axes of the plate and were sufficiently large to produce conditions of plane strain at the crack front. Crack propagation was monitored during load-controlled testing and the results fitted to equations of the form⁽¹¹⁾,

$$\frac{da}{dN} = C(\Delta K)^m$$

Bowen⁽⁷⁶⁾ found that the data were composed of two subsets, one set of orientations were characterised by $m = 2.5$, the m value of the other orientations was about 4.1.

The orientations which exhibited the lower m value produced symmetrical slip conditions at the crack front while satisfying the



plane strain conditions. In the specimens of the other orientations, plane strain boundary conditions and a symmetrical slip process at the crack front were incompatible. This difference in behaviour is also revealed in the fracture surfaces. Failures in tests giving rise to low m values had fracture surfaces which showed uniform striations while the fracture surfaces of the high m value specimens had a very irregular topography. Crack propagation resulting in a low m value has been associated with a pure fatigue mode of propagation, controlled by the reversible plastic strain at the crack tip, while a higher m value has been associated with non-crystallographic crack advance, incorporating some degree of monotonic failure such as ductile tearing⁽⁷⁶⁾.

The effect of the relative orientation of the cyclic stress axis to the axes of textured Ti-6Al-4V plate was clearly demonstrated by Tchorzewski and Hutchinson⁽⁶⁴⁾. They demonstrated that the fatigue crack path is not determined by the applied stress alone but the influence of texture may cause the crack to deviate from the plane which is normal to the applied stress axis. Significant deviation of the crack plane was found to occur in specimens in which the notch front was parallel to the plane of the original sheet and the initial directions of crack propagation more inclined at 22.5°, 45° and 67.5° to the rolling direction. For the $\{11\bar{2}0\}\langle 1\bar{1}00\rangle$ texture found in this material symmetrical slip conditions are not produced at the crack tip in specimens of those orientations. To explain the behaviour, a model was developed which was based on Neumann's "sliding-off" model⁽³⁰⁾ of fatigue crack propagation. For the three orientations, which produce crack deviation from the plane of maximum normal stress, slip in direction at $\pm 45^\circ$ to the stress axis cannot be accommodated by

identical processes. Sliding-off in one direction is easy, requiring predominantly basal slip, while slip in the other plane of maximum shear stress requires more difficult $\langle c + a \rangle$ -type slip. The asymmetry of slip at the crack tip was confirmed by mapping the crack tip plastic strain field using the technique of selected area channelling patterns to demonstrate that the crack deviation is towards the direction of easier slip.

2.6.5.3 Zircalloy

The deleterious effect of twinning upon the rate of fatigue crack propagation has also been observed in textured zircalloy^(77,78). The results of this investigation suggested that accelerated rates of fatigue crack propagation occurred by the production of twins in the crack tip plastic zone during the compression half of the cycle and cracking of the twin interface during the following tensile half cycle. It was also noted that fatigue crack initiation was influenced by the crystallographic orientation of surface grains. Swaged rod, which had developed a fibre texture, had a uniform distribution about the circumference of cracks which had formed at the intersection of $\{1010\}$ slip planes. However, cracking in specimens machined from plate material was characterised by the orientation of the surface relative to the axes of the plate, since the thermomechanical treatment had produced a texture in which the basal poles were clustered about the normal direction of the plate. Thus, the orientation of grains with respect to the surface normal is very different in the two orientations where the surface normals correspond to two of the axes of the plate. (In this investigation, specimens were machined to the form of round, hour-glass shaped specimens with the long axis parallel to the original

transverse direction of the textured plate). For orientations away from the original plate normal, cracking was reported to occur at the intersection of slip planes, in a similar manner to the process in the swaged material. However, when the surface normal was parallel to a high density of (0002) poles cracking occurred at 90° to the stress axis⁽⁷⁷⁾.

The anisotropy of fatigue properties of zircalloy also produces a cyclic stress-strain response which is orientation dependent⁽⁷⁸⁾. It was found that the cyclic stress-strain response varied with the positioning of the diametral extensometer about the minimum circumference of the hour-glass specimens. Strain controlled testing showed that the diametral strain amplitude parallel to the original rolling direction of rolled and annealed plate material was much greater than the diametral strain amplitude parallel to the original plate normal at the same normal stress amplitude. Since the plate normal coincided with a high density of basal poles strain in this direction would have to be accommodated by non-basal slip or twinning and therefore the diametral strain in this direction is smaller than at other orientations.

CHAPTER 3

Experimental Methods

3.1 Introduction

The experimental methods employed were already well established techniques in the fields of texture research and fatigue research. The procedures used in the preparation of material were based on well documented behaviour of copper with regard to thermomechanical processing^(79,80,81). The texture analysis utilised x-ray goniometry and computer manipulation of the data to generate the crystallite orientation distribution function. The fatigue properties were characterised by constant amplitude-life and fatigue crack propagation experiments using specimens machined at specific orientations to the specimen reference areas. The data were supplemented by optical and scanning electron microscopical observations.

3.2 Material Preparation

The aim of the material preparation was to produce a range of texture in copper without the introduction of extraneous factors, e.g., all annealing was performed in vacuum in order to minimise the deleterious effect of oxygen upon the mechanical properties. It is also difficult to vary texture severity while maintaining constancy of grain size and shape. However, since the monotonic mechanical properties of copper are only weakly dependent upon grain size⁽⁸²⁾ the grain size and shape were the two factors which were allowed to vary at the same time as the texture.

The material was prepared in three different forms: for a preliminary series of experiments a thin sheet displaying a very strong cube texture was produced, while the specimens for strain-life testing were produced from thermomechanically processed plate and fibre textured rod. The processing details and the relevant material codes are as follows:

3.2.1 Thin Sheet

MBCUB: was prepared from 95% cold rolled OFHC copper sheet. 150 mm x 300 mm x 0.6 mm specimens were annealed in a vacuum furnace at 1020K for 4 hours.

3.2.2 Plate

All plate material was produced by thermomechanically processing 50 mm x 300 mm x 460 mm blocks of electrolytically pure copper supplied by Enfield Rolling Mills. The chemical analysis of the material is given in Table 2. In order to induce textures the blocks were rolled individually in a 200 ton Robertson Mill equipped with 250 mm diameter rolls. During rolling the rolls were well lubricated with oil to provide conditions of minimum friction. The reduction was performed incrementally in order to encourage homogeneity of deformation and the reduction per pass was limited to 5% of the plate thickness before that pass.

III80: Reduced from 50 mm to 25 mm thickness on the Robertson Mill, subsequently reduced to 9.5 mm thickness by rolling on a Hille 60 ton mill and equipped with 170 mm diameter rolls. Rolling was performed under low friction conditions and the reduction per pass was less than 5%.

NUJIG: Reduced from 50 mm to 9.5 mm thickness on the Robertson mill.

CROCP: Cold rolled 88% on the Robertson mill.

G8585: Cold rolled as for III80, subsequently annealed in a vacuum furnace at 625K for 6 hours.

In order to facilitate reference to the material codes a summary of the material codes and processing conditions is provided as a fold-out inside the back cover.

3.2.3 Rod

The preparation of fibre textured rod was based largely on the work of Dillamore and Roberts⁽⁷⁹⁾ and Freda and Cullity⁽⁸³⁾. In the latter paper it was reported that the end texture after cold drawing was heavily dependent on the starting texture. Thus, in order to produce variations in the fibre textures two castings were made from identical melts of 99.5% pure copper (chemical analysis shown in Table 2). Both melts were vertically cast as 76 mm diameter ingots, about 300 mm in length. Casting A was solidified in a mould comprising a moulded sand base and a copper chill vertical wall. The mould for casting B consisted of a copper chill base and moulded sand wall. The moulds are shown in Figure 28. Since the texture of cold drawn copper has been reported as a duplex $\langle 100 \rangle + \langle 111 \rangle$ fibre and the primary dendrites in copper form along $\langle 100 \rangle$ it was intended that the variation in casting procedure should promote or discourage the formation of the $\langle 100 \rangle$ fibre texture component on subsequent deformation. Subsequently both castings were mechanically cleaned and warm extruded (800K) to 15 mm diameter rod in a Fielding 1000 tonne vertical extrusion press. Sections of the rod were drawn through a series of dies at room temperature using a powered cold drawing bench. The rod was well lubricated to minimise friction

effects and the series of die diameters in order of use was: 16.8 mm, 15.7 mm, 14.7 mm, 13.6 mm, 12.7 mm, 11.9 mm, 11.3 mm, 10.7 mm, 10.2 mm, 9.65 mm and 9.1 mm. After cold drawing the ends of the rod were discarded due to the inhomogeneous nature of the deformation in those regions. Subsequently portions of the rods were cut into short lengths and annealed as rough machined fatigue specimens in vacuum for 10^4 s at 770K. Four materials were therefore prepared in the form of textured rod. The relevant material codes and processing parameters are:

- FAREN - Cast A extruded and cold drawn as described above.
- FBREN - Cast B extruded and cold drawn as described above.
- A3500 - Drawn as FAREN, subsequent anneal in vacuum for 3 hours at 770K.
- B3500 - Drawn as FBREN, subsequent anneal in vacuum for 3 hours at 770K.

N.B. Prior to annealing all cold worked materials were chemically etched in order to remove the surface layer of inhomogeneous deformation and thus prevent the development of texture inhomogeneity on annealing.

3.3 Texture Measurement

3.3.1 Introduction

In order to produce quantitative x-ray texture measurements it is imperative that complete pole figures are determined. The most commonly used reflection technique, the Schultz method⁽⁸⁴⁾, collects intensity data for a set of reflecting planes along an angular spiral track which is centred on the specimen rolling plane normal. While this method has

an advantage in that absorption corrections are not required within 65° of the spiral centre, since within this range the correction for absorption is exactly compensated by the change in volume of the diffracting material, it is not possible to determine the complete, and hence quantitative, pole figure by this method. In order to determine complete pole figures the basic Schultz technique must be supplemented either by superimposing the results of both back reflection and transmission techniques from specimens parallel to the rolling plane or by utilising specimens in which the plane normal lies at the centre of a quadrant of the pole figure, as described by Lopata and Kula⁽⁸⁵⁾ and Meieran⁽⁸⁶⁾. Since the transmission-reflection technique requires the comparison of data in the region in which the inaccuracy of both techniques is increasing, this method is deemed inaccurate and the techniques of Lopata and Kula⁽⁸⁵⁾ and Meieran⁽⁸⁶⁾ were employed.

3.3.2 Specimen Fabrication

The computer programmes (see Section 4.2.1) which were used to analyse the x-ray data are based on a spiral which is centred at equal angles to the rolling direction, the transverse direction and the rolling plane normal. In order to produce such specimens the composite specimen technique which was based on that of Elias and Heckler⁽⁸⁸⁾ was employed. In employing this technique it is important to recognise that the texture which is measured is an average value within the volume of the material from which the specimen is constructed, in particular, this method involves 'through-thickness' averaging which is required in the prediction of mechanical properties. Also, since the thermomechanical procedures employed in the processing of cubic metals tend to produce textures which display (at least) orthotropic symmetry, it is possible to produce an average composite specimen by stacking the

components of the composite specimen in the manner described by Morris (89). While such a technique was employed for the quantitative assessment of texture partial pole figures employing specimens parallel to the rolling plane (or fibre axis) were also produced in order to verify the assumption of orthotropic symmetry. This assumption was not found to be invalid for the materials used.

The importance of accuracy in specimen production required that different methods were used to produce composite specimens from thin sheet, plate and rod respectively.

3.3.2.1 Thin Sheet

The composite specimen was produced by cutting strips at 45° to the rolling direction using a powered guillotine. The specimens were chemically etched, stacked and bonded using Araldite. The bonded block was subsequently sliced at an angle of 54.7° to the through thickness direction to produce the required face. The procedure is described in Figure 29 which is reproduced from reference 89, the method itself is essentially that described by Elias and Heckler⁽⁸⁸⁾.

3.3.2.2 Plate

While thin sheet may be conveniently cut at the angle of 45° required by the method of ref.88 it is impossible to employ the same procedure for thicker material, also sectioning at 45° using a powered saw was not found to be sufficiently accurate. Therefore, composite specimens were produced by cutting strips at 90° to the rolling direction, stacking these in the manner illustrated in Figure 30 in order to average along the rolling direction. The required slice was then cut from the bonded block by a powered cut off wheel by holding the block in a specially designed jig which is shown in Figure 31.

3.2.2.3 Rod

Although texture inhomogeneity in the sheet and plate materials was found to be insignificant, preliminary work indicated that considerable texture inhomogeneity existed in cold drawn materials. It is obvious therefore, that the specimen for x-ray work must be fabricated from a volume of material which corresponds to that employed in the fatigue investigation, i.e., the central 4 mm diameter of rod. Specimen production was therefore more complex in this situation.

The cold drawn rods were cut into 50 mm lengths which were machined and mechanically polished on a lathe to 5 mm diameter. The deformed layer was removed by chemical etching to reduce the diameter to 4 mm. The rods were stacked in a close-packed arrangement and bonded using an epoxy resin to form a block of 25 mm square cross-section. Slices were cut from the block using a powered cut-off wheel and the jig shown in Figure 31.

Texture specimens corresponding to FAREN and FBREN were prepared as described above. The specimens required for A3500 and B3500 were prepared from surplus slices from the blocks of cold drawn material. The slices were mechanically polished on both faces and lightly etched, as a compromise between removing the deformed layer and preserving the geometric face. The slices were then annealed in vacuum for 10^4 s at 770 K. On annealing, the slices broke up due to the decomposition of the epoxy resin and consequently refabrication of the slices was necessary. The rods were cleaned in chloroform to remove organic products, lightly etched in dilute nitric acid to remove any possible oxide layer. The rods were arranged in a close-packed array with the required face parallel to a firm flat substrate. The block was consolidated by setting in 'Metaserv Cold-Mount'. It is considered that the similarity

of annealing practice between the texture specimens and the fatigue specimens is desirable, at the expense of possible introduction of errors due to the laborious fabrication technique.

3.2.2.4 Fatigue Specimen

In order to investigate the possibility of texture development as a result of strain cycling a composite texture specimen was fabricated from a fatigue specimen of material G8585 which was subjected to 5320 cycles at total strain range of 0.0037, which corresponds to between 30 to 80% of life at this strain amplitude. Elliptical slices were cut from the gauge length of the specimen using a carbide slitting wheel, the chuck which held the specimen was machined to align the specimen correctly. The individual slices were arranged on a steel backing plate and cemented into position.

3.2.3 Specimen Preparation

After slicing, the specimens were mounted on a steel backing plate and mechanically polished to a 1 μ m finish. The polished faces were chemically polished in a solution of

100 cc Orthophosphoric Acid
100 cc Glacial Acetic Acid
100 cc Nitric Acid

at 341K to 345K, to remove the deformed layer due to mechanical abrasion. After chemical polishing the specimens exhibited a bright scratch-free surface.

3.2.4 Data Acquisition

{111}, {200} and {220} quadrant pole figures were measured using a

Siemens Texture goniometer of the type described by Neff⁽⁹⁰⁾, in which the specimen is rotated about an axis normal to its surface and also about an axis which is coplanar with the incident and diffracted beams. The incident radiation was produced by a copper target operated at 40 KV and 16 mA and was filtered by a nickel foil to remove the $k\beta$ component thus leaving the $k\alpha$ components with wavelengths of about 1.539×10^{-10} m. The data sampling technique was similar to that described by Heckler et al⁽⁹¹⁾, consisting of continuous counting and outputting the accumulated count at 5 second intervals onto paper tape. By initially orienting the specimen so that the rolling plane normal, or in the case of rod the fibre axis, lies in the plane of the goniometer circle (see Figure 32) and the specimen plane normal is inclined at 60° to the plane containing the incident and diffracted beam the orientation of the reflecting plane normals follows the spiral path indicated in Figure 33, the points on the spiral indicate the measuring points.

The Bragg reflection position was located by setting the specimen incident beam angle at the approximate angle and scanning the detector about the approximate 2θ value until the maximum count rate was obtained. During the setting up process the receiving slit on the detector was reduced to 2 mm in order to locate exactly the Bragg condition, the slit was, however, widened to 6 mm during data acquisition in order to ensure that the whole of the peak was included. Background counts were obtained immediately after each pole figure measurement by moving the counter tube away from the Bragg condition and counting for 50 seconds in that position.

3.3 Preliminary Experiments

30 mm wide strips were cut from the sheet material MBCUB with the

long axis of the strips inclined at 0° , 45° or 90° to the rolling direction. The specimens were placed in a template-jig and filed to shape (Figure 34). The specimens were longitudinally polished to 600 grit and then chemically polished in orthophosphoric/acetic/nitric acid solution to a bright shiny finish. Constant load-amplitude/life tests were conducted in an Amsler-Vibraphore electro-mechanical resonance machine. In each case the load amplitude was adjusted so that the applied stress amplitude was 30.5 mPa. Tests were conducted in tension-tension with the minimum load as close to zero as possible. Failure was considered to be the complete separation of the specimen into two halves.

3.4 Mechanical Testing

The fatigue response of the various materials was assessed by two sets of experiments, namely constant strain amplitude/life tests and fatigue crack propagation tests.

3.4.1 Strain-Life Testing

3.4.1.1 Specimen Preparation

The materials utilised for the strain-life test series were III80, G8585, FAREN, FBREN, A3500 and B3500.

Three sets of specimens were prepared from the plate material III80. Rectangular cross-section specimen blanks were cut from the plate in three orientations such that the long axis of the blank lay in the rolling plane and inclined to the rolling plane by 0° , 45° or 90° . The through thickness direction was marked on one end of each blank prior to machining to the form of "F.G.6" standard fatigue samples (Figure 35).

Two sets of specimens were produced from plate material G8585, oriented at 45° and 90° to the rolling direction respectively, in a similar manner to those produced from III80.

F.G.-6 specimens were directly machined from rod material FAREN and FBREN. As noted in Section 3.2.3, the specimens for materials A3500 and B3500 were rough machined from the corresponding rods of cold worked material, prior to annealing and then given a final light machine after annealing.

After machining the gauge lengths of the specimens were longitudinally polished to 600 grit using a powered longitudinal polishing apparatus. The specimen gauge lengths were finally electropolished using the apparatus shown in Figure 36 in a solution of

350 cc Glacial Acetic Acid
75 gm Chromic Oxide
15 cc Distilled Water

The polishing conditions were found to be very variable but the best polish was obtained at 15V and an initial current of 0.2 A, although this decreased during polishing. About 0.2 mm was removed from the gauge length diameter in one hour. The diameters of the specimen gauge lengths were measured using a travelling microscope.

3.4.1.2 Fatigue Testing

The specimens were tested in a 25 KNMTS closed loop servo-hydraulic testing machine under constant strain amplitude control about zero mean stress. The strain was measured by a clip gauge extensometer and the control signal was generated as a variable amplitude sine wave. The load was measured by a tension-compression load cell mounted in series with the specimen. Non-slipping contact between the extensometer knife

edges and the specimen was assured by wrapping the relevant portions of the gauge length in a thin band of adhesive tape. This is shown in Figure 37. Woods metal grips were employed to eliminate cross-over error at zero stress and to prevent the application of lateral stresses by the gripping system.

The tests were continuously monitored by an oscilloscope which was connected to the output of the load cell, data were also recorded intermittently in the form of load-strain hysteresis loops on an x-y recorder. The intervals at which the loops were recorded were adjusted so that the penultimate loop had been taken at not less than half the number of cycles at which the final loop was taken. Although tests were run at frequencies between 0.5 and 25 Hz, the loops were always recorded at 0.1 Hz due to the mechanical limitations of the recording system. The testing machine was equipped with an automatic counter and also a failure detection mechanism which was set to detect separation of the specimen into two halves.

The monotonic mechanical properties for each set of specimens were also determined by performing tension tests on at least two specimens from each set using the closed loop machine.

3.4.1.3 Elastic Modulus Measurement

The elastic modulus is an important parameter in analysing the cyclic response of materials. In order to ensure greater accuracy in the determination of the Young's Modulus E this was measured by a separate series of experiments. The technique adopted was the acoustic resonance method described by Northcliffe and Roberts⁽⁹²⁾. The apparatus is shown in Figure 38. The sine wave oscillator excites the drive transducer which causes the specimen to be vibrated. The receiving

transducer detects the energy transmitted along the bar, by observing the output of this transducer the resonance position may be noted and the exact frequency is measured by a digital counter. The relationship between the resonant frequency, specimen dimensions and elastic modulus is given by Chalmers and Quarrell⁽⁹³⁾.

$$f_i = x_i \frac{F(t.d)}{L^2} \left(\frac{E}{\rho}\right)^{\frac{1}{2}} \dots\dots(3.1)$$

where $F(t.d.) = \frac{t}{4\pi\sqrt{3}}$ for thin strip

where t is the thickness of the strip in the plane of bending and

$$x_i = 22.37, 61.67, 120.8, 200, 298.6, 417$$

for i = 1 to 6.

In equation (3.1),

- L = length of bar
- t = thickness of bar
- E = Elastic modulus
- ρ = density of material.

ρ was subsequently measured by a flotation method. The parameter x is dimensionless and the units of equation (3.1) conform to the S.I. convention.

3.4.2 Crack Propagation Testing

3.4.2.1 Specimen Preparation

Three materials were employed namely NUJIG, CROCP and ANNCP. Single edge notch specimens (see Figure 39) were machined from the materials in two orientations, with the long axis of the specimen at 45° or 90° to

the rolling direction (Figure 40). After machining the specimens were mechanically polished to 1 μm finish and then electropolished in the Chromic/Acetic acid solution described in Section 3.4.1.1 using the apparatus shown in Figure 41 to produce a bright mirror-like finish.

3.4.2.2 Crack Propagation Testing

Fatigue crack propagation tests were conducted in tension-tension in an Amsler Vibraphore under constant load amplitude conditions. Crack propagation was monitored by observing the progress of the crack trace across the broad face of the specimen using a travelling microscope equipped with a graduated eyepiece. The crack length was measured at intervals of 5 or 10 x 10³ cycles. It was also found necessary to measure the crack length on both faces of the specimen due to non-uniform crack growth.

3.5 Observation Procedures

3.5.1 Optical Techniques

Standard metallographic techniques were employed to characterize grain size and shape of all the materials prior to mechanical testing. Low power optical microscopy was also employed in the preliminary observation of fractured specimens.

3.5.2 Scanning Electron Microscopy

After mechanical testing, the fracture surfaces and the slip markings on the sides of the specimens were observed at magnifications up to 20000 x in a Philips PSEM 500 scanning electron microscope equipped with a motorised goniometer stage.

CHAPTER 4

Data Management

4.1 Introduction

The data from the fatigue testing procedures and the texture measurements were analysed using three sets of computer programmes which are described in the relevant sections below.

4.2 Strain-Life Data

4.2.1 Parametric Method

This approach to strain amplitude-life testing has been described comprehensively by Mitchell⁽⁹⁴⁾ and Dabell et al⁽⁹⁵⁾ and is based on the suggestion by Morrow⁽⁷⁾ that the cyclic response of a material may be specified by a set of constants which may be regarded as cyclic material parameters. It has found considerable application as a design criterion against fatigue failure^(94,95). Effectively, the approach ignores the relative proportions of saturation response, crack nucleation and short crack propagation and considers only the life up to where a specific amount of fatigue damage has been accumulated, i.e. until a standard size fatigue specimen has separated into two portions. (The applicability of such a criterion to fatigue design and component testing is obvious, in that such a fatigue life corresponds to the development of a detectable flaw). While this criterion may lack a certain stringency in that the separate stages of deformation are not considered in isolation it does, however, avoid the problem of delineating the various stages, i.e.

when does an intrusion within a slip band cease to be a notch and become a short crack?

The data are obtained from the strain amplitude tests in the form of, stress-strain hysteresis loops (Figure 42), applied strain amplitude and the number of reversals to failure. The cyclic stress-strain data which are required are those which are developed by the fatigue process and also relate the cyclic stress-strain behaviour as most of the fatigue damage is accumulated. The data were therefore taken from the loops recorded during the saturation stage and the parameters employed in the analysis are therefore:

$\frac{\Delta \epsilon_T}{2}$ the applied strain amplitude

$\frac{\Delta \epsilon_p}{2}$ the plastic strain amplitude at saturation

$\frac{\Delta \sigma}{2}$ the stress amplitude observed at saturation under the applied strain range

$2N_f$ the number of reversals to failure

E the elastic modulus in the direction of testing.

The "cyclic stress-strain" approach considers that the fatigue resistance of a material is determined by the relationship between the cyclic strain amplitude and the corresponding cyclic stress amplitude, in a similar manner to the monotonic stress-strain curve⁽⁹⁴⁾. The cyclic stress-strain response is described by

$$\frac{\Delta \sigma}{2E} + \left(\frac{\Delta \sigma}{2K'} \right)^{1/n'} = \frac{\Delta \epsilon_e}{2} + \frac{\Delta \epsilon_p}{2} = \frac{\Delta \epsilon_T}{2} \quad \dots (4.1)$$

where the relationships between elastic and plastic stresses and strains

are similar to those which describe monotonic behaviour. The parameters K^1 and n^1 are the cyclic stiffness constant and the cyclic hardening exponent respectively.

The strain-life data may also be analysed parametrically. In 1910, Basquin⁽⁹⁶⁾ noted that the fatigue life of materials under high cycle fatigue conditions followed the relation

$$\frac{\Delta\sigma}{2} = \text{const}*(N_f)^{-b} \quad \dots\dots(4.2)$$

Similarly, the Coffin-Manson^(97,98) relation described fatigue life in the low cycle fatigue regime,

$$\frac{\Delta\epsilon_p}{2} = \text{const}*(N_f)^{-c} \quad \dots\dots(4.3)$$

The cyclic stress-strain approach considers that fatigue life is determined by the applied strain level and the material response. The relationship between fatigue life and the imposed strain amplitude is based on the Coffin-Manson and Basquin laws by apportioning damage between the elastic and plastic strain components,

$$\frac{\Delta\epsilon_t}{2} = \frac{\Delta\epsilon_p}{2} + \frac{\Delta\epsilon_e}{2} = \epsilon_f^1(2N_f)^{-c} + \frac{\sigma_f^1}{E}(2N_f)^{-b} \quad \dots\dots(4.4)$$

where the parameters are defined as,

- ϵ_f^1 cyclic fracture strain
- σ_f^1 cyclic fracture stress
- c Coffin-Manson exponent
- b Basquin Exponent

$2N_f$ is defined as the number of reversals to failure, i.e. twice the number of cycles to failure. The parameters ϵ_f^1 , σ_f^1 , c and b are not independent but are related by the parameters n^1 and K^1 . It is easily shown that

$$n^1 = \frac{b}{c} \quad \dots\dots(4.5)$$

and

$$K^1 = \frac{\sigma_f^1}{(\epsilon_f^1)^{n^1}} \quad \dots\dots(4.6)$$

4.2.2 Computer Program

In order to analyse the strain amplitude-life data in terms of the parameters described above, a computer programme was written. The text of the program is given in Appendix I. The data inputted to the program describes a series of strain-life tests, detailing for each test the applied total strain amplitude, the plastic strain amplitude at saturation, the corresponding stress amplitude and the number of reversals to failure. The first three parameters are illustrated in Figure 42. The elastic modulus, determined by the resonance method, is inputted as a separate parameter.

The computer program is based on a least-squares regression fit to equations (4.1) and (4.4) by transferring the data to logarithmic axes. Since the six parameters are not independent a comparison is possible between the results of the cyclic stress-strain analysis and the strain-life analysis. The program was run on an IBM 370 computer at the University of Cambridge computer laboratory. The data ~~were~~ stored on disc file which was automatically accessed by the program. The material parameters were outputted as printed parameters and the regression lines were calculated. The use of computers in this manner facilitates the further manipulation of the data e.g. representation of the fatigue life as a function of

the parameter $\sqrt{\Delta\sigma \Delta\epsilon} E$ as suggested by Watson and Rebbeck⁽⁹⁹⁾.

4.2.3 Precision of Material Parameters

The precision of the parameters calculated by the computer program relies on the precision of the measurements from the hysteresis loops, the inherently statistical nature of the process of fatigue failure⁽³⁹⁾ and the assumption that the relationship between the stress and strain amplitudes and the fatigue life may be described by equations (4.1) and (4.4). A lack of precision in the data became evident when calculations of the elastic modulus were performed on the loop data. The subject of errors will be discussed more fully in later sections (Chapters 5 and 6), however, the computer program was written to accommodate the discrepancies. The program analyses the data by two methods. At first the program calculates the elastic strain amplitude by subtracting the plastic strain amplitude from the imposed strain amplitude while the second time through the program calculates the elastic strain amplitude as the quotient of the stress amplitude and the elastic modulus as calculated from the resonance method. No attempt was made to employ a mean elastic modulus since this approach inevitably leads to the calculation, for some data points, of elastic strains which are larger than the imposed strain amplitude.

4.3 Crack Propagation

4.3.1 Analysis of Crack Propagation Data

The crack propagation data were obtained as a table of crack length measurements (a), as a function of the number of cycles (N), at constant load amplitude ΔP . As noted in Chapter 2, fatigue crack growth is often described as a function of the applied stress intensity

at the crack tip. The simplest relation is that suggested by Paris⁽¹⁰⁰⁾

$$\frac{da}{dN} = C(\Delta K)^m \quad \dots\dots(4.7)$$

4.3.2 Computer Program

The crack propagation data were analysed using the computer program written by Davenport⁽¹⁰¹⁾. This program is based on the spline curve fitting procedure described by McCartney and Cooper⁽¹⁰²⁾. The a v N data are fitted to a polynomical of L -th degree, incorporating N number of splines. Having the data in the form of a mathematical function permits differentiation of the expression at each data point. The program also employs the compliance functions described by Walker and May⁽¹⁰³⁾ to calculate the value of ΔK the cyclic stress intensity from the applied load amplitude, the mean load and the crack length. Thus, tabulated data of crack propagation rate as a function of applied stress intensity amplitude are obtained.

The computer program was run on the ICL 1906S computer at the University of Sheffield computing service. Library graph plotting routines were employed to present the data and the calculated points in four plots:

- (a) normalised crack length vs normalised number of cycles.
- (b) crack propagation rate vs normalised crack length.
- (c) $\log \left(\frac{da}{dN} \right)$ vs $\log \Delta K$.
- (d) recalculated normalised crack length - number of cycles data from plot (c).

The program also calculates the values of c and m in equation (4.7) using

a least squares regression method.

4.3.3. Precision of Crack Propagation Data

The method of spline fitting is a very powerful analytic tool in that it permits a series of data points to be very closely followed by the curve fitting routine. The graph plotting facility permits the data to be reviewed and the "fitted" parameters to be compared with the raw data in order that the optimum values of N and L, the number of splines and the degree of the polynomial, may be chosen. Although it may appear that the largest possible values of N and L should be chosen, the precision of the technique is hampered by the precision, or otherwise, of the experimental data i.e. at large values of N and L the curves tend to follow the scatter in the experimental data⁽¹⁰⁴⁾. Thus, the usefulness of the analytical program was, in general, limited by the empirical data and the values of N and L were normally limited to 2 and 4 respectively.

The major source of errors in the crack propagation experiments is associated with the crack length measurements, although it is recognised that some degree of error is implicit in the load cell output from the testing machine. In fact, the method of measuring crack growth gives rise to two sets of errors. The first set of errors result from attempting to measure the line trace using an optical technique and merely reflect the uncertainty of the method. The second set of errors occur due to the necessity of relating the crack trace to the through thickness crack profile.

The relationship between the crack trace and the crack front profile is not simple and it has been shown that crack growth is decelerated by a free surface. Thus, the crack front in the interior of the specimen is consequently advanced with regard to the crack trace

on the free surface⁽¹⁰⁵⁾. It is expected, however, that since the crack front should maintain a uniform profile, the error introduced by this assumption would affect only the crack position and not the crack propagation rate. The error should, therefore, be acceptable.

A more serious source of error occurs when crack growth does not occur uniformly on both faces in a direction normal to the stress axis. This particular problem was experienced with specimens taken from certain orientations. The crack plane traces which developed on the broad faces of the SEN specimen were found to be rotated from the notch root direction, on one face the rotation was in a clockwise sense and in an anti-clockwise direction on the other face. The lengths of the inclined traces were also found, in general, to be unequal. In order to utilise the computer programs and also to permit comparison with other data, the crack length was calculated by measuring the projected crack length in the notch direction on each face and calculating the arithmetic mean. This procedure introduces two further sources of error. Firstly, the use of the mean projected crack length is difficult to justify when the compliance factors for the K calibration are calculated for uniform crack fronts. Secondly, the stress intensity calculated by the program is, of course, K_I , the appropriate value for mode I opening. It should be recognised that for such a complex crack front the crack opening mode also comprises elements of mode II and mode III opening (Figure 43). Consequently, it must be recognised that the main source of inaccuracy in this procedure is the use of ΔK_I to describe crack propagation under conditions which do not produce mode I opening. However, the purpose of the crack propagation measurements was not to generate values of ΔK_I for copper (indeed, due to the gross plasticity which occurs during deformation

of copper the relevance of K , which is based on linear elastic fracture mechanics, is questionable) but to compare and contrast the rates of crack propagation in textured copper specimens of different orientations. Since the development of non-plane strain conditions at the crack front is a direct consequence of preferred crystallographic orientation it is felt that, despite the inaccuracies of this procedure, the method of comparison may be regarded as valid for this situation.

4.4 Texture Analysis

4.4.1 Analysis

Analysis and manipulation of the texture data was performed on an IBM 370 /165 computer using the programs described by Kallend⁽⁸⁰⁾ which had been modified and transcribed into PL/1 versions by Morris⁽⁸⁹⁾.

4.4.2 Pole Figures

The pole figure intensities recorded on paper tape were transformed by computer onto a polar grid, the value at each point on the polar grid being calculated by linear interpolation between the corresponding four nearest data points on the spiral grid. Intensities were thus obtained, normalised over the whole pole figure in order to produce values relative to random, at 5° intervals circumferentially and radially from the centre of the pole figure. The uncorrected intensity data were employed since it had been shown previously that corrections for defocussing effects were unnecessary for angles less than 65° from the centre of the spiral⁽⁸⁷⁾.

The pole figures were plotted on a computer controlled plotter, using contouring facilities in order to produce convenient contour intervals.

4.4.3 The Crystallite Orientation Distribution Function

Although pole figures have been used by many authors to describe the results of texture research, this form of presentation of data is incomplete since a pole figure describes the distribution of a set of crystallographic plane normals with respect to the sample axes but does not specify the relative orientations, with respect to the sample axes, of the directions which lie in the plane. A more complete and quantitative description is possible by using the crystallite orientation distribution function (c.o.d.f.). The method was developed independently by Bunge⁽¹⁰⁶⁾ and Roe⁽¹⁰⁷⁾ and has since become a well established technique of texture research⁽¹⁰⁸⁾. Detailed analyses of the technique are available^(80,106,107) so the function will be described only briefly in this section. An outline of the mathematical analysis which describes the relation between the pole figure data and the c.o.d.f. is presented in Appendix II.

The c.o.d.f. describes the probability of a unit volume crystallite having an orientation, specified by the Euler angles ψ, θ and ϕ , with respect to a set of reference axes. The convention adopted is that proposed by Roe⁽¹⁰⁹⁾. The angles ψ, θ and ϕ are defined for a given crystallite orientation by the rotations required in order to align the principal axes of the crystallite with the set of physical axes, in texture research the reference axes are generally the rolling and transverse directions and the rolling plane normal in plate material. The rotations are described in Figure 44. The rotations θ and ψ align the crystallite z-axis and the rolling plane normal while the angle ϕ specifies the rotation about this axes.

As described in Appendix II, the c.o.d.f. is generated as a series expansion with coefficients W_{LMN} , in a manner analogous to the synthesis of a function of one variable by the use of a Fourier series, as

$$w(\theta\psi\phi) = \sum_{L=0}^{\infty} \sum_{m=-L}^{+L} \sum_{n=-L}^{+L} W_{Lmn} Z_{Lmn}(\xi) e^{-in\psi} e^{-in\phi} \dots (4.8)$$

where $\xi = \cos \theta$ and Z_{Lmn} is a generalisation of the associated Legendre function.

In practice, the series must be truncated and in this investigation the series was truncated at the twentieth order, i.e.

$$w(\theta\psi\phi) = \sum_{L=0}^{20} \sum_{m=-L}^{+L} \sum_{n=-L}^{+L} W_{Lmn} Z_{Lmn}(\xi) e^{-in\psi} e^{-in\phi} \dots (4.9)$$

At this level the errors due to truncation and experimental imprecision are of the same order⁽⁸⁰⁾.

4.4.4.1 Estimation of Errors in the c.o.d.f.

Having generated the c.o.d.f. from pole figure data it is important to assess the accuracy of the information. Inaccuracy of the c.o.d.f. may result from truncation errors or from experimental errors. Experimental errors may result from sources such as misalignment of the slices during fabrication of the block, imprecise cutting and polishing of the slice and misalignment of the specimen in the goniometer circle at the start of the cycle. A further source of experimental error is the stability of the x-ray source (which was measured as a standard deviation of 0.5% over a typical period of a pole-figure run).

Due to the symmetry conditions of the cubic system, it can be shown that in principle, the W coefficients may be determined out to the 22nd order from two independent pole figures. The use of three pole figures allows an estimation of the experimental errors. The coefficients are determined by a least squares regression technique as described by Kallend⁽⁸⁰⁾. The residuals, which effectively represent the difference between the measured pole figure and the pole figures

which would be calculated from the c.o.d.f. are employed to evaluate the errors involved in the set of empirical data.

The representation of both pole figure data and the c.o.d.f. by finite series introduces truncation errors. The truncation errors in the pole figure data are easily estimated since both the complete function and the truncated functions are available. This is not so in the case of the c.o.d.f. The truncation error in the c.o.d.f. was estimated using the method described by Kallend⁽⁸⁰⁾ which involves extrapolation of the series coefficients from the calculated values.

4.4.4.2 Description of Textures by the c.o.d.f.

The W-coefficients, once generated, may be employed to calculate the c.o.d.f. by equation (4.9). For a material of the cubic system and a texture which exhibits orthotropic symmetry, all distinct orientations are contained within the range

$$0 < \psi < \frac{\pi}{2}$$

$$0 < \phi < \frac{\pi}{2}$$

$$0 < \theta < \tan^{-1}\left(\frac{1}{\cos \phi}\right), \quad \phi < \frac{\pi}{4}$$

$$0 < \theta < \tan^{-1}\left(\frac{1}{\sin \phi}\right), \quad \phi > \frac{\pi}{4}$$

The c.o.d.f. is presented, therefore, as a contoured function in constant ϕ sections of Euler space in the range:

$$0 \leq \phi \leq \frac{\pi}{2}$$

$$0 \leq \theta \leq \frac{\pi}{2}$$

$$0 \leq \psi \leq \frac{\pi}{2}$$

Davies et al⁽¹¹⁰⁾ have published charts of the relevant sections of Euler space, which correspond to planes which are located in the vicinity of a high density of low index orientations, (Figure 45). The charts relate positions in Euler space, i.e. ψ, θ, ϕ , to ideal crystallographic orientations (hkl) rolling plane, [uvw] rolling direction. Thus, the maxima and minima of the c.o.d.f. may be related to ideal crystallographic orientations.

Although the c.o.d.f. is a complete description of the texture it is more useful to be able to describe textures in a shorter form. To achieve this the maxima of the c.o.d.f. may be described in terms of the maximum function height and the position with particular reference to the chart of ideal orientations. A further parameter which describes the severity of the texture is the standard deviation of the function from uniformity. This has been designated the texture severity parameter by Kallend⁽⁸⁰⁾ who has shown that it is readily calculated from the coefficients

$$t.s.p. = 4\sqrt{2} \pi^2 \left(\sum_{L=1}^{20} \sum_{m=-L}^L \sum_{n=-L}^L W_{Lmn} W_{Lmn} \right)^{\frac{1}{2}} \dots (4.10)$$

4.4.5 Application of the c.o.d.f. to Cyclic Properties

Because the c.o.d.f. is a complete quantitative description of the crystallographic texture, its application is much broader than merely describing textures. Two applications have been employed in the present work, namely the prediction of mechanical anisotropy based on preferred orientation and the development of preferred orientation under cyclic straining.

4.4.5.1 Prediction of Mechanical Properties

The prediction of material anisotropy has been described by Kallend and Davies⁽¹¹¹⁾. As shown in Appendix II, the calculations are based on the orthogonality relationship of spherical harmonics⁽¹¹²⁾. The anisotropic property of a single crystal $g(\psi\theta\phi)$ may be developed as a series of spherical harmonics with coefficients G_{Lmn} . For a crystal array described by the c.o.d.f. $w(\psi\theta\phi)$ the average value of the property in the direction $\psi = 0, \phi = 0, \theta = 0$ is given by

$$\bar{g} = 4\pi^2 \sum_{L=0}^{\infty} \sum_{m=-L}^{+L} \sum_{n=-L}^{+L} G_{Lmn} W_{Lmn} \quad \dots\dots(4.11)$$

In order to calculate the value of this property at angles of α, β and γ , with respect to the reference axes, which are used to generate the W coefficients, those axes are rotated by α, β and γ . The new W coefficients are related to the old set by

$$W^1_{Lmn} = \left(\frac{2}{2L+1}\right)^{\frac{1}{2}} \sum_{p=-L}^L W_{Lpn} Z_{Lpm}(\cos\beta) e^{-ip\alpha} e^{-im\gamma} \quad \dots\dots(4.12)$$

In considering anisotropy in the plane of flat material, equations (4.11) and (4.12) reduce to

$$\bar{g}(\alpha) = 4\pi^2 \sum_{L=0}^{\infty} \sum_{m=-L}^{+L} \sum_{n=-L}^{+L} G_{Lmn} W_{Lmn} \cos n\alpha \quad \dots\dots(4.13)$$

4.4.5.1.1 Prediction of Elastic Modulus

The calculations of average elastic moduli were performed using the program written by Kallend and modified by Bateman⁽¹¹³⁾. The upper bound solution, due to Voigt⁽¹¹⁴⁾, determines the elastic stiffness by considering that all the grains are subject to the same strain. The

lower bound solution, due to Reuss⁽¹¹⁵⁾, effectively averages the elastic compliance as the model assumes that all grains are subject to the same stress. Hill⁽¹¹⁶⁾ has postulated that the arithmetic mean of the Voigt and Reuss averages should more clearly approximate the behaviour of weakly textured materials.

4.4.5.1.2 Prediction of Yield Stress Anisotropy

The yield stress anisotropy was determined in order to correlate texture with the cyclic yield stress, defined as the 0.2% offset stress in the cyclic stress-strain curve. It has been reported⁽²²⁾ that the cyclic stress-strain curves of single and polycrystalline copper may be compared by using the Taylor factor. The use of the Taylor factor implies that the deformation conforms to the premises of the model of Taylor⁽¹¹⁷⁾-Bishop and Hill⁽¹¹⁸⁾. The Taylor model assumes that all grains behave as if they were subjected to the same strain as that which is applied macroscopically and is an upper bound solution, in contrast, the Sachs⁽¹¹⁹⁾ model implies stress continuity and is a lower bound solution. Assuming that the same mode of deformation occurs in a given material, regardless of the direction of cyclic straining, the anisotropy of cycle plasticity may be predicted using the Taylor or Sachs theories.

The upper bound solution was determined using the method of Kallend⁽⁸⁰⁾ which employs the method of Taylor and Bishop and Hill, incorporating the criterion of Hosford and Backofen⁽¹²⁰⁾. In this analysis the value of m (the Taylor factor) is determined for a given incremental strain ($d\epsilon_{11}$) as a function of the contraction ration, r , where,

$$r = \frac{R}{1 + R} \quad \dots\dots(4.14)$$

and
$$R = \frac{d\epsilon_{22}}{d\epsilon_{33}} \dots\dots(4.15)$$

The r-value which produces the minimum value of the Taylor factor is considered to be operative. Thus, not only is the Taylor factor calculated but the expected ratio of the width strain to the thickness strain is determined. The lower bound solution is determined by the premise that slip in each grain is governed by Schmid's Law⁽¹²¹⁾.

4.4.6 Application of the c.o.d.f. to Texture Development

4.4.6.1 Quantitative Assessment of Texture Development

The method of spherical harmonics facilitates the study of texture development. In particular, it enables the identification of depleted and augmented regions of Euler space. The difference between two textures is obtained by subtraction of the two c.o.d.f.'s. If the two functions are obtained in the form of spherical harmonics, the corresponding W-coefficients may be subtracted to produce a set of W-coefficients which represent the difference function, i.e.,

$$\Delta W_{Lmn} = {}^1W_{Lmn} - {}^2W_{Lmn}$$

The difference may be plotted in the same manner as the c.o.d.f. with regions of positive intensity corresponding to supplemented orientations and regions of negative intensity corresponding to depleted regions. This technique was employed to study the texture changes in material C8585.

4.4.6.2 Simulation of Texture Deformation

Although fatigue deformation is often considered to occur without

the production of lattice rotation⁽¹⁷⁾ it has been suggested that texture development may occur during cyclic loading and indeed that this phenomenon may be used to monitor the accumulation of fatigue damage⁽⁵⁹⁾. The c.o.d.f. facilitates the study of texture development and stability. Computer simulations of texture development under monotonic loading have been reported by Kallend and Davies⁽¹²²⁾ and van Houtte⁽¹²³⁾. Fatigue deformation was simulated using the method described by Kallend⁽⁸⁰⁾.

Discrete crystal orientations were generated to represent a desired c.o.d.f. Approximately 1000 crystals were generated for each texture as it was found that this number produced an unambiguous match with experimentally measured c.o.d.f.'s. The technique of Kallend employs an incremental strain tensor to describe the macroscopic deformation. The lattice rotations caused by strain cycling were calculated using a modification of the strain tensor such that the initial strain increment was $+\epsilon_{11}/2$, the second strain increment $-\epsilon_{11}$ and the third increment was $+\epsilon_{11}$. Subsequent increments were achieved by

$$\Delta\epsilon_n = (-1)^n \epsilon_{11}$$

Using values of 0.25 and 0.0025 for ϵ_{11} simulations were performed for 375 cycles in steps of 75 cycles.

The simulations thus model constant amplitude strain cycling parallel to the rolling direction. The lattice rotations were calculated according to the maximum work principle of Bishop and Hill⁽¹²⁴⁾ assuming $\{111\}\langle 1\bar{1}0\rangle$ slip systems as described in Reference (122). Texture simulations were performed using six different sets of crystal orientations. These are described in Table 3.

4.4.7 Texture Data Management

The data management system is summarised in Figure 46.

CHAPTER 5

Results

5.1 Microstructural Characterisation

5.1.1 Metallographic Observations

Standard polishing and etching procedures were employed to characterise the grain structure of the materials. All the materials were observed to consist of single phase material together with small oxide particles which were occasionally observed in the rod material. While the plate material was observed to contain some oxide, the particles were somewhat more prevalent in the rod material. It was also noticed that the thin sheet material contained a dispersion of oxide.

The grain sizes were measured by the linear intercept method. The cold rolled materials were observed to consist of elongated grains, while the annealed materials consisted of a fine equiaxed grain structure. The thin sheet material displayed a somewhat coarser grain size than the plate or rod materials. The results are presented in Table 4. (In the case of the elongated grain structures, the diameter which is presented is that normal to the axis of elongation).

5.1.2 Texture Data

5.1.2.1 Thin Sheet Material

The texture of the thin sheet material, code MBCUB, is shown in Figure 47. The texture consists of a severe cube orientation, $\{100\}[001]$,

of height 54 times random. The severity parameter of 5.47 also reflects the very high degree of crystallographic texture in this material. Although the maximum function height is large, and the severity parameter is also great, integration of the c.o.d.f. shows that only 25 to 40 % of the material volume is oriented within 10° of the cube position. The imprecision of this measurement is caused by the large truncation errors involved when dealing with sharp textures. This material, despite the imprecision of the texture data, was chosen for preliminary work because of the high severity of the texture.

5.1.2.2 Plate Material

The c.o.d.f. plots for materials III80, G8585, NUJIG and CRCOP are shown in Figures 48 to 51 respectively. These textures are much less severe than that used for the preliminary experiments and are considered to be more typical of the textures to be found in commercially processed cubic metals. A consequence of the lower severity of the textures is a reduction in the truncation error of the c.o.d.f., thus the c.o.d.f. tends to describe the low severity textures more accurately than it does the higher severity textures. The five materials all display a shear-type texture with $\{100\}\langle 011\rangle$ as the major component. This is, however, not the texture component which is usually reported to develop after homogeneous heavy rolling reductions, and, is thought to be a consequence of rolling thick material on comparatively small diameter rolls⁽¹²⁵⁾. It is, however, a useful component to develop for the programme of fatigue studies since the existence of this component should encourage a similarity of properties in the 0° and 90° directions. It should be noted that the major component, while having a large influence on the mechanical properties does not totally

determine them. Thus, a complete description of the texture, i.e. the c.o.d.f., is required for the prediction of anisotropy rather than "single crystal" type calculations which only employ the major component of the texture (such as prediction for the materials used would conclude that the 0° and 90° orientations were identical).

5.1.2.3 Rod Material

In analysing the texture data of the rod material, the co-ordinate system of the rod was aligned in the goniometer such that the long axis of the rod corresponded to the direction which is conventionally aligned with the rolling plane normal in plate materials. While this conversion may seem somewhat incongruous, in that the axis of elongation of the rod is aligned with the axis of compression of the rolled material, the c.o.d.f. plots, as employed, display the expedient property that fibre textures parallel to the normal direction are shown as straight lines in the constant sections of euler space. The c.o.d.f. plots in Figures 52 to 65 correspond to materials FAREN, FBREN, B3500 and A3500, respectively. It should be noted that the cold worked materials, FAREN and FBREN display a predominant $\langle 111 \rangle$ fibre texture although FBREN shows a significant (3.0x random) $\langle 100 \rangle$ fibre component. The annealed materials display a duplex $\langle 100 \rangle + \langle 111 \rangle$ fibre texture with the stronger component being the $\langle 100 \rangle$ fibre in each case.

The c.o.d.f. data are summarised in Table 5.

5.1.3 Mechanical Property Predictions

The plastic property predictions based on the Taylor-Bishop and Hill model are presented in Table 6. The yield stress is expressed in terms of Taylor units, i.e. referred to the shear stress required to cause slip on the primary slip plane. While the calculation is internally

consistent, i.e. the yield stress in a given direction may be compared to that in another direction within the same material, it does not take into account the effect of other parameters such as grain size or dislocation density. Thus, difficulty may be experienced in relating the Taylor factors for different materials, e.g. materials in either the cold worked or the annealed condition.

Also included in the plastic property predictions in Table 6 is the variation of the r-value (the plastic strain ratio). The r-value is the ratio of the incremental width and thickness strains at yielding⁽¹²⁶⁾, i.e.

$$r = \frac{d\epsilon_{22}}{d\epsilon_{33}} \quad \dots\dots(5.1)$$

for deformation under a uniaxial tensile stress σ_{11} .

The directions of the strain axes are conveniently specified by the stress axis of the specimen and by considering the strain in the through thickness direction of the sheet to be ϵ_{33} . The strain ϵ_{22} is then in the direction which is mutually orthogonal to the other two axes. The necessity to consider the effect of plastic strain ratio was shown by Lee^(77,78) who used diametral extensometry during strain controlled fatigue testing of zircalloy. The plastic strain ratio may also be expected to influence crack propagation⁽⁶⁹⁾.

The elastic properties shown in Table 6 are calculated according to the methods of Reuss⁽¹¹⁵⁾, Voigt⁽¹¹⁴⁾ and Hill⁽¹¹⁶⁾ as described in Section 4.4.5.1.1.

5.2 Elastic Modulus Measurements

The data measured in order to calculate the Young's modulus of the

materials employed in the investigation are given in Table 7. The Youngs modulus in the long direction of the strip is calculated for each resonance of the strip by solving equation (3.1), employing the relevant coefficient. Only those resonances which were clearly distinguishable and repeatable were employed. The arithmetic mean of the moduli calculated for each resonance is taken to be the Youngs modulus in the specified material and direction.

The moduli determined by this method may be compared with the moduli calculated from texture measurements and the modulus measured during a tension test. In particular, the modulus, as determined by this latter technique is employed in analysing fatigue data of soft materials, in which it may be impractical to determine the Young's modulus by a tensile test method.

5.3 Preliminary Experiments

The results of fatigue testing at a constant stress amplitude of ± 30.5 MPa are given in Table 8. The data are the averages of measurements from five specimens of each orientation. Since the sheet specimens were initially in the annealed condition, it was necessary to increase the stress amplitude on starting the test from zero up to 30.5 MPa. However, because this procedure occupied only the first few hundred cycles, it is not expected to have a significant effect upon the fatigue lives recorded. As denoted in Table 8, the data from 0° and 90° specimens fell within the same scatter band and thus the reported life is the average of ten specimens. The specimens taken from the 45° orientation displayed a greater fatigue life under the stress cycling conditions which were imposed, i.e. 6.1×10^6 vs. 1.43×10^6 cycles for the other group of data. Since failure was defined as the total

separation of the specimen the orientation dependence of the life measured under these conditions reflects the orientation dependence of both the nucleation and the propagation stages.

5.3.1 Fractographic Observations of Thin Sheet Material

In all cases the fatigue cracks initiated at one edge of the broad face of the specimen and, during the later stages of the fatigue test, were observed to propagate across the broad face of the specimen. In a similar manner to the grouping of the stress-life data, it was observed that fatigue crack growth, in the 0° and 90° oriented specimens, occurred in a direction at 90° to the stress axis while the 45° oriented specimens displayed growth at an angle of about 60° to the stress axis (Figure 56). It should be noted that the measurement of 60° was reproducible within $\pm 1^\circ$. This orientation is, therefore, significantly different from that predicted for tensile fracture by ductile shear in a thin sheet of isotropic material. In that case, the angle between the trace of the fracture surface on the broad face and the stress axis is predicted to be 54.7° (127). Subsequent metallographic sectioning showed that the fracture in the 0° and 90° specimens occurred on a plane which was normal to the stress axis. The specimens oriented at 45° to the rolling direction displayed a more complex fracture surface when through thickness sectioning was employed. Near the initiation site the fracture plane was oriented at about 30° to the through thickness direction, while at longer crack lengths the crack developed a complementary facet, inclined to the through thickness direction, by about 30° in the opposite sense to the initial fracture plane (Figure 57). The measurements of the orientations of the fatigue fracture surfaces are summarised in Table 8.

Scanning electron microscopy also reveals the change of fracture plane in the 45° oriented specimens and the development of a "roof-top" appearance. Figure 58 is a stereo pair illustrating this feature. The flat, macroscopically planar, fracture of the specimens oriented in the cube directions is illustrated in Figure 59. The most noticeable feature of such fracture surfaces is the chevron-type markings which apparently indicate the macroscopic direction of propagation. Similar markings are evident in Figure 58, with the heads of the chevron markings forming the "roof-top" of the fracture surface. At higher magnifications it is observed that the chevron markings are formed as the result of localised fatigue crack growth occurring on four sets of planes. This is conveniently revealed by stereo pair microscopy, as in Figure 60. At the higher magnification, it is possible to resolve the fine markings which are continuous across the line of intersection of the two planes which form the chevron marking (Figure 61). These markings are the familiar fatigue striations which are often reported on fatigue fracture surfaces of ductile materials.

It is clear that while the striations lie at approximately 90° to the direction of crack propagation some local deviation may occur (Figure 60). High magnification *fractographs* of the specimens oriented at 45° to the rolling direction are strikingly similar to those taken from the cube orientations. It may, therefore, be suggested that on a microscopic scale the mechanism of fatigue crack growth is the same over all the specimens. It would appear that the effect of texture is to reorient the direction of crack growth and thus to determine the macroscopic fracture path. Although the chevron-type markings were observed to be parallel to the $\langle 110 \rangle$ type directions of a single crystal aligned with the cube component of texture, it was not possible to identify the

fracture planes which form the chevrons with a crystallographic plane since the fracture facets extend over several grains. Although the possibility exists that grains of a similar orientation may be contiguous, thus producing a larger effective grain size, the extent of the chevron markings, which lie across many grains over the width and thickness of the specimen, precludes such a single crystal type effect. Thus, although PSB cracking occurs on $\{111\}$ planes, the facets shown in Figure 61 should not be associated with specific $\{111\}$ planes. However, it is obvious that the crack orientation is controlled by the crystallography of the major component.

5.3.2 Preliminary Conclusions from Thin Sheet Experiments

While the results of the preliminary experiments will be discussed in detail in Chapter 6, in conjunction with the results of the cyclic stress-strain experiments and of the crack propagation tests, it is possible to draw a number of preliminary conclusions with regard to the effect of texture on fatigue.

- (1) In an equiaxed single phase material in which the only source of anisotropy was a strong crystallographic texture, the fatigue resistance in the direction at 45° to the cube axes was significantly higher than in the 0° and 90° directions.
- (2) The macroscopic fatigue fracture path is influenced by the texture, in particular, the development of flat fracture surfaces is related to the relative through-thickness yielding, specified by the r-value (see Table 6). A low r-value results in a macroscopically non-planar fatigue fracture.

- (3) Crystallographic preferred orientation produces anisotropy of fatigue properties in copper in the absence of other forms of anisotropy. The anisotropy may be rationalised by the texture measurements.

5.4 Cyclic Stress-Strain Investigation

The results of the cyclic stress-strain/strain-life measurements are presented in Tables 9 to 16. In order to avoid elongation of the material codes, a shortened form will be employed to distinguish the various orientations of the specimens of the plate material. Thus, I8045 implies the 45° orientation from plate III80 and G8590 implies the 90° orientation from plate G8585. The data were calculated from the hysteresis loop which was recorded at the half-life. Premature failures, which were associated with knife edge fretting etc., are noted, but are not used in the strain life analysis. Examination of the raw data reveals considerable variation of the elastic modulus as measured from the hysteresis loops. This phenomenon is often encountered in cyclic stress-strain testing e.g., see Reference 127. In the present situation, this error arises from two sources. Firstly, the elastic modulus is calculated by dividing the stress amplitude by the difference between the total strain amplitude and the strain width of the hysteresis loop. The fractional error in the quotient is therefore controlled by the errors which occur during the subtraction of the two larger quantities, this produces a small quantity with an accompanying large fractional error. The second form of error results from the idealised treatment of the hysteresis loop in Figure 42. Figure 62 shows a series of hysteresis loops recorded during a strain controlled fatigue test, in comparison with Figure 42, two discrepancies may be

noted. Firstly, the straight sides of the loop appear to curve before crossing the strain axis. The second dissimilarity occurs at the loop tips where the turning points do not appear as sharp reversals but are rounded so that the maxima of stress and strain do not occur at the same point. This phenomenon may be ascribed to stress relaxation effects combined with the application of a sinusoidal control signal⁽¹²⁹⁾. Near the reversal points the applied strain rate becomes increasingly small and, thus, stress relaxation effects produce an anelastic component of strain. The effect of cycling frequency and waveforms are shown in Figure 62. The loops were recorded at two speeds and using both sinusoidal and triangular waveforms to drive the hydraulic ram. It is obvious that the sharper loop is produced by fast cycling under a triangular waveform and the most rounded loop by slower cycling using a sinusoidal control signal.

Despite such effects, it is normal⁽¹³⁰⁾ practice to employ waveforms in constant strain amplitude testing and the technique was consequently employed in this investigation. Indeed, it appears that, in the present work, the idealised loop shape is never attained and there is strong evidence to suggest that this phenomenon is not uncommon. High speed digitising⁽¹³¹⁾ of hysteresis loop data indicates that the problems outlined above occur at most frequencies employed in strain-life data acquisition. Effectively, therefore, three different strains should be allowed for in the analysis, elastic, plastic and anelastic. However, since it is impossible for truly elastic deformation to produce damage the anelasticity must be accounted for by the Basquin and Coffin-Manson relationships. The idealisation of Figure 42 is therefore considered to be a reasonable approximation and the errors are accommodated by ascribing the plastic strain to the strain width of the loop and the elastic strain to the stress amplitude divided by the elastic modulus

in the direction of testing. The elastic modulus is determined separately in a monotonic test or by a resonance method. The total strain amplitude may be recalculated by adding the elastic and plastic components. The difference between the recalculated value and the total strain as measured directly from the hysteresis loops is found to be small, an example of such a set of data is given in Table 17.

Employment of this technique with the rejection of plastic strain levels of unacceptable accuracy, typically a limit of 10^{-4} was set as the lowest acceptable level of plastic strain amplitude, was found to be more consistent than other methods of analysis. (For example, one technique which is used to analyse strain-life data averages the elastic moduli which are calculated from the loops, recalculates the elastic strain using the stress amplitude, and calculates the plastic strain amplitude by subtraction. This may result in the calculation of a negative plastic strain amplitude!). It is also suggested that since the analysis is effectively founded on the empirical laws of Coffin⁽⁹⁷⁾ and Basquin⁽⁹⁶⁾, the data which should be employed in the analysis are those to which the relevant laws pertain, i.e. the plastic strain width of the hysteresis loop and the stress amplitude of the hysteresis loop.

The computer program which was written on the basis of the above analysis is reproduced in Appendix I. The material parameters which were calculated from the strain-life data are given in Table 18. The cyclic stress-strain curves for the materials are calculated from the material properties and are given in Figures 63 to 70. The strain-life curves, including the elastic and plastic lines, are shown in Figures 71 to 78.

5.5 Fatigue Crack Propagation Investigation

The fatigue crack propagation data were analysed as described in

Section 4.3. A typical series of graphs is presented in Figure 79. This series shows a set of data that was considered to be well fitted by the programme and the values of L and N. The values of the constants C and m are tabulated in Tables 19 and 20. The Tables also show the value of ΔK_7 (as suggested by Rieux et al⁽⁵⁶⁾) which is the stress intensity amplitude required to attain a growth rate of 10^{-10} m/cycle.

In general, the cracks which were grown in the 45° oriented specimens developed forms which showed traces which deviated by up to 20° from the trace of the plane which was perpendicular to the stress axis. While, in the material CROCP the sense of the deviation was found to be the same on each face, in the 45° specimens from NUJIG plate the sense of rotation was found to be different on the two faces, i.e. on one face the crack plane trace was rotated from the perpendicular plane towards the top grip and on the opposite face the trace was rotated in the direction of the lower grip. In the case of material CROCP, it did not appear that the crack plane trace tended to rotate so that propagation was aligned along the long dimension of the grains.

The data appear to fall into two distinct subsets which are characterised by the value of the Paris law exponent m, one set has m of the order of 3.5, the other has a lower value of the order of 2.0. The lower value of m correlates very well with the materials which displayed a planar fracture. Since the values of C and m are somewhat interdependent, a more exact correlation may be made with the value of ΔK_7 . The orientations which exhibited slant crack growth also displayed the higher values of ΔK_7 , i.e. a higher stress intensity amplitude is required to enforce the specified rate of crack propagation. Thus the specimens which display planar crack growth (usually the cube oriented specimens) exhibit faster crack propagation under the same stress intensity amplitude.

It is also evident that the data from the material of lower severity, CROCP, exhibit greater variance than the data from NUJIG.

5.6 Scanning Electron Microscopy Observation

5.6.1 Strain-Life Specimens

5.6.1.1 Specimen Sides

Examination of the polished sides of the specimens showed profuse slip markings, intrusion-extrusion pairs and occasionally, secondary cracks. The purpose of this part of the investigation was primarily to identify the sites of crack nucleation. In all the specimens examined the mode of crack nucleation was observed to be the same. Figure 80 shows a secondary crack which has not developed into a failure, the crack has developed from an intrusion in a highly localised band of deformation, i.e. a P.S.B. It was rarely possible to examine closely the actual site of failure since post fracture damage tended to obscure detail, it is, however, reasonable to assume that the mode of nucleation of the cracks which did not propagate to failure is identical to that of the cracks which result in failure.

On closer examination, it is apparent that the intrusion-extrusion pairs may result from a number of different slip configurations. The different types of markings have been reported after fatigue of aluminium⁽⁶⁵⁾. The types of markings illustrated by Figure 81 correspond to the markings categorised by Arnell and Teer⁽⁶⁵⁾ as "single slip bands", "intersecting slip bands", "herring-bone patterns" and "severe surface rumpling". It was found that fatigue cracks were found to grow only from the intrusion-extrusions which developed from long slip bands in grains which displayed only one set of parallel slip bands (Figure 82).

Surface cracks were also observed in grains which displayed markings of the last three types described by Arnell and Teer but these, however severe, were not observed to develop into propagating fatigue cracks.

The roles of grain boundaries and twin boundaries in the nucleation of fatigue cracks are somewhat ill-defined. While there is no evidence that fatigue cracks nucleate in twin or grain boundaries, it appears that such boundaries may help to establish an embryonic crack which has formed within a P.S.B. Figure 83 shows a stereo pair in which the fatigue crack has nucleated in a P.S.B. and grown to impinge upon the twin boundary, the incompatibility of deformation is relieved by propagation of the crack along the twin and grain boundaries. The stereo pair in Figure 83 clearly shows the large depth of the crack after it has become established in the twin and grain boundaries.

5.6.1.2 Fracture Surfaces

The investigation of fracture surfaces of specimens which have been subjected to fully reversed strain cycling is complicated by artifacts caused by post fracture damage as the fracture surfaces impinge during the compressive half cycles causing detail to be obscured. However, despite the occurrence of "smearing" it was always possible to observe areas which had suffered relatively little post fracture damage. All the fracture surfaces displayed three distinct zones;

- (i) a zone near the nucleation site which was often featureless due to smearing by the compressive forces and inclined at between 30° and 45° to the stress axis,
- (ii) an intermediate zone on which features typical of fatigue could be observed (this was frequently normal to the stress axis, although slant fracture surfaces were also obtained), and

(iii) a region of ductile shear caused by monotonic fracture.

Figure 84 shows a low magnification S.E.M. micrograph in which nucleation has, in fact, occurred at three separate sites and the growing cracks have coalesced to produce a larger crack which has grown across the cross section of the specimen.

The fracture surfaces near the initiation site correspond to the Stage I growth⁽³⁾ of the embryonic fatigue cracks. Very little detail was observable in this region. The fracture surfaces formed during Stage II growth, whether during planar or slant growth, were found to exhibit two distinct types of features. All the annealed materials displayed very marked fatigue striations and exhibited a very ductile fracture surface. Figure 85 shows a typical set of fatigue striations which were observed in a depressed region of the fracture surface, presumably protected from post fracture damage by the elevated regions which surrounded it. (This also indicates that the smearing is not caused by mating of the surfaces immediately after the crack has passed but by damage when the crack has grown to a considerably longer length).

Similar ductile features were observed on the fracture surfaces of material IIII80 for the 0° and 90° orientations at all stress levels. Figure 86 corresponds to propagation at high rate, large strain amplitude and long crack length, and illustrates the exceptionally ductile nature of the fracture. The striations lie on small ledges which appear to be separated from each other by sheared surfaces. The striations can be seen to be continuous from one ledge to another so that the region which produces the peak of a striation on the ledge will develop a depression on the shear surface.

The Stage II fracture regions in the other cold worked specimens displayed pronounced facet-like features, (shown in Figure 87) in

contrast to the ductile appearance of the other specimens. The most striking contrast is between corresponding specimens of III80 material in the 0° or 90° orientations and the 45° orientation. The 45° oriented specimens display the facet-like features shown in Figure 87 in contrast to the ductile striations exhibited by the 0° and 90° oriented specimens (Figure 86). Closer examination of the cube oriented specimens of III80 revealed facet-like features at locations close to the crack nucleation sites (Figure 88). It was also noted that the facet-like features tended to be more prevalent at shorter crack lengths and in specimens subjected to lower amplitude strain cycling.

The position of the sites of fatigue crack nucleation, and the subsequent direction of crack propagation were found to be unrelated to the reference directions in the plate materials.

5.6.2 Crack Propagation Specimens

The fatigue cracks produced during the crack propagation experiments displayed surprisingly rough features. At very short crack lengths, presumably within the plastic zone of the starter notch, the cracks are reasonably planar (Figure 89). At longer crack lengths the crack morphology becomes less planar, exhibiting macroscopic peaks and troughs.

The appearance of the fracture surfaces of all specimens are very similar when viewed at high magnification. Figure 90 shows a typical surface. The facet-like features appear very similar to those noted on the fracture surfaces of the strain-life specimens, the ductile striations which had been evident on the more ductile fracture surfaces of the strain-life specimens were, however, not observed. Although experiments were attempted using soft specimens, these were not successful in producing fatigue cracks without gross cross section yielding.

It is also possible that well marked ductile striations were not observed on the fracture surfaces of the crack propagation specimens because the crack propagation rates were below those encountered during the strain life testing, since in the crack propagation testing, the tests were terminated before the crack reached 70% of the specimen width.

5.7 Texture Development During Fatigue

5.7.1 Simulation

The results of the simulations based on the Taylor-Bishop and Hill model of plastic deformation are given in Table 3 (together with the starting textures). The fatigue simulations tend to develop components in the positions $\{100\}\langle 031\rangle$ and $\{100\}\langle 013\rangle$, the relative strengths of the components in each orientation are dependent on the prior "deformation". Thus, the cube textured material tends to develop a much lower severity as the peak width at $\{101\}\langle 010\rangle$ broadens towards $\{001\}\langle 031\rangle$. Similarly, the shear texture, $\{100\}\langle 011\rangle$ develops a much broader peak, enveloping the $\{100\}\langle 031\rangle$ orientations, eventually developing small side peaks in those orientations.

5.7.2 Experimental Measurement of Texture Development During Fatigue

The texture which was measured from the specimen which had been subjected to 5300 cycles at ± 0.0037 strain amplitude is shown in Figure 91. This should be compared with the initial texture G8585 which is shown in Figure 49. The most emphatic difference is that the peak height has fallen from 7.7x random to 4.7x random and similarly, the severity has also decreased from 0.98 to 0.68. The quantitative

nature of the c.o.d.f. and its formulation as a series expansion, permit the difference function of two c.o.d.f.'s to be evaluated. Thus, the relative changes in orientation may be evaluated between Figure 91 and Figure 49. This difference function is plotted in Figure 92. It is clear that while the orientations near $\{100\}\langle 011\rangle$ have become depleted, no specific orientations have been preferentially augmented.

The results of the texture measurements indicate, therefore, that in contrast to the predictions of the simulations based on the theory of Taylor and Bishop and Hill, the action of fatigue cycling is to randomise the texture.

CHAPTER 6

Discussion

The review of the literature has shown that the fatigue properties of cubic single crystals are expected to be orientation dependent. By expressing the cyclic stress-strain curves, in terms of the resolved shear stress and strain amplitudes, Laird⁽¹³²⁾ has shown that materials deforming by wavy slip should be expected to display a unique cyclic stress strain curve. The anisotropy of cyclic behaviour is, therefore, dependent upon the Taylor factor. Kettunen⁽¹⁴⁾ attempted to rationalise the behaviour of single crystals and polycrystals using the Taylor factor. Inherent in these approaches has been the premise that the polycrystals which were employed for comparative purposes were free from texture and exhibited a Taylor factor of 3.06 (which corresponds to a randomly oriented aggregate of crystals).

The effect of orientation on the rate of crack nucleation in single crystals was demonstrated by Avery et al⁽²⁶⁾ and a corresponding dependence of the orientation dependence of the development of surface topography in polycrystals was noted by Arnell and Teer⁽⁶⁵⁾, i.e. grains which developed long straight slip bands were oriented so that the stress axis lay at the centre of the stereographic triangle. It appears that the rate of crack propagation in single crystals is also influenced by the crystal orientation⁽³⁸⁾. However, these data may not be directly relevant to the fatigue of polycrystals since crack growth data has been correlated with the tendency towards multiple slip⁽⁴⁰⁾ and, in polycrystals, it would be expected that the constraints of

neighbouring grains would promote polyslip in all grains.

The only data which have examined the effect of preferred orientation on cyclic properties are those of Nair and LeMay⁽¹³³⁾. These workers correlated a difference in the fatigue properties in the transverse and rolling directions of cold rolled plate with texture measurements. It was also found that in materials which displayed either "cube" or "random" textures the two orthogonal orientations produce much more similar fatigue behaviour. Unfortunately, Nair and LeMay were only able to correlate distinct differences in fatigue behaviour with distinct differences in orientation, e.g. Nair considers that the S-N data for the annealed copper polycrystals form a single curve (see Figure 93). However, it could be argued that the orientations are not identical but that the scatter bands of the two data-sets overlap. Similarly, the use of incomplete pole figures is an inadequate description of the texture. In particular, the presence of a strong cube texture component does not per-se mean that the 0° and 90° orientations are texturally identical since the presence of minor components will affect the anisotropy of mechanical properties. Also, it is possible that grain shape may affect the S-N curve. Because the only differences that Nair and LeMay⁽⁶⁰⁾ found in the fatigue data were in the cold worked specimen it has not been proved conclusively that the difference in fatigue properties is attributable to texture since in one orientation the long grain boundaries are parallel to the stress axis while in the other the boundaries are perpendicular to the stress axis.

6.1 Preliminary Experiments

In order to assess the possibility of textural effects in the fatigue of copper it is necessary to remove any other causes of anisotropy and also to ensure that the anisotropy due to texture is as

large as possible. Fortunately, cold rolled copper sheet may be annealed to produce an equiaxed grain structure which exhibits a strong cube texture component, thus fulfilling the conditions of strong crystallographic anisotropy and weak microstructural anisotropy. The texture data for the sheet material MBCUB indicate that the 0° and 90° orientations are texturally equivalent. This implies that the large cube component dominates the mechanical anisotropy and that no significant minor components exist. (A situation which is probably untrue for the material of Nair. Reference 133, Figure 5.4).

The data from the preliminary experiments clearly show that under stress amplitude controlled conditions of high cycle fatigue the stress-life data falls into two sets, the 0° and 90° specimens form one set at a lower life while the 45° oriented specimens showed enhanced fatigue resistance in that regime. Using the yield stress calculated for the three orientations by the Taylor⁽¹¹⁷⁾-Bishop and Hill⁽¹¹⁸⁾ method it is found that the 0° and 90° orientations display similar yield stresses which are below the yield stress calculated for the 45° orientation. Thus, the fatigue data at constant stress amplitude shows that the materials with the lower yield stress fail prematurely, i.e. the fatigue data agrees qualitatively with the texture prediction.

On the basis of these results, it is not possible to discriminate between the nucleation and propagation phases of fatigue crack growth. However, since crack propagation at such a low stress level occupies a small fraction of life⁽³⁾ it is clear that the nucleation of fatigue cracks is dependent on the texture and orientation. It appears that texture also affects the fatigue crack propagation. The fracture behaviour will be more fully discussed in conjunction with the fatigue crack propagation data from series NUJ1G and CROCP but the results of the fractographic observations on the thin sheet fractures do indicate

the effect of texture. Although the high magnification views of the fatigue fracture surfaces are very similar, the macroscopic topography of the fracture surfaces depends on the orientation, the cube oriented specimens exhibit flat fractures and the 45° specimens have slant or roof-top type fracture. It appears, therefore, that the micromechanism of fatigue crack propagation is the same for all the specimens while the macroscopic crack orientation is determined by the texture.

It is tempting to analyse the fracture in terms of crack propagation along $\{111\}$ type planes as suggested by Laird⁽³⁾. Neumann⁽³¹⁾ suggests that slip is controlled by slip on two $\{111\}\langle 1\bar{1}0\rangle$ systems producing crack fronts aligned along $\langle 110\rangle$ type directions. The macroscopic fracture plane depends on the relative amounts of slip on the systems at the crack tip. This explanation is acceptable in the description of crack propagation in single crystals but it should be noted that the fractures produced in the fatigue of thin sheet display chevron markings over distances which are larger than the grain size of the material. Since the material is not a single crystal, approximately only 25% of the volume is oriented within 10° of the $\{001\}\langle 110\rangle$ orientation, such a rigorous crystallographic argument should not be applied. However, this model, which has also been suggested by Pelloux⁽¹³⁴⁾, may be applied in a more generalised form. Rieu et al⁽⁵⁵⁾ suggested that the slip occurs in "bands of shear" at the crack tip, as opposed to slip on a specific plane. The orientation of the bands and the sense of the shears is prescribed, of course, by crystallographic considerations. If the macroscopic shearing behaviour is now considered it will be seen that the shear at the crack tip must be influenced by texture.

In the case of the cube textured material, strain is easily accommodated within the plane of the sheet if the stress axis lies at 0° .

or 90° to the rolling direction. Conversely, elongation at 45° to the rolling direction results in considerable through-thickness straining, see R-value in Table 5. Since the crack propagation, in the case of thin sheet, always began at the edge of one of the broad faces, crack propagation occurs to accommodate an elongation in the direction of the stress axis. In the cube oriented specimens it appears that macroscopic plane strain conditions are maintained at the crack tip.

Although local deviations occur, the effect of the notch and the constraints imposed by the texture effectively produce macroscopic plane strain crack propagation, even in specimens of such thinness! Due, however, to the low R-ratio of the 45° oriented specimens the shear at the crack tip cannot be accommodated by plane strain and a slant mode of fracture develops. Thus, the crack tip deformation is accommodated by a system of shears which do not lie in the plane of the sheet. While considerable thinning of the specimen occurred at the crack tip in the 45° specimens, it may not be totally correct to regard the difference between the two fractures as simply plane stress vs plane strain. Because of the orientation of the fracture surface in relation to the through thickness direction the fracture may contain some degree of mode III opening. The effect of the crack angle on the rate of crack propagation is not shown by these data but Rieu et al⁽⁵⁶⁾ showed that planar fractures occurred at faster rates than propagation which was not perpendicular to the stress axis.

6.2 Strain-Life

The strain-life/cyclic stress-strain approach considers that the endurance of a material under fatigue conditions is determined by the mechanical response under cyclic loading, which can be described by the cyclic stress-strain curve. This approach implies that for a given

applied strain amplitude the material will develop a unique stress amplitude. This description of the stable stress-strain response is facilitated if materials exhibit the classical response of rapid hardening or softening followed by a saturation stage which is terminated only by fracture. The cyclic stress strain curve is determined by the saturation stress amplitudes as a function of the applied strain amplitudes. However, many materials do not exhibit a true saturation stress, but often display a continuous slow softening. For example, Abel⁽¹³⁵⁾ has noted that the saturation apparently exhibited by single crystals of copper is really producing softening at very slow rates (10^{-7} per cycle). Since the lack of saturation is often more marked it is imperative to define a comparative point at which to determine the stress and strain amplitudes. This point is often taken as the half life⁽¹³⁶⁾.

The use of the cyclic stress-strain curve from saturation values implies that the material structure attains a stability under the cyclic conditions and it follows that the rate of accumulation of fatigue damage is determined by the dislocation substructure. Feltner and Laird^(6,21) suggested that "wavy slip" materials should display unique cyclic stress strain curves which would be independent of prior mechanical history. Conversely, materials which exhibited low stacking fault energy were observed to display cyclic stress-strain responses which were dependent on mechanical history, i.e., the "saturation" stress at a given strain amplitude would be raised by pre-strain. The question of the uniqueness of the cyclic stress-strain behaviour of wavy slip materials has recently been clarified by Laird et al⁽¹³⁷⁾. While the uniqueness of the cyclic stress strain curve of copper has been widely accepted, the data of Tuler and Morrow⁽¹³⁸⁾ is at variance with this view, since they found that heavily cold worked material

displayed a cyclic saturation stress which was not uniquely determined by the applied strain amplitude. The work of Feltner and Laird which concluded that copper exhibited a unique cyclic stress-strain cycle was limited to low levels of pre-strain ($\sim 20\%$). The data presented by Laird et al⁽¹³⁸⁾ shows that heavily cold worked copper displayed a cyclic stress strain curve which lay considerably above the cyclic stress strain curve of annealed material. Similarly, Lukas and Klesnil⁽¹³⁹⁾ reported that, while the cyclic stress-strain curves of copper in the annealed and 20% tensile pre-strained conditions coincided, the curves for 30% and 40% prestrained material were found at increased stress levels.

The cyclic stress-strain curves which are shown in Figures 63 to 70 show a similar demarcation, the cold worked materials display cyclic stress strain curves which rise considerably above the curves of the annealed materials. A similar trend is observed in the strain-life curves. At high strain, the total strain-life curves lie within the same region, although the four curves which relate to the annealed material lie below three of the four curves for the cold worked materials.

In the high cycle fatigue regime all the data pertaining to the cold worked materials lie below the annealed copper data. The correlations between plastic strain amplitude and fatigue life do not appear to discriminate between cold worked and annealed materials while the plots of the Basquin relationship show that the cold worked materials lie above the annealed materials. (The plots of total strain amplitude vs life, plastic strain amplitude vs life and elastic strain amplitude vs life are given in Figures 94-96).

The difference in fatigue lives of cold worked materials and annealed materials was originally noted by Kemsley⁽¹⁴⁰⁾ who compared

the lives of annealed and cold worked copper specimens under constant stress amplitude cantilever bending. The cold work material produced longer fatigue lives. Similarly the data presented by Nair (see Figure 25) show that cold worked materials exhibit enhanced life in comparison to the same material which is fatigued from an annealed state. It is exceptionally difficult to compare the fatigue life data with work that has been published previously since the different methods of collecting and presenting fatigue life data result in a profusion of S/N curves from stress controlled tests, total strain-life curves and plastic strain life curves from tests performed under different conditions of strain control. Additionally, while the use of cantilever bending facilitates the gathering of S/N data, the stress levels calculated for this type of deformation often ignore the strain hardening properties of the specimen, Karjalainen⁽¹⁴¹⁾ has pointed out that this is a common source of error which produces discrepancies between fatigue data measured by uniaxial cycling and those obtained by bending. It is, therefore, only possible, in comparing the present data to previously published results, to remark that these results are of the same magnitude and follow similar trends to the data available in other publications.

The assessment of textural effects is facilitated by the method of machining specimens from different orientations of the same plate, thus maintaining constant all factors except crystallographic orientation. As mentioned above, it is also the intention to compare the data from annealed plate material with annealed fibre material and similarly to compare data from cold worked specimens. However, the discussion will be facilitated by initially comparing only the data from specimens taken from the same plate.

The texture of the cold rolled plate material is shown in Figure 48. This is not the texture which is usually reported for cold rolled copper and did not generate the cube texture component on subsequent recrystallisation. The data are, therefore, not directly comparable with those of Nair⁽¹³³⁾ and LeMay and Nair⁽⁶⁰⁾. The mechanical property predictions which are given in Table 6 indicate that the 0° and 90° orientations should be almost identical while the 45° orientation should have different mechanical properties. The strain amplitude-life and cyclic stress-strain data fall into two groups, the 0° and 90° specimens produce one data-set while the 45° orientation produces data which obviously belongs to a different set. The strain-life curves show that the 45° orientation produces a superior life at all strain levels under constant strain amplitude cycling while the cyclic stress-strain curves indicate that for a given imposed level of strain the stress amplitude developed by the 45° orientation is lower than in the 0°-90° specimens. This correlation, in which the material that displays the stronger cyclic stress strain curve also displays the inferior life under strain cycling agrees both with the premises of the cyclic stress strain method of fatigue analysis, and in particular, with the parametric approach which was employed. This follows since Morrow⁽⁷⁾ has shown that in order for the constants in the life equation to be related to the cyclic stress-strain curve the accumulation of fatigue damage must be related to the hysteresis work involved during cycling. That is, if σ_f^1 and ϵ_f^1 represent a point on the cyclic stress strain curve they do so because damage accumulation is determined by the area of the hysteresis loop. Since in this investigation (and in most investigations into the cyclic properties of metals) the parameters characterising the cyclic stress strain curve agree when calculated either from strain-life or saturation stress

and strain amplitude values it is to be expected that the material with the lower stress-strain curve exhibits superior life under imposed strain controlled cycling. The converse, i.e. that the stronger material exhibits the longer life, would be expected under stress controlled cycling. This was observed for the thin sheet material.

The agreement between the 0° and 90° orientations seems to indicate that there is little effect of grain orientation on the fatigue properties and that the difference in the fatigue properties observed in the 45° oriented specimens is due to crystallographic texture. Since the grain shape exhibited a ratio of about 20 (consistent with a rolling reduction of 80%) it may be assumed that if copper exhibited a grain size effect then the 0° and 90° orientations should be influenced by the grain shape. The present results suggest that the cyclic properties of copper are not influenced by grain size, as proposed by Laird⁽³⁾, and agrees with the theoretical predictions of Thompson et al⁽⁸²⁾. The result is in agreement with the data of Bucci and Thompson⁽¹⁴²⁾ who demonstrated that fatigue crack growth in truly polycrystalline f.c.c. metals is not influenced by grain size and confirms that Nair and LeMay⁽⁶²⁾ were correct in ascribing the difference in fatigue properties of their cold worked materials to textural effects.

The elastic modulus measurements are in the ratio,

$$\frac{E_{45}}{E_{90}} = \frac{115}{121} = 0.95 \quad \dots (6.1)$$

while the predicted ratio of the Youngs moduli are all lower, of the order of 0.82. The plastic property predictions agree quite well with the ratio of the cyclic yield stress as defined by S^1 , the cyclic stress amplitude produced by a cyclic plastic strain amplitude of 0.2%,

i.e. the ratio of the 45° data to the $0-90^\circ$ data is 1.045 for the predictions based on the Taylor-Bishop and Hill theory and 1.050 for the values in Table 18. On this basis it appears possible to predict from the texture measurements that the orientation which exhibits the higher flow stress will display poorer fatigue resistance under conditions of imposed strain cycling. In the case of material III80 the elastic properties bear a similar orientation dependence to the plastic properties and thus the orientation which is predicted by x-ray measurements to be soft is also able to accommodate the total strain amplitude at a lower stress amplitude. (It is emphasized that elastic and plastic properties do not have the same origin, the plastic properties depend on the f.c.c. structure and the $\{111\}\langle\bar{1}10\rangle$ slip mode while the elastic properties depend on the single crystal elastic constants c_{11} , c_{12} and c_{44} which are material constants).

Because the cold rolled material developed a retained shear component on recrystallisation at low temperature (at higher recrystallisation temperatures the texture was almost totally random) the mechanical property predictions at 0° and 90° were identical and therefore specimens were taken from only the 45° and 90° orientations. Due to the lower texture severity of G8585 the difference between the 90° and 45° orientations is not as pronounced as in III80. Consequently, the fatigue data are found to exhibit greater similarity than in the case of the cold worked material. The strain-life and cyclic stress-strain data follow the same trends as the data from the cold worked material. The 45° orientation shows superior life and a slightly lower cyclic stress strain curve compared to the 90° orientation. The scatter in these data, however, is greater than for the cold rolled plate. This is more obvious on the cyclic stress-strain curves than in the strain-life plots. However, the coefficients of correlation

show that the data can be fitted more accurately by two distinct curves than by one set which includes all the data. It is obvious, however, that the two sets of data are covered by the "factor of two" spread which is usually considered to be acceptable in fatigue data⁽³⁹⁾. Quantitatively the values of the elastic moduli, as measured, and the 2% cyclic yield stress calculated from the cyclic stress strain curves are in reasonable agreement with the values calculated from the cyclic stress strain curves are in reasonable agreement with the values calculated from the texture measurements.

$$\frac{S_{45}^1}{S_{90}^1} : \frac{M_{45}}{M_{90}} = 0.96\theta : 0.970 \quad \dots(6.2)$$

where S is the 2% offset stress amplitude and M is the corresponding Predicted Taylor factor, while the elastic moduli appear to correlate with the Reuss average i.e. the predicted values of 112GPa and 99.8GPa.

The cold worked rods show little difference in the predicted elastic moduli and yield stresses along the axis of the rod. Similarly, the cyclic stress-strain curves which are developed by the strain life data are very close together. Surprisingly, the strain-life curves appear to diverge somewhat more than should be predicted from the cyclic stress strain curves. In particular, the curves for material FAREN lie below the curves for FBREN on both plots. However, the cyclic stress-strain curves are calculated on the basis of the stress strain amplitudes and not on the n^1 and K^1 values derived from the strain-life data. It is noticeable (see Table 18) that there is a greater discrepancy between the n^1 and K^1 values calculated by the two methods for these sets of data than for the other sets of data. The ratio of the cyclic yield stress is almost equivalent to the ratio of the calculated Taylor Factors,

however, since this ratio is of the order of 1.005, any error is certainly within the limits of experimental measurement.

The annealed fibre textured materials similarly displayed cyclic stress strain curves, which lie very close to each other. Again, the texture measurements indicate that the mechanical properties should be very similar. The predicted Taylor factors for A3500 and B3500 are 3.036 and 3.086 respectively, a ratio of 0.983, which compares to the cyclic offset stress amplitudes of 156 and 159 MPa, a ratio of 0.981. The strain-life data indicate that the material A3500 has a flatter curve than B3500, since the plastic strain-life lines are closely aligned. The difference must be ascribed to the difference in the elastic strain-life relation, A3500 displaying a much more horizontal curve. Comparing the predicted values of the elastic modulus it is found that the B3500 material shows a much lower elastic modulus than predicted by the texture measurements. It is suspected, therefore, that these discrepancies are related and that higher value of the modulus for B3500 would agree with the texture measurements and would agree more closely with the hysteresis loop data, although measurement of the modulus was exceptionally difficult on the loops from the annealed rod material. The effect of change in the modulus in this manner would be to produce a more horizontal line, primarily by reducing the contribution of the elastic strain in the low cycle region. However, since the data from A3500 and B3500 are obviously very similar the results have been presented as shown in order to illustrate how susceptible the strain-life parameters are to the selection of constants. This effect is important since it illustrates that techniques of analysis which employ the technique of averaging the elastic modulus do not minimise errors but tend to propagate them. It should also be noted that the correct modulus pertaining to a given set of specimens should always

be measured since the variation of elastic modulus due to texture can be significant (see Table 18) consequently, the use of an average elastic modulus, e.g. from standard tables will influence the correlations in the cyclic stress strain analysis.

The effect of the incorrect choice of the elastic modulus is shown in Table 18. The material code B35XX refers to the stress-strain, strain-life data of material B3500, analysed using an elastic modulus of 122 GPa. (This value was calculated from the elastic modulus of A3500 by assuming that the ratio of the elastic moduli of the two materials may be predicted by texture measurements). The cyclic stress-strain curve and the strain-life curves calculated for the parameters given in Table 18 are shown in Figures 97 and 98 respectively. These data coincide with the data of A3500 more accurately than when the data are analysed using the lower value of the elastic modulus. It may be expected that since the annealed materials were exceptionally soft the measurements of the elastic moduli may be in error. Thus, it is concluded that the difference in cyclic properties between A3500 and B3500 is not due to textural effects but is due to inaccuracy of the stress-strain analysis.

Comparison between the plate materials and the rod material shows that the elastic modulus predictions for all the materials are in agreement with the measured values, correlating more closely with the Reuss average than with the Voigt or Hill values. The predicted values of the Taylor factor of the annealed materials are of the same order for both plate and rod materials. However, the cyclic stress-strain curves of the rod materials lie below the curves of the plate materials. Similarly, the strain-life curves for the rod material lie below the strain-life curves for the plate material. The difference in the cyclic stress-strain parameters, however, is seen to be small.

In particular, the parameters ϵ_f^1 and c are very similar for A3500, G8545 and G8590. The elastic strain-life parameters show less agreement, which results in the rod materials displaying superior life in the high cycle fatigue regime. It should be noted that data were not measured in this regime due to the impracticality of such an experiment. A fatigue test which lasts for 5×10^8 cycles would take 27 days even at 100Hz which is the maximum cycling frequency of a servo-hydraulic testing machine. Life predictions using the cyclic stress-strain approach tend to be conservative in this regime since the analysis ignores the possibility of a fatigue limit. The cyclic stress-strain relationships, of course, reflect the greater stiffness of the plate materials. Since the materials did not differ greatly in grain size, and it appears from the cold worked material III80 and reports in the literature that grain size has no effect on fatigue properties, it is difficult to explain this discrepancy. The hysteresis loop traces shown in Figure 99 show the same behaviour. The rod material shows a sharper yielding behaviour, i.e. the "turnover" is more pronounced, but the work hardening is lower. (The agreement between the loop shape and the cyclic stress-strain curve has been noted by Morrow and Halford⁽¹⁴³⁾ and has been employed as a rapid technique in the assessment of the cyclic stress-strain curve⁽¹³⁶⁾).

In the case of the cold worked materials, the cyclic stress-strain curves of the fibre textured materials lie above the cyclic stress-strain curves for the cold rolled plate specimens. This is predicted by the Taylor factor, calculated from the texture measurements, but is in contradiction to the data for the annealed materials. The fibre textured materials also display lower fatigue life in the high cycle regime. In this case, it appears, therefore, that the stronger material displays the lower fatigue life.

Bhat and Laird⁽²²⁾ and Mughrabi⁽¹⁴⁴⁾ have shown that the cyclic stress-strain curves of single crystals and polycrystalline f.c.c. metals may be compared by employing the Taylor factor to transform the tensile stress and strain amplitudes to shear stress and strain amplitudes. Furthermore, Laird⁽¹⁶⁾ has shown that the fatigue limit of polycrystalline copper may be predicted from the value obtained from single crystals oriented for single slip⁽¹⁶⁾. The use of the Taylor factor in this manner may be criticised since the Taylor factor actually relates to deformation on more than one slip system. (Strictly, the Taylor factor relates the macroscopic tensile stress to the arithmetic sum of the shear strains on the individual slip systems⁽¹⁴⁵⁾, i.e.

$$\sum_i \gamma_i / \sigma = M \epsilon \quad) \quad \dots\dots(6.3)$$

If the cyclic stress-strain data are analysed in the manner proposed by Bhat and Laird, the data fall into two sets which coincide with the annealed and cold worked initial states respectively (Figure 100). For clarity, the data have been replotted on logarithmic co-ordinates in Figures 101 and 102 for the annealed and cold worked materials respectively. The two sets of data analysed using a least squares fit on logarithmic co-ordinates to the equation

$$\Delta\tau = \kappa^{11} (\Delta\gamma)^{n^{11}} \quad \dots\dots(6.4)$$

The straight lines which are drawn on Figures 101 and 102 represent the results of the regression analysis, which are also presented in Table 21. The data for the individual sets of material were calculated

from the longitudinal cyclic stress strain analyses reported in Table 18,

$$\frac{\Delta\tau}{2} = \left(\frac{\Delta\sigma}{2}\right)/M \quad \dots\dots(6.5)$$

and
$$\frac{\Delta\gamma_p}{2} = M \left(\frac{\Delta\epsilon_p}{2}\right) \quad \dots\dots(6.6)$$

if
$$\left(\frac{\Delta\sigma}{2}\right) = \kappa^1 \left(\frac{\Delta\epsilon_p}{2}\right)^{n^1} \quad \dots\dots(6.7)$$

similarly,
$$\left(\frac{\Delta\tau}{2}\right) = \kappa^{11} \left(\frac{\Delta\gamma_p}{2}\right)^{n^{11}} \quad \dots\dots(6.8)$$

therefore,
$$n^{11} = n^1 \quad \dots\dots(6.9)$$

and
$$\kappa^{11} = \frac{\kappa^1}{M(1+n^1)} \quad \dots\dots(6.10)$$

Figure 101 shows that the cyclic stress-strain data of the annealed materials, when expressed in terms of shear stress and strain amplitudes forms a reasonable single data set, although it is seen that the data from material G8585 lie consistently above the data from the rod specimens. Since the metallographic analysis displayed little difference between the two sets of material and spectrographic chemical analysis was unable to detect any compositional differences between the two sets of materials, it is not possible to ascribe this discrepancy to any particular source.

Figure 102 shows the correlation for the shear stress-shear strain data for the cold worked materials. In this case, the fibre textured materials are seen to produce data sets which lie above the data from the plate material. This difference must be due to the different amounts of cold work in the two sets of materials. As Laird⁽¹³⁷⁾ has shown, the

cyclic stress-strain curve of wavy slip materials is not independent of prior cold work. The uniqueness of the cyclic stress-strain curve is determined by the ability of the imposed cyclic deformation to overwhelm the dislocation structure created by prior deformation and to develop a sub-structure which is characterised only by the amplitude of the cyclic deformation. The dislocation structures which are usually found in fatigue, i.e. cells⁽⁶⁾, walls⁽⁶⁾, ladders⁽¹⁴⁶⁾ are all low energy configurations⁽¹⁶⁾ and the initial dislocation structure must be reformed into such a structure during the rapid hardening/softening stage of cycling. Winter⁽¹⁴⁷⁾ has described the microstructure of fatigued copper single crystals in terms of the PSB structure which carries the plastic strain and a matrix structure of a higher plastic resistance which consists of dislocation dense arrays of dislocation dipoles and multipoles and is, therefore, a higher energy configuration. The metastable structure is preserved because, since the plastic strain is concentrated in the P.S.B.'s, the dislocation motion necessary to rearrange the dipoles and multipoles does not occur in the matrix structure.

The rapid hardening/softening stage is therefore, determined by the prior cold work and the applied strain amplitude and achievement of a stable saturation stage is determined by the ability of the strain amplitude to break down the cold worked dislocation structure. Therefore, while the cold work in the rolled plate and the drawn rods is approximately equivalent, the difference in prior cold work and the deformation state (i.e. rolling vs drawing) produces different sub-structures and hence, the cyclic shear stress-shear strain curves are different. It should be noted, however, that the annealed materials exhibit a higher degree of cyclic work hardening than the cold worked

materials and it might be expected that at higher plastic strain amplitudes, the cyclic stress-strain response would be similar for the annealed and cold worked materials. (It has been suggested that cold worked materials would eventually attain a saturation state which is determined by a history independent cyclic stress-strain curve if fracture could be prevented⁽¹³²⁾).

It appears therefore, that the textural dependence of the cyclic stress-strain response of copper (and presumably of other wavy slip f.c.c. metals) may be rationalised using the Taylor factor to reduce the longitudinal cyclic stress-strain curve to a resolved shear stress-shear strain curve. However, due to the discrepancies between the different sets of data, it must be concluded that, while the effect is detectable and may be predicted quantitatively within a given aggregate, it is of secondary importance in comparison to effects such as cold work. Also, the effect of texture would be further abated in the presence of microstructural anisotropy e.g. see Appendix III for the effect of MnS inclusions on the fatigue properties of textured SAE 4161 C-Mn steel.

Kettunen⁽¹⁴⁾ has similarly suggested that the Taylor factor may be used to analyse S/N data and has shown that the S/N data for copper single crystals of various orientations may be reduced to a single curve by plotting the resolved shear stress on the primary slip plane against the number of cycles to failure. The same author also attempted to compare the S/N curves of single crystal and polycrystalline iron (see Figures 17 and 18). However, it is obvious that the predictions and the data diverge at higher strains, which is the very region in which the Taylor theory ought to be more applicable.

In order to relate single crystal properties to the stress or strain life data of polycrystals, it is necessary to understand how

fatigue failure occurs. Obviously, fatigue damage and hence crack nucleation can only occur by the accumulation of locally non-reversed plastic strain⁽³⁾. Unfortunately, microplasticity may occur under nominally elastic conditions thus, the strain-amplitude-life curve is analysed in terms of two components of the strain, elastic and plastic. It should, therefore, be emphasized that truly elastic strain cannot cause fatigue failure and, indeed, anelastic strain should similarly be reversible. The elastic strain life correlations must then relate to microplastic strain which may be non-reversed.

For all the specimens which were examined, fatigue failure occurred in a similar manner. In particular, cracks were always observed to be associated with grains which showed a specific set of slip bands i.e. long parallel bands. Arnell and Teer⁽⁶⁵⁾ observed that failures in fatigued aluminium were associated with grains which showed similar markings. Employing x-ray microdiffraction they were able to show that the grains which developed such markings were oriented so that the stress axis lay at the centre of the stereographic triangle. The slip markings observed on the grains which were susceptible to cracking were found to conform with these data using a trace analysis technique. Thus, the failure process is dependent on the cyclic deformation which is experienced by a grain in the "soft" orientation and the textural dependence of the fatigue process should be determined by the relation between the macroscopic stresses and strains and the microscopic stresses and strains.

The problem of relating a macroscopic stress-strain state to a microscopic stress-strain state is very similar to the problem of crack nucleation at a notch, see Figure 103. Topper et al⁽¹⁴⁸⁾ employed Neubers⁽¹⁴⁹⁾ rule to relate the stress and strain at a notch root to

the macroscopically imposed stress state. Similarly, Smith et al⁽¹⁴⁹⁾ have suggested that mean stress effects may be accommodated by employing a single stress-strain function, $\sigma_{\max} \Delta \epsilon$ which governs the fatigue of metals.

In a similar manner to the assumption that the fatigue of notched bodies is controlled by the local stress-state it will be assumed that the fatigue of polycrystals is governed by the stress state in a grain of a soft orientation. Employing the function $\frac{\Delta \sigma}{2} \frac{\Delta \epsilon}{2}$ is equivalent to describing the accumulation of fatigue damage in terms of the hysteresis work which is absorbed during a single cycle (Morrow⁽⁷⁾ points out that this factor strictly pertains only to the plastic work and the quantity should be multiplied by a shape factor which describes the hysteresis loop). Using equations 6.5 and 6.6 it can be shown that

$$\Delta \sigma \Delta \epsilon = \Delta \tau \Delta \gamma \quad \dots\dots(6.11)$$

Again, this should strictly relate only to plastic work but it will be used to describe the total work due to the uncertain nature of the deformation in the nominally elastic region of the strain life curve. The curves of the function $\Delta \sigma \Delta \epsilon / 4$ vs $2N_f$ are shown in Figures 104 to 107 for the data which were presented earlier in Figures 63 to 78. Because of equation 6.11, in plotting the product of the longitudinal stress and strain amplitudes, one is effectively plotting the local shear work i.e. $\Delta \tau \Delta \gamma$ against the fatigue life. If, therefore, the cyclic stress-strain response of the material can be expressed as a unique shear stress-shear strain curve, then the fatigue life data should be dependent upon a similar function of the local shear stress and strain amplitudes providing, of course, that damage is always accumulated in the same manner. Since fracture was always observed in

the same type of grain, and it must be emphasised that in a truly polycrystalline material, there will always be some grains which are oriented favourably, it is reasonable to assume that the deformation may be characterised by damage accumulation in the region in which failure occurs. Figure 104 shows that by plotting the data in this manner, the two sets of data points fall almost on the same curve, the solid lines which are shown on the diagram correspond to the predicted value of the function $\frac{\Delta \epsilon}{2} \frac{\Delta \sigma}{2}$ calculated from the materials parameters σ_f^1 ϵ_f^1 b and c which were given in Table 18. Similarly, the data for the cold worked rods is presented in Figure 105 and the values of the function for the annealed plate and rod materials are plotted in Figures 106 and 107 respectively. The data plotted for material B3500 correspond to the analysis using the corrected value of the elastic modulus as described earlier.

Comparison of the plots in Figures 104 to 107 with the total strain-life curves in Figures 71 to 78 show that the data for similar materials, i.e. of the same origin and of the same degree of cold work, have been reduced to a single data set irrespective of textural differences. The differences between the different materials are still discernable, especially as a function of cold work. The cold worked materials still display a greater endurance particularly in the high cycle fatigue regime. Comparing the cold worked fibre texture data with the cold worked plate data i.e. Figure 105 vs Figure 104, shows that the data fall very close together and may be described by a single curve. Although the data for the annealed materials falls very closely together, it is obvious that there is a systematic trend for the data for the plate material to lie above those for the rod material. This is similar to the trend in the total strain life plots and should also be correlated with the shear stress amplitude-

shear strain amplitude curve shown in Figure 101 where the data from the G8585 was found to lie consistently above that for the rod materials.

6.3 The Development of Texture During Fatigue

The development of texture during fatigue could influence the material response to the imposed cyclic deformation and it is therefore important to establish whether fatigue causes the development of a new texture. The results of the simulations are clearly at odds with the experimental evidence e.g. Table 3 vs Figure 92. The predictions of the Taylor-Bishop and Hill theory state that fatigue should impose a texture of the type $\{001\}\langle 110 \rangle + \{001\}\langle 310 \rangle$ while the experimental data indicate that the influence of the cyclic deformation is to randomise the texture.

Inakazu and Yamamoto⁽⁵⁸⁾ showed that drawn aluminium wire exhibited a greater endurance in high cycle fatigue due to the presence of texture components lying between $\{110\}\langle 1\bar{1}1 \rangle$ and $\{112\}\langle 11\bar{1} \rangle$. It was suggested that the greater endurance of this material was due to the stability of these orientations under strain cycling. The texture measurements made in this investigation were made on specimens cut from the surface of the fatigued rod. Figure 108 illustrates the difference between the textures generated by the present fatigue simulations and the stable orientations suggested by Inakazu and Yamamoto. This is not in agreement with the predictions using the present simulation technique. Using the present technique, the simulation of texture developed under torsional conditions would produce texture components which are related to the $\{001\}\langle 310 \rangle$ and $\{001\}\langle 110 \rangle$ texture components by a rotation of 45° about the normal direction for a torsional axis parallel to the normal direction.

The findings of the present experimental work agree with the conclusions of Hayashi and Suzuki⁽⁵⁷⁾ that fully reversed cyclic deformation tends to randomise the texture. These authors suggested that the rearrangement occurred during the rapid hardening stage of fatigue and was accomplished by the formation of subgrains which are rotated with respect to each other. The re-orientation could be accomplished by the formation of a dislocation cell structure, equivalent to the P.S.B. type of structure and Winter⁽¹⁵¹⁾ has recently shown that the P.S.B. structure may be found in the interior grains in fatigued polycrystalline copper. The postulate that crystallographic re-orientation may be accomplished by the formation of dislocation cells is in disagreement with the findings of Laird et al⁽¹³⁷⁾ who suggested that the difference between the cell structures of materials which were initially cold worked or annealed was that only the annealed structures contained cell walls which were balanced with respect to dislocations of opposite signs. Such conclusions are based on transmission electron microscopy which shows little contrast across a fatigue dislocation cell boundary e.g. see Figure 109 which is taken from reference 152. It is, however, clearly not possible to state that the imaging conditions across a cell wall are identical and that the orientation of adjacent cells are, therefore, identical. If a small mis-match is permitted across a cell boundary, the accumulated mis-match across a grain could be significant and therefore the randomisation could be accommodated by this process.

The major objection to the use of the Taylor-Bishop and Hill approach is therefore that it fails to predict the generation of texture during fatigue. Recently, Rasmussen and Pedersen⁽¹⁵³⁾ have attempted to describe the fatigue of polycrystalline f.c.c. metals by employing a Sachs-type approach. The basis of their approach is that within

P.S.B.'s slip occurs on the primary slip system only. The persistent slip bands are considered to be lenticular platelets which are constrained by the surrounding matrix region. This constraint develops a back stress within the slip band which must be subtracted from the saturation stress of polycrystals in order to compare the cyclic shear stress-shear strain curve with that of single crystals. By employing this technique, Rasmussen and Pedersen were able to show that the cyclic shear stress-shear strain curves of polycrystalline and single crystals of copper can be made to coincide by using the Sachs factor rather than the Taylor factor, i.e. for a random aggregate $M = 2.24$ rather than 3.06. There is, however, in this work a small difference between the cyclic shear stress-shear strain curve from the single crystals and the curve calculated on the basis of the Sachs model for polycrystals. Figure 110 is reproduced from reference 153, bearing in mind that,

$$\Delta\sigma = \Delta\sigma/M \quad \text{and} \quad \Delta\gamma_p = M\Delta\epsilon_p$$

It can be seen that the effect of increasing M is to lower the shear stress amplitude and to extend the region of the plateau. This plateau in the cyclic stress strain curve has been reported by Laird⁽¹⁶⁾ and Mughrabi⁽¹⁴³⁾ using Taylor type calculations and has been attributed to the regime in which the imposed cyclic plastic strain may be accommodated within one or more P.S.B.'s which operate at a specific strain amplitude. The volume fraction of material which is occupied by the P.S.B. structure varies until the whole of the material is consumed by the P.S.B. structure.

It appears, therefore, that a choice between the Sachs or Taylor model cannot be made using the examination of the cyclic shear stress-shear strain curves. In the present work the major criticism of the Taylor model has been that it fails to predict the development of texture during fatigue. However, the Sachs model, involving slip on only one system, would predict that fatigue deformation should not affect the texture. Witzel^(154, 155) has employed torsional fatigue to study the development of texture under cyclic deformation. Using very large cyclic strain amplitudes, $0.02 < \frac{\Delta\gamma}{2} < 0.16$, Witzel concludes that torsional fatigue should develop a $\{110\}\langle 1\bar{1}0\rangle$ to $\{112\}\langle 11\bar{1}\rangle$ described by Inakazu and Yamamoto⁽⁵⁸⁾. It should be emphasised, however, that the strain amplitudes employed by Witzel are exceptionally large (and there must always be some imprecision associated with the measurements of mechanical properties when strain gradients exist across the gauge section of the specimen). The $\{110\}\langle 1\bar{1}0\rangle$ component is also predicted to develop during monotonic torsional deformation. It is possible, therefore, that the large strain amplitude employed by Witzel may produce texture development which is not typical of fatigue at lower strain amplitudes.

Due to the nature of the cyclic hardening curves, it is suggested that any textural changes should occur before saturation. During saturation, the dislocation structure remains stable and presumably the slight softening observed by Abel⁽¹³⁵⁾ occurs due to a sharpening of the dislocation structure but is not related to any major orientation changes. The development of a 3-D dislocation structure requires that deformation occurs on more than one slip system. Thus, the model which is employed to predict the variation of yield stress as a function of orientation should take this into account. It is most probable that the major cause of the difference between the predicted texture development and the empirical measurement is that fatigue is

a localised process while the Taylor theory is based on the concept of homogeneous deformation. Consequently, while a single grain may deform in an apparently homogeneous manner, i.e. it maintains the same shape and has an apparently uniform dislocation structure, the accumulation of damage is localised e.g. the slip markings in Figure 82. Thus, while the stress-strain relationship may be predicted by the Taylor theory the rotations calculated by the theory may be invalid due to the inhomogeneity of distribution of the damage.

6.4 Fatigue Fracture

The cyclic stress-strain experiments produce only limited information relative to the fracture behaviour. Due to the small size of the specimens fatigue crack propagation is very rapid because of the rapid decrease of the net cross section. Fractography of the smooth sided specimens revealed that the nucleation of the fatigue cracks was related to grain orientation and was not related to the orientation of the specimen reference axes. As noted earlier, the fatigue cracks were found to nucleate in grains which developed a specific type of slip pattern. In particular the cracking appears to be enhanced in the presence of twin and grain boundaries. These results are in agreement with the results of Boettner et al⁽¹⁰⁾ who showed that twin boundaries may be susceptible sites for fatigue crack nucleation. It has been shown that in low stacking fault copper alloys that the formation of annealing twins can subsequently influence the topographical development during fatigue. For example, the grain boundaries on which twinned grains impinge may be subjected to large strain incompatibilities and are thus suitable sites for fatigue crack initiation⁽¹⁵²⁾. Kim and Laird^(156,157) have reported optical observations including interferometric measurements of grain boundary cracking of copper in high

strain fatigue. They state that during cyclic deformation, the grain boundaries may exhibit large amounts of highly localised deformation which is especially severe if the slip was directed towards the boundary over a long distance. In order to perform their optical measurements, however, Kim and Laird were constrained to use polycrystalline copper of large grain sizes. The observations reported in section 5.6.1.1 were conducted at higher magnification and it is probable that the discrepancies between the present results and those of Kim and Laird are due to the stress concentrating effects of grain and twin boundaries being of more importance in the finer grained material used in this investigation. It is also probable that the higher resolutions of a scanning electron microscope facilitates the observation of cracking within the P.S.B. whereas optical microscopy is able only to detect the large relative motion of the two sides of the grain boundary after the embryonic crack has grown out of the slip band and along the grain boundary.

To some extent these data and the results of Arnell and Teer⁽⁶⁵⁾ are at odds with the results of the single crystal work of Avery et al⁽²⁶⁾, who showed that the slip band extrusion rate was related to the shear stress on the cross slip system. There is also conflict with the results of Kemsley and Paterson^(17,18) who showed that the coarse slip band development was associated with greater cross slip. Figure 81 shows that the simple slip pattern developed in the susceptible grains is by no means the most severe damage and it is therefore wrong to associate the general coarseness of topographical development with easy crack nucleation. The work of Avery et al⁽²⁶⁾ may not be relevant to the polycrystalline behaviour since in the case of single crystals deformation on more than one system is determined only by the crystal orientation whereas in polycrystals the tendency to deform on more

than one slip system is imposed by the requirements of strain compatibility across grain boundaries.

The appearance of the fracture surfaces of the specimens tested under fully reversed strain cycling was complicated by the smearing effects caused by the compressive deformations. The major features, however, can be described by the appearance of ductile striations or the facet-like features illustrated in Figure 87. The ductile striations were more prevalent in the annealed materials and in the cold worked materials at higher loads. The facet-like features appear at lower strain amplitudes and are usually found closer to the notch. Nair and LeMay^(61,62) noted similar behaviour and analysed the difference in fracture surface appearance in terms of Wood's⁽⁵⁾ models of fatigue failure. In particular, they suggested that the facets were produced by a limited ductility fracture mode which involved brittle crack propagation along dislocation cell boundaries (i.e. Woods F-mechanism). However, Awatani et al⁽¹⁵⁸⁾ have shown using T.E.M. that fatigue cracks do not employ cell boundaries as preferential paths but propagate across the cells.

Facets have been reported in copper, at low crack propagation rates⁽¹⁵⁹⁾ and under ultrasonic fatigue⁽¹⁶⁰⁾, in brass⁽¹⁶¹⁾, in aluminium^(162,163) and in aluminium alloys^(36,65,67). The exact determination of the crystallographic orientation of the facets is difficult due to the very severe deformation produced by the propagation of the fatigue cracks. Etch pitting and electron channeling pattern observations were unable to identify the crystallography of the facets found in this investigation. Because of the degree of deformation at the fracture surface, it is incorrect to describe the facets as a brittle mode of failure and it is probable that the facets form due to crystallographic constraints on the deformation at the crack tip. It is also highly

probable that this mode of failure is influenced by environmental effects (159). Priddle and Walker⁽¹⁶⁴⁾ have reported that similar facets which they found on the fatigue fracture surfaces of 316 stainless steel, were most numerous when the reverse plastic zone at the crack tip was approximately equal to the grain size. However, the x-ray measurements suggested that the facets were parallel to {111}, which is in contradiction to the work of Garrett and Knott⁽⁶⁷⁾, Forsyth et al⁽⁶⁶⁾ and Koterazana and Shino⁽¹⁶²⁾ on aluminium alloys who reported {100} fracture facets. The latter authors rule out the possibility of brittle cleavage in the precipitation hardened alloy by noting that the fracture facets were found to consist of fine striations and slip lines when examined at high magnification. Weber and Hertzberg⁽¹⁶¹⁾ claim to have found facets of {111}, {110} and {100} types on the fracture surfaces of 70/30 Brass fatigued at low crack growth rates.

In the present investigation, it has not been possible to identify the crystallographic orientation of the facets, although the presence of the facets has been correlated with lower crack propagation rates. The facets were most prevalent on the fracture surfaces of the 45° specimens of III80. The influence of texture produces a low Taylor factor for this orientation and encourages through thickness yielding which is reflected by the high R-value (Table 6). Presumably, at low values of the stress intensity amplitude the softer material is more easily able to accommodate the stress intensity at the crack tip by plastic flow and fracture occurs on a localised scale, producing the faceted-type appearance which has been correlated with the restricted plastic zone size.

The major effect of texture on fatigue crack growth appears to be the ability to reorient the crack growth away from the direction which is normal to the stress axis. Tables 19 and 20 show that the orientations

which displayed slant type fractures were found to display significantly lower crack propagation rates when measured in the manner described i.e. projected onto the plane which is normal to the stress axis. In this case, the calculation of ΔK_I is actually invalid since the analysis should consider the stress field at the tip of the crack which is oblique to the stress axis. However, the use of " ΔK_I " is not, in this case, meant to imply the mode I stress intensity amplitude but merely a mathematical function of the crack length and the applied load (in particular it relates to the uncracked cross-section and the macroscopically applied load).

The effect of specimen thickness on the fatigue crack propagation has been reported by Ritchie et al⁽¹⁶⁵⁾ and Heiser and Mortimer⁽¹⁶⁶⁾. The fracture plane in both investigations was found to develop a slant orientation i.e. at 45° to the through thickness direction, as the thickness was reduced. The two sets of results are, however, contradictory as regards the effect of specimen thickness on the rate of fatigue crack propagation. Ritchie et al showed that at constant ΔK the fatigue crack growth rate in thicker specimens is faster than in thinner specimens, while Heiser and Mortimer found that the exponent "m" in the Paris equation increased as the thickness of the specimen increased and concluded that the rate of fatigue crack propagation was accelerated by plane strain conditions at the crack front. Garrett⁽¹⁶⁷⁾ has suggested that the problem is not, however, simply a question of "plane stress" vs. "plane strain" but of the opening mode at the crack tip and that there is a difference in the macroscopic opening of the crack. It is frequently observed that due to a change in loading or at a particular crack length the crack propagation changes from a planar to a slant mode (or v.v.).

Pook⁽¹⁶⁹⁾ has suggested that slant growth is favoured over planar growth at specific regimes of ΔK although this is only a necessary but not a sufficient condition for the tensile-to-shear transition. Pook has also noted the effect of crystallographic texture in suppressing slant crack growth by inhibiting through thickness yielding. Schijve⁽¹⁷⁰⁾ has shown that the problem may be much more complex than a simple dependence on the ability to develop plane strain crack propagation by showing that internal fatigue cracks which grow in vacuum develop a shear mode of failure while cracks which grow in a more aggressive environment do so in a tensile manner. However, Schijve⁽¹⁷⁰⁾ did comment that the slant fracture appeared to be related to the original axes of the plate from which the specimens were taken and, thus, was probably influenced to some degree by texture.

In the present investigation, the faster crack propagation rates were observed in specimens which developed macroscopically planar fractures. Besides being in agreement with the results of Heiser and Mortimer these data correlate with the work of Rieu et al⁽⁵⁶⁾, Neumann⁽³¹⁾ and Neumann et al⁽⁵⁴⁾ who observed that crack propagation was faster when planar fracture surfaces were obtained. The correlations between crack growth rates in flat and shear mode have been made under constant loading conditions⁽¹⁶⁵⁻¹⁷⁰⁾ while the studies of the interaction of mixed mode opening have tended to study the effect of an increasing secondary component of stress on the crack propagation while maintaining the primary constant, i.e. increasing ΔK_{II} while maintaining ΔK_I constant^(171,172). Under such conditions it has been shown that an increase in ΔK_{II} causes an increased rate of fatigue crack propagation under constant ΔK_I . Pook⁽¹⁷³⁾ has demonstrated that the effect of propagation is primarily controlled by the residual mode I stress intensity in mixed mode opening and Hurd and Irving⁽¹⁷⁴⁾ have most recently shown

that for a given absolute amplitude of the stress intensity crack propagation under mode III is much slower than under mode I.

The present results, therefore, reflect the different modes of crack propagation as a function of texture. The stress intensity at the tip of a slant crack contains components ΔK_I , ΔK_{II} and ΔK_{III} while the stress intensity at the tip of a planar crack is effectively dependent on ΔK_I only. However, the mode I stress intensity in the two cases is not the same. For the same loading conditions and the same projected crack length the mode I opening stress intensity at the tip of a slant crack is much less than at the tip of a flat crack⁽¹⁷³⁾.

i.e.

$$\Delta K_I = KA \sin^2 \beta$$

$$\left. \frac{da}{dN} \right|_1 = \left. \frac{da}{dN} \right|_{abs} \cos \beta$$

where β is the angle between the crack plane and the stress axis and $\left. \frac{da}{dN} \right|_1$ is the projected crack propagation rate while $\left. \frac{da}{dN} \right|_{abs}$ is the rate of crack extension which occurs along the crack. Garrett⁽¹⁶⁷⁾ has also shown that the frequently observed point of inflexion in crack propagation curves as a function of applied ΔK is due to a tensile-to-shear transition and is effectively caused by a reduction in the mode I stress intensity amplitude associated with the reorientation of the crack. More recently, Sih and Barthelemy⁽¹⁷⁵⁾ have used an energy density criterion of damage accumulation to show that under constant loading conditions deviation of the crack orientation from the direction normal to the stress axis, lying in the plane perpendicular to the stress axis, should result in a decrease in the rate of crack propagation.

Despite the different macroscopic appearance of the fracture surfaces of the crack propagation specimens the microscopic views of

the fracture surfaces appeared very similar. Although the fracture surfaces of the smooth sided specimens displayed greater differences microscopically it should be emphasized that these were obtained at much higher rates of propagation and presumably there is some influence of monotonic deformation e.g., the shear features in Figure 86 which link the regions of striations⁽¹⁷⁵⁾. Under conditions of lower stress intensity it appears that the microscopic modes of crack propagation are very similar in thin sheet (Figure 61), fully reversed strain controlled fatigue (Figure 87) and thick plate S.E.N. specimens (Figure 90).

There is, however, a fundamental difference between the fractures in the thin sheet and in the specimens machined from the thicker plate. In the thin sheet specimens the orientation which produces slant growth is inclined at 45° to the rolling direction. The slant fracture observed in the S.E.N. specimens also occurs in the 45° specimens yet the major components of the two textures, {001}<100> and {001}<110> are related by a 45° rotation about the rolling plane normal. Consequently, while the slant fracture in the sheet material occurs at the lowest value of the R-value, the slant fracture in the thicker material occurs in the orientation which is predicted to develop the higher R-value (see Table 6).

It is difficult to resolve the paradox of these two contradictory textural effects and no firm explanation can be presented. However, a tentative rationalisation may be advanced as follows. The difference in the thin sheet behaviour is regarded primarily as due to plane stress conditions prevailing in the 45° specimen while plane strain conditions prevail at the crack tip in the 0° and 90° orientations. Table 6 shows that in the 0° and 90° orientations shear is easily accommodated within the plane of the sheet thus the deformation at the

crack tip (see Figure 111) may be confined to planar shears within the bands as suggested by Laird⁽¹⁰⁾ Neumann⁽³¹⁾ and Rieu⁽⁵⁵⁾, i.e. the bands shown in Figure 111 contain only shears which lie in the plane of the crack tip thus the crack grows in the direction z if the shears are equal. This is probable since the slip direction in f.c.c. materials is $\langle 110 \rangle$ and the directions at 45° to the stress axis in the 0° and 90° are parallel to the $\langle 110 \rangle$ directions of the major component of the texture. In the 45° specimens in-plane yielding is suppressed according to Table 5 and the predominant constraint is one of plane stress. At the tip of a crack nucleus the deformation is concentrated and a plane strain condition develops along a band which is inclined to the stress axis⁽¹²⁷⁾. The crack is then constrained to develop along the band. In the case of a fatigue crack it is probable that the stress concentration produces the plane strain at the crack tip which causes the propagation of a small band of through thickness strain ahead of the crack at the prescribed angle. The fatigue crack is then constrained to propagate along the band of reduced net cross-section and the process continues. For an isotropic solid the shear band formed in monotonic plane stress ductile fracture is formed at 54° to the stress axis. It can be shown however, that this angle is a function of the anisotropy of the material⁽¹²⁷⁾.

In the case of the thicker material, it is assumed that plane strain conditions prevail at the crack tip, due to the thickness of the material, for both orientations. For the 90° orientation, the shear bands at the crack tip may be formed at about 45° to the rolling direction. Table 5 indicates that in this region, the R-ratio is large and thus shear along the bands ϵ_s as shown in Figure 111, is possible with the suppression of deformation along the line of intersection of the two bands. Therefore, the crack is able to propagate in plane strain

in the manner described by Rieu et al⁽⁵⁵⁾ and a planar fracture is produced which as has been noted earlier, tends to produce rapid crack propagation. In the case of the 45° specimens if the bands form at about 45° to the tensile axis the r-value predictions of Table 5 suggest that in-plane shears are suppressed at the expense of through thickness shears, i.e. the shears ϵ_{th} in Figure 111 are promoted. However, due to the thickness of the specimen, the parts of the specimen, through which the crack has already passed, constrain the crack tip to resist the through thickness strain. The deformation at the crack tip may, therefore, be achieved by producing through thickness strains which are in the opposite sense in each band. The shears at the crack tip thus constitute a mixture of mode I and mode III, antiplane shear, opening. Presumably, under the influence of these shears, the crack reorients to produce a slant crack orientation. The complex set of shears continue to operate as the crack reorients and the lower rate of growth may be ascribed to the mixed mode of crack opening as postulated by Garrett⁽¹⁶⁷⁾.

In summary, therefore, it appears that the influence of texture on the fatigue crack morphology is different in thick and thin material. In thin materials, cracks may propagate perpendicular to the through thickness direction and the stress axis of the strains at the crack tip can be accommodated within the plane. If the texture tends to induce through thickness strain, the controlling influence becomes the requirement of plane stress and propagation occurs by a process of through thickness strains along a shear band which is inclined to the stress axis. In this case, the strain along the direction of the shear band is expected to be very small. In contrast, in the thicker material, the fatigue cracks propagate by the action of shear bands at the crack

tip but because of the thickness of the material in this case the deformation should be parallel to the direction of the band in order to attain flat crack growth. If the texture causes the tendency towards through thickness deformation in the shear bands, the crack reorients into a slant mode.

Due to the similarity of high magnification micrographs of the different fatigue fracture surfaces examined in this investigation, it must be concluded that texture has very little effect on the microscopic mode of failure. The influence of texture on crack propagation may be rationalised by considering the constraints imposed by the bulk of the material upon the slip processes which may act at a given site in the crack front. The requirements of the compatibility of strain at the crack front should counteract the perhaps favourable local crystallography to produce more uniform crack growth. Thus, even though one particular grain may be favourably oriented for crack growth the crack front may not accelerate through that grain because of the arresting effect of contiguous grains. Similarly the microscopic crack plane is probably determined not only by the local crystallography, as proposed by Neumann⁽³¹⁾ and Pelloux⁽¹³⁴⁾, but also by the orientation of the crack in surrounding grains. It would, therefore, be wrong to suggest that fatigue crack propagation must occur on {hkL} planes in a polycrystalline material under conditions of ductile fatigue failure.

CHAPTER 7

Summary, Conclusions and Suggestions for Further Work

7.1 Summary and Conclusions

1. The experimental results have shown that texture affects the cyclic stress-strain response and the strain amplitude-life curve of copper tested in fatigue.

2. Within a given material the effect of preferred orientation on the cyclic stress-strain relation may be predicted by texture analysis. The magnitude of the texture influence is dependent upon the severity of the texture and is much more important in copper than grain size effects. This may, however, not be true for materials which have been observed to exhibit grain size dependence of fatigue properties. It is also expected that the effect of texture may be of secondary importance in the presence of microstructural anisotropy such as elongated inclusions.

3. Although the Taylor theory was found to predict the orientation dependence of the cyclic properties, it has been shown that the development of texture as predicted by the Taylor theory does not agree with the empirical measurements of texture developments during fatigue. It was found that in practice, fatigue tends to randomise the texture. It has been suggested that the failure of the Taylor theory to predict the generation of texture results from the inhomogeneous nature of fatigue deformation.

4. It has been noted that in comparing the predictions of texture with the fatigue behaviour, the errors involved in the fatigue analysis are much greater than those involved in texture measurements. The uncertainty in fatigue data results from the inherently *statistical* nature of the failure process so that small differences due to textural effects may be obscured by the imprecision of the fatigue results.

5. Although the use of the parametric expression of fatigue properties in terms of σ_f^1 , ϵ_f^1 , b , c , n^1 and K^1 may be expected to reduce the errors involved in assessing texture effects it has been shown that the cyclic stress-strain analysis is subject to serious errors if care is not taken in ascribing the relevant portions of damage to the elastic and plastic regimes respectively. In particular, this is relevant since the texture influences the elastic modulus and this parameter is frequently employed to apportion the strain ranges. It has been shown that the incorrect choice of the elastic modulus has a significant effect on the cyclic stress-strain analysis.

6. It has been found that, within the same material, the orientations which develop the greater resistance to constant strain cycling show a softer cyclic stress-strain curve and that the strength of the cyclic stress strain curves may be predicted on the basis of texture measurements.

7. It has been shown that the different cyclic stress-strain curves may be rationalised to a single cyclic shear stress shear strain ($\Delta\tau$ vs $\Delta\gamma$) for materials with the same starting condition by using the appropriate Taylor factor. The cyclic stress strain curve was not

found to be independent of strain history although the harder materials exhibited a lower degree of cyclic work hardening than the softer ones. It is suggested that the cyclic stress-strain curve is determined by the ability of the applied strain amplitude to cause a breakdown of the prevailing dislocation structure and generate a dislocation structure which uniquely determines the cyclic stress-strain curve. It is suspected that the history dependence or otherwise of the cyclic stress-strain curve is a function of the prior mechanical history and the applied strain amplitude.

8. Examination of the slip markings on the sides of the specimens revealed that the slip line patterns were dependent upon the orientation of the grain. It was found that fatigue cracks did not nucleate in the grains which displayed the apparently most severe surface damage but in grains oriented primarily for single slip which developed long narrow parallel slip bands. Particularly prone to crack nucleation were regions where the long slip bands impinged on twin and grain boundaries.

9. The strain amplitude-life data were reanalysed in terms of the parameter $\Delta\sigma\Delta\epsilon \propto 2N_f$ and it was shown that this tends to produce a function which is independent of orientation. The independence of this function has been rationalised by noting that fatigue failures were always nucleated in grains of the same orientation. It is suggested that the function $\Delta\sigma\Delta\epsilon$ is identical to the function $\Delta\tau\Delta\gamma$ which are the shear stress and shear strain amplitudes respectively in the weakest grain. Thus, it is effectively assumed that the failure process is related to the damage accumulation in the weakest grain because of the uniqueness of the shear cyclic stress-strain curve.

10. The effect of preferred orientation on fatigue crack propagation is to cause reorientation of the crack to promote strain compatibility at the crack tip. When this induces a slant-type fracture the rate of crack propagation is found to be reduced.

11. The criteria for slant-type fracture were found to be different in thin materials and thick materials. In thin materials, slant fracture was found to occur when the texture was unable to contain the strain within the plane of the sheet. The slant-type fatigue fracture in this case was considered to be due to the propagation of the crack along a shear band which forms at an acute angle to the stress axis. In thick materials, the slant-type fracture forms because the shear bands which form at the crack tip (and produce the increments of crack growth) are constrained by the material thickness not to produce thinning of the material while the textural influence tends to promote through thickness yielding. In this case, the crack is observed to re-orient into a slant mode and to accommodate the shears in the slip bands by employing a mixed mode of crack tip opening.

7.2 Suggestions for Further Work

It has been established that textural effects may influence fatigue processes in a pure f.c.c. metal which deforms by wavy slip. Before applying the results to more complex commercially applicable systems, it would be desirable to investigate the effect of texture on the fatigue properties of cubic metals which do not deform readily on $\{111\}\langle 110 \rangle$ systems with easy cross slip.

1. Pure single phase f.c.c. metal of low stacking fault energy may be investigated since the restrictions of

planar slip may produce a more severe dependence upon crystallographic orientation.

Single phase b.c.c. metals and alloys should be investigated to determine whether the difference in slip modes between b.c.c. and f.c.c. metals proves significant in fatigue.

2. Super pure material, e.g. Fe may be investigated to determine the relevance of symmetric slip, which has been shown (see Chapter 2) to influence the fatigue of single crystals, on the textural effects in polycrystals of b.c.c. materials.
3. The influence of pencil glide deformation on the anisotropy of fatigue properties may be different from that of restricted glide.

The examination of textural anisotropy ^{of the} fatigue of commercially applicable materials may require studies of,

4. Precipitation hardening alloys since these often display precipitate morphologies which are orientation dependent. Such an orientation dependence may influence the single crystal anisotropy and hence affect the textural influences on the fatigue of polycrystals.
5. The relative effects of microstructural anisotropy might be investigated. In a commercial steel,

anisotropy may result from texture, phase distribution and morphology, e.g., ferrite grain shape, and the orientation of elongated inclusions.

6. The present investigation has also revealed the very interesting interaction between specimen size and texture upon the rate of fatigue crack propagation. Further investigations into the effects of stress state and texture on the mode of crack propagation would appear to provide a promising area of research.

References

REFERENCES

1. Laird C., "The Cyclic Deformation of Metals and Alloys" in "Treatise on Material Science and Technology Vol.6: Plastic Deformation of Metals" ed. E. Arsenault, Academic Press, New York (1975), p.101.
2. Grosskreutz J.C., Phys. Stat. Sol., 47b, (1971), 359.
3. Laird C., "The Influence of Metallurgical Structure on Fatigue Crack Propagation" in "Fatigue Crack Propagation - ASTM-STP 415", ASTM Philadelphia, (1967), 139.
4. Frost N.E., Marsh K.J. and Pook L.P., "Metal Fatigue", Clarendon Press, Oxford (1974).
5. Wood W.A., "Four Basic Types of Metal Fatigue" in "Treatise on Material Science and Technology Vol.5", ed. H. Herman Academic Press, New York, (1974).
6. Feltner C.E. and Laird C., Acta Met., 15, (1967), 1621.
7. Morrow J., "Cyclic Plastic Strain Energy and Fatigue of Metals" in "Internal Friction Damping and Cyclic Plasticity - ASTM-STP 378", ASTM Philadelphia, (1965), 43.
8. Forsyth P.J.E. and Ryder D.A., Metallurgia, 63, (1961), 117.
9. Polmear I.J. and Bainbridge I.F., Phil. Mag., 4, (1959), 1293.
10. Boettner R.C., McEvily A.J. and Lin Y.C., Phil. Mag., 10, (1964), 95.
11. Paris P.C. and Erdogan F., J. Basic Eng., Trans. ASME(D), 85, (1963), 528.
12. Broom T. and Ham R.K., Proc. Roy. Soc., 251, (1959), 186.
13. Roberts E. and Honeycombe R.W.K., J. Inst. Met., 41, (1962-63), 134.

14. Kettuner P.O., *Phil. Mag.*, 16, (1967), 253.
15. Kettuner P.O., *Acta. Met.*, 15, (1967), 1275.
16. Laird C., *Mat. Sci. and Eng.*, 22, (1976), 231.
17. Patterson M.S., *Acta. Met.*, 3, (1955), 491.
18. Kemsley D.S. and Patterson M.S., *Acta. Met.*, 8, (1960), 453.
19. Wadsworth N.J., *Acta. Met.*, 11, (1963), 663.
20. Sastry S.L., Ramaswami B. and Goetz F., *Met. Trans.*, 7A, (1976), 243.
21. Feltner C.E. and Laird C., *Acta. Met.*, 15, (1967), 1633.
22. Bhat S.P. and Laird C., *Scripta Met.*, 12, (1978), 687.
23. Finney J.M. and Laird C., *Phil. Mag.*, 31, (1975), 339.
24. Mughrabi H., *Mat. Sci. and Eng.*, 33, (1978), 207.
25. Stubbington C.A. and Forsyth P.J.E., *J. Inst. Met.*, 86, (1957-58), 90.
26. Avery D.H., Miller G.A., and Backofen W.A., *Acta. Met.*, 9, (1961), 892.
27. Laird C. and Feltner C.E., *Trans AIME-TMS*, 239, (1967), 1074..
28. Woods P.J., *Phil Mag.*, 28, (1973), 155.
29. McEvily A.J. and Boettner R.C., *Acta. Met.*, 11, (1963), 725.
30. Neumann P., *Acta. Met.*, 17, (1969), 1219.
31. Neumann P., *Acta. Met.*, 22, (1974), 1155.
32. Laird C. and Smith G.C., *Phil. Mag.*, 7, (1962), 847.
33. Donch J.C. and Haasen P., *Zeit für Met.*, 62, (1971), 780.
34. Leverant G.R. and Gell M., *Met. Trans.*, 6A, (1975), 367.
35. Duquette D.J., Gell M. and Piteo J.W., *Met. Trans.*, 1, (1970), 3107.
36. Nageswararao M. and Gerold V., *Metal Science*, 11, (1977), 31.
37. Meyer R., Gerold V. and Wilhelm M., *Acta. Met.*, 25, (1977), 384.
39. Pook L.P., *J. Soc. Environ. Eng.*, 15, (1976), 3.
40. Ishii H. and Weertmann J., *Met. Trans*, 2, (1971), 3441.
41. Weertmann J., *Int. J. Frac. Mech.*, 2, (1966), 460.
42. Santner J.S. and Fine M.E., *Met. Trans.*, 7A, (1976), 583.
43. Yeske R.A. and Weertmann J., *Met. Trans.*, 5, (1974), 2033.

44. Hempel M.R., "Slip Band Formation and Fatigue Cracks under Alternating Stress" in "Basic Mechanisms of Fatigue - ASTM-STP 237", ASTM, Philadelphia, (1958), 52.
45. Nine H.D., J. Appl. Phys., 46, (1975), 3260.
46. Nine H. D., Appl. Phys. Lett., 22, (1973), 382.
47. Nine H.D., Scripta. Met., 4, (1970), 887.
48. Etermad B. and Guiu F., Scripta. Met., 8, (1974), 931.
49. Doner M., Di Primio J.C. and Salkoritz E.I., Acta. Met., 21, (1973), 1547.
50. Nine H. D., J. Appl. Phys., 44, (1973), 4875.
51. Mughrabi H. and Wüthrich C., Phil. Mag., 33, (1976), 1406.
52. Neumann R., Zeit für Met., 66, (1975), 26.
53. Nine H. D., Phil. Mag. 33, (1976), 1406.
54. Neumann P., Vehoff H. and Fuhlrott H., "On the Mechanism of Fatigue Crack Growth" in "I.C.F.-4 Fracture 1977", Pergammon Press, London (1978), 1313.
55. Rieux P., Driver J. and Rieu J., Acta. Met., 27, (1979), 145.
56. Davies G. J., J. of Metals, 28, (1976), 21.
57. Hayashi I. and Suzuki S., "Investigation on the Axisymmetrical Deformation Texture of Polycrystalline Copper under Static Load and Cyclic Load" in "Proc. 20th Congress on Materials Research", Soc. of Mat. Sci., Japan (1977), 18.
58. Inakazu N. and Yamamoto H., J. Jap. Inst. Met., 39, (1975), 339.
59. Packer M.E., and Coyle R.A., Metal Science, 12, (1978), 421.
60. Le May I. and Nair K.D., J. Basic Eng. Trans. ASME(D), 91, (1970), 115.
61. Nair K. D. and Le May I., Metallography, 4, (1971), 243.
62. Nair K.D. and Le May I., "The Use of Electron Fractography in

Interpreting the Mechanism of Fatigue Crack Propagation"
in "Electron Microfractography - ASTM STP 453", ASTM
Philadelphia, (1969), 134.

63. Ruberg T., Ph.D. Thesis, University of Cambridge, (1973).
64. Tchorzewski R.W. and Hutchinson W.B., Metal Science, 12, (1978),
109.
65. Arnell R.D. and Teer D.G., Met. Sci. J., 3, (1969), 126.
66. Forsyth P.J.E., Stubbington C.A. and Clark D., J. Inst. Met., 90,
(1961-62), 238.
67. Garrett G.G. and Knott J.F., Acta. Met., 23, (1975), 841.
68. Fukui Y., Higo Y. and Nunomura S., J. Jap. Inst. Met., 41, (1977),
400.
69. Richards C.E., Acta. Met., 19, (1971), 583.
70. Pook L.P., Metal Science, 10, (1976), 334.
71. Miller K.J., Metal Science, 11, (1977), 432.
72. Burke M.A. and Davies G.J., "The Correlation of Textures and
Fatigue" in "Strength of Metals and Alloys", ed. P. Haasen,
V. Gerold and G. Kosters, Pergammon, London (1979), 1181.
73. Fegredo D.M., Met. Trans, 3, (1972), 1943.
74. Larson F.R. and Zarkades A., "Improved Fatigue Life in Titanium
through Texture Control" in "Texture and Properties of
Materials", The Metal Society, London (1975), 210.
- ⁷⁵ Bowen A.W., *ibid* p218
76. Bowen A.W., Acta. Met., 23, (1975), 1401.
77. Lee D., "The Effect of Plastic Anisotropy in the Low Cycle Fatigue
Behaviour of Zircalloy" in "Mechanical Behaviour of
Materials", Soc. Mat. Sci., Japan (1972), 165.
78. Lee D., Met. Trans., 3, (1972), 315.
79. Dillamore I.L. and Roberts W.T., Met. Rev., 10, (1965), 271.
80. Kallend J.S., Ph.D. Thesis, University of Cambridge, (1970).

81. "Öztürk T., Ph.D. Thesis, University of Cambridge, (1979).
82. Thompson A.W., Baskes M.I. and Flanagan W.F., Acta. Met., 21, (1973), 1017.
83. Freda A. and Cullity B.D., Trans. AIME-TMS, 215, (1959), 530.
84. Shultz L.G., J. Appl. Phys., 20, (1949), 1030.
85. Lopata S. and Kula E., Trans. AIME-TMS, 224, (1962), 865.
86. Meieran E.S., Rev. Sci. Inst., 33, (1962), 319.
87. Pospiech J. and Jura J., Zeit für Metal., 65, (1974), 324.
88. Elias J. A. and Heckler A.J., Trans. AIME-TMS, 239, (1967), 1237.
89. Morris P.P., Ph.D. Thesis, University of Cambridge, (1976).
90. Neff H., Siemens Review, 31, (1957), 93.
91. Heckler A.J., Elias J.A. and Woods P., Trans. AIME-TMS, 239, (1967), 1241.
92. Northcliffe J. and Roberts M., J.I.S.I., 157, (1947), 345.
93. Chalmers B. and Quarrell A.G., "The Physical Examination of Metals", Edward Arnold, London, (1960), 567.
94. Mitchell M.R., "Fundamentals of Modern Fatigue Analysis for Design" in "ASM - Fatigue and Microstructure Seminar - St. Louis 1976", ASM, Metals Park, (1977).
95. Dabell B.J., Hill S.J., Eaton D.E. and Watson P., J. Soc. Environ. Eng., 16, (1976), 3 .
96. Basquin O.H., Proc. ASTM, 10, (1910), 625.
97. Coffin L.C., Trans. ASME, 76, (1954), 931.
98. Manson S.S., "Behaviour of Materials Under Conditions of Thermal Stress" in "Heat Transfer Symposium", University of Michigan Press, (1953), 9.
99. Rebbeck R.G. and Watson P., Railway Eng. Journal, (1975), 1.

100. Paris P.C. and Erdogan F., J. Basic Eng. Trans. ASME(D), 85, (1963), 528.
101. Davenport R.T., Ph.D.Thesis, University of Salford, (1977).
102. McCartney L.N. and Cooper P.M., N.P.L. Report 'Mat. App. 23', (1972).
103. Walker B.F. and May M.J., BISRA Open Report MG/E/307/67, (1967).
104. Hurd N.J., Ph.D. Thesis, University of Sheffield, (1979).
105. Knott J.F., "Fundamentals of Fracture Mechanics", Butterworth, London, (1975).
106. Bunge H.J., "Mathematische Methoden der Texturanalyse", Akademie-Verlag, Berlin (1969).
107. Roe R.J., J. Appl. Phys., 36, (1965), 2024.
108. Hutchinson W.B. and Hatherly M., "An Introduction to Textures in Metals", Institute of Metallurgists, London, (1979).
109. Roe R.J. and Krigbaum R.S., J. Chem. Phys., 40, (1964), 2608.
110. Davies G.J., Goodwill D.J. and Kallend J.S., J. Appl. Cryst., 4, (1971), 67.
111. Kallend J.S. and Davies G.J., in Quantitative Relation between Properties and Microstructure, Israel, U.P. (1970), 45.
112. Pursey H. and Cox H.L., Phil. Mag., 45, (1954), 295.
113. Bateman R.M., Unpublished Work.
114. Voigt W., "Lehrbuch der Krystallphysik", B.G. Tuebner Verlag Liepzig, (1929).
115. Reuss A., Zeit. Any. Math. Mecha., 9, (1929), 49.
116. Hill R., Proc. Phys. Soc., A65, (1952), 349.
117. Taylor G.I., J. Inst. Met., 62, (1938), 307.
118. Bishop J.F.W. and Hill R., Phil. Mag., 42, (1951), 414.
119. Sachs G., Zeit. v. Deuts. Ing., 72, (1928), 734.
120. Hosford W. and Backofen W.A., "Strength and Plasticity of Textured

Materials" in "Fundamentals of Deformation Processing",
Syracuse U.P., (1964).

121. Schmid E. and Boas W., "Plasticity of Crystals", Hughes, London,
(1950).
122. Kallend J.S. and Davies G.J., Phil. Mag., 28, (1976), 21.
123. Van Houtte P., Acta. Met., 26, (1978), 591.
124. Bishop J.F.W. and Hill R., Phil. Mag., 42, (1951), 1298.
125. Truzkowski W., Krol J. and Major B., Met. Trans., 11A, (1980), 749.
126. Backofen W.A., "Deformation Processing", Addison Wesley, London,
(1972), 47.
127. Hill R., "The Mathematical Theory of Plasticity", Clarendon Press,
Oxford, (1951).
128. Holt J.M. and Stewart B.R., SAE Technical Paper No. 79046, (1979),
Soc. Auto. Eng. Inc., Warrendale (Pa).
129. Wetzel R.M., Private Communication.
130. ASTM Designation E606-77T ASTM Book of Standards pt. 10, (1977),
ASTM Philadelphia.
131. Callender W.R., Private Communication.
132. Laird C., "Recent Advances in Understanding the Cyclic Deformation
of Metals and Alloys" in "Work Hardening in Tension and
Fatigue", AIME (1977), New York, 150.
133. Nair K.D., Ph.D. Thesis, University of Saskatchewan, (1970).
134. Pelloux R.M., "Fracture - 2nd Int. Conf.", Chapman and Hall,
London, (1969), 731.
135. Abel A., Mat. Sci. and Eng., 36, (1978), 117.
136. Landgraf R.W., Morrow J. and Endo T., J. of Material, 4, (1969), 176.
137. Laird C., Finney J.M., Schwartzmann R. and De la Veaux R., J. Test
and Evaluation, 3, (1975), 435.

138. Tuler R. and Morrow J., "Cycle Dependent Stress-Strain Behaviour of Metals - Theoretical and Applied Mechanics Report No. 239", University of Illinois, (1963).
139. Lukas P. and Klesnil M., "Cyclic Stress-Strain Response in the Low Amplitude Region" in "Work Hardening in Tension and Fatigue", AIME, New York, (1977), 177.
140. Kemsley D.S., J. Inst. Met., 87, (1958-59), 10.
141. Karjalainen L.P., Metal Science, 12, (1978), 571.
142. Bucci R. and Thompson A.W., Met. Trans, 4, (1973), 1173.
143. Morrow J. and Halford G.R., Proc. ASTM, 62, (1962), 695.
144. Mughrabi H., Scripta Met., 13, (1979), 479.
145. Kocks U.F., Acta Met., 6, (1958), 85.
146. Awatani A., Katagira K., Omura A. and Shiraishi T., Met. Trans., 6A, (1975), 1029.
147. Winter A.T., Phil. Mag., 28, (1973), 57.
148. Topper T.H., Wetzel R.M. and Morrow J., J. of Materials, 4, (1969), 200.
149. Neuber H., J. Appl. Mech., (Dec. 1961), 544.
150. Smith K.N., Watson P. and Topper T.H., J. of Matls., 5, (1970), 767.
151. Winter A.T., Acta. Met., 28, (1980), 963.
152. Burke M.A., M.S. Thesis, University of Pittsburgh, (1977).
153. Rasmussen K.V. and Pedersen O.B., Private Communication, Riso Nat. Lab. Denmark.
154. Witzel W., Scripta Met., 13, (1979), 665.
155. Witzel W., "The Problem of the Saturation Range in Low Cycle Fatigue" in "5th Meeting of Working Group on Service Strength - Stuttgart 1979", Deutscher Verband für Materialprüfung e.v. Stuttgart, 1979.

156. Kim W.H. and Laird C., *Acta. Met.*, 26, (1978), 777.
157. Inckle A.E., Birbeck G. and Waldron G.W.J., *J. Mat. Sci.*, 8, (1973),
1058.
158. Awatani A., Nakai H. and Katagira K., *Met. Trans.*, 9A, (1978),
111.
159. Inckle A.E., Birbeck G. and Waldron G.W.J., *J. Mat. Sci.*, 8,
(1973), 1058.
160. Stanzl S.E., *Scripta Met.*, 14, (1980), 749.
161. Weber J.H. and Hertzberg R.W., *Met. Trans.*, 2, (1971), 3498.
162. Koterazawa R. and Shimo D., *J. Soc. Mat. Sci. Japan*, 25, (1976),
535.
163. Hur K.S., Nam S.W., Maeng S.C. and Chun S.S., *J. Korean Inst. Met.*,
15, (1977), 477.
164. Priddle E.K. and Walker F.E., *M. Mat. Sci.*, 11, (1976), 386.
165. Ritchie R.O., Smith R.F. and Knott J.F., *Met. Sci.*, 9, (1975),
485.
166. Heiser F.A. and Mortimer W., *Met. Trans.*, 3, (1972), 2119.
167. Garrett G.G., *Met. Trans.*, 10A, (1979), 648.
168. Schijve J., *Eng. Frac. Mech.*, 6, (1974), 245.
169. Pook L.P., *Metal Sci.*, 10, (1976), 334.
170. Schijve J., *Eng. Frac. Mech.*, 10, (1978), 359.
171. Miller K.J., *Metal Sci.*, 11, (1977), 432.
172. Iida S. and Kobayashi S.A., *Trans. ASME(D), J. Basic Eng.*, 91,
(1969), 764.
173. Pook L.P., *Eng. Frac. Mech.*, 3, (1971), 205.
174. Hurd, N.J. and Irving P.E., to be published in ASTM STP series,
ASTM Philadelphia - Presented at ASTM Balharbour Con-
ference, November 1980.
175. Sih G.C. and Barthelemy B.M., *Eng. Frac. Mech.*, 13, (1980), 439.
176. Hoepner D.W., *Met. Sci.*, 12, (1978), 489.

3
Appendices

APPENDIX 1

```

1  FATIGUE: 00000010
2  PROCEDURE (PARMLIST) OPTIONS(MAIN); 00000020
3  /*THIS PROGRAM FITS A SET OF STRAIN-LIFE FATIGUE DATA TO THE */ 00000030
4  /*MATERIAL PARAMETERS SIGMA',EPSILON',b,c,K',N' AS */ 00000040
5  /* IN THE RELATION, */ 00000050
6  /*Et/2=SIGMA'/E*(2Nf)**-b + EPSILON'*(2Nf)**-c */ 00000060
7  /*USING A LEASTSQUARES FIT ON LOGARITHMIC STRAIGHT LINES,THE */ 00000070
8  /* DATA IS INPUTTEDAS TOTAL-STRAIN,PLASTIC-STRAIN,STRESS AND */ 00000080
9  /* # OF REVERSALS TOFAILURE. */ 00000090
10 /* The first time through the program uses the static elastic */ 00000100
11 /* elastic modulus and the stress amplitude to determine the */ 00000110
12 /* elastic strain amplitude,the second time it uses the */ 00000120
13 /* differenc between the total strain and the strain width of */ 00000130
14 /* the hysteresis loop as the elastic strain amplitude */ 00000140
15 DECLARE 00000150
16   PARMLIST CHAR(12) VAR, 00000160
17   BPARM(2) CHAR(6), 00000170
18   APARM CHAR(12), 00000180
19   STATMOD FLOAT DECIMAL INITIAL(0), 00000190
20   ROUTE FIXED(1,0) INITIAL(0), 00000200
21   MODIFE(50) FLOAT DECIMAL INITIAL((50)0), 00000210
22   (NN, 00000220
23   I, 00000230
24   J, 00000240
25   N) FIXED(4,0) INITIAL(0), 00000250
26   (ELPSO, 00000260
27   ELPSTP) FLOAT DECIMAL INITIAL(0), 00000270
28   ( EPLSO, 00000280
29   PLST) FLOAT DECIMAL INITIAL(0), 00000290
30   BASEDATA(50,6)FLOAT DECIMAL INITIAL((300)0), 00000300
31   LOGDATA(50,6) FLOAT DECIMAL INITIAL((300)0), 00000310
32   (RPLSO, 00000320
33   RPLST, 00000330
34   EPLST, 00000340
35   EPLSTP) FLOAT DECIMAL INITIAL(0), 00000350
36   ( PLSCOUNT, 00000360
37   PLSREV, 00000370
38   SQPLST, 00000380
39   SQPLSREV, 00000390
40   PLSCROSS, 00000400
41   PSTST, 00000410
42   STRESS, 00000420
43   SQSTRESS)FLOAT DECIMAL INITIAL(0), 00000430
44   ( ELSCOUNT, 00000440
45   ELST, 00000450
46   ELSREV, 00000460
47   SQELST, 00000470
48   SQELSREV, 00000480
49   ELSCROSS) FLOAT DECIMAL INITIAL(0), 00000490
50   MODL FIXED(2,0) INITIAL(0), 00000500
51   ( MODULUS, 00000510
52   SQMOD, 00000520
53   SIGMASQ, 00000530
54   SIGMA, 00000540
55   AVENOD) FLOAT DECIMAL(12) INITIAL(0), 00000560
56   (ALPHA, 00000570
57   LOGC, 00000570
58   EPSILONF, 00000580

```

59	PLASR) FLOAT DECIMAL INITIAL(0),	00000590
60	(BETA,	00000600
61	LOGB,	00000610
62	BASQUIN,	00000620
63	SIGMAEFF) FLOAT DECIMAL INITIAL(0),	00000630
64	(ELASR,	00000640
65	ENPRIME,	00000650
66	KAYPRIME,	00000660
67	OFFSET) FLOAT DECIMAL INITIAL(0),	00000670
68	(LOGK,	00000680
69	KPRIME,	00000690
70	NPRIME,	00000700
71	CYCLICR,	00000710
72	SPRIME) FLOAT DECIMAL INITIAL(0),	00000720
73	TITLE CHARACTER(8);	00000730
74	DECLARE	00000740
75	UNLIST ENTRY EXT;	00000750
76	ON ENDFILE (FDATA)	00000760
77	GO TO START;	00000770
78	NN=0;	00000780
79	APARM=PARMLIST;	00000790
80	CALL UNLIST(APARM, ', ', BPARM, N);	00000800
81	TITLE=BPARM(1);	00000810
82	STATMOD=BPARM(2);	00000820
83	LAB:	00000830
84	NN=NN+1;	00000840
85	GET FILE(FDATA) LIST((BASEDATA(NN,I) DO I=1 TO 4));	00000850
86	GOTO LAB;	00000860
87	START:	00000870
88	NN=NN-1;	00000880
89	DO I=1 TO NN;	00000890
90	BASEDATA(I,6)=STATMOD;	00000900
91	BASEDATA(I,5)=BASEDATA(I,3)/BASEDATA(I,6);	00000910
92	/* N.B.USING STRESS AND ELASTIC MODULUS TO CALCULATE */	00000920
93	END;	00000930
94	/* ELASTIC STRAIN*/	00000940
95	GO TO CALC;	00000950
96	AGAIN:	00000960
97	DO I=1 TO NN;	00000970
98	BASEDATA(I,5)=BASEDATA(I,1)-BASEDATA(I,2);	00000980
99	BASEDATA(I,6)=BASEDATA(I,3)/BASEDATA(I,5);	00000990
100	END;	00001000
101	CALC:	00001010
102	DO I=1 TO NN;	00001020
103	DO J=1 TO 6;	00001030
104	LOGDATA(I,J)=LOG(BASEDATA(I,J));	00001040
105	END;	00001050
106	END;	00001060
107	PLSCOUNT=0;	00001070
108	PLST=0;	00001080
109	PLSREV=0;	00001090
110	SQPLST=0;	00001100
111	SQPLSREV=0;	00001110
112	PLSCROSS=0;	00001120
113	PSTST=0;	00001130
114	STRESS=0;	00001140
115	SQSTRESS=0;	00001150
116	ELSCOUNT=0;	00001160

117	ELST=0;	00001170
118	ELSREV=0;	00001180
119	SQELST=0;	00001190
120	SQELSREV=0;	00001200
121	ELSCROSS=0;	00001210
122	PLASTIC:	00001220
123	DO N=1 TO NN;	00001230
124	IF BASEDATA(N,2)<E-03 THEN	00001240
125	GOTO ELASTIC;	00001250
126	PLSCOUNT=PLSCOUNT+1;	00001260
127	PLST=PLST+LOGDATA(N,2);	00001270
128	PLSREV=PLSREV+LOGDATA(N,4);	00001280
129	SQPLST=SQPLST+LOGDATA(N,2)**2;	00001290
130	SQPLSREV=SQPLSREV+LOGDATA(N,4)**2;	00001300
131	PLSCROSS=PLSCROSS+LOGDATA(N,4)*LOGDATA(N,2);	00001310
132	PSTST=PSTST+LOGDATA(N,2)*LOGDATA(N,3);	00001320
133	STRESS=STRESS+LOGDATA(N,3);	00001330
134	SQSTRESS=SQSTRESS+LOGDATA(N,3)**2;	00001340
135	ELASTIC:	00001350
136	ELSCOUNT=ELSCOUNT+1;	00001360
137	ELST=ELST+LOGDATA(N,5);	00001370
138	ELSREV=ELSREV+LOGDATA(N,4);	00001380
139	SQELST=SQELST+LOGDATA(N,5)**2;	00001390
140	SQELSREV=SQELSREV+LOGDATA(N,4)**2;	00001400
141	ELSCROSS=ELSCROSS+LOGDATA(N,4)*LOGDATA(N,5);	00001410
142	END;	00001420
143	MODULUS=0;	00001430
144	SQMOD=0;	00001440
145	YOUNGS:	00001450
146	DO MODL=1 TO NN;	00001460
147	MODULUS=MODULUS+BASEDATA(MODL,6);	00001470
148	SQMOD=SQMOD+BASEDATA(MODL,6)**2;	00001480
149	END;	00001490
150	SIGMA=ABS((SQMOD-MODULUS**2/NN)/(NN-1));	
151	SIGMA=SQRT(SIGMA);	
152	AVEMOD=MODULUS/NN;	00001510
153	ALPHA=- (PLSCROSS-PLST*PLSREV/PLSCOUNT)/(00001520
154	SQPLSREV-PLSREV**2/PLSCOUNT);	00001530
155	LOGC=(PLSREV*PLSCROSS-PLST*SQPLSREV)/(00001540
156	PLSREV**2-PLSCOUNT*SQPLSREV);	00001550
157	EPSILONF=EXP(LOGC);	00001560
158	BETA=- (ELSCROSS-ELST*ELSREV/ELSCOUNT)/(00001570
159	SQELSREV-ELSREV**2/ELSCOUNT);	00001580
160	LOGB=(ELSREV*ELSCROSS-ELST*SQELSREV)/(00001590
161	ELSREV**2-ELSCOUNT*SQELSREV);	00001600
162	BASQUIN=EXP(LOGB);	00001610
163	BASQUIN=EXP(LOGB);	00001620
164	SIGMAEFF=BASQUIN*AVEMOD;	00001630
165	ENPRIME=BETA/ALPHA;	00001640
166	KAYPRIME=SIGMAEFF/EPSILONF**ENPRIME;	00001650
167	OFFSET=KAYPRIME*(0.002)**ENPRIME;	00001660
168	RPLSO=(PLSCROSS-PLST*PLSREV/PLSCOUNT);	00001670
169	RPLST=PLSCOUNT* SQRT(SQPLSREV/PLSCOUNT-(PLSREV/PLSCOUNT)**2);	00001680
170	RPLST=RPLST*SQRT(SQPLST/PLSCOUNT-(PLST/PLSCOUNT)**2);	00001690
171	PLASR=RPLSO/RPLST;	00001700
172	ELPSO=(ELSCROSS-ELST*ELSREV/ELSCOUNT);	00001710
173	ELPSTP=ELSCOUNT*	00001720
174	SQRT(SQELSREV/ELSCOUNT-(ELSREV/ELSCOUNT)**2);	00001730

```

175     ELPSTP=ELPSTP*SQRT(SQELST/ELSCOUNT-(ELST/ELSCOUNT)**2);          00001740
176     ELASR=ELPSO/ELPSTP;                                             00001750
177 CYCLIC:                                                              00001760
178     LOGK=(PSTST*PLST-STRESS*SQPLST)/(PLST**2-SQPLST*PLSCOUNT);      00001770
179     KPRIME=EXP(LOGK);                                                00001780
180     NPRIME=(PSTST-STRESS*PLST/PLSCOUNT)/(                               00001790
181     SQPLST-PLST**2/PLSCOUNT);                                         00001800
182     SPRIME=KPRIME*0.002**NPRIME;                                       00001810
183     CYCLICR=(PSTST-STRESS*PLST/PLSCOUNT)/PLSCOUNT;                 00001820
184     CYCLICR=CYCLICR/SQRT(SQPLST/PLSCOUNT-(PLST/PLSCOUNT)**2);      00001830
185     CYCLICR=CYCLICR/                                                 00001840
186     SQRT(SQSTRESS/PLSCOUNT-(STRESS/PLSCOUNT)**2);                   00001850
187 TABLE:                                                              00001860
188     PUT PAGE;                                                         00001870
189     PUT SKIP(4) EDIT('FATIGUE DATA ANALYSIS FOR ',TITLE)          00001880
190     COLUMN(10),A(28),A(8));                                           00001890
191     IF ROUTE=0 THEN                                                  00001900
192     PUT SKIP                                                         00001910
193     EDIT(                                                             00001920
194     'Fatigue analysis employing static modulus and stress amplitude
195     to calculate the elastic strain range'
196     )(
197     COL(16),A(100));                                                 00001960
198     ELSE                                                              00001970
199     PUT SKIP                                                         00001980
200     EDIT(                                                             00001990
201     'Fatigue analysis employing total strain and plasti strain to c
202     alculate the elastic strain range'
203     )(
204     COL(18),A(97));                                                 00002030
205     PUT SKIP(3) EDIT('STRAIN-LIFE DATA')(COLUMN(53),A(18));        00002040
206     PUT SKIP(2) EDIT('CYCLIC PLASTIC PARAMETERS')(                  00002050
207     COLUMN(40),A(25));                                               00002060
208     PUT SKIP EDIT('COFFIN EXPONENT = ',ALPHA)(                      00002070
209     COLUMN(30),A(18),E(14,6));                                       00002080
210     PUT SKIP EDIT('CYCLIC FRACTURE STRAIN = ',EPSILONF)(           00002090
211     COLUMN(30),A(25),E(14,6));                                       00002100
212     PUT SKIP EDIT('CORRELATION COEFFICIENT RP = ',PLASR)(           00002110
213     COLUMN(30),A(29),E(14,6));                                       00002120
214     PUT SKIP(2) EDIT('CYCLIC ELASTIC PARAMETERS')(                  00002130
215     COLUMN(40),A(25));                                               00002140
216     PUT SKIP EDIT('BASQUIN EXPONENT = ',BETA)(                      00002150
217     COLUMN(30),A(19),E(14,6));                                       00002160
218     PUT SKIP EDIT('CYCLIC FRACTURE STRESS = ',SIGMAEFF)(           00002170
219     COLUMN(30),A(25),E(14,6));                                       00002180
220     PUT SKIP EDIT('CORRELATION COEFFICIENT RE = ',ELASR)(           00002190
221     COLUMN(30),A(29),E(14,6));                                       00002200
222     PUT SKIP                                                         00002210
223     EDIT('MEAN ELASTIC MODULUS = ',AVEMOD,'STANDARD DEVIATION = ',   00002220
224     SIGMA)(COLUMN(30),A(23),E(14,6),A(21),E(14,6));                 00002230
225     PUT SKIP                                                         00002240
226     EDIT('CYCLIC STRESS-STRAIN PARAMETERS FROM STRAIN-LIFE DATA')( 00002250
227     COLUMN(40),A(53));                                               00002260
228     PUT SKIP EDIT('CYCLIC STIFFNESS CONSTANT = ',KAYPRIME)(         00002270
229     COLUMN(30),A(28),E(14,6));                                       00002280
230     PUT SKIP EDIT('CYCLIC HARDENING EXPONENT = ',NPRIME)(           00002290
231     COLUMN(30),A(28),E(14,6));                                       00002300
232     PUT SKIP EDIT('0.2% OFFSET STRESS = ',OFFSET)(                  00002310

```

233	COLUMN(30),A(21),E(14,6));	00002320
234	PUT SKIP(3) EDIT('CYCLIC STRESS-STRAIN ANALYSIS')(00002330
235	COLUMN(50),A(29));	00002340
236	PUT SKIP(2) EDIT('CYCLIC STIFFNESS CONSTANT = ',KPRIME)(00002350
237	COLUMN(30),A(26),E(14,6));	00002360
238	PUT SKIP EDIT('CYCLIC HARDENING EXPONENT = ',ENPRIME)(00002370
239	COLUMN(30),A(28),E(14,6));	00002380
240	PUT SKIP EDIT('0.2% OFFSET STRESS = ',SPRIME)(00002390
241	COLUMN(30),A(28),E(14,6));	00002400
242	PUT SKIP EDIT('CORRELATION COEFFICIENT RC = ',CYCLICR)(00002410
243	COLUMN(30),A(29),E(14,6));	00002420
244	/*END*/	00002430
245	DO I= 1 TO NN;	00002440
246	MODIFE(I)= BASEDATA(I,2)+BASEDATA(I,5);	00002450
247	END;	00002460
248	PUT SKIP(3) EDIT('DATA DEVELOPED BY THIS CALCULATION')(00002470
249	COL(31), A(34));	00002480
250	PUT SKIP	00002490
251	EDIT('Total strain','Plastic strain','Stress','Reversals to',	00002500
252	'Elastic strain','Elastic','Corrected strain')(00002510
253	COL(1),A(12),COL(17), A(14),COL(35),A(6),COL(52),A(12),COL(68),	00002520
254	A(14),COL(86),A(7), COL(104),A(16));	00002530
255	PUT SKIP	00002540
256	EDIT('Amplitude','Amplitude','Amplitude','Failure', 'Amplitude',	00002550
257	'Modulus','Amplitude')(00002560
258	COL(4),A(9),COL(20),A(9),COL(37),A(9),COL(55), A(7),COL(71),	00002570
259	A(9), COL(88),A(7),COL(110),A(9));	00002580
260	DO I= 1 TO NN;	00002590
261	PUT SKIP	00002600
262	EDIT(BASEDATA(I,1),BASEDATA(I,2),BASEDATA(I,3),BASEDATA(I,4),	00002610
263	BASEDATA(I,5),BASEDATA(I,6),MODIFE(I))(00002620
264	COL(1),E(14,6),COL(17),E(14,6), COL(35),E(14,6),COL(52),	00002630
265	E(14,6),COL(68),E(14,6),COL(86),E(14,6),COL(104), E(14,6));	00002640
266	END;	00002650
267	ROUTE=ROUTE+1;	00002660
268	IF ROUTE =1 THEN	00002670
269	GO TO AGAIN;	00002680
270	FINISH:	00002690
271	END FATIGUE;	00002700

APPENDIX II

The Mathematical Relationship Between the c.o.d.f. and The Pole Distribution

The data are measured as a set of data points $q(\zeta, \eta)$ describing the orientation distribution of the pole i as a function of the polar and azimuthal angles, $\cos^{-1}\zeta$ and η , with respect to the sample axes. These data may be described by a series expansion

$$q_i(\zeta, \eta) = \sum_{L=0}^{\infty} \sum_{m=L}^L Q_{Lm}^i P_m^L(\zeta) e^{-im\eta}$$

where Q_{Lm}^i are the series coefficients and P_L^m are the associated Legendre polynomials.

The coefficients Q_{Lm}^i may be determined due to the orthogonality of Legendre polynomials i.e.,

$$\int_{-1}^{+1} P_L^m(\zeta) \cdot P_{L'}^m(\zeta) d(\zeta) = \begin{cases} 1 & \text{if } L = L' \\ 0 & \text{if } L \neq L' \end{cases}$$

hence,

$$Q_{Lm}^i = \frac{1}{2\pi} \int_0^{2\pi} \int_{-1}^{+1} q_i(\zeta, \eta) P_L^m(\zeta) e^{-im\eta} d\zeta d\eta$$

The crystallite orientation distribution function, c.o.d.f., also may

be expressed as a series of spherical harmonics,

$$w(\psi\xi\phi) = \sum_{L=0}^{\infty} \sum_{m=-L}^L \sum_{n=-L}^L W_{Lmn} Z_{Lmn}(\xi) e^{-im\psi} e^{-in\phi}$$

where Z_{Lmn} is a generalisation of the associated legendre function and W_{Lmn} are the series coefficients.

The relationship between the c.o.d.f. and the $q_i(\zeta\eta)$ and thus between the coefficients Q_{Lm}^i and W_{Lmn} is obtained by setting a temporary co-ordinate system $x'y'z'$ such that the z' axis coincides with the i -plane normal. Thus,

$$\begin{aligned} \psi' &= \eta & \text{and} \\ \xi' &= \zeta \end{aligned}$$

which produces:

$$q_i(\zeta\eta) = \int_0^{2\pi} W'(\zeta\eta\phi') d\phi'$$

where $W'(\psi'\xi'\phi')$ is the c.o.d.f. with respect to the temporary co-ordinate system. Expanding q_i and W'

$$\sum_{L=0}^{\infty} \sum_{m=-L}^L Q_{Lm}^i P_L^m(\zeta) e^{-im\eta} = \int_0^{2\pi} \sum_{L=0}^{\infty} \sum_{m=-L}^L \sum_{n=-L}^L W'_{Lmn} Z_{Lmn}(\zeta) e^{-im\eta} e^{-in\phi'} d\phi'$$

integrating,

$$\sum_{L=0}^{\infty} \sum_{m=-L}^L Q_{Lm}^i P_L^m(\zeta) e^{-im\eta} = 2\pi \sum_{L=0}^{\infty} \sum_{m=-L}^L W_{Lm0} Z_{Lm0}(\zeta) e^{-im\eta}$$

now since $P_i^m(\zeta) = Z_{Lm0}(\zeta)$

by comparison,

$$Q_{Lm}^i = 2\pi W'_{Lm0}$$

The relationship between the coefficients W'_{Lmn} and the coefficients W_{Lmn} is related by the legendre addition theorem:

$$W'_{Lmn} = \left[\frac{2}{2L+1} \right]^{\frac{1}{2}} \sum_{p=-L}^{+L} W_{Lmp} P_L^p(\cos \theta_i) e^{-ip\phi_i}$$

This statement represents, for a given value of L, a set of linear simultaneous equations with $2L + 1$ unknowns. However, crystal and specimen symmetry restrict the values of Q_{Lm}^i and W_{Lmn} . For cubic crystal symmetry and orthotropic specimen symmetry:

(i) Q_{Lm}^i and W_{Lmn} are real

(ii) When $L = 2$ $W_{Lmn} = Q_{Lm} = 0$
 $L \neq 2K$ $W_{Lmn} = Q_{Lm} = 0$
 $m \neq 2K$ $W_{Lmn} = Q_{Lm} = 0$
 $n \neq 2K$ $W_{Lmn} = Q_{Lm} = 0$

(iii) $W_{Lmn} = W_{Lm\bar{n}} = W_{L\bar{m}n} = W_{L\bar{m}\bar{n}}$

(iv) $Q_{Lm} = Q_{L\bar{m}}$

(v) For fixed values of L and m the W_{Lmn} values are linearly related.

Thus,

$$Q_{Lm}^i = \frac{1}{2\pi} \int_0^{2\pi} \int_{-1}^{+1} q_i(\zeta\eta) P_L^m(\zeta) \cos m\eta \, d\zeta \, d\eta$$

$$W(\psi\xi\phi) = \sum_{L=0}^{\infty} \sum_{m=-L}^L \sum_{n=-L}^L W_{Lmn} Z_{Lmn}(\xi) \cos(m\psi+n\phi)$$

and the set of simultaneous equations becomes

$$Q_{Lm}^i = 2\pi \left[\frac{2}{2L+1} \right]^{\frac{1}{2}} \sum_{p=-L}^{+L} W_{Lmp} P_L^p(\cos \theta_i) \cdot \cos(p\phi_i)$$

This set of equations, taken together with the conditions i) to v) may now be solved. The W_{Lmn} coefficients may be determined up to the 22nd order by measuring two complete pole figures.

APPENDIX III

Cyclic Stress-Strain/Strain-Life Properties of SAE 4161

Specimens were taken in the 90° and the 45° orientations from a rolled plate of SAE-4161 steel (0.9% Cr 1% Mn). After rough machining the fatigue specimens were quenched and tempered prior to final machining and polishing of the gauge length. The specimens were tested in the same manner as described earlier for the copper specimens and the texture measurements were made on specimens cut from the rolled plate which were heat treated with the specimen blanks.

The c.o.d.f. is shown in Figure A3-1. The cyclic stress-strain curves for the two orientations are shown in Figure A3-2, along with the monotonic curves for the two orientations. Figure A3-3 shows the strain-life data with the curves which were produced by the parametric analysis.

The c.o.d.f. shows that the material is textured only very weakly, severity parameter = 0.11 and the max:fn ht = 1.3. The mechanical properties predicted on this basis show a very slight degree of anisotropy. The predictions are confirmed by the cyclic and monotonic stress strain curves shown in Figure A3-2. (The monotonic curves have been drawn while ignoring the yield points since the yield point effects were found to be only small perturbations on the curve and the cyclic stress-strain curves do not display this phenomenon thus complicating comparisons between the two sets of data). The comparison between the cyclic and monotonic data shows the necessity to design on the basis of fatigue data rather than monotonic since considerable plastic strain

may be produced by cyclic loading well below the monotonic yield point.

The strain-life data, however, shows a considerable degree of anisotropy. Figure A3-3 shows that the cyclic anisotropy is most marked in the range $10^2 < 2N_f < 10^5$. This range of life corresponds to strain amplitudes between 5×10^{-3} and 1×10^{-2} , a range of strain amplitudes over which the cyclic stress strain responses of the two orientations are very similar.

The anisotropy is, therefore, caused by an effect other than preferred crystallographic orientation. Examination of the fracture surfaces revealed a further manifestation of the anisotropy of the fatigue properties. Macroscopic examination of the fractures showed that all specimens developed planar fractures but, whereas in the 90° specimens the fracture plane was normal to the stress axis, the fracture plane in the 45° specimens was steeply inclined to the stress axis. By comparing the fracture surface orientation with the reference markings on the specimens the fracture surfaces were, in all cases found to coincide with the transverse plane of the rolled plate (Figure A3-4). Scanning electron microscopy of the fracture surfaces showed that the fracture was composed of ductile areas separated by regions which contained elongated inclusions e.g., Figure A3-5. Energy dispersion x-ray analysis facilitated element mapping and Figure A3-6 shows that the inclusion contains a high concentration of manganese. It is, therefore, concluded that the inclusions are the well-known type II MnS stringers which have been reported to have a deleterious influence on the mechanical properties of steels^{a1, a2}.

It is difficult to ascribe a definite role to the MnS inclusions in accelerating the failure of the smooth sided fatigue specimens. The inclusions may influence both nucleation and propagation of fatigue cracks, indeed the absence of fatigue markings around the inclusions

may indicate that decohesion has occurred during the rolling processes designed to induce texture. Whether or not decohesion occurs prior to fatigue the region around the inclusion is subject to the stress concentrating effect of the inclusion/void, the fracture path appears to be constrained to follow the alignment of the inclusions which are known to align parallel to the rolling direction^{a1}. In the case of the 90° specimens it is expected that the stress concentrating effect of the inclusions would produce accelerated fatigue fracture in the usual orientation, normal to the stress axis. In the case of the 45° specimens the fatigue crack is constrained to propagate at 45° to the stress axis and the mode I stress intensity amplitude ΔK_I is consequently reduced as compared to the case in which the inclusions lie perpendicular to the stress axis (167). (Of course, in the case which actually pertains the rate of propagation for slant propagation is greater than for 90° propagation with the inclusions at 45° to the stress axis).

The anisotropy in strain-life behaviour may therefore be ascribed to the stress concentrating effects of aligned inclusions. The fatigue anisotropy was found to correlate with the monotonic fracture behaviour in which the 90° specimens exhibited a 15% reduction in area while the R.A. for the 45° specimens was 30%. The fatigue data shows that in the regime $10^2 < 2N_f < 10^5$ the 45° specimens display a increase in life of the order of a factor of five. Therefore, although the cyclic stress-strain response is adequately predicted by the texture data, the anisotropy of fracture behaviour, for both monotonic and cyclic deformation, is controlled by microstructural anisotropy in the form of elongated inclusions. Although, in this investigation, the texture which was induced in the steel was very weak, it is expected that, since the anisotropy due to the inclusions is so pronounced, even if very strong textures could be induced the fracture

behaviour would still be dominated by the inclusion content and morphology.

Auxiliary References:

- a1 Baker, T.J. and Charles, J.A., "Effect of Second Phase Particles on the Mechanical Properties of Steel", Proc. ISI/BISRA Conf. March 1971, ISI (1971).
- a2 Kiessling, "The Effect of Sulphide Inclusions on the Mechanical Properties of Steel", p.187.

Tables

TABLE 1

Comparison of the persistent slip band markings on copper and copper-aluminium⁽⁴⁾.

	Copper	Copper - 5 atomic % aluminium
Distribution of persistent slip bands	Grouped bands, which are separated by regions of inactive surface	Fairly uniform distribution; in some regions there are groups of persistent slip bands with small regions of inactive surface between the groups. This effect is not as prominent as in copper.
Length of slip lines on (541) surface	Mostly over 200 μ m, though some are shorter, particularly in the irregularly shaped bands	Mostly 50 to 200 μ m long, some shorter segments.
Length of slip line on (111) surface	Generally considerably greater than 200 μ m	Generally 100 to 400 μ m long, but many considerably shorter segments in banded regions.
Directions of persistent slip bands.	Delineate trace of primary slip plane	Delineate trace of primary slip plane.
Direction of bands of persistent slip bands	Often delineate trace of primary slip plane, but some bands have orientations which do not correspond to simple crystallographic directions	For the crystals studied (52, 54) very few bands present, the orientations of the bands present being close to that of the primary slip plane, though there is no simple crystallographic direction associated with them.

TABLE 2
CONCENTRATION (%)

ELEMENT	CAST A	CAST B	PLATE
P	<.005	<.005	<.001
Sb	<.02	<.02	<.001
Pb	<.01	<.01	<.005
As	<.02	<.02	<.001
Si	<.02	<.02	<.001
Bi	<.02	<.02	<.001
Mn	<.02	<.02	<.001
Be	<.02	<.02	<.001
Sn	<.02	<.02	<.001
Se	<.02	<.02	<.001
Cd	<.02	<.02	<.001
Zn	<.02	<.02	<.001
Ag	<.02	<.02	<.001
Ni	<.02	<.02	<.001
Ca	<.02	<.02	<.001
Fe	<.02	<.02	<.001
Al	<.02	<.02	<.001
In	<.02	<.02	<.001
O	.00045	.00045	.00005

Table 3

Changes in Texture Parameters during Simulated Fatigue

Texture Type	Principal texture component(s)	<u>Before Simulation</u>		<u>After Simulation</u>		
		Maximum function height*	Texture severity parameter**	Principal texture components	Maximum function height*	Texture severity parameter**
(a)	strong {100}<001>	54.0	5.47	{100}<001>	31.0	3.78
(b)	weak {100}<001>	5.0	0.48	{100}<001> +{100}<013>	9.2	1.34
(c)	retained rolling tube {110}<112>- {112}<111>	8.6	1.69	retained rolling tube +{100}<013>	10.1	2.44
(d)	mixed retained rolling + cube	6.4	1.57	mixed retained rolling + cube + {100}<013>	8.3	1.80
(e)	{100}<011>	7.7	0.98	{100}<011> + {100}<013>	12.4	1.76
(f)	random	1.5	0.33	{100}<011> + {100}<013>	5.5	0.91

* times random

** a random texture has a zero value

TABLE 4
GRAIN SIZE MEASUREMENTS

ELEMENT	GRAIN SIZE (μ .)	GRAIN SHAPE
III80	5*	Elongated in rolling dirn.
FAREN	4*	Elongated along rod axis
FBREN	4*	Elongated along rod axis
G8585	18#	Equiaxed
A3500	19#	Equiaxed
B3500	13#	Equiaxed
MBCUB	140\$	Equiaxed

* measured on the section normal to the long dimension of the grain structure, assuming "pancake" grain shape

Assuming equiaxed grain shape

\$ Measured on the plane parallel to the rolling plane, assuming equiaxed grain shape

TABLE 5
TEXTURE DATA

MATERIAL	MAJOR COMPONENT	MAXIMUM Fn. Ht.	SEVERITY
MBCUB	100 <001>	54.0	5.47
III80	100 <011>	7.7	0.98
G8585	100 <011>	4.0	0.52
NUJIG	100 <011>	3.5	0.87
CROCP	100 <011>	2.9	0.72
FAREN	<111>FIBRE	10.8	1.65
FBREN	<111>FIBRE+	14.3	1.97
	<100>FIBRE	3.0	
B3500	<100>FIBRE+	5.1	0.90
	<111>FIBRE	3.28	
A3500	<111>FIBRE+	3.0	0.85
	<100>FIBRE	2.85	

TABLE 6
MECHANICAL PROPERTY PREDICTIONS

MATERIAL	ANGLE TO R.D.	YIELD STRESS	R-VALUE	ELASTIC MODULUS		
				REUSS	VOIGT	HILL
III80	0	3.013	0.244	117	152	135
	45	2.884	0.667	93	124	108
	90	3.010	1.157	114	150	132
G8585	0	3.026	0.443	110	145	127
	45	2.997	0.769	102	137	119
	90	3.089	0.564	112	148	130
MBCUB	0	2.899	0.032	85	111	98
	45	3.001	0.007	115	150	133
	90	2.993	0.614	90	120	105
NUJIG	0	3.185	0.716	122	157	140
	45	2.984	0.88	99	133	116
	90	2.922	0.245	108	144	126
CROCP	0	3.156	0.466	128	161	144
	45	2.926	1.200	95	126	110
	90	2.993	0.116	117	152	135
FAREN	TT	3.219	1.309	135	168	151
FBREN	TT	3.233	1.209	133	165	149
B3500	TT	3.086	0.709	115	151	133
A3500	TT	3.036	0.937	111	147	130

TABLE 7

RESONANCE DETERMINATION OF ELASTIC MODULUS														
MATERIAL	SPECIMEN	DIMNS		RESONANT FREQUENCIES					ELASTIC MODULUS					
CODE	ANGLE	t	l						E11 Pa				AVERAGE	
	TO R.D.	(M)	(M)										(GPa)	
III180	90	4.82E-3	9.49E-2	2099	5619	10159	18066	24379	1.27	1.96	1.17	0.99	120	
	45	4.75E-3	1.17E-1	1224	3665	7078			1.043	1.226	1.195		116	
	90	4.63E-3	9.06E-2	1713	5137				.983	1.16			107	
68585	45	3.06E-3	1.25E-1	679	1989	3976	6591		1.00	1.134	1.18	1.18	110	
	0	3.84E-3	9.27E-2	1839	4577	13822			1.43	1.17	1.02		121	
	90	5.62E-4	8.77E-2	230	552	1109	1839		.84	.64	.67	.67	.68	69
MBCUB	45	6.00E-4	8.47E-2	327	1677	2751	4463		1.29	1.16	1.14	1.35	124	
	0	4.46E-4	8.62E-2	183	549	971	1230	1650	.78	.93	.75	.80	81	
FAREN	TT	7.52E-4	1.23E-1	189	566	1087	1787		1.2	1.42	1.37	1.35	133	
FBREN	TT	7.91E-4	1.24E-1	189	432	859	1724		1.14	.78	.81	1.19	97	
A3500	TT	1.66E-3	1.35E-1	311	877	1796	2904	4354	6081	1.97	1.01	1.11	1.07	105
B3500	TT	1.21E-3	1.10E-1	349	1021	2039	3380	5007	1.04	1.18	1.22	1.23	118	

TABLE 8
THIN SHEET FATIGUE DATA

ORIENTATION	CYCLES TO FAILURE (E+6 cycles)	ANGLE BETWEEN TRACE OF FRACTURE PLANE AND STRESS AXIS	
		BROAD FACE	THIN FACE
0 AND 90	1.43 ± 0.16	90°	90°
45	6.1 ± 3.0	61 ± 1°	64 ± 5°

TABLE 9

MECHANICAL PROPERTIES FOR I8045

MONOTONIC DATA

ELASTIC MODULUS=108.5GPa

YIELD STRENGTH=328.0MPa.

U.T.S.=340.0MPa

CYCLIC DATA

STRAIN AMPLITUDE	FATIGUE LIFE (REVS)	STRESS AMPLITUDE (MPa)	PLAS.STRN. AMPLITUDE	ELASTIC MODULUS (GPa)
0.00940	2000	217.0	0.00780	135.6
0.00463	7740	197.0	0.00300	120.8
0.00275	128260	191.0	0.00097	107.3
0.00194	358000	178.0	0.00030	108.5
0.00170	1582800	158.0	0.00030	112.8

TABLE 10

MECHANICAL PROPERTIES FOR I8000

MONOTONIC DATA

ELASTIC MODULUS=121.6GPa

YIELD STRENGTH=335.0MPa.

U.T.S.=350.0MPa

CYCLIC DATA

STRAIN AMPLITUDE	FATIGUE LIFE (REVS)	STRESS AMPLITUDE (MPa)	PLAS.STRN. AMPLITUDE	ELASTIC MODULUS (GPa)
0.00482	5660	215.0	0.00313	127.2
0.00281	29700	205.0	0.00113	122.0
0.00187	178100	175.0	0.00043	121.5
0.00138	1076400	179.0	0.00019	150.4

MECHANICAL PROPERTIES FOR I8090

MONOTONIC DATA

ELASTIC MODULUS=111.9GPa

YIELD STRENGTH=312.0MPa.

U.T.S.=349.0MPa

CYCLIC DATA

STRAIN AMPLITUDE	FATIGUE LIFE (REVS)	STRESS AMPLITUDE (MPa)	PLAS.STRN. AMPLITUDE	ELASTIC MODULUS (GPa)
0.00188	172200	181.0	0.00060	141.4
0.00113	8147400	147.0	0.00003	133.6
0.00490	6178	209.0	0.00310	116.1
0.00950	1580	239.0	0.00790	149.3

TABLE 11

MECHANICAL PROPERTIES FOR 68545

MONOTONIC DATA

ELASTIC MODULUS=103.5GPa

YIELD STRENGTH=131.3MPa.

U.T.S.=268.0MPa

CYCLIC DATA

STRAIN AMPLITUDE	FATIGUE LIFE (REVS)	STRESS AMPLITUDE (MPa)	PLAS.STRN. AMPLITUDE	ELASTIC MODULUS (GPa)
0.00255	38200	150.0	0.00120	111.1
0.00250	38200	140.0	0.00125	112.0
0.00844	720	208.0	0.00625	94.9
0.00500	3780	187.0	0.00330	110.0
0.00385	18500	155.0	0.00185	77.5
0.00169	249720	126.0	0.00060	115.5
0.00120	3746680	95.4	0.00014	90.0
0.01000	700	208.0	0.00750	83.2
0.00387	10200	168.0	0.00225	103.7

TABLE 12

MECHANICAL PROPERTIES FOR 68590

MONOTONIC DATA

ELASTIC MODULUS=110.0GPa

YIELD STRENGTH=119.2MPa.

U.T.S.=272.0MPa

CYCLIC DATA

STRAIN AMPLITUDE	FATIGUE LIFE (REVS)	STRESS AMPLITUDE (MPa)	PLAS.STRN. AMPLITUDE	ELASTIC MODULUS (GPa)
0.01000	390	228.0	0.00810	120.0
0.00510	3740	183.0	0.00325	98.9
0.00263	60080	149.0	0.00125	107.9
0.00126	752960	111.0	0.00030	115.6
0.00350	9340	186.0	0.00212	134.7
0.00250	88000	158.0	0.00120	121.5
0.00200	120860	133.0	0.00082	112.7
0.00146	450000	100.0	0.00028	84.7

TABLE 13

MECHANICAL PROPERTIES FOR FAREN

MONOTONIC DATA
 ELASTIC MODULUS=126.7GPa
 YIELD STRENGTH=251.1MPa.
 U.T.S.=290.0MPa

CYCLIC DATA

STRAIN AMPLITUDE	FATIGUE LIFE (REVS)	STRESS AMPLITUDE (MPa)	PLAS.STRN. AMPLITUDE	ELASTIC MODULUS (GPa)
0.00805	1872	272.0	0.00603	134.6
0.01006	1334	283.0	0.00775	122.5
0.00205	6200	232.0	0.00076	179.8
0.00503	4280	239.0	0.00331	138.9
0.00404	7998	246.0	0.00213	128.7
0.00099	430000	118.0	0.00001	120.4
0.00200	87800	225.0	0.00002	113.6
0.00151	345000	181.0	0.00011	129.2
0.00303	17758	271.0	0.00105	136.8

TABLE 14

MECHANICAL PROPERTIES FOR FBREN

MONOTONIC DATA
 ELASTIC MODULUS=125.0GPa
 YIELD STRENGTH=255.2MPa.
 U.T.S.=310.0MPa

CYCLIC DATA

STRAIN AMPLITUDE	FATIGUE LIFE (REVS)	STRESS AMPLITUDE (MPa)	PLAS.STRN. AMPLITUDE	ELASTIC MODULUS (GPa)
0.01000	1286	288.0	0.00760	120.0
0.01240	268	332.0	0.00958	118.0
0.00740	2102	267.0	0.00544	136.2
0.00497	6544	251.0	0.00247	100.4
0.00305	43560	229.0	0.00122	125.1
0.00250	80200	225.0	0.00083	134.7
0.00219	92340	218.0	0.00062	138.8
0.00819	832	298.0	0.00581	125.2
0.00395	14140	234.0	0.00210	126.4
0.00200	139140	229.0	0.00027	132.3

TABLE 15

MECHANICAL PROPERTIES FOR A3500

MONOTONIC DATA
 ELASTIC MODULUS=115.2GPa
 YIELD STRENGTH=154.4MPa.
 U.T.S.=247.0MPa

CYCLIC DATA

STRAIN AMPLITUDE	FATIGUE LIFE (REVS)	STRESS AMPLITUDE (MPa)	PLAS.STRN. AMPLITUDE	ELASTIC MODULUS (GPa)
0.00200	87490	126.0	0.00089	113.5
0.00149	227800	135.0	0.00037	120.5
0.00506	3220	163.0	0.00350	104.4
0.00375	4356	165.0	0.00230	113.7
0.00502	1400	169.0	0.00359	118.1
0.00300	11396	156.0	0.00164	114.7
0.00247	28420	151.0	0.00116	115.2
0.00097	615360	115.0	0.00019	147.4

TABLE 16

MECHANICAL PROPERTIES FOR B3500

MONOTONIC DATA
 ELASTIC MODULUS=111.2GPa
 YIELD STRENGTH=157.0MPa.
 U.T.S.=252.0MPa

CYCLIC DATA

STRAIN AMPLITUDE	FATIGUE LIFE (REVS)	STRESS AMPLITUDE (MPa)	PLAS.STRN. AMPLITUDE	ELASTIC MODULUS (GPa)
0.00197	32500	134.0	0.00083	117.5
0.00300	12600	159.0	0.00165	117.7
0.00600	4190	180.0	0.00431	106.5
0.00700	1462	184.0	0.00531	108.8
0.00900	1258	185.0	0.00712	98.4
0.00400	6500	165.0	0.00236	100.6
0.00500	4046	170.0	0.00348	111.8
0.00253	12800	145.0	0.00126	114.1
0.00095	1111200	96.8	0.00019	127.3
0.00146	327660	122.0	0.00049	125.7

TABLE 17
 FATIGUE DATA ANALYSIS FOR G8545

Fatigue analysis employing static modulus and stress amplitude to calculate the elastic strain range

STRAIN-LIFE DATA

CYCLIC PLASTIC PARAMETERS

COFFIN EXPONENT = 4.445437E-01
 CYCLIC FRACTURE STRAIN = 1.328072E-01
 CORRELATION COEFFICIENT RP = -9.974163E-01

CYCLIC ELASTIC PARAMETERS

BASQUIN EXPONENT = 9.117228E-02
 CYCLIC FRACTURE STRESS = 3.834185E+02
 CORRELATION COEFFICIENT RE = -9.948167E-01
 MEAN ELASTIC MODULUS = 9.900000E+04 STANDARD DEVIATION = 3.498571E+01

CYCLIC STRESS-STRAIN PARAMETERS FROM STRAIN-LIFE DATA

CYCLIC STIFFNESS CONSTANT = 5.800869E+02
 CYCLIC HARDENING EXPONENT = 2.041008E-01
 0.2% OFFSET STRESS = 1.621648E+02

CYCLIC STRESS-STRAIN ANALYSIS

CYCLIC STIFFNESS CONSTANT 5.765171E+02
 CYCLIC HARDENING EXPONENT = 2.050918E-01
 0.2% OFFSET STRESS = 1.621625E+02
 CORRELATION COEFFICIENT RC = 9.924557E-01

DATA DEVELOPED BY THIS CALCULATION

Total strain Amplitude	Plastic strain Amplitude	Stress Amplitude	Reversals to Failure	Elastic strain Amplitude	Elastic Modulus	Corrected strain Amplitude
2.550000E-03	1.200000E-03	1.500000E+02	3.820000E+04	1.515151E-03	9.900000E+04	2.715151E-03
2.500000E-03	1.250000E-03	1.400000E+02	3.820000E+04	1.414141E-03	9.900000E+04	2.664141E-03
8.439999E-03	6.249998E-03	2.080000E+02	7.200000E+02	2.101010E-03	9.900000E+04	8.351006E-03
4.999999E-03	3.300000E-03	1.870000E+02	3.780000E+03	1.888889E-03	9.900000E+04	5.188886E-03
3.850000E-03	1.850000E-03	1.550000E+02	1.850000E+04	1.565656E-03	9.900000E+04	3.415656E-03
1.690000E-03	5.999999E-04	1.260000E+02	2.497200E+05	1.272727E-03	9.900000E+04	1.872727E-03
1.200000E-03	1.400000E-04	9.539999E+01	3.746680E+06	9.636362E-04	9.900000E+04	1.103636E-03
9.999998E-03	7.499997E-03	2.080000E+02	7.000000E+02	2.101010E-03	9.900000E+04	9.601004E-03
3.870000E-03	2.250000E-03	1.680000E+02	1.020000E+04	1.696970E-03	9.900000E+04	3.946967E-03

TABLE 18
MATERIALS PARAMETERS FROM STRAIN-LIFE AND CYCLIC STRESS-STRAIN DATA

MATERIAL	STRAIN-LIFE PARAMETER			STRESS-STRAIN PARAMETERS									ELASTIC MODULUS	
	PLASTIC		ELASTIC	STRAIN-LIFE ANALYSIS			CYCLIC STRESS-STRAIN ANALYSIS			r				
	f	-c	r	f (MPa)	-b	r	K (MPa)	n	S (MPa)		K (MPa)	n		S (MPa)
G8548	.132	.445	.997	383	.0912	.995	580	.2041	162	577	.2051	162	.993	99.
G8590	.124	.439	.980	370	.0845	.936	552	.237	167	739	.193	169	.983	112
A3500	.135	.473	.982	272	.0618	.951	354	.124	157	339	.130	156	.919	118
B3500	.213	.504	.979	505	.125	.978	737	.181	158	479	.248	155	.966	105
I8045	.327	.510	.978	295	.0409	.948	322	.0758	196	312	.0803	195	.917	115
I8090	.488	.574	.997	327	.0474	.970	346	.0825	207	346	.0825	207	.972	121
FAREN	.234	.810	.980	597	.104	.971	534	.127	241	529	.128	241	.978	133
FBREN	.181	.677	.981	560	.0875	.980	766	.133	245	564	.1834	246	.938	126
B35XX	.213	.504	.979	366	.0922	.978	485	.181	155	479	.183	155	.986	122

TABLE 19
FATIGUE CRACK DATA FOR NUJIG

SPECIMEN	MODE	m	C	K
90.2	FLAT	1.67	7.2E-10	0.306
90.3	FLAT	1.41	3.9E-9	0.074
90.4	FLAT	3.03	7.3E-13	2.372
90.6	FLAT	2.07	8.7E-11	1.069
45.2	SLANT	3.36	1.0E-14	12.6
45.3	SLANT	2.78	1.6E-12	4.43
45.5	SLANT	3.31	1.2E-13	7.63

TABLE 20
FATIGUE CRACK DATA FOR CROCP

SPECIMEN	MODE	n	C	K
90.1	FLAT	1.91	3.3E-7	0.538
90.2	FLAT	4.42	6.4E-10	3.62
90.3	FLAT	3.68	2.90E-9	2.616
45.1	SLANT	4.35	3.84E-9	2.12
45.2	SLANT	2.41	4.81E-8	1.353
45.3	SLANT	3.12	5.93E-9	2.459
45.4	SLANT	3.33	4.9E-9	2.46

TABLE 21

MATERIAL	TAYLOR FACTOR	K'' (MPa)	n''	r	S'' (MPa)
FAREN	3.219	121	.1215	.978	76.4
FBREN	3.233	126	.1548	.938	74.5
A3500	3.036	96	.1308	.919	51.4
B3500	3.986	117	.2482	.986	50.2
G8590	3.089	193	.1927	.983	54.7
G8545	2.997	150	.2268	.993	54.1
I8090	3.010	92	.2075	.972	67.6
I8045	2.884	88	.1951	.917	71.8
COLD WORKED		150	.136	.75	63.2
ANNEALED		127	.175	.95	42.6

Figures

24

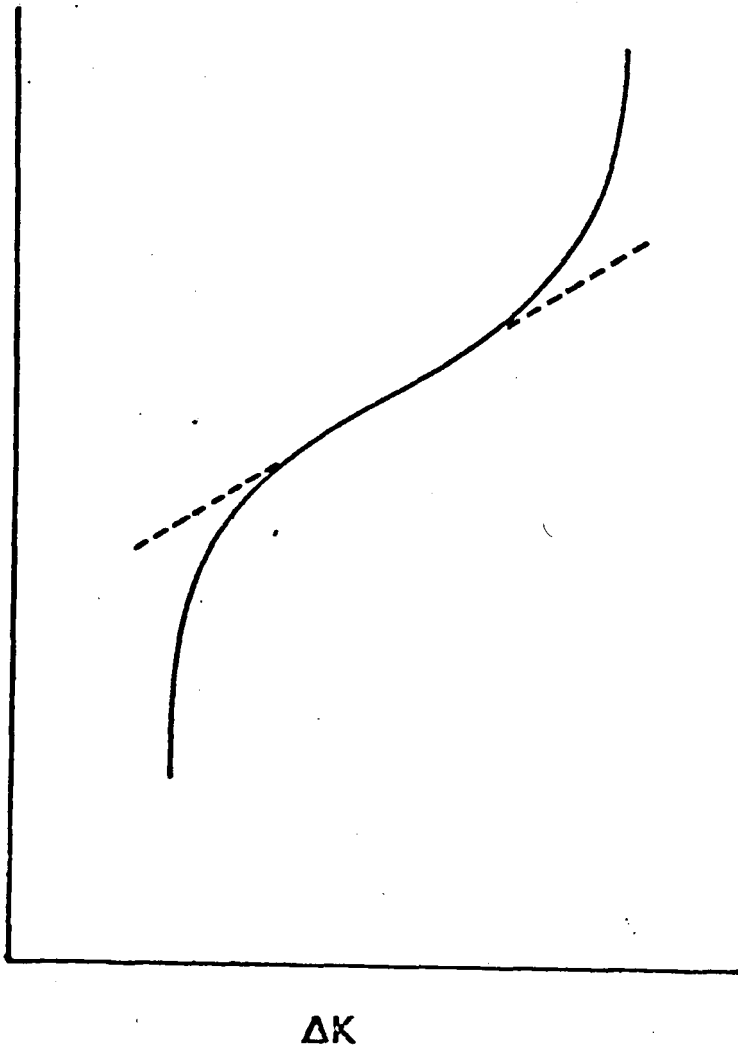


Figure 1.

General form of the dependence of the rate of fatigue crack propagation upon the applied stress intensity. The dotted line indicates the regime in which the relation $da/dN = C(\Delta K)^m$ may be applied.

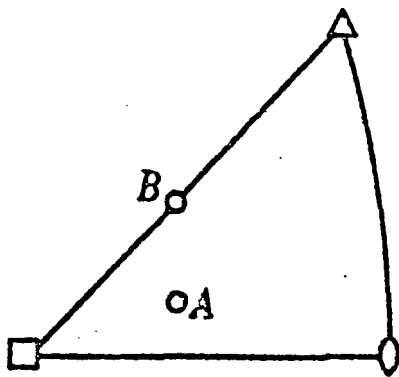
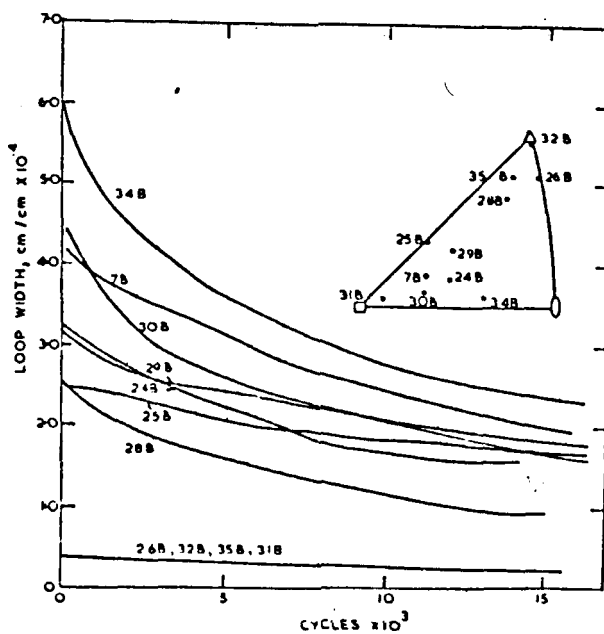


Figure 2.

The orientations of the stress axes in the crystals employed by Broom and Ham (ref. 12).



Crystal	Fatigue Shear Stress, g mm ⁻²	Cycles to Failure
34B	± 700	80,300
7B	± 680	426,000
30B	± 700	185,000
29B	..	114,000
24B	..	293,000
25B	..	637,000
28B	..	323,000
26B	..	> 2 · 10 ⁶
32B
35B
31B

Figure 3.

The cyclic hardening response of aluminium single crystals fatigued at a cyclic shear stress = $\pm 700 \text{ gm mm}^{-2}$. The orientation of the tensile axes with respect to the crystal axes is shown in the inset. The accompanying table indicates the differences in fatigue life (taken from ref. 13).

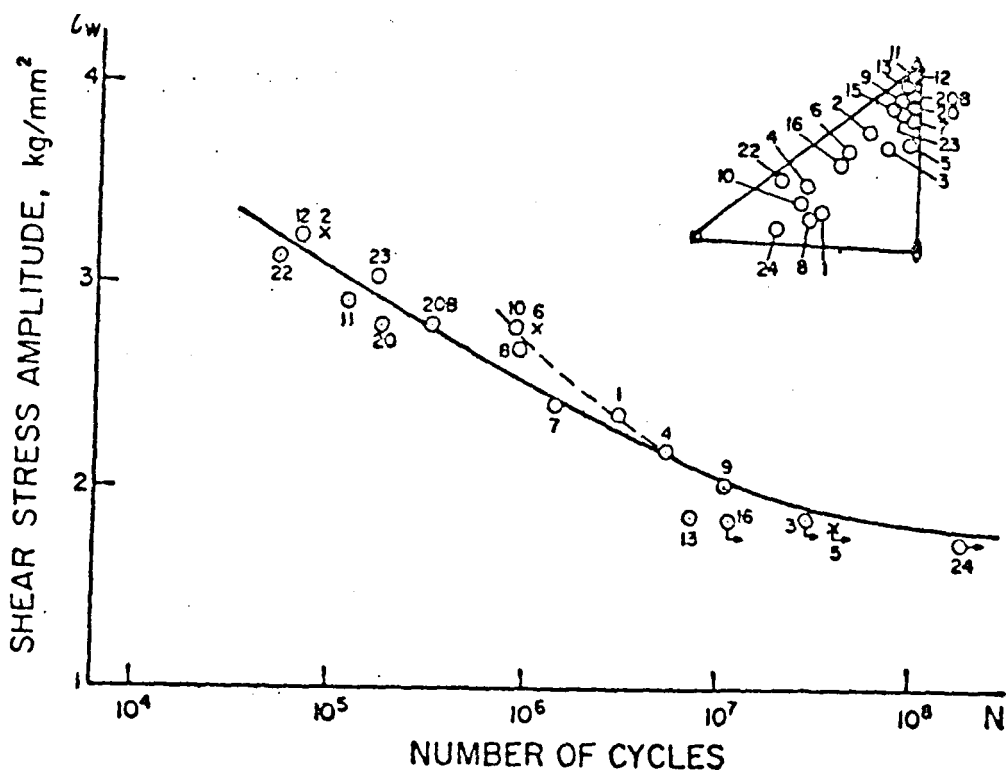


Figure 4. The S/N curve of copper single crystals expressed by Kettunen (ref. 14) in terms of the shear stress amplitude on the primary slip system.

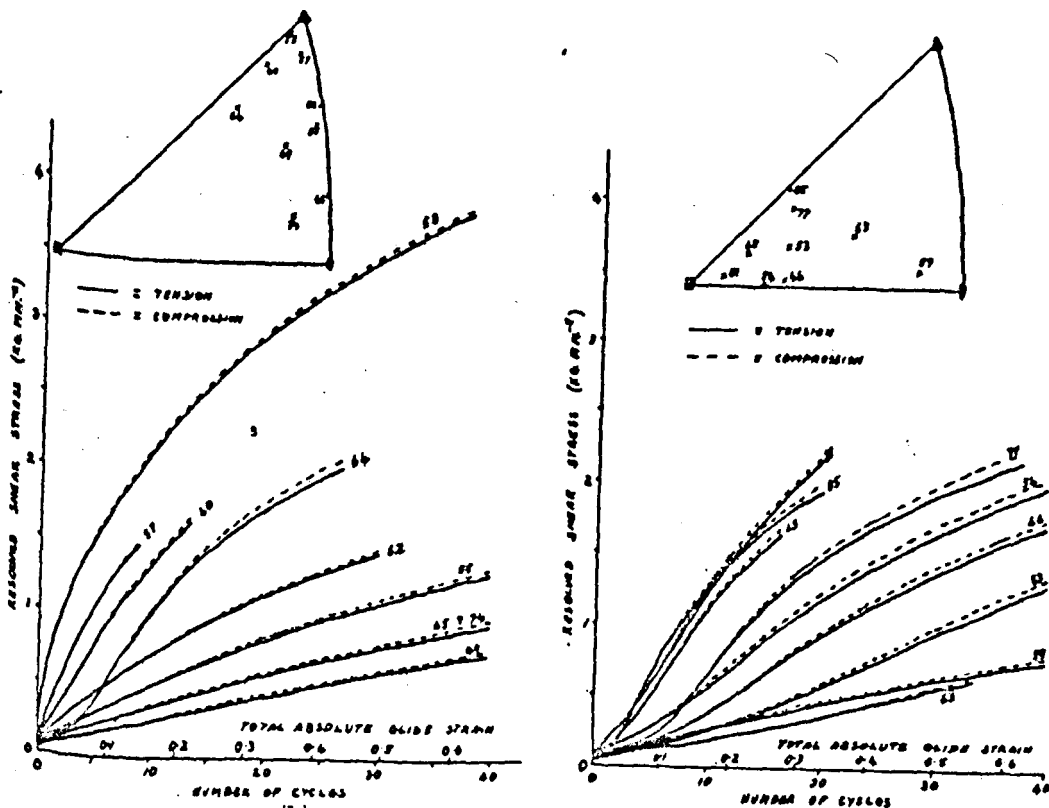


Figure 5. The anisotropic cyclic hardening of copper single crystals as demonstrated by Patterson (ref. 17). The inset figures show the relative stress axis - crystal orientations. The plots show the maximum resolved shear stresses, in tension and compression, as the cyclic hardening occurs.

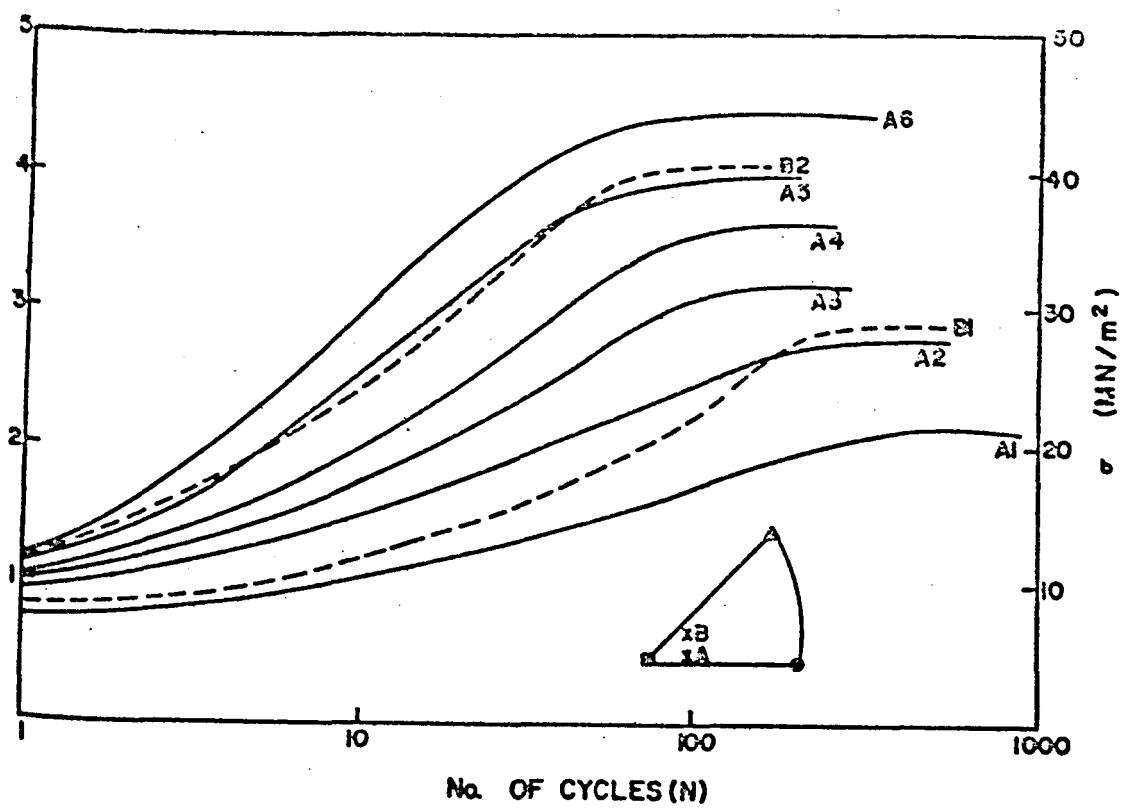


Figure 6.. The data of Sastry et al, illustrating the anisotropy of cyclic hardening of silver single crystals (ref. 20).

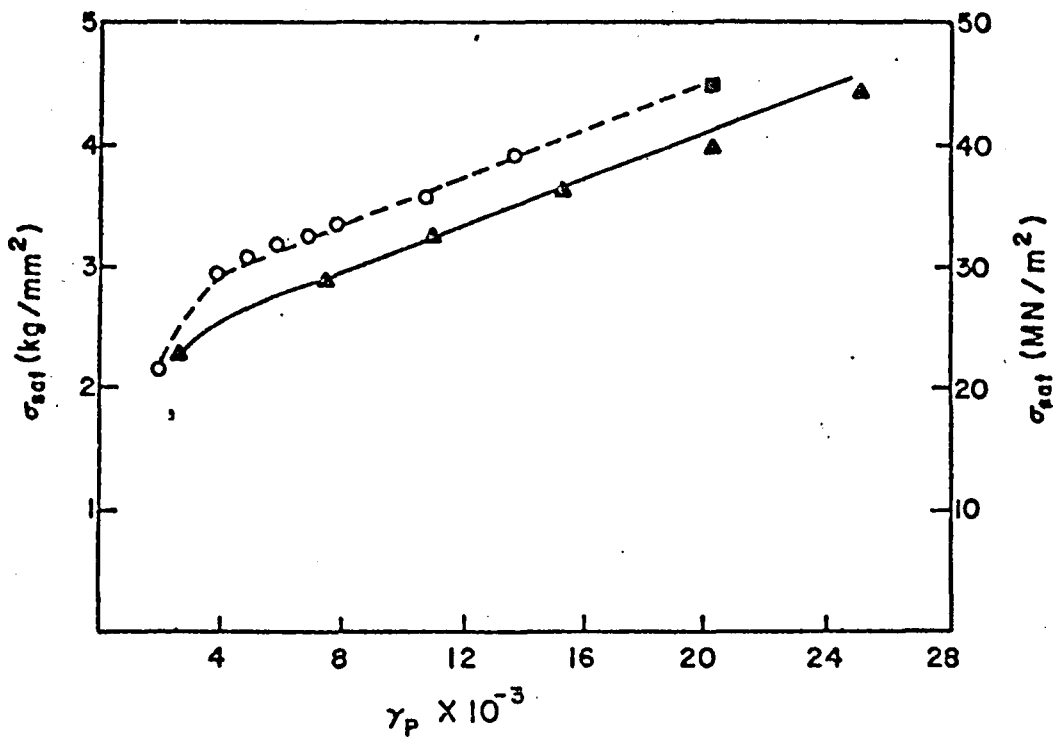


Figure 7. The cyclic stress-strain curves of silver (—) and copper (----) single crystals. Taken from Sastry et al (ref. 20).

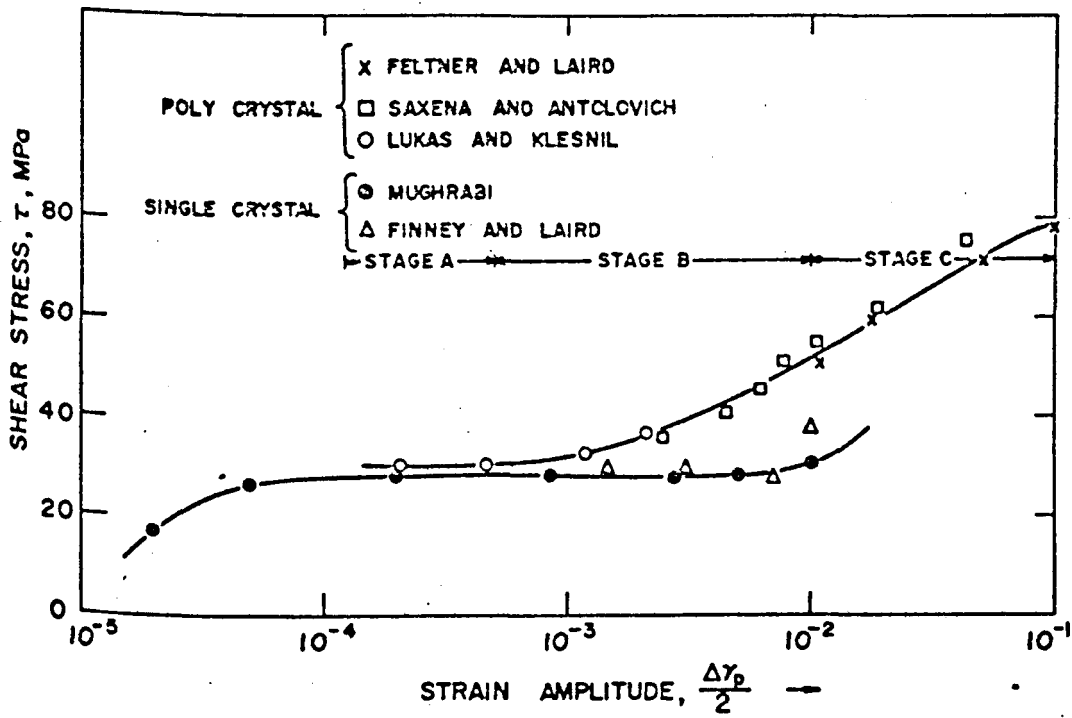


Figure 8. The cyclic stress-strain curves of copper single crystals and polycrystals expressed by Bhat and Laird (ref. 22) in terms of the shear stress amplitude and the shear strain amplitude.

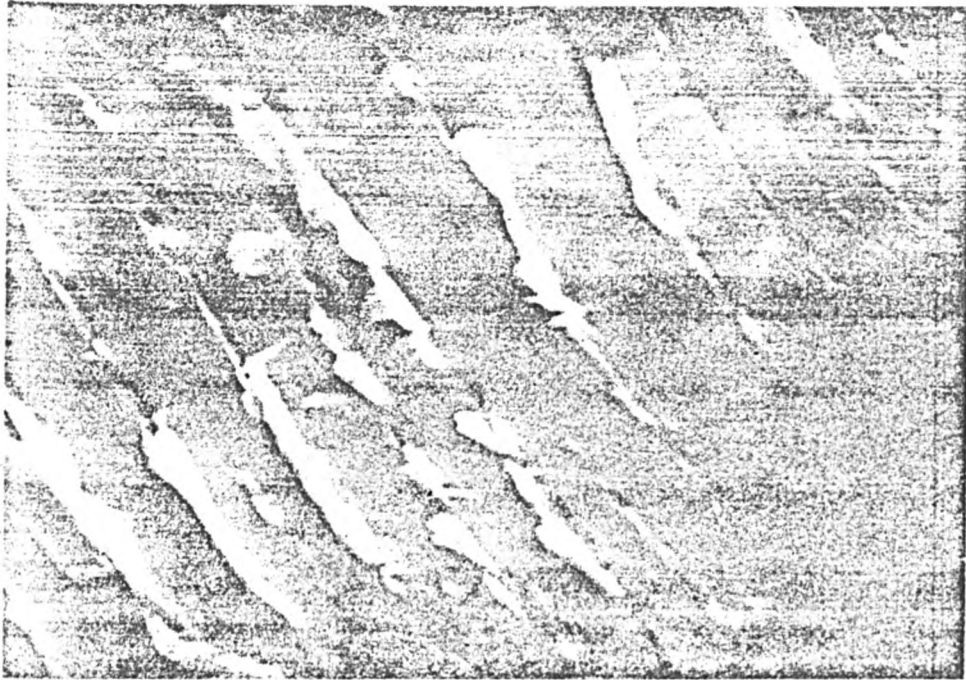


Figure 9. The development of intrusion/extrusion pairs within the PSB's in fatigued copper.

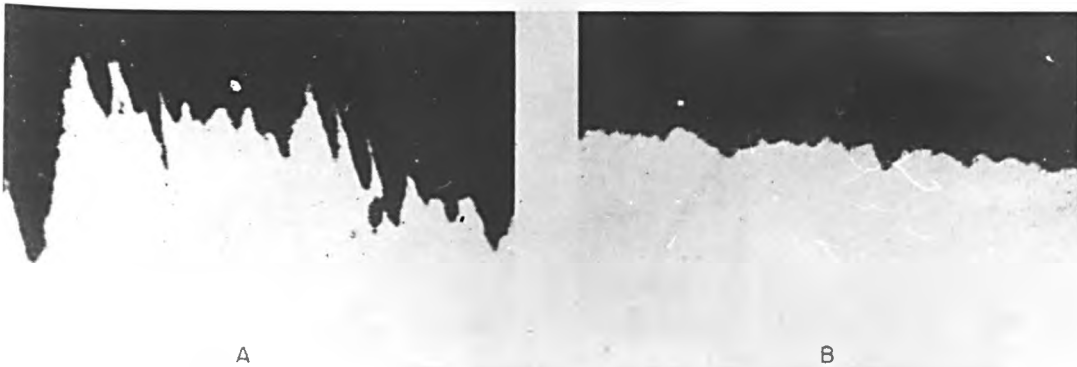
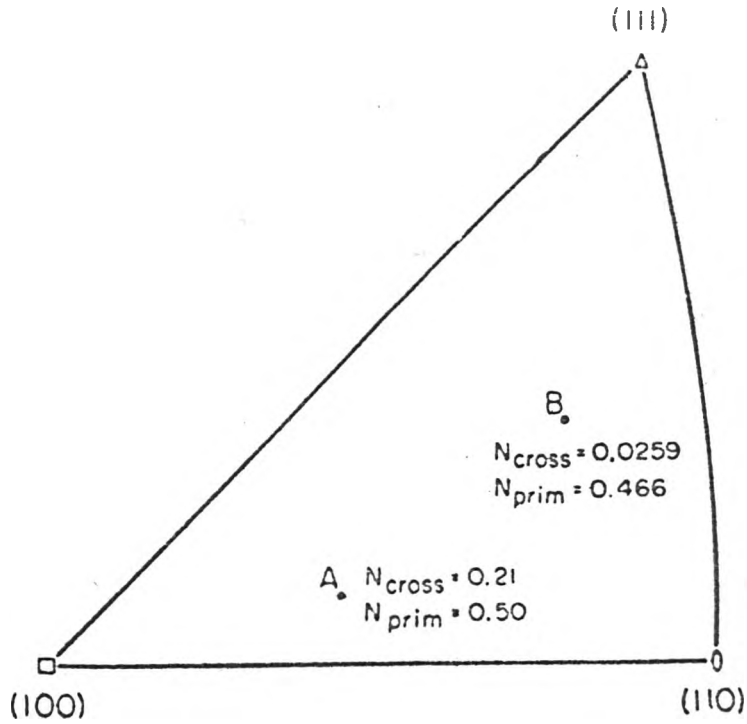
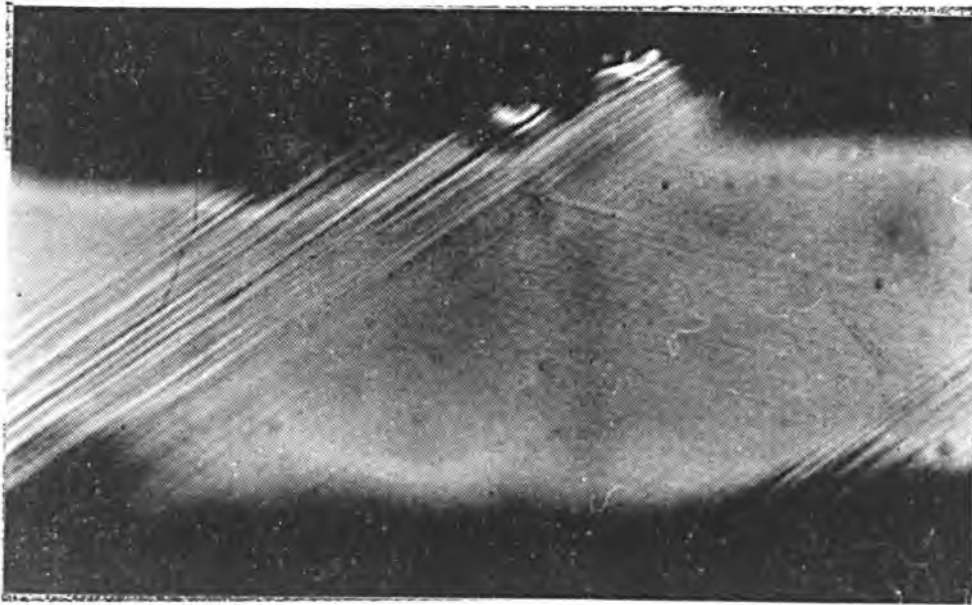


Figure 10. From ref. 26. The difference in extrusion rate of copper single crystals as a function of the shear stress on the cross-slip system. Both crystals were fatigue hardened, electropolished and then given 50 additional cycles. The extrusions are shown by taper sectioning (ref. 26).

B



A

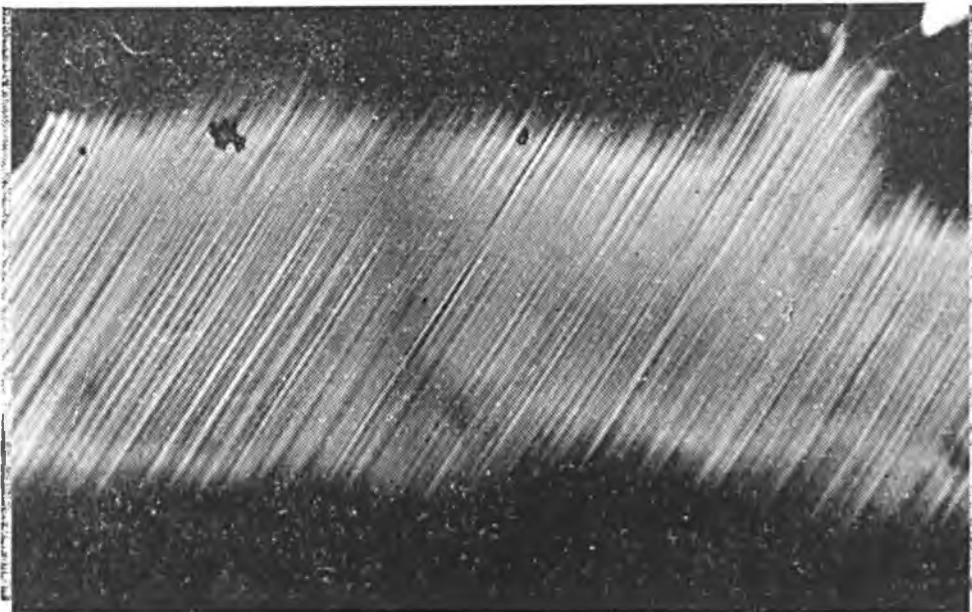
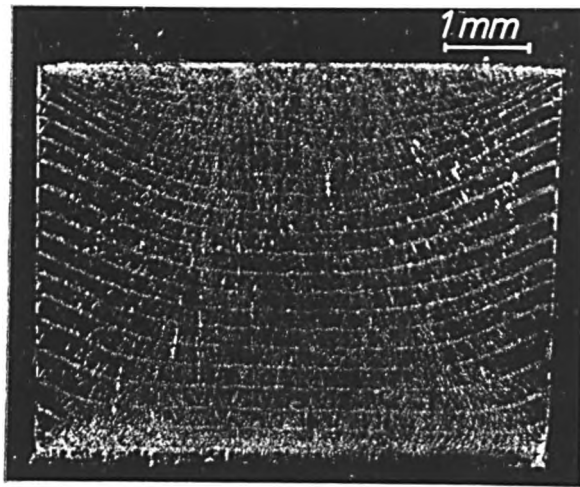
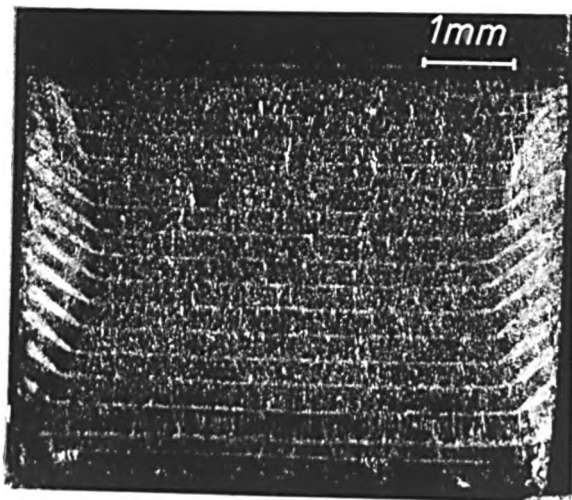


Figure 11. The differences in slip line pattern developed in fatigue copper single crystal. Crystal A oriented for easy glide. Crystal B oriented so that the cyclic stress axis lay close to $\langle 111 \rangle$, (ref. 17).



(a)



(b)

Figure 12. Optical micrographs of the fatigue fracture surfaces of notched copper single crystals from the work of Neumann (ref. 31). Crack propagation is from top to bottom. The white markings indicate crack rest lines every 400 cycles due to the programmed loading employed. The difference in crack front orientation is caused by the orientations of the crystals with respect to the stress axes and crack fronts.

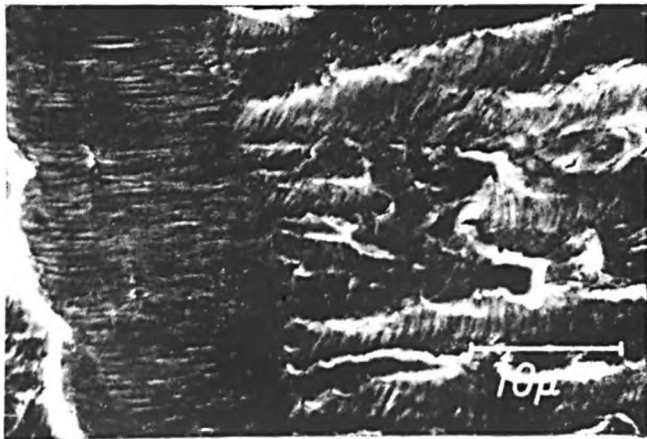
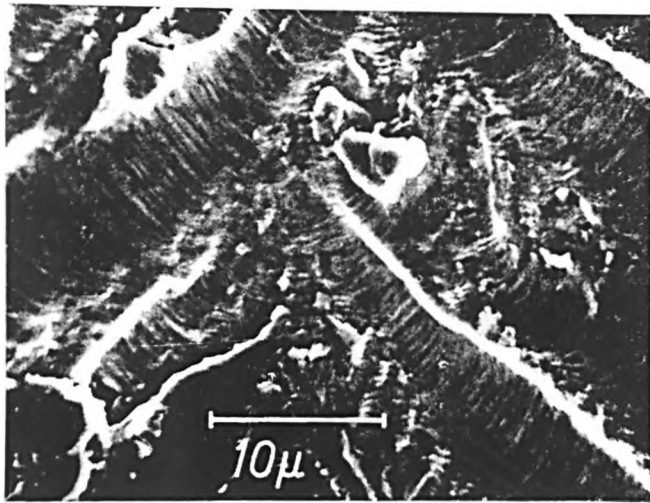


Figure 13. SEM Fractographs of fatigue fracture surfaces of copper single crystals from ref. 31, which indicate that the local direction of crack propagation is always perpendicular to $\langle 011 \rangle$ directions.

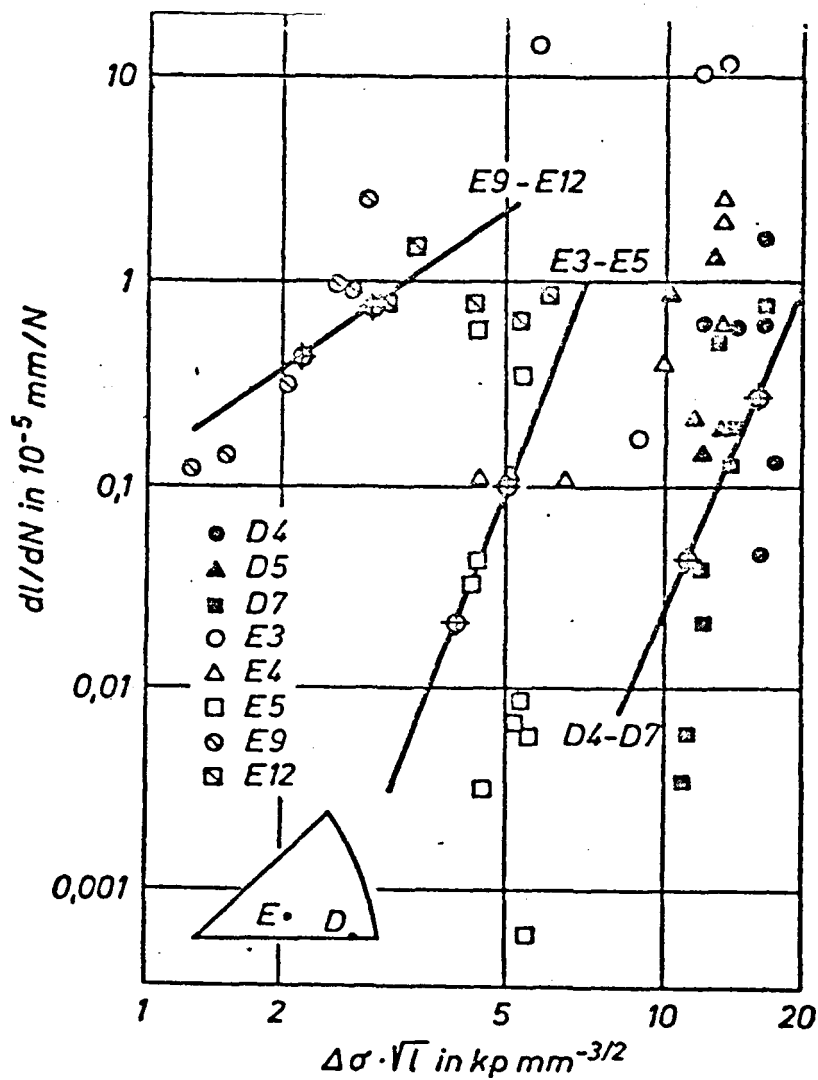


Figure 14. The crack propagation data of Donch and Haasen for copper single crystals. The inset shows the crystal-stress axis orientations. (ref. 33).

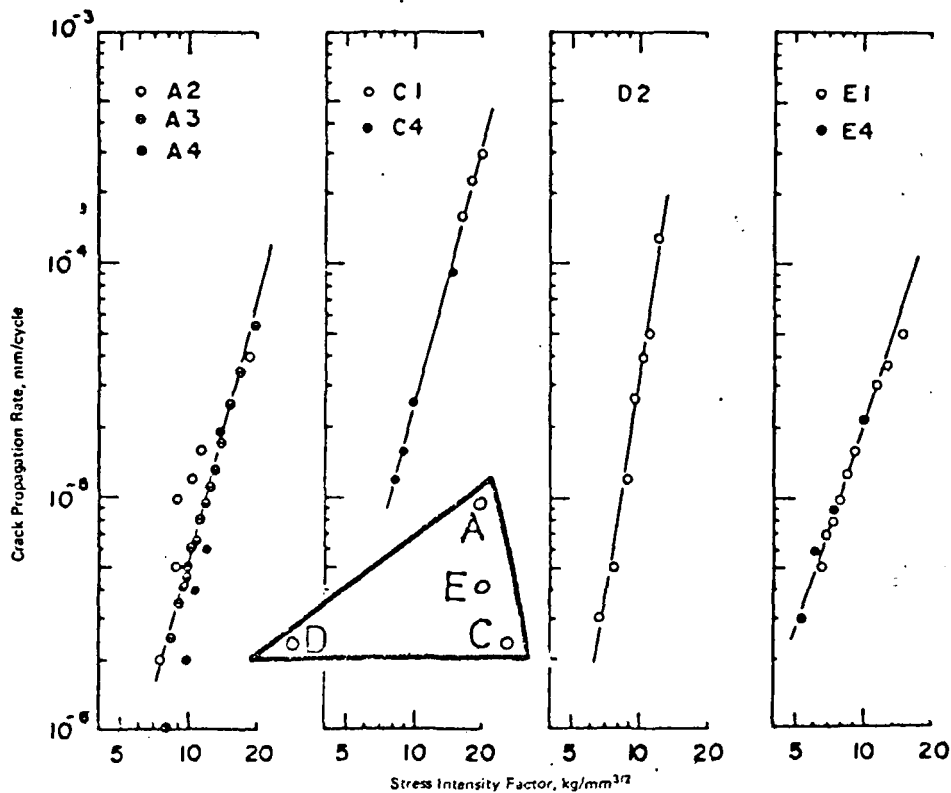


Figure 15. The crack propagation data of Ishii and Weertmann for copper single crystals. The inset shows the crystal-stress axis orientations. (ref. 40).

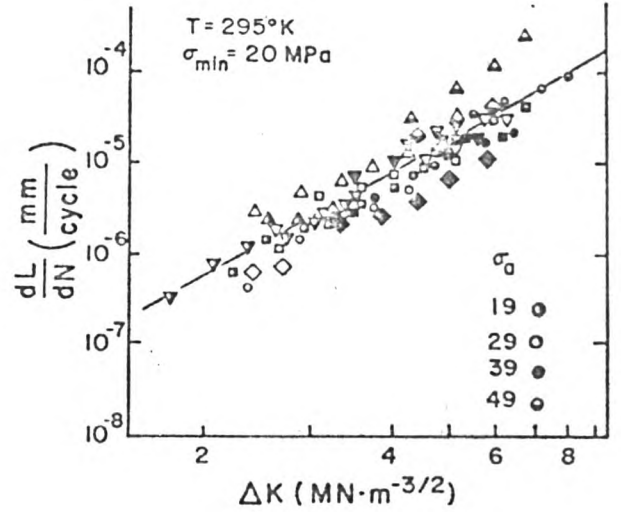
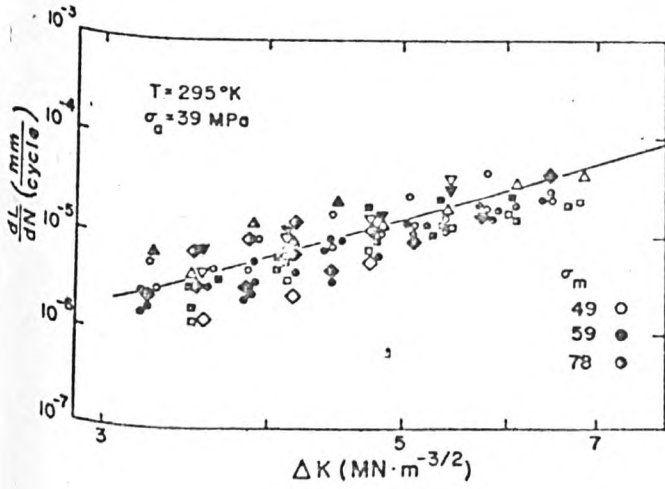
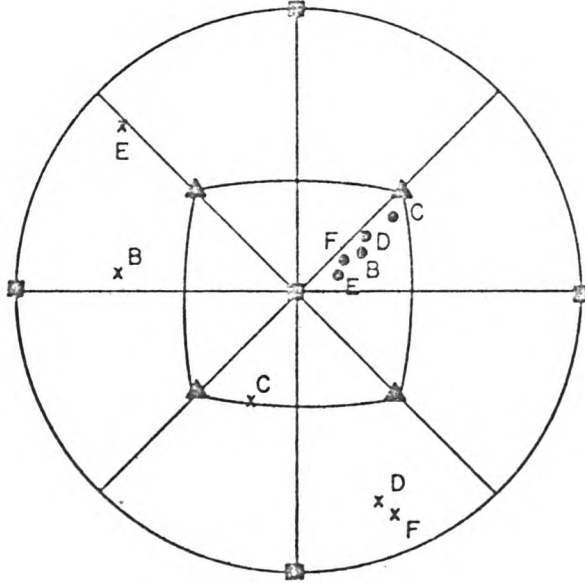


Figure 16.

The crack propagation data of Yeske and Weertmann (ref. 43). The shape of the point indicates the orientation (poly O, B \diamond , D \square , E ∇ , F \triangle). The shading indicates the cyclic stress range as shown.

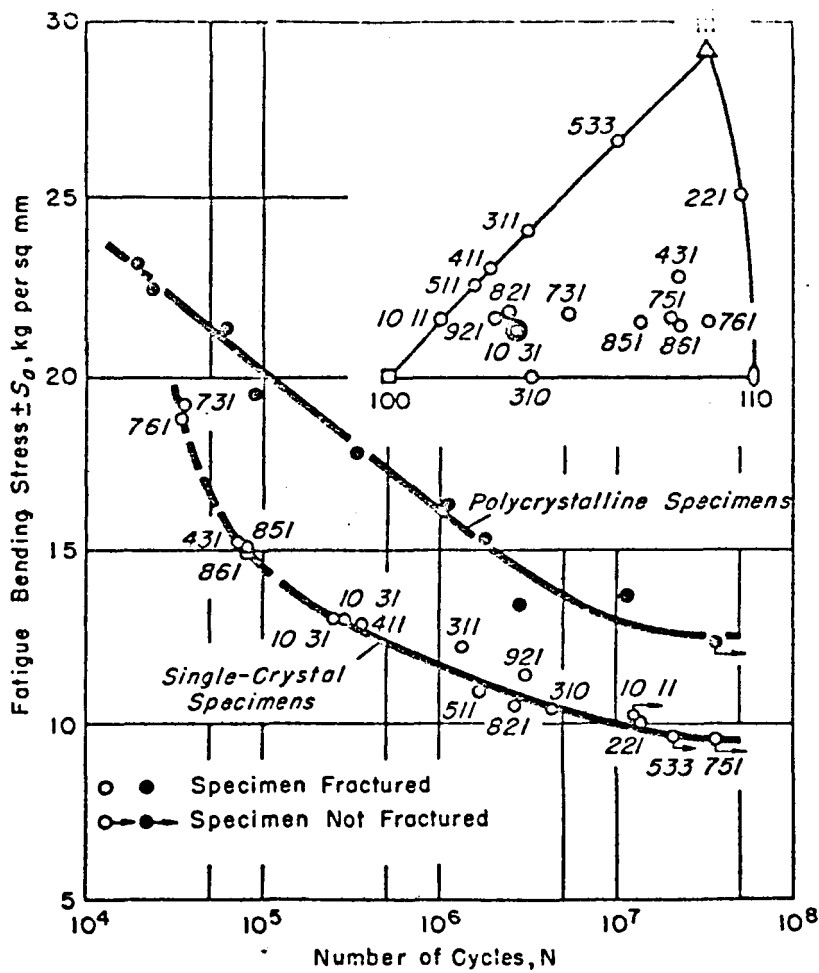


Figure 17. The S/N data of iron single crystals. Orientation of crystals shown in inset, from Hempel ref. 44.

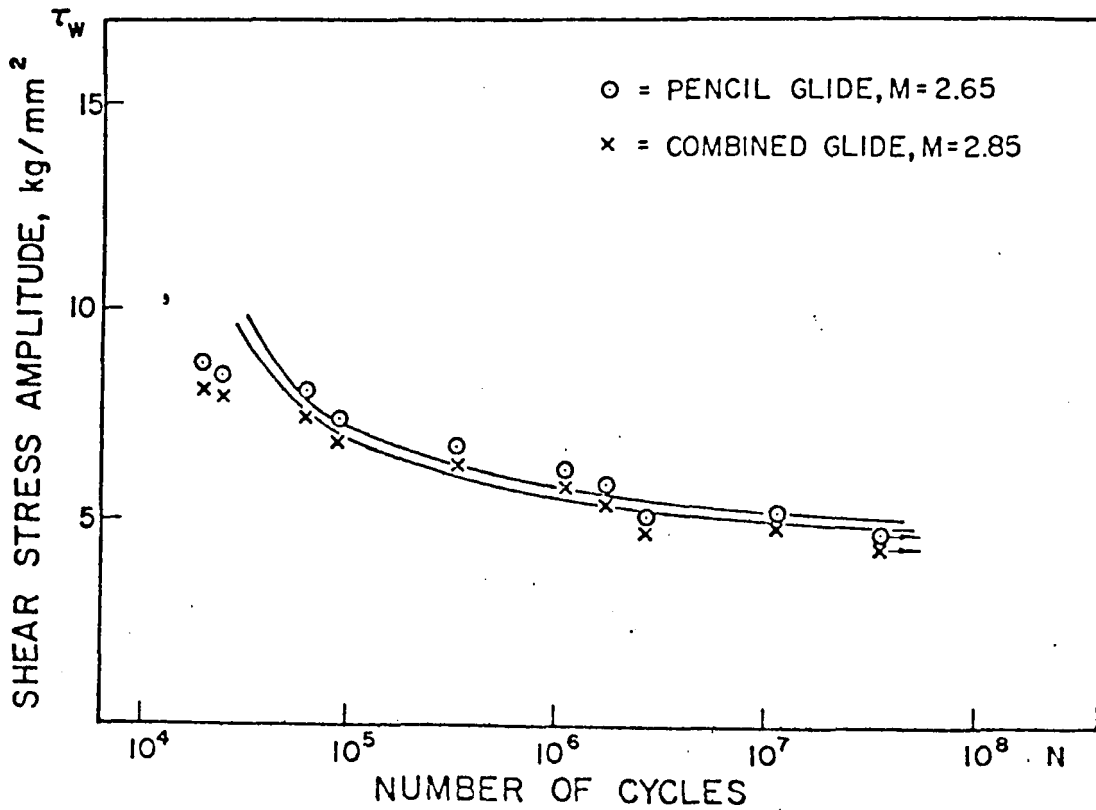


Figure 18. The data of fig. 17 as reanalysed by Kettunen (ref. 15).

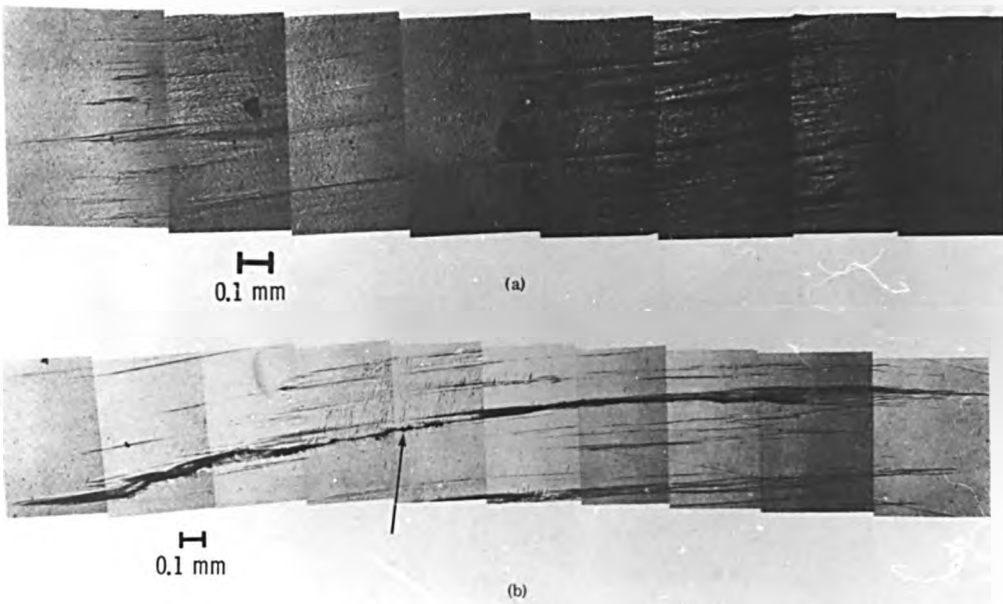


Figure 19. The lenticular shaped markings due to asymmetric cyclic slip in torsionally fatigued niobium single crystals as reported by Nine ref. 45.

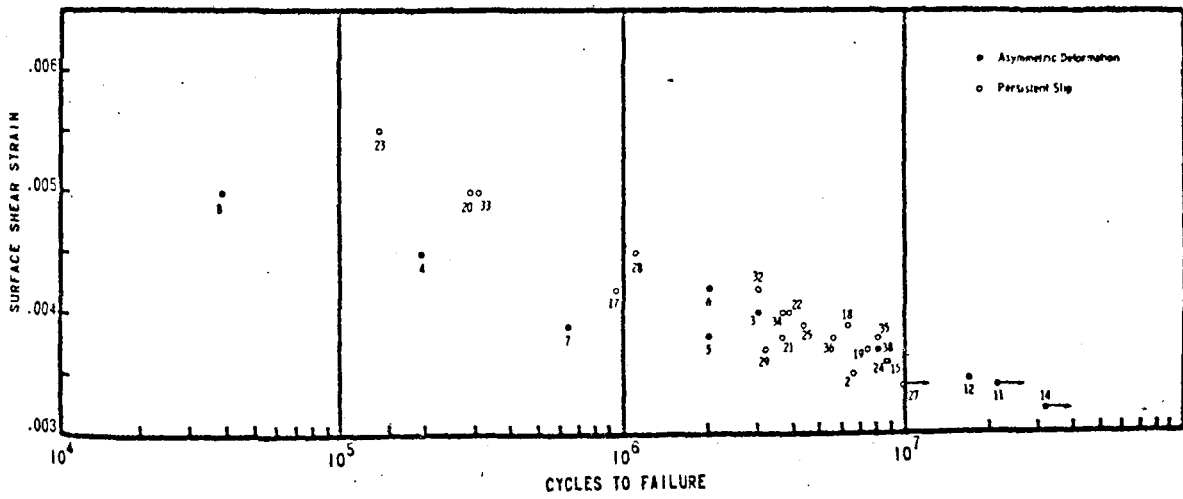


Figure 20. The S/N data of torsionally fatigued niobium single crystals from Nine, ref. 45, indicating that the data consist of two distinct populations.

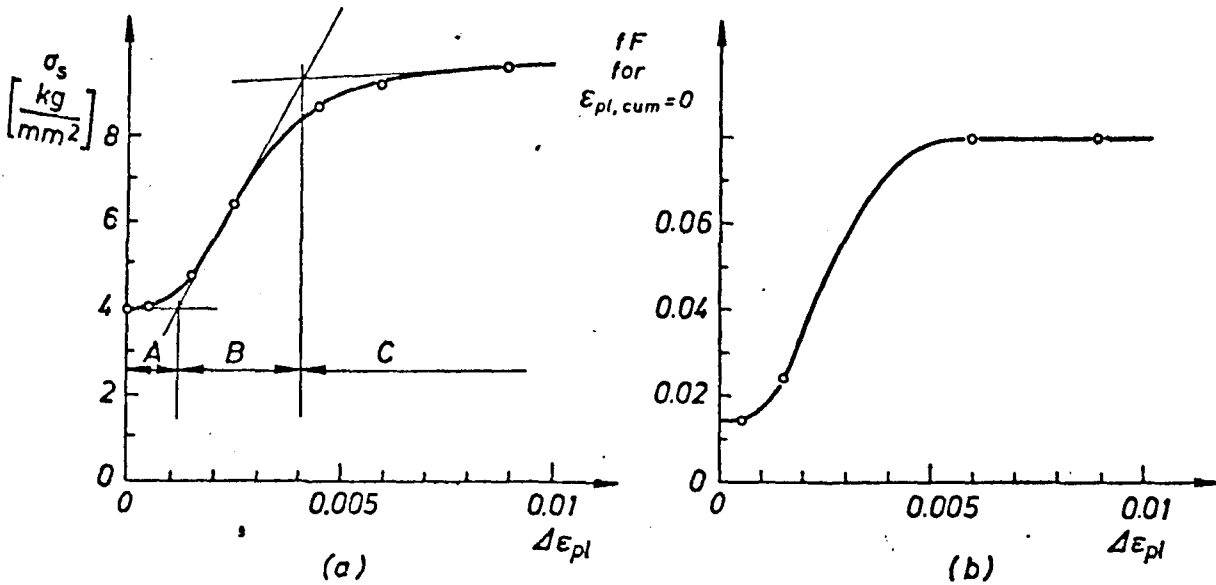


Figure 21. a) The Cyclic stress-strain for iron single crystals reported by Mughrabi and Wuthrich (ref. 51) showing a three stage curve.
 b) The dependence of the degree of slip asymmetry upon the applied strain amplitude.

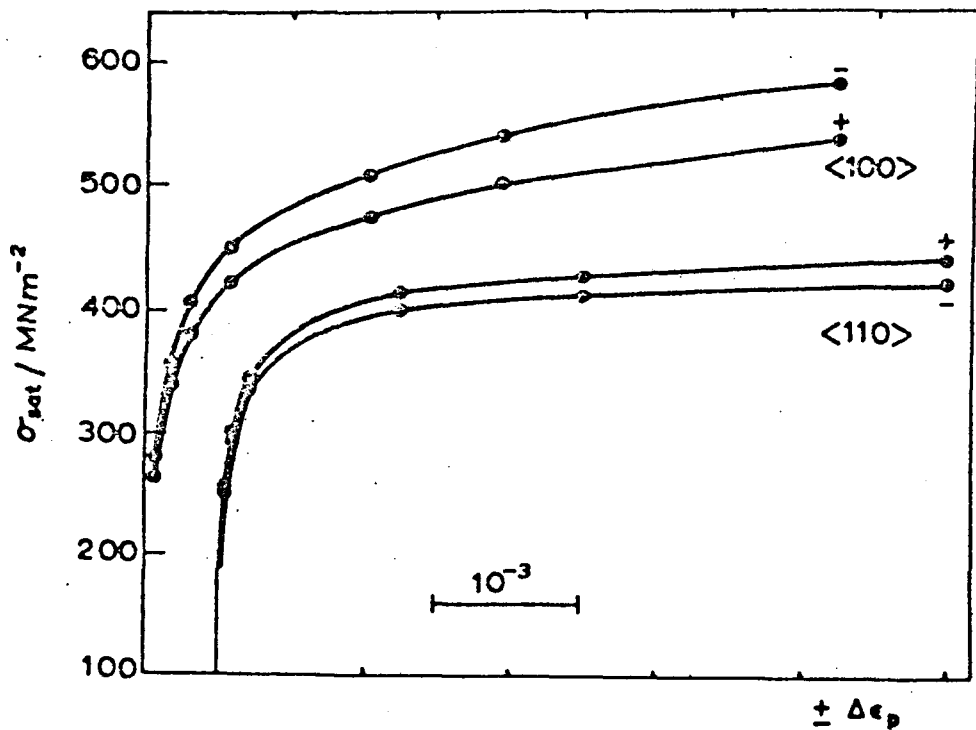


Figure 22. The cyclic stress-strain behaviour of molybdenum single crystals reported by Etemad and Guiu (ref. 48).

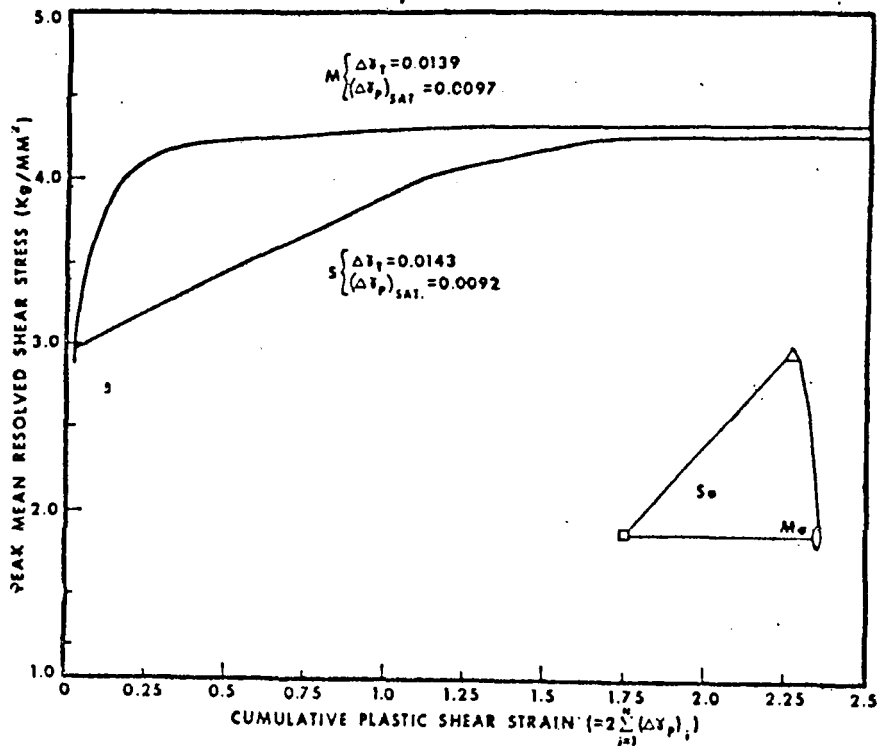


Figure 23. The cyclic stress-strain data of Doner et al for niobium single crystals (ref. 49).

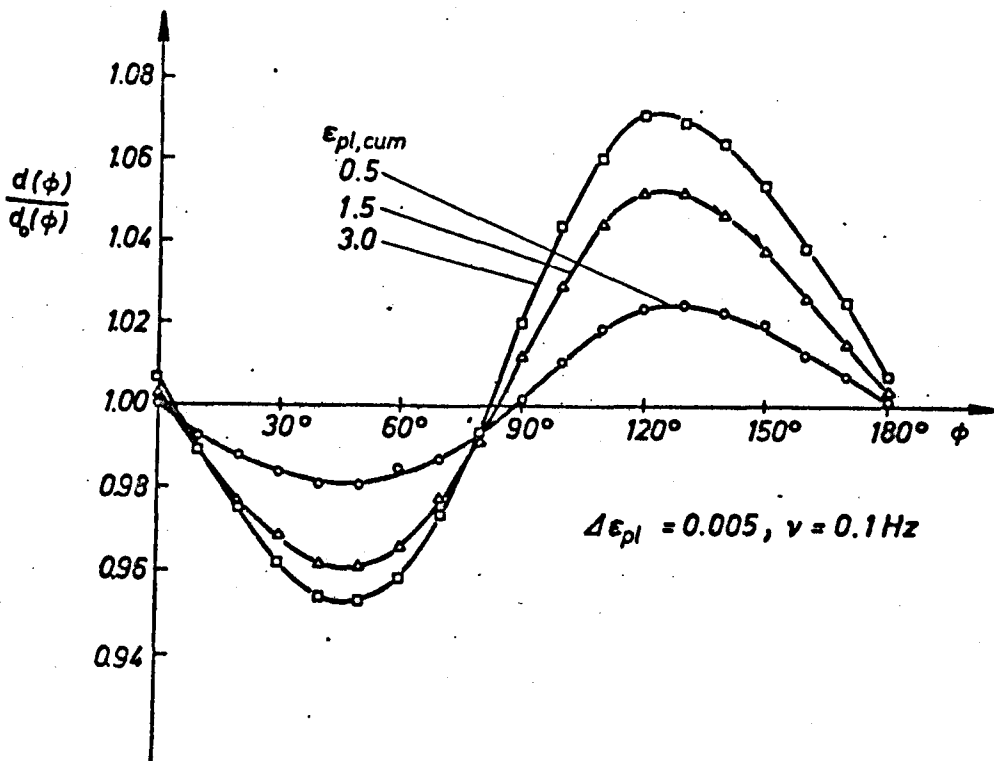
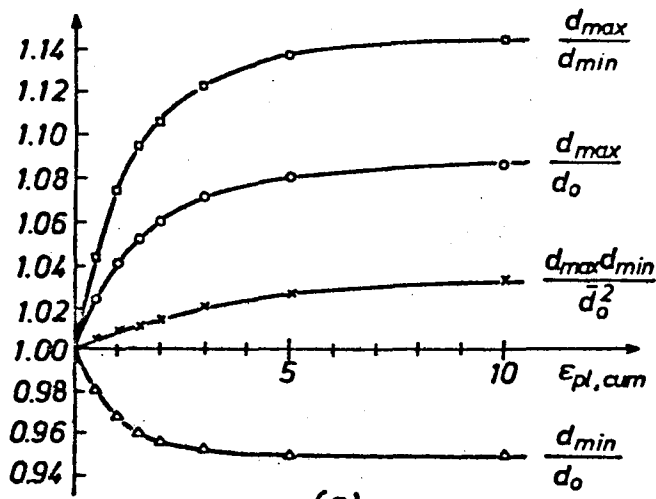


Figure 24.

The shape changes in initially circular cross section iron single crystals after cycling due to slip asymmetry from Mughrabi and Wuthrich (ref. 51).

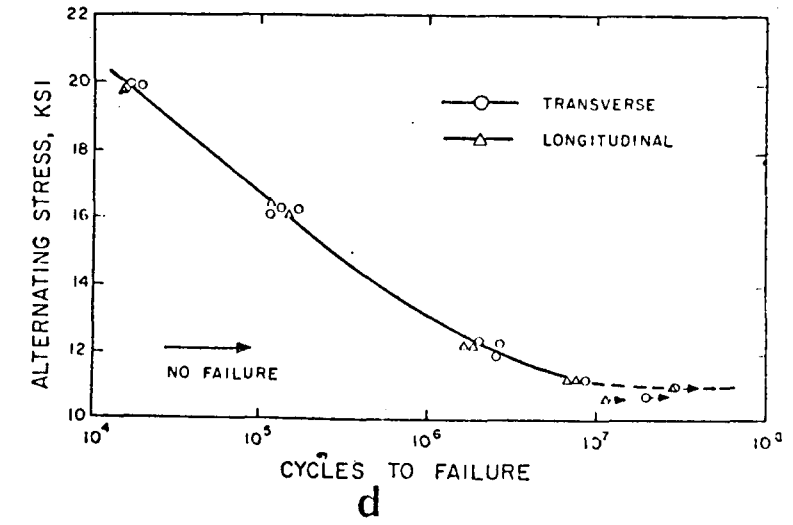
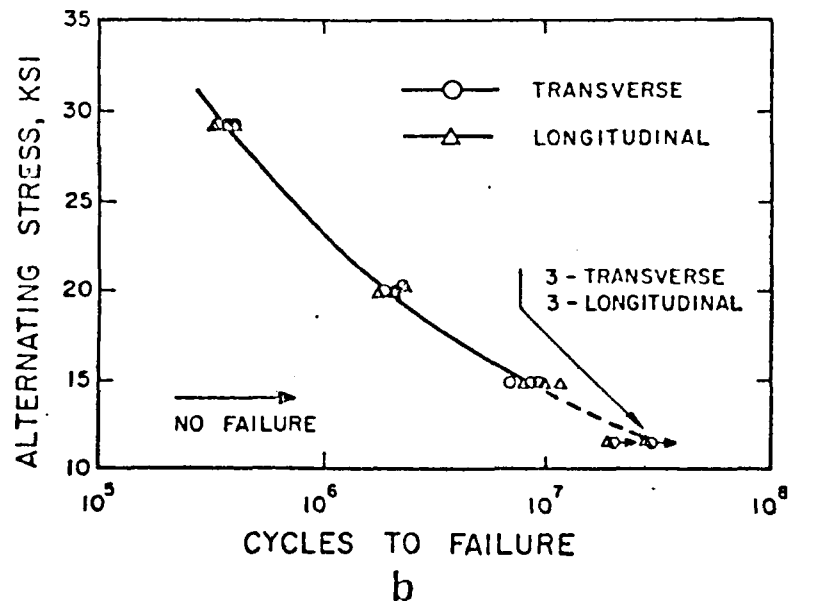
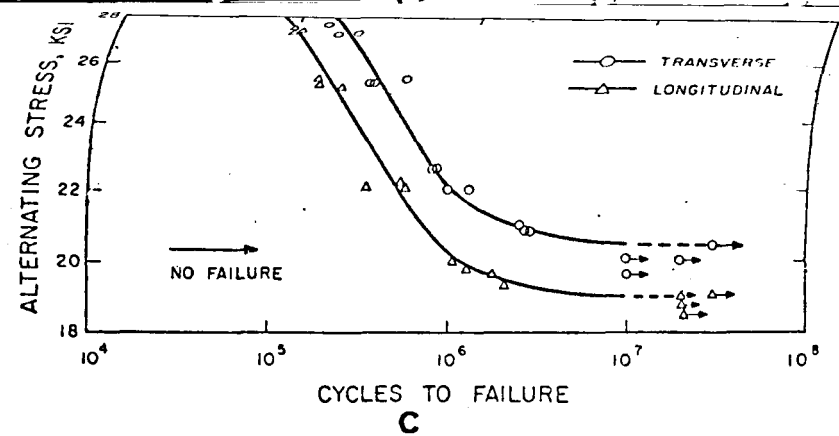
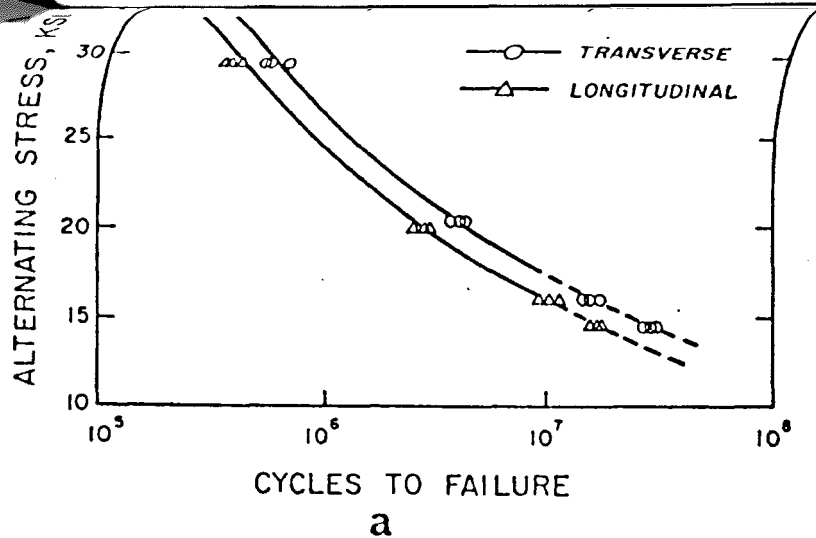


Figure 25. The S/N curves of textured polycrystalline materials, a) cold rolled copper, b) annealed copper, c) cold rolled Al-Mg alloy, d) annealed Al-Mg alloy. The specimens were taken from the transverse or longitudinal directions of the plate as shown (ref. 59).

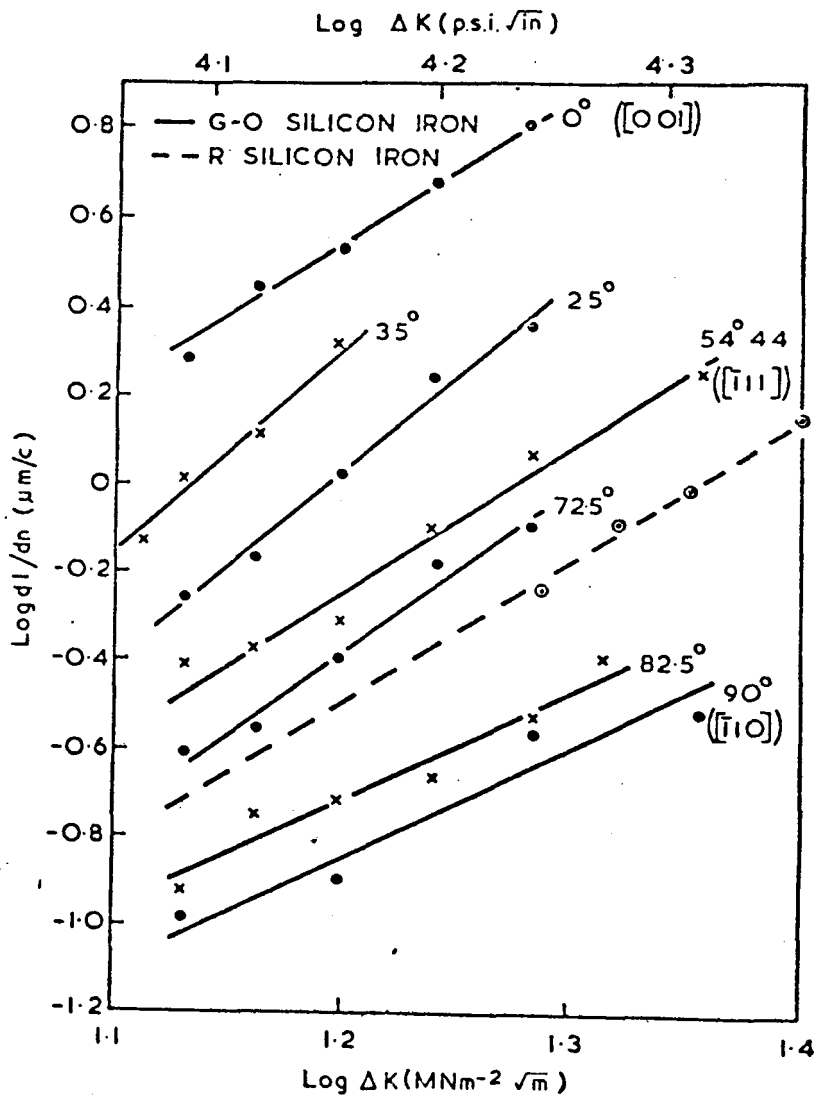


Figure 26. The effect of testing direction, rotation of the stress axis from the sheet rolling direction, upon the rate of fatigue crack propagation in grain oriented (G-O) and random textured (R) silicon iron. (from ref. 68.)

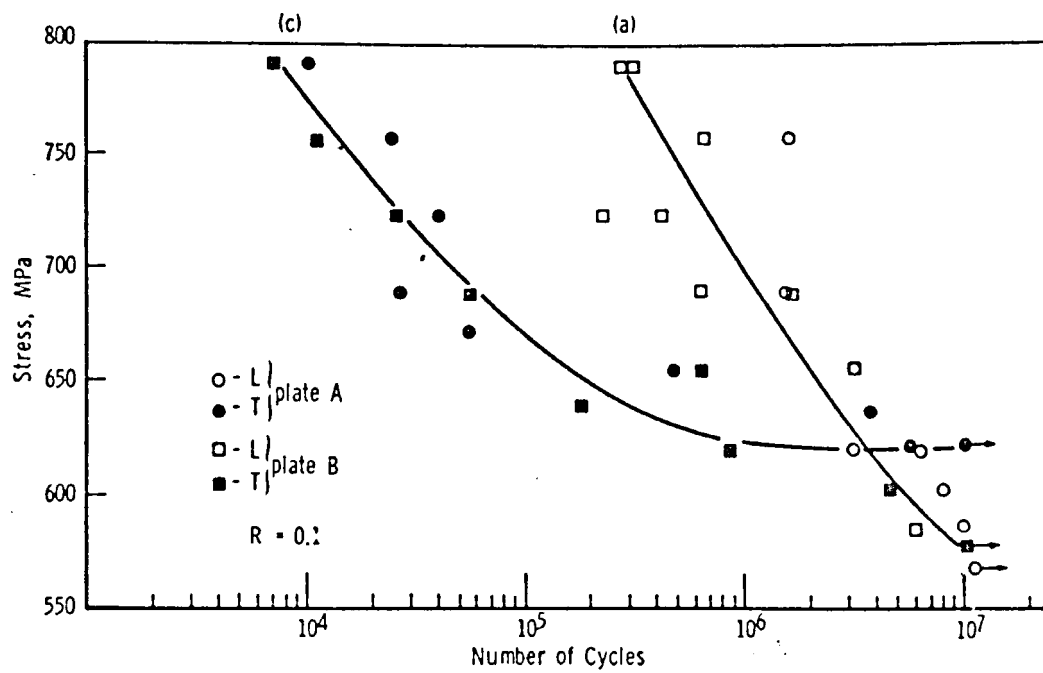


Figure 27 The effect of testing direction on the fatigue properties of textured Ti-4Al-4V plate. (ref.73)

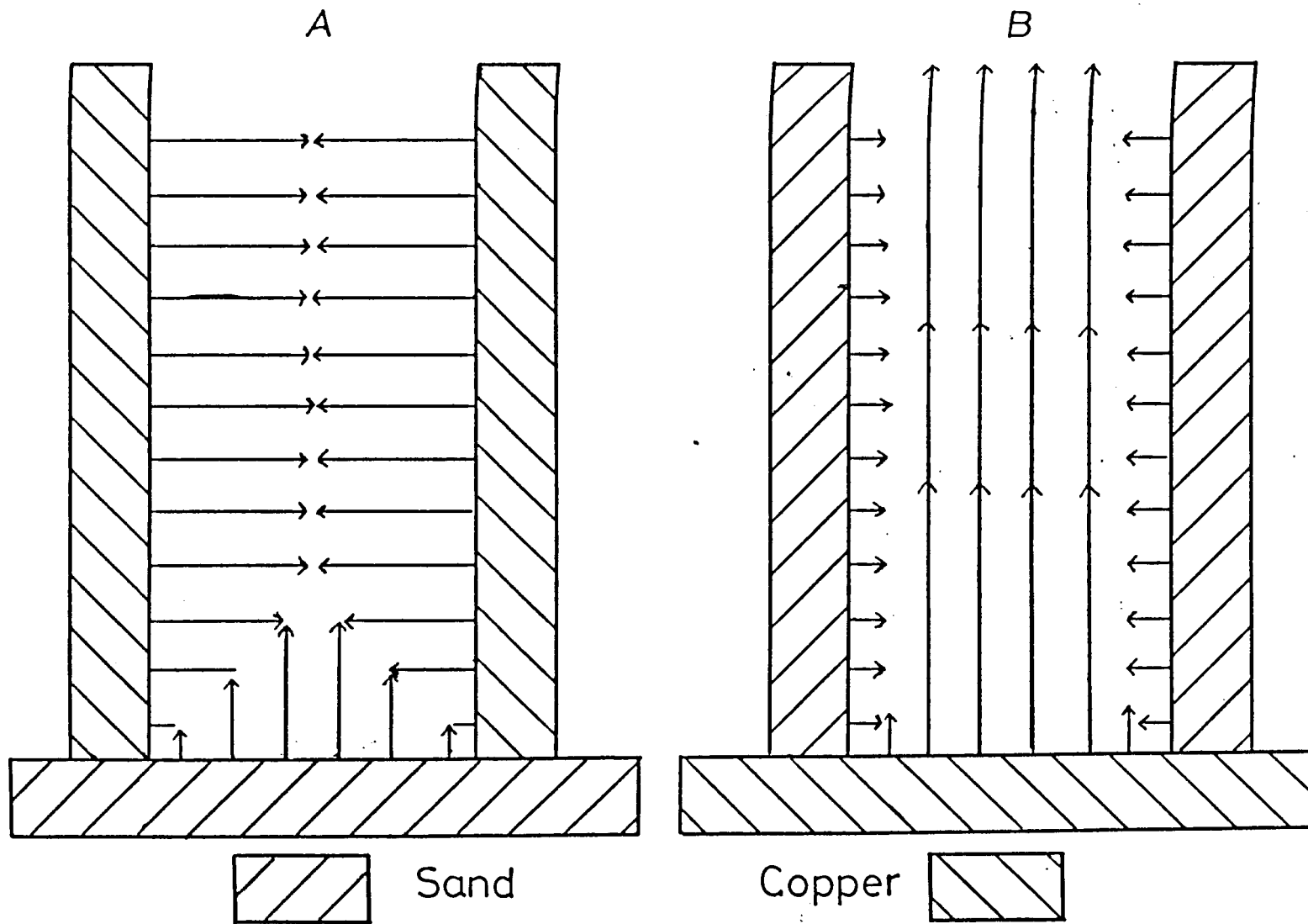


Figure 28 Moulds employed in casting billets for extrusion.

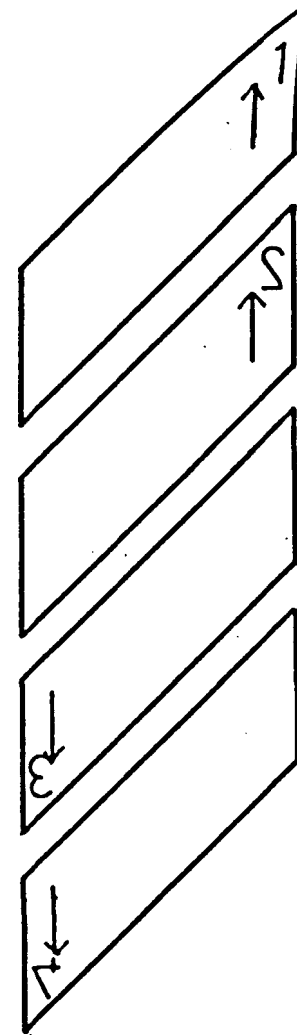
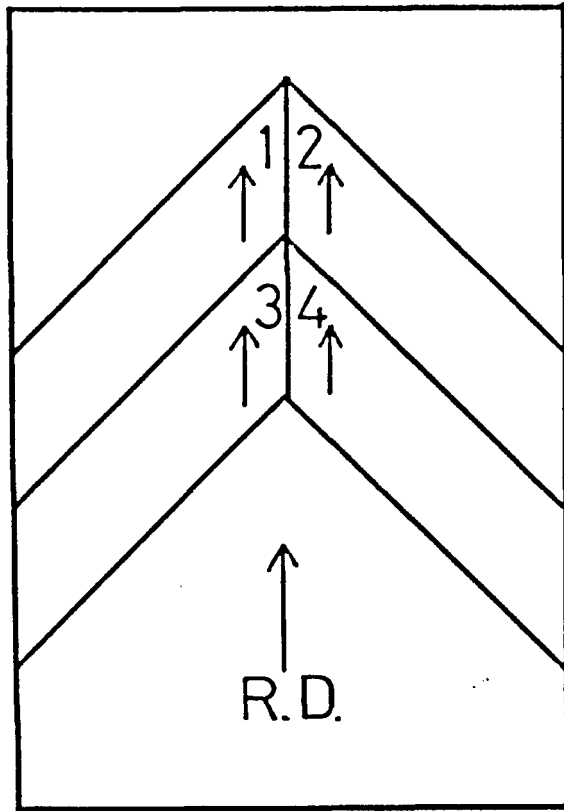


Figure 29 The stacking sequence used to ensure averaging of the quadrant pole figure during the fabrication of composite samples from thin sheet material.

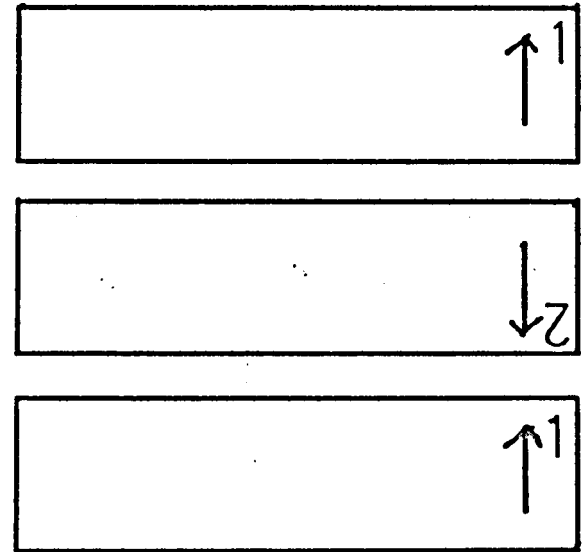
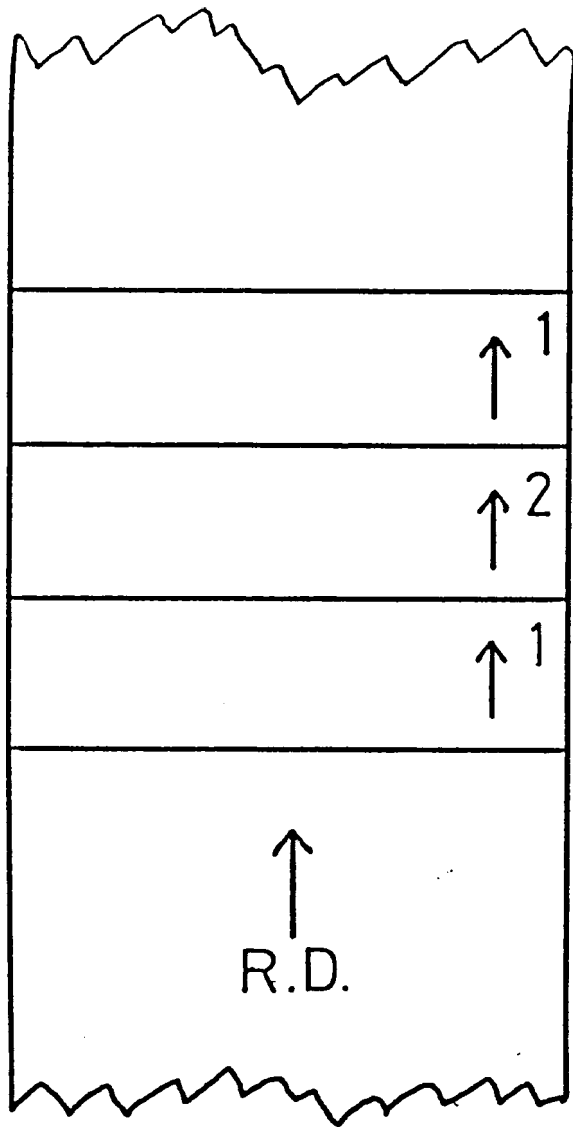


Figure 30 The stacking sequence used to fabricate a composite from thick plate.

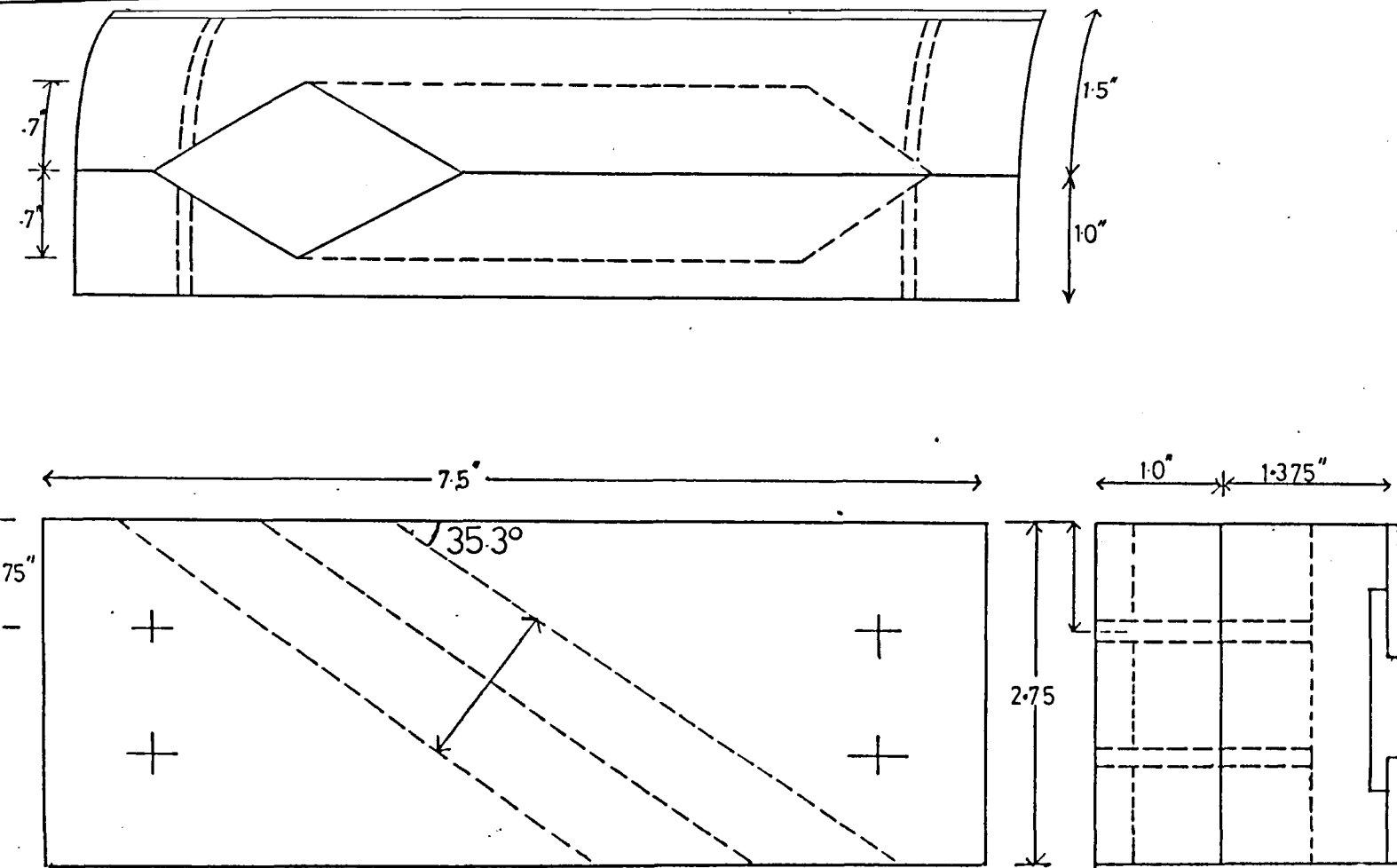


Figure 31 Plan drawing of alignment jig employed to slice the blocks produced by the bonding process described in figure 30.

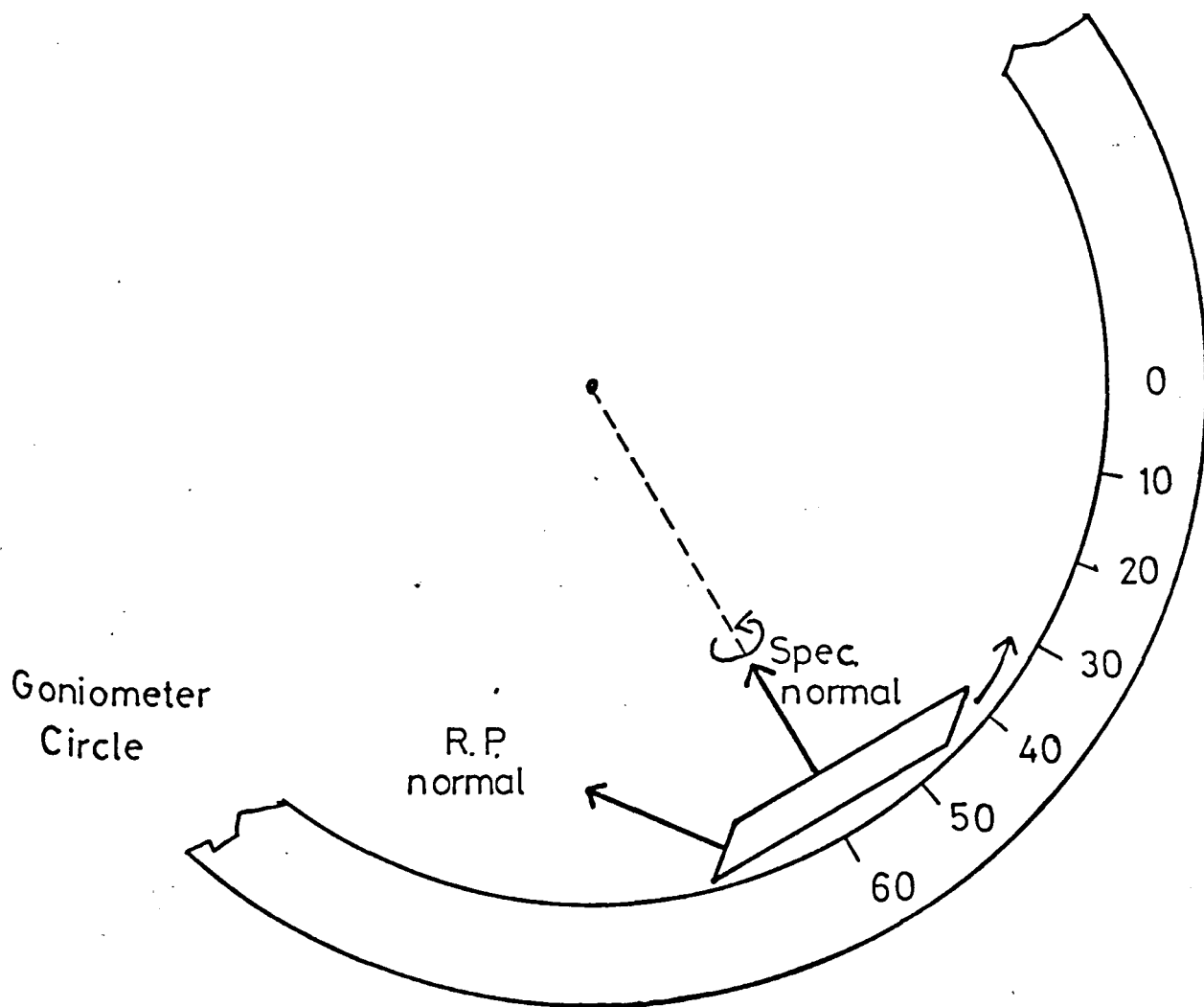
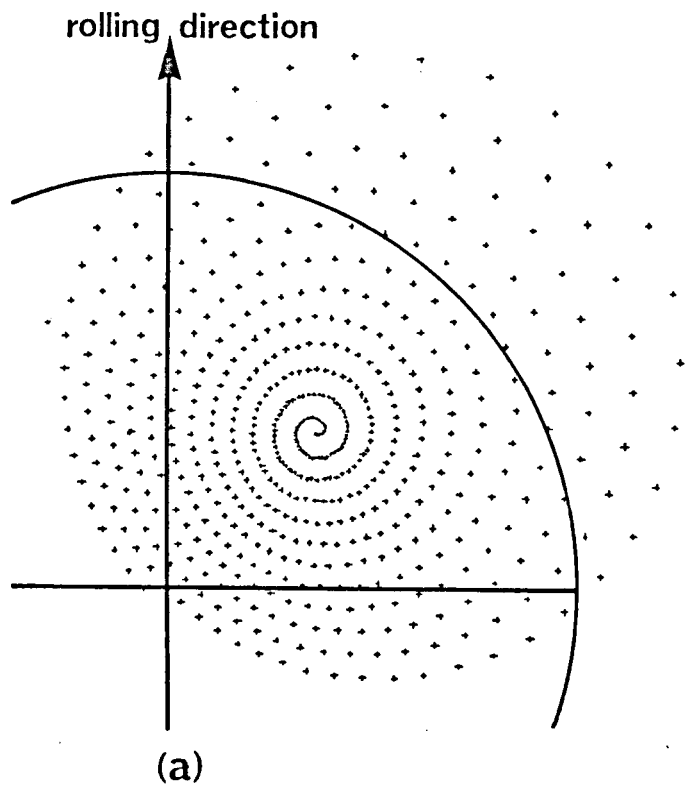


Figure 32 Schematic diagram of the starting position of the texture specimen in the goniometer circle. This position corresponds to the beginning of the spiral in fig.33.



(a)

Figure 33 The spiral path traced by the diffracting plane normal during data acquisition. The crosses indicate the data sampling points.

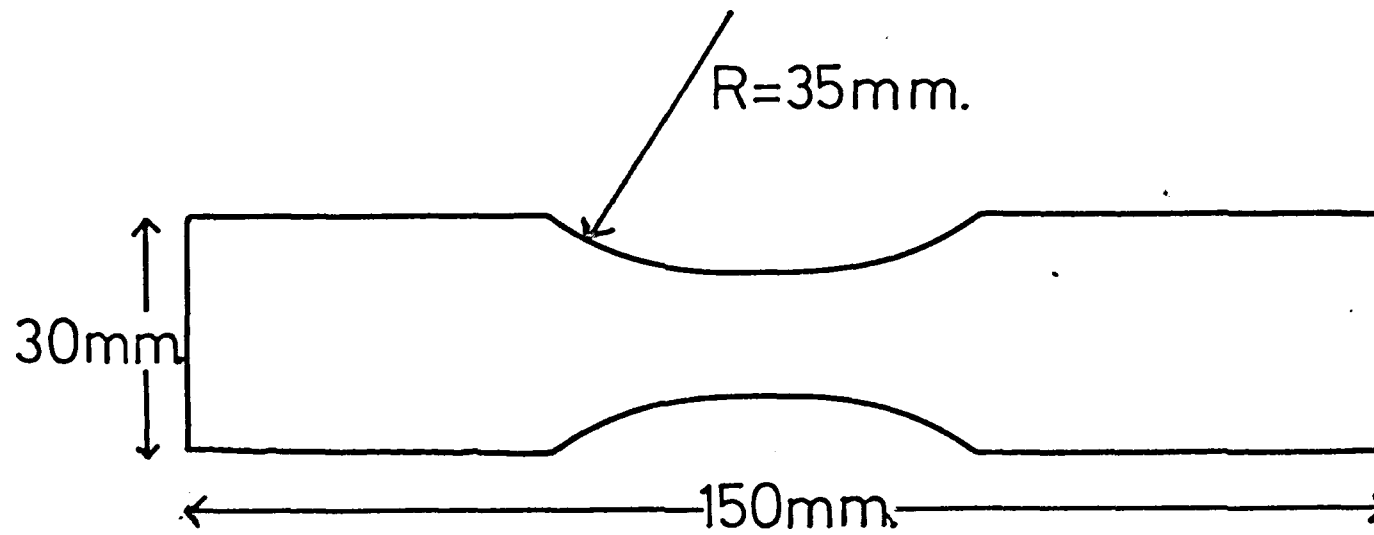


Figure 34 The thin sheet fatigue specimens produced by filing in a template jig.

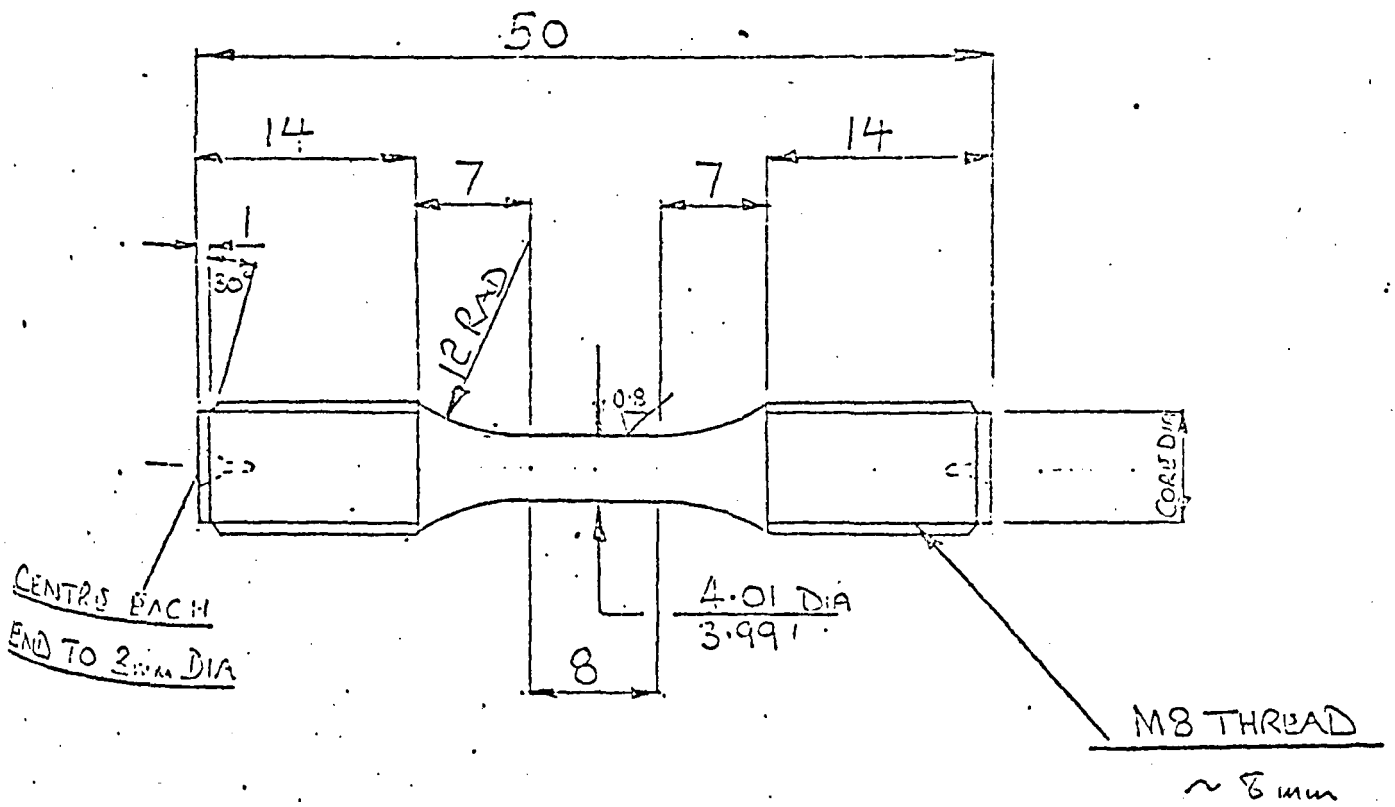


Figure 35 FG-6 fatigue specimen dimensions.

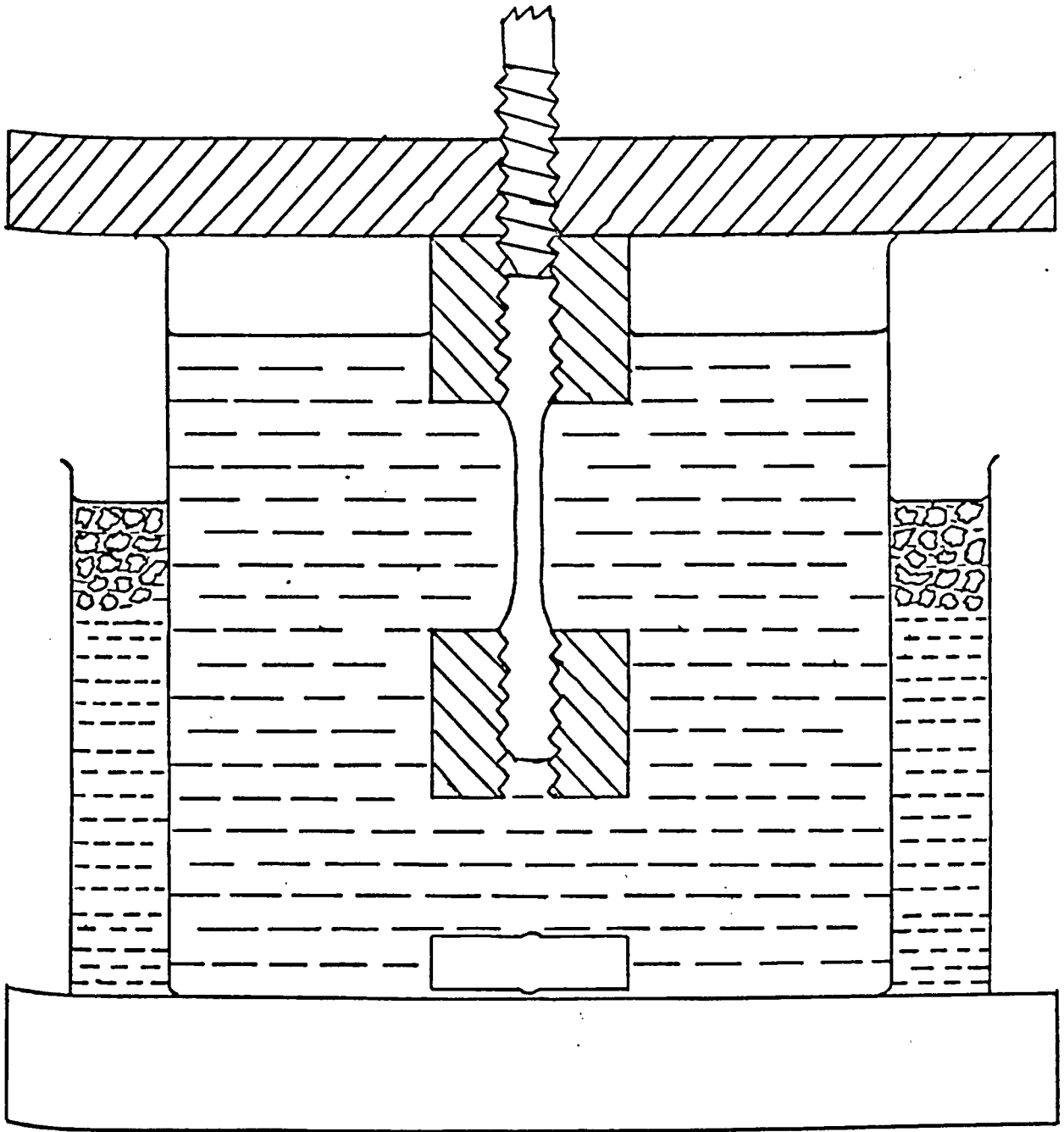


Figure 36 The electropolishing apparatus used for FG-6 specimens.

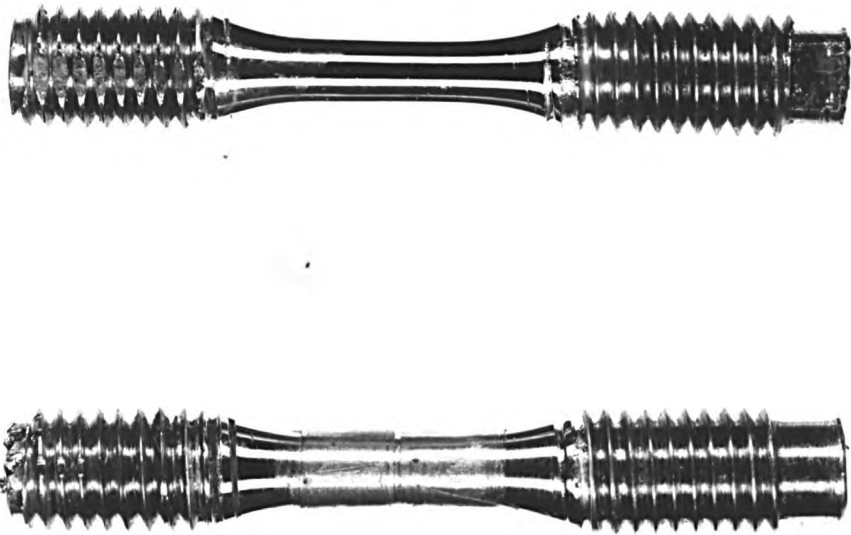


Figure 37 FG-6 specimens after electropolishing. The upper specimen shows the finish required. The lower specimen shows the strips of tape used to ensure non sliding contact.

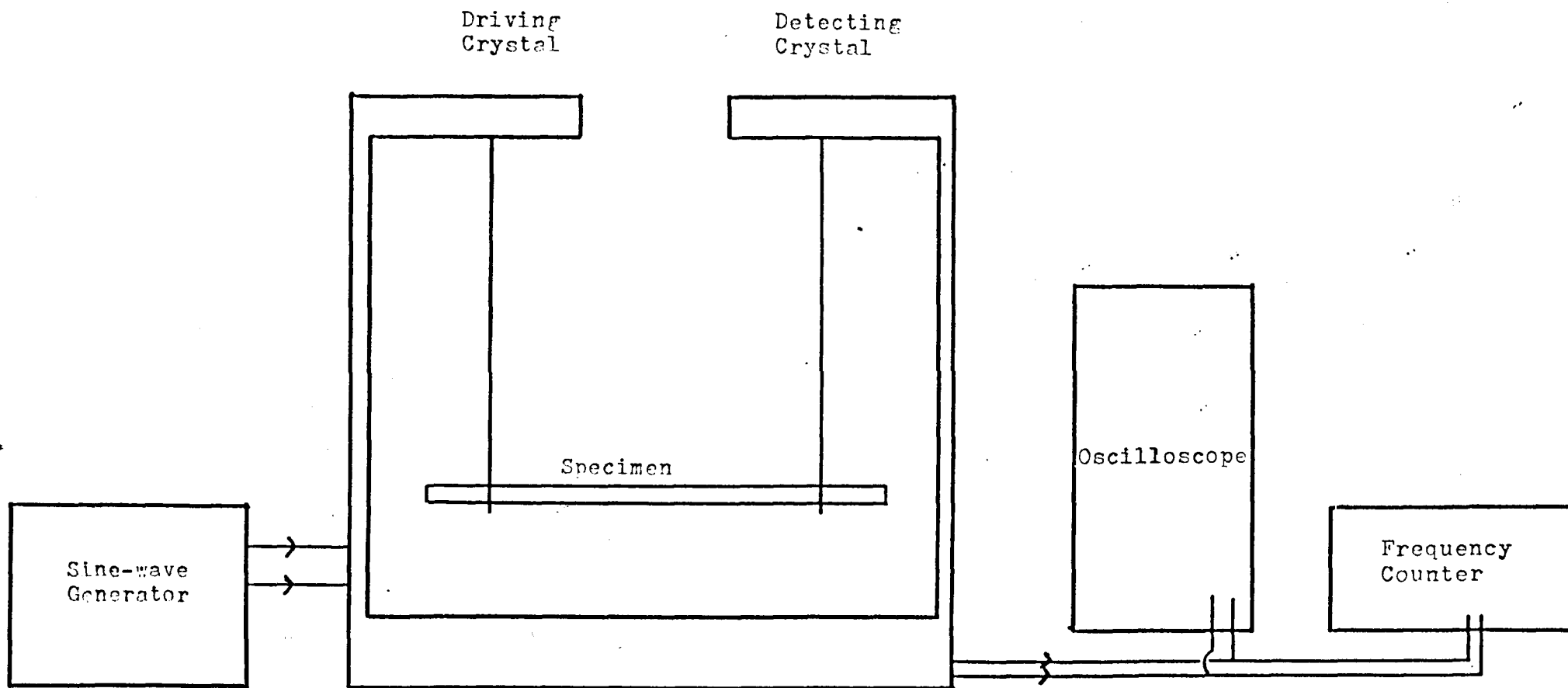
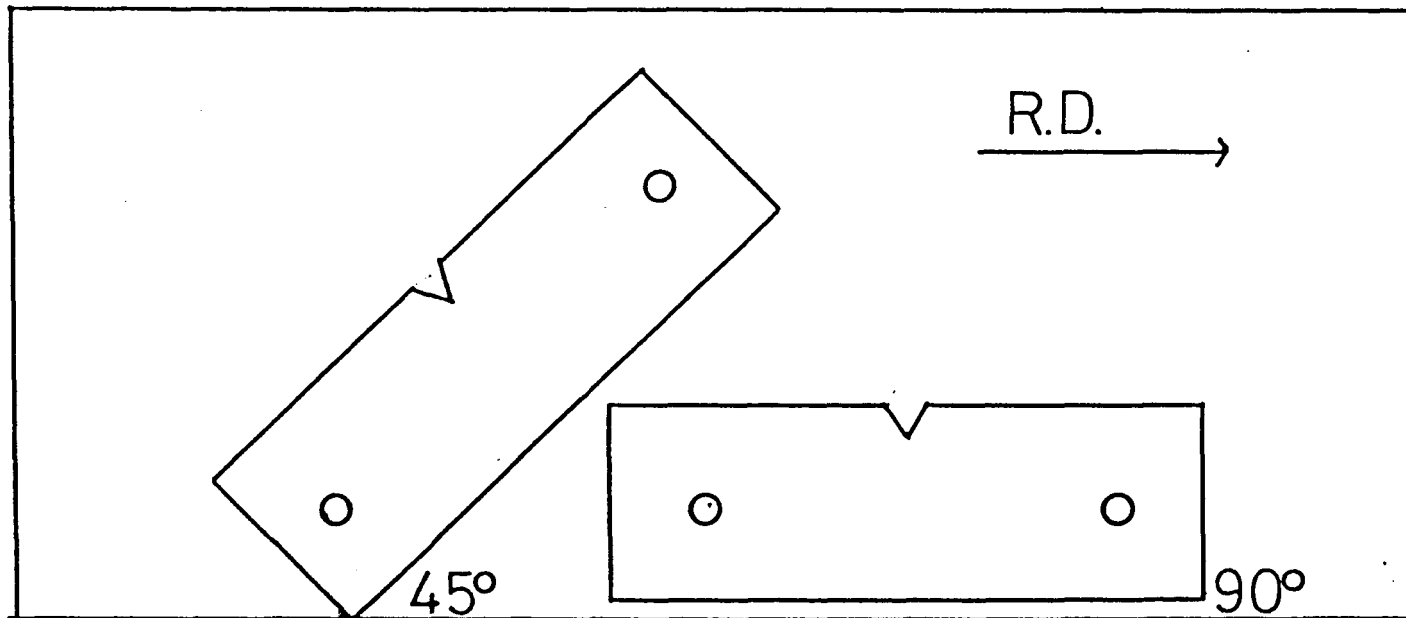


Figure 38 Schematic representation of apparatus employed to determine the resonant frequency of the copper strips in order to calculate the elastic modulus.

Figure 40

CRACK PROPAGATION SPECIMENS

Texture (001)[110] + Random
c.o.d.f. maximum 4.5
c.o.d.f. severity 0.87



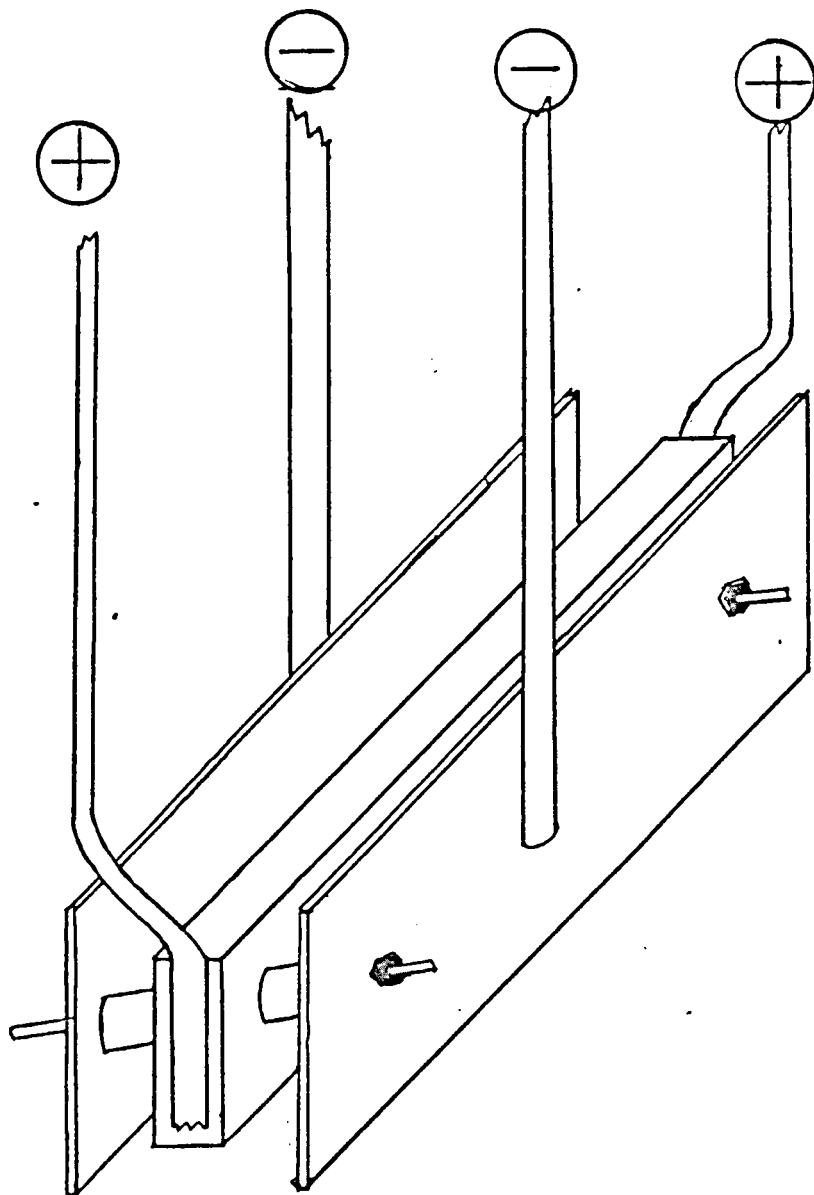


Figure 41 The electropolishing apparatus used for SEN specimens.

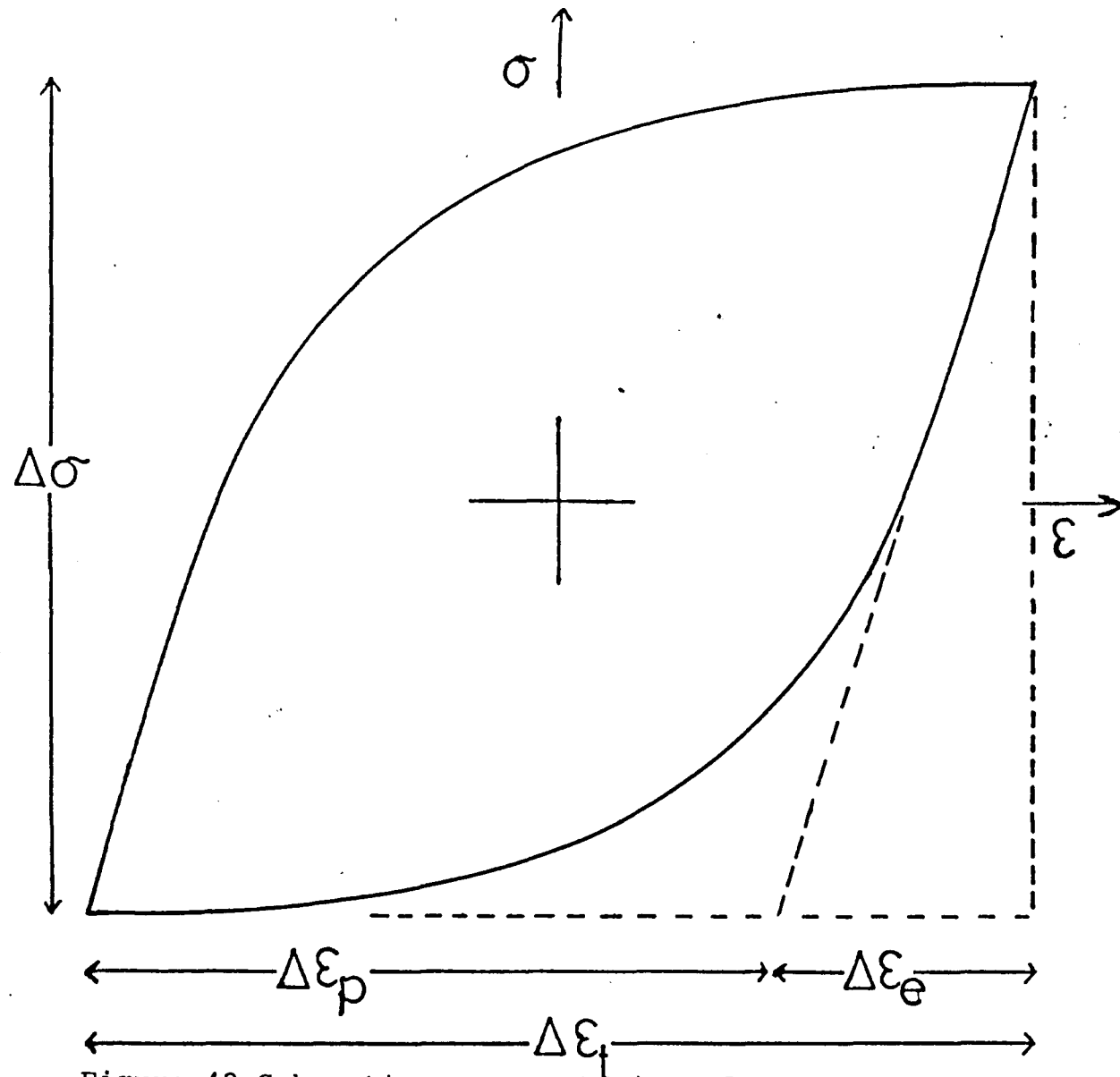
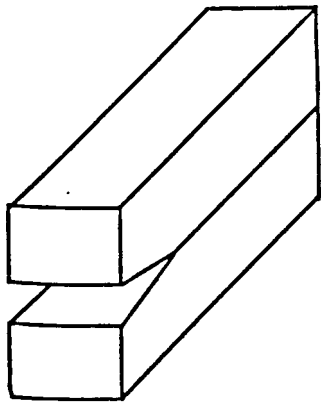
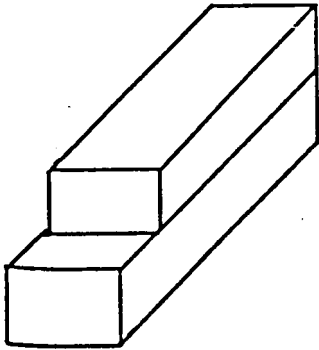


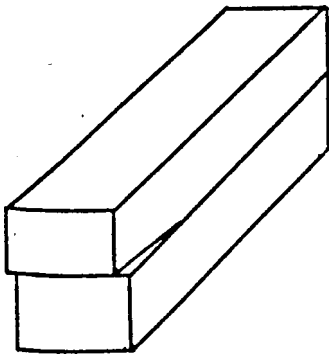
Figure 42 Schematic representation of a stress-strain hysteresis loop



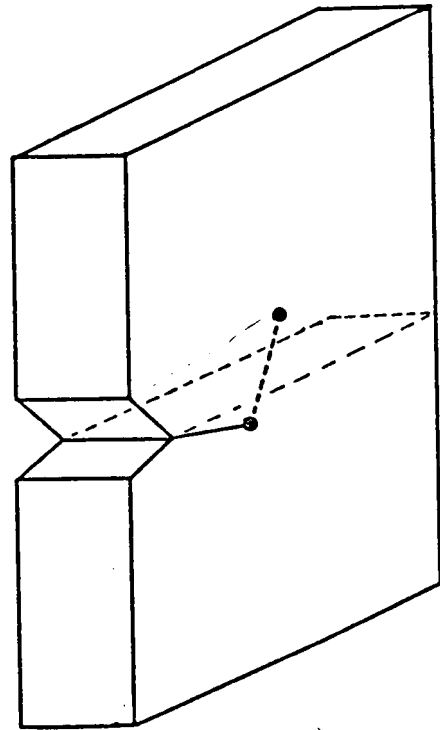
Mode 1



Mode 2



Mode 3



Complex Crack-opening
Mixed-Mode

Figure 43 Schematic representation of modes I, II and III opening of a crack, together with a schematic diagram of the complex crack orientation observed in some specimens.

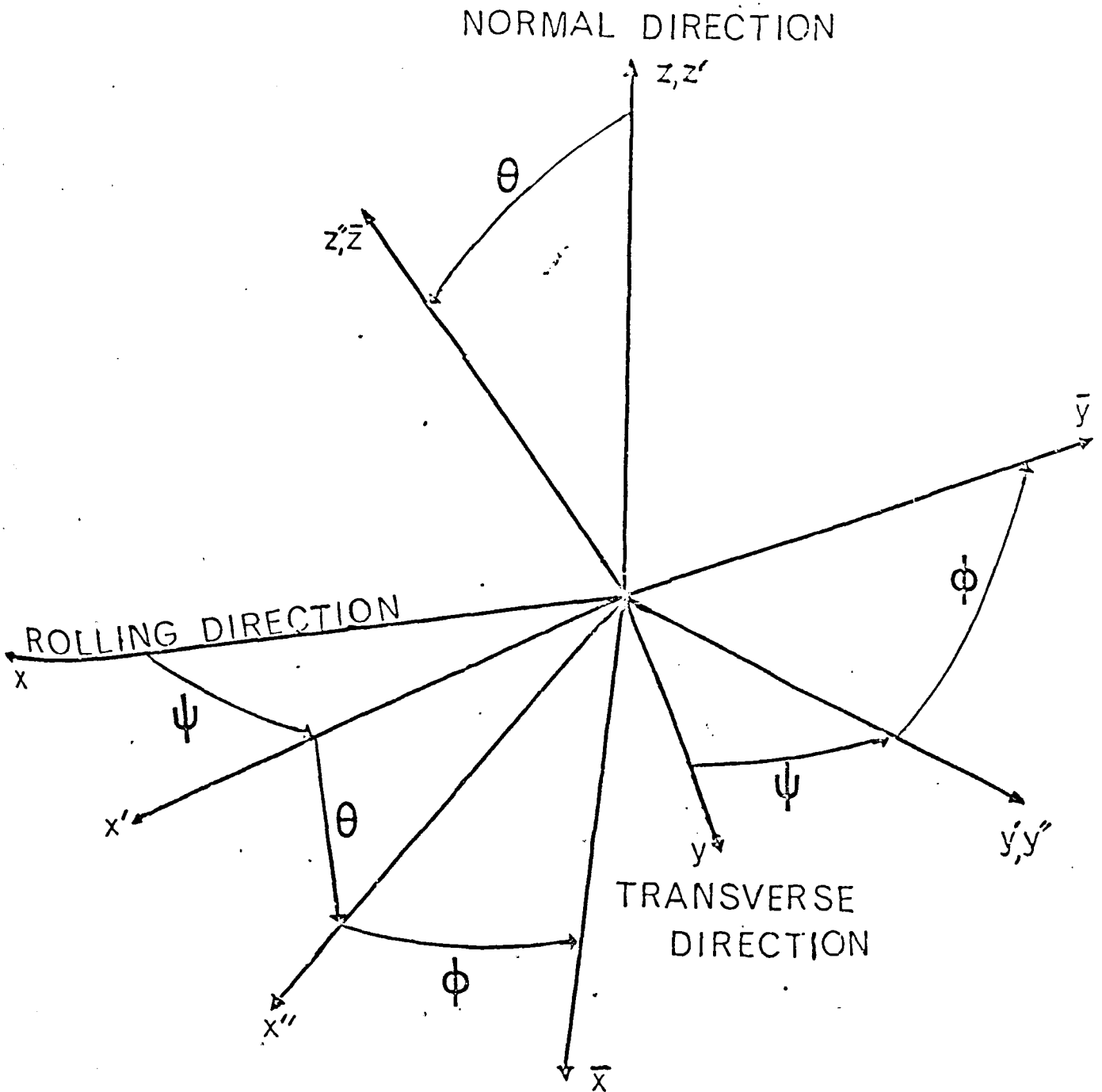


Figure 44 The set of Euler angles used in the c.o.d.f.

TEXTURE RESEARCH GROUP

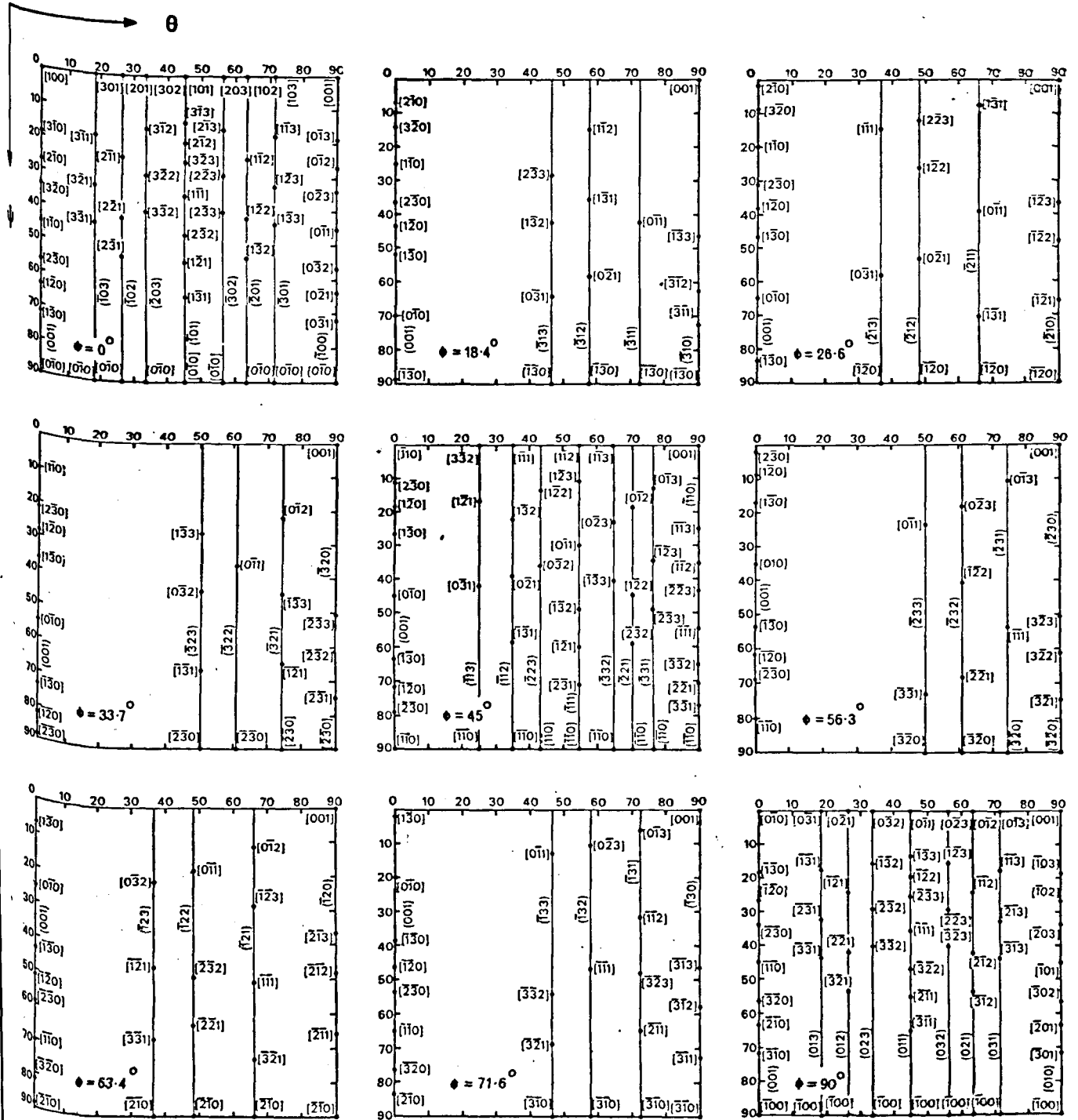


Figure 45 The index chart of ideal orientations for the c.o.d.f. (refllo).

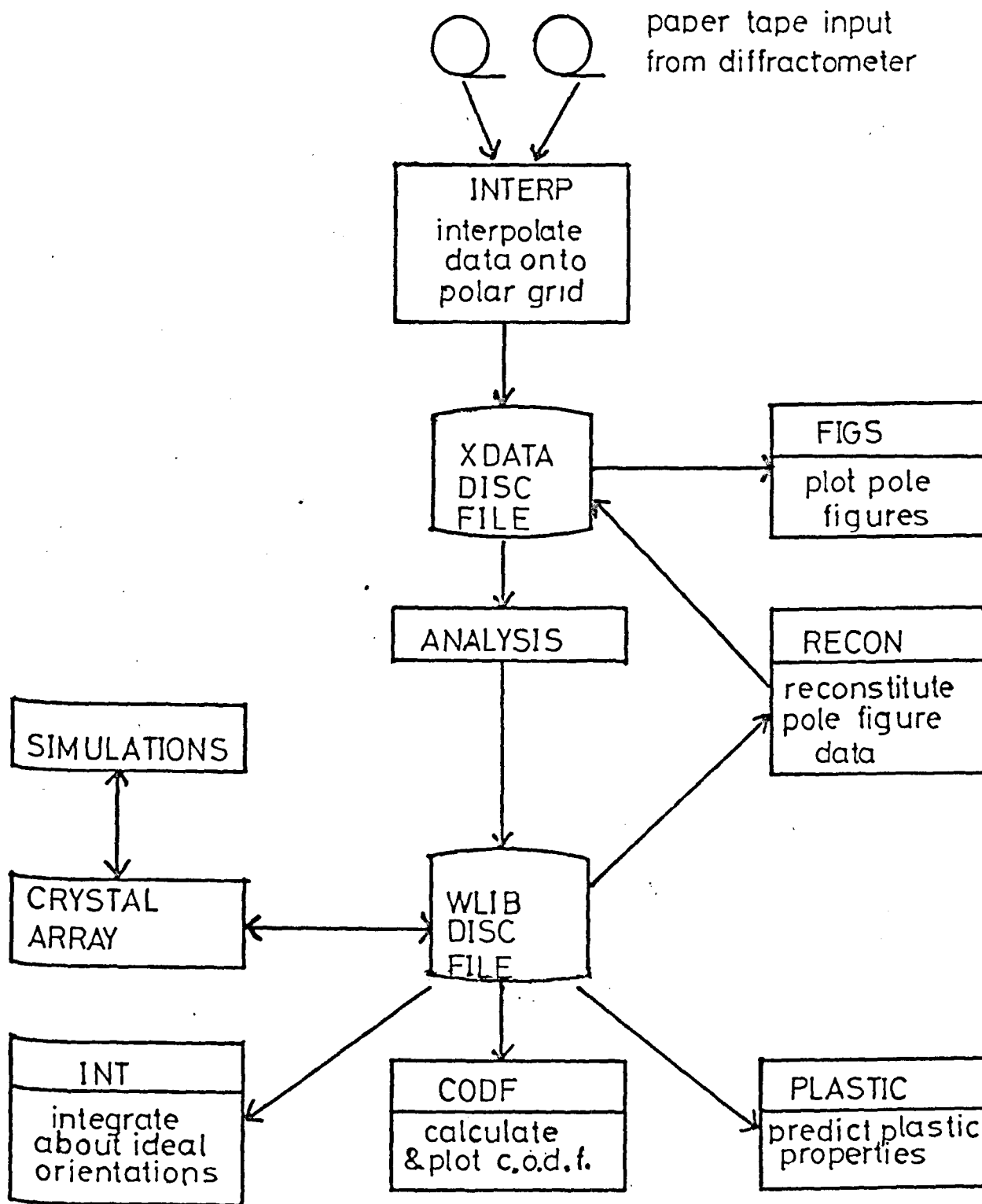


Figure 46 Diagrammatical summary of texture analysis management system.

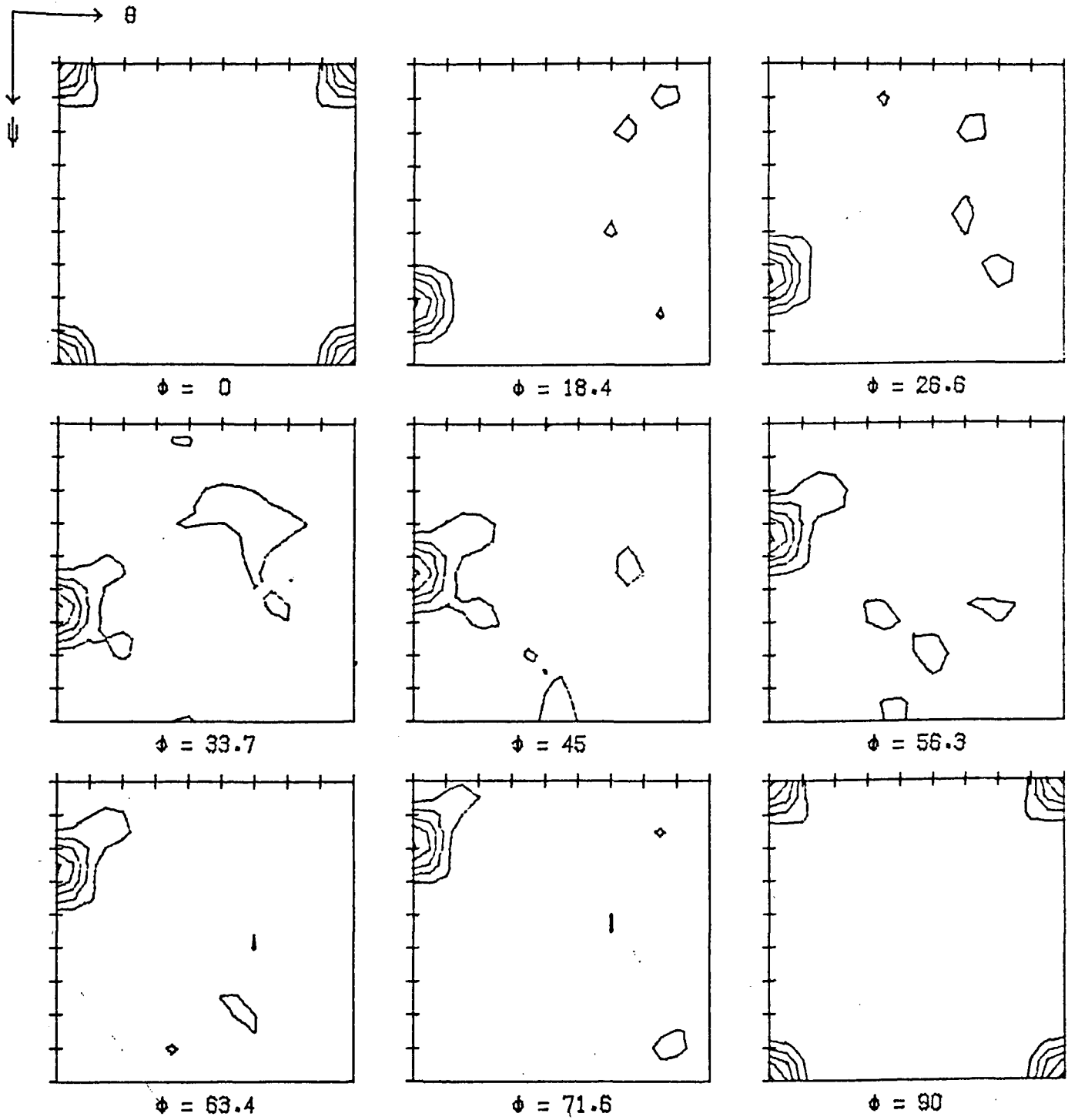


Figure 47 C.o.d.f. plot of MBCUB. Contour interval $10 \times$ random. Max. Fn. Ht. $54 \times$. Severity 5.47.

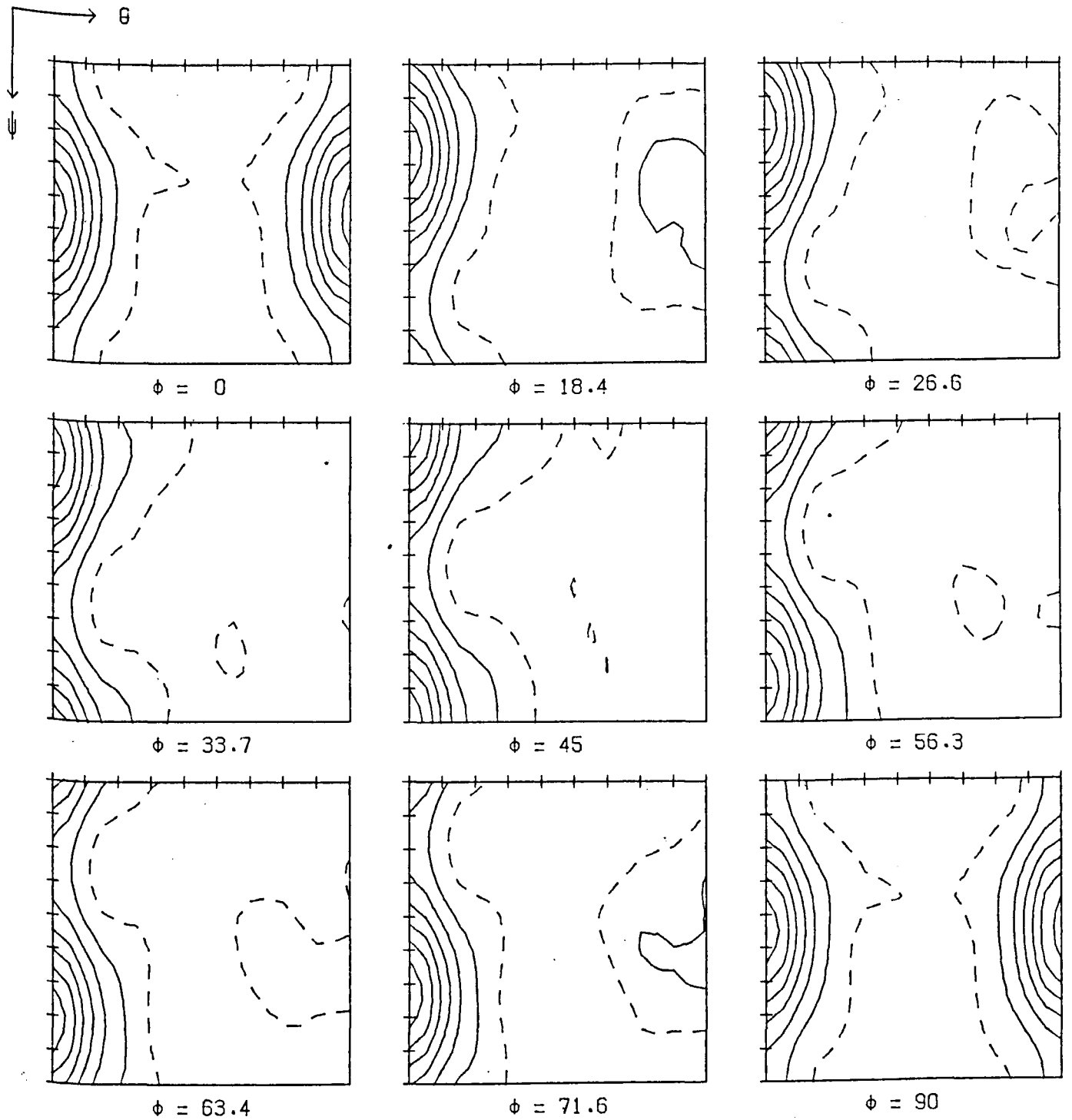


Figure 48 C.o.d.f. plot of III80. Contour interval 1x random. Max. Fn. Ht. 7.7x. Severity 0.98.

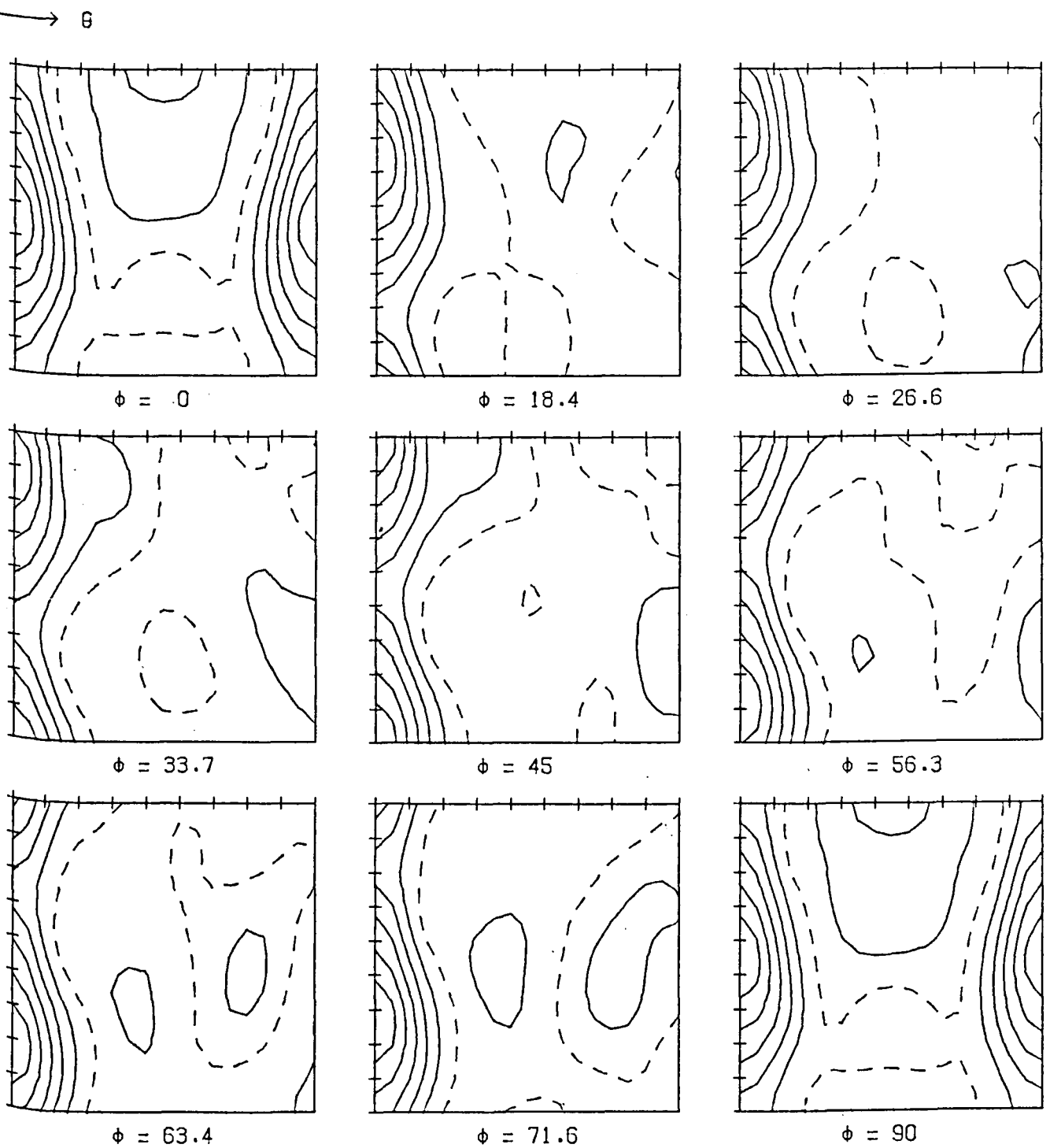


Figure 49 C.o.d.f. plot of G8585. Contour interval 0.5x random. Max. Fn. Ht. 4.0. Severity 0.52.

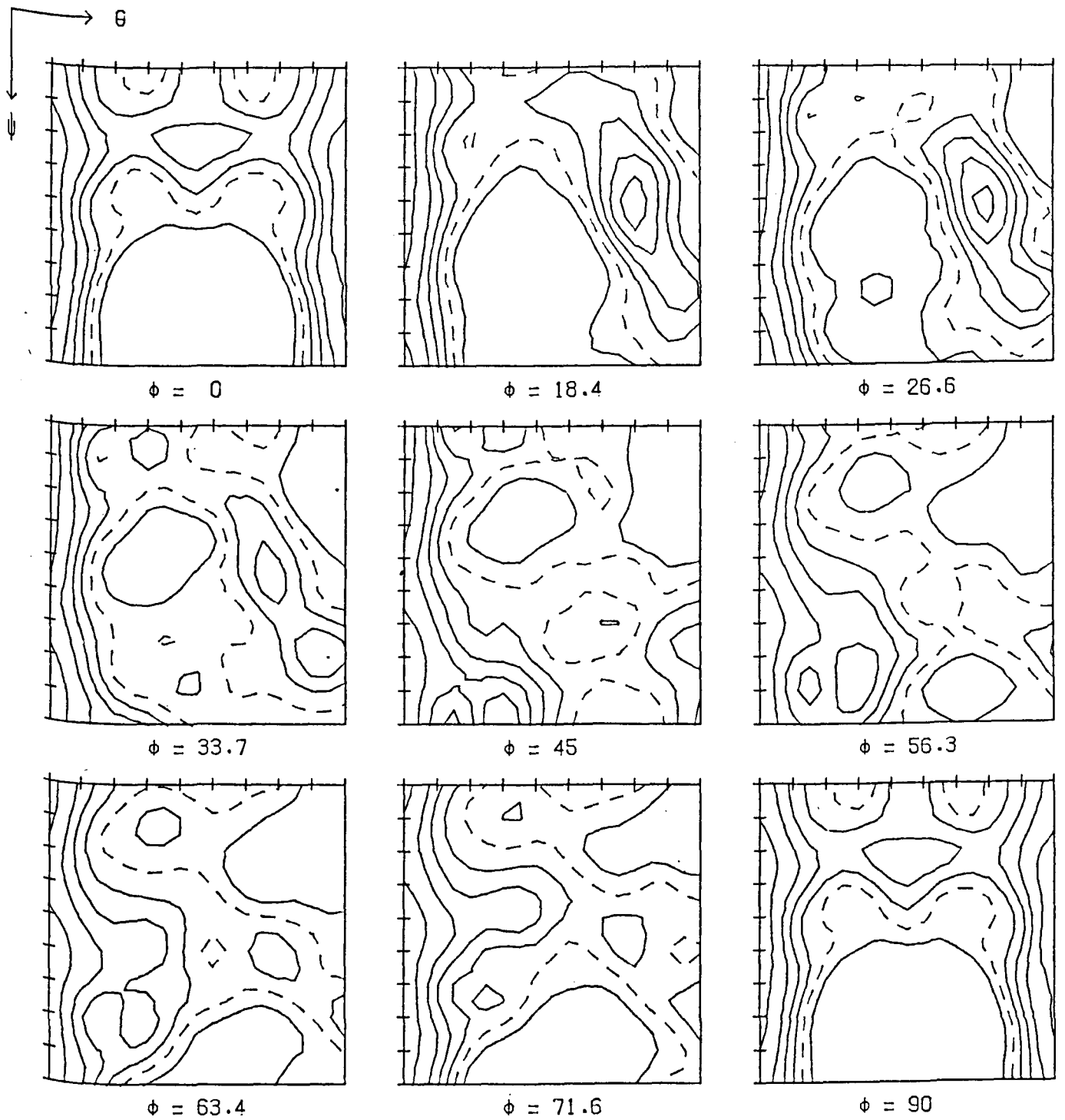


Figure 50 C.o.d.f. plot of NUJIG. Contour interval 0.5x random. Max. Fn. Ht. 3.8. Severity 0.87.

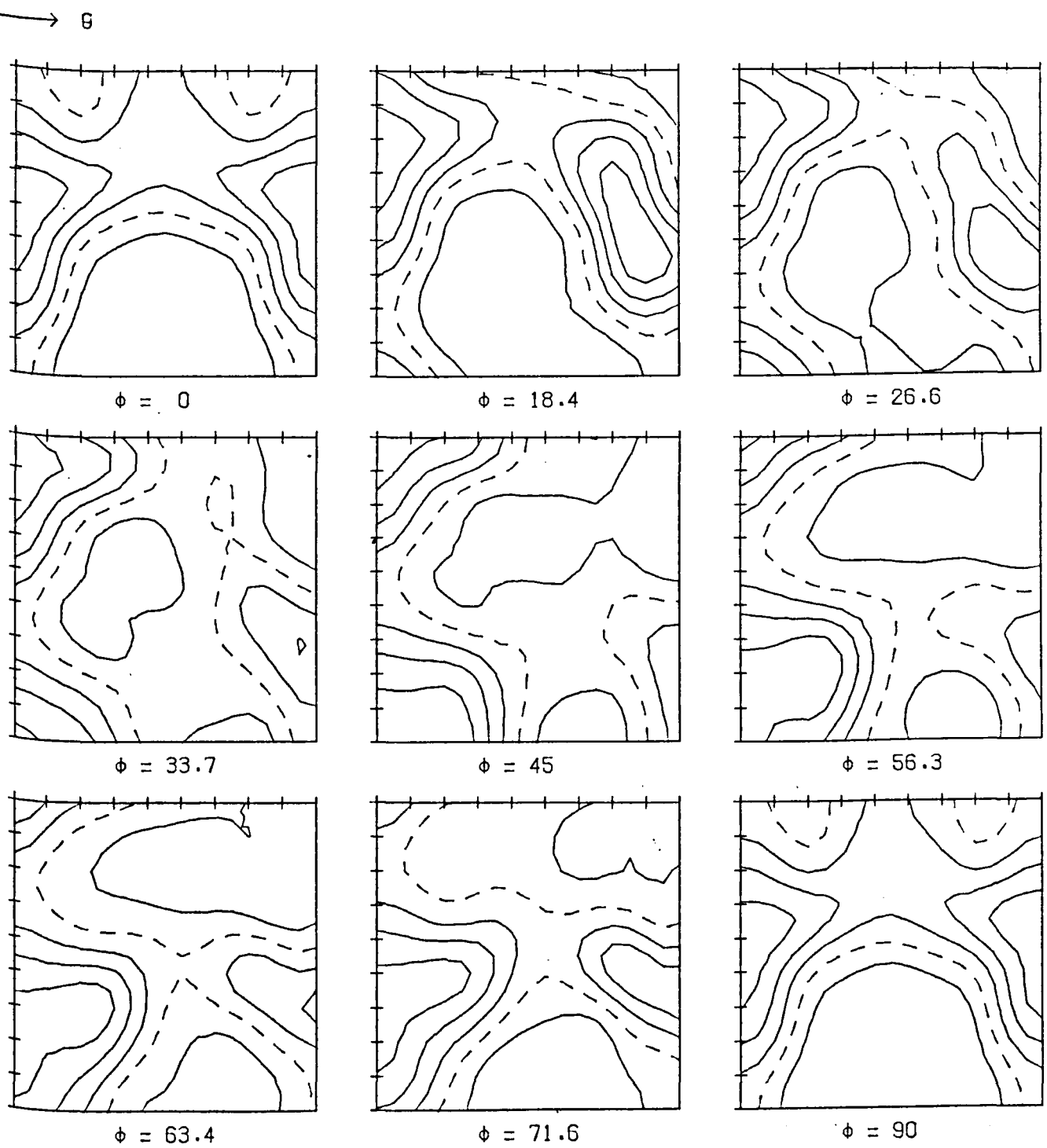


Figure 51 C.o.d.f. plot of CROCP. Contour interval 0.5x random. Max. Fn. Ht. 2.9x. Severity 0.72.

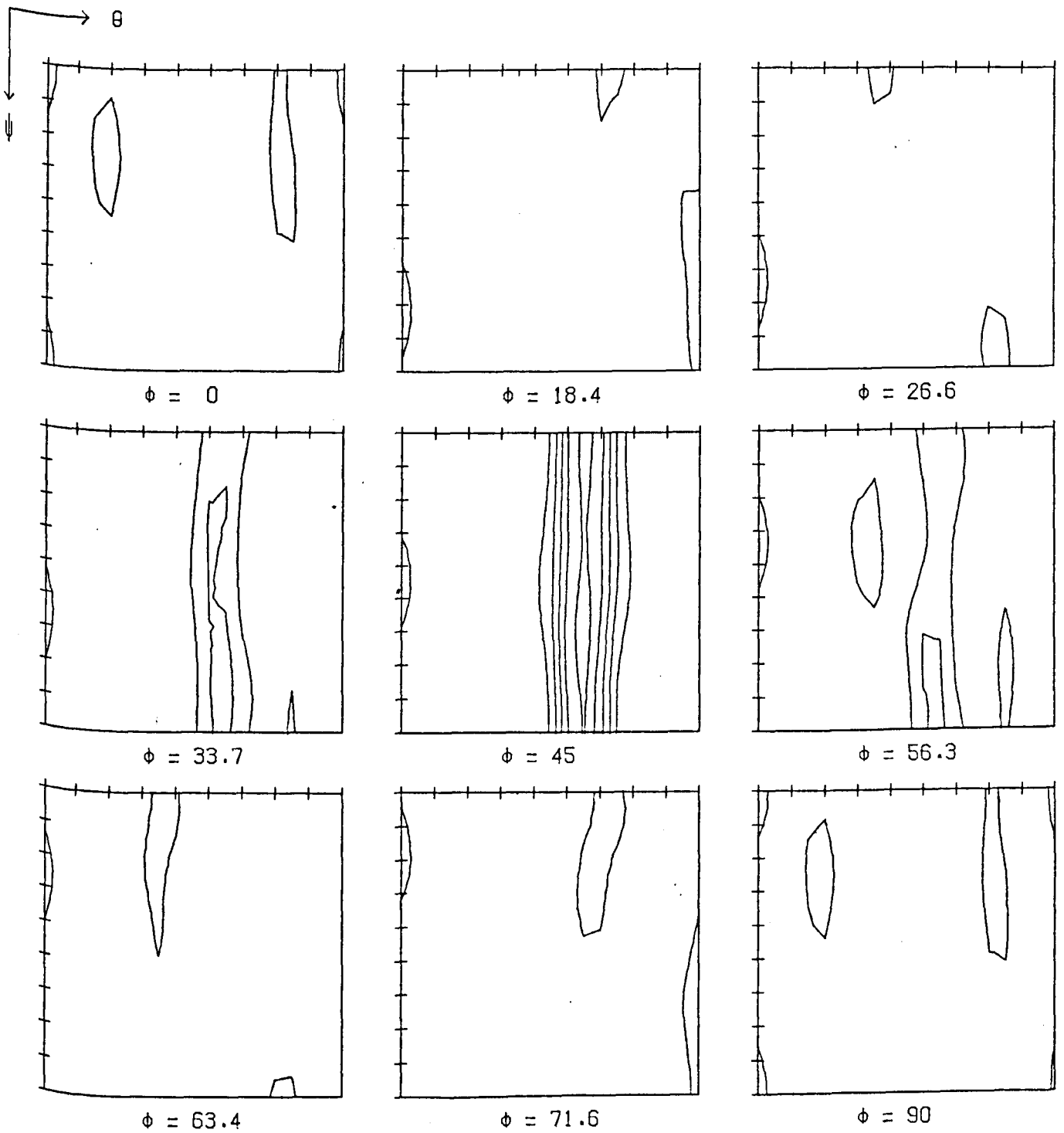


Figure 52 C.o.d.f. plot of FAREN. Contour interval 2x random. Max. Fn. Ht. 11.3x. Severity 1.68.

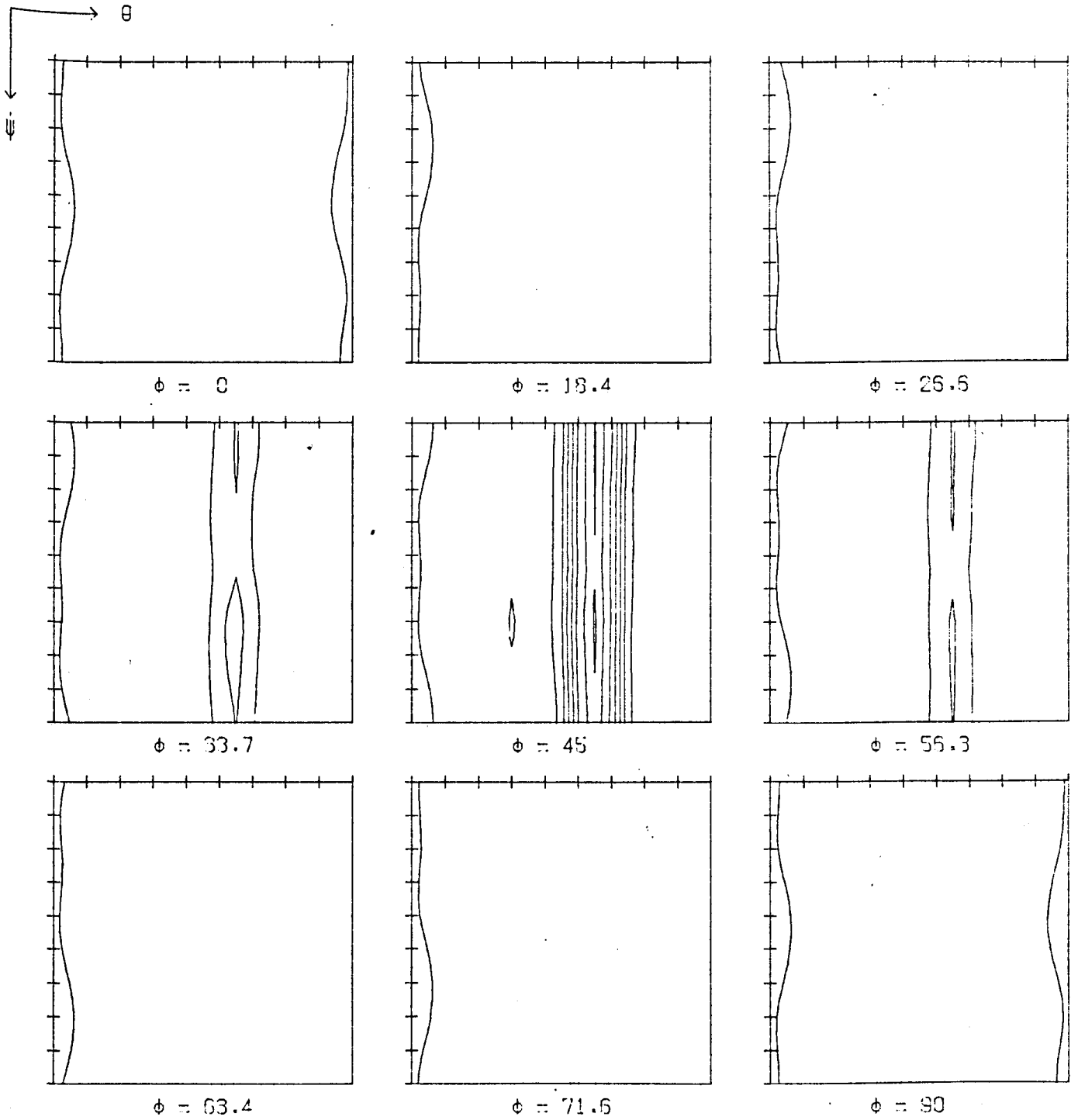


Figure 53 C.o.d.f. plot of FBREN. Contour interval
 2x random. Max.Fn.Ht. 14.3x. Severity 1.97

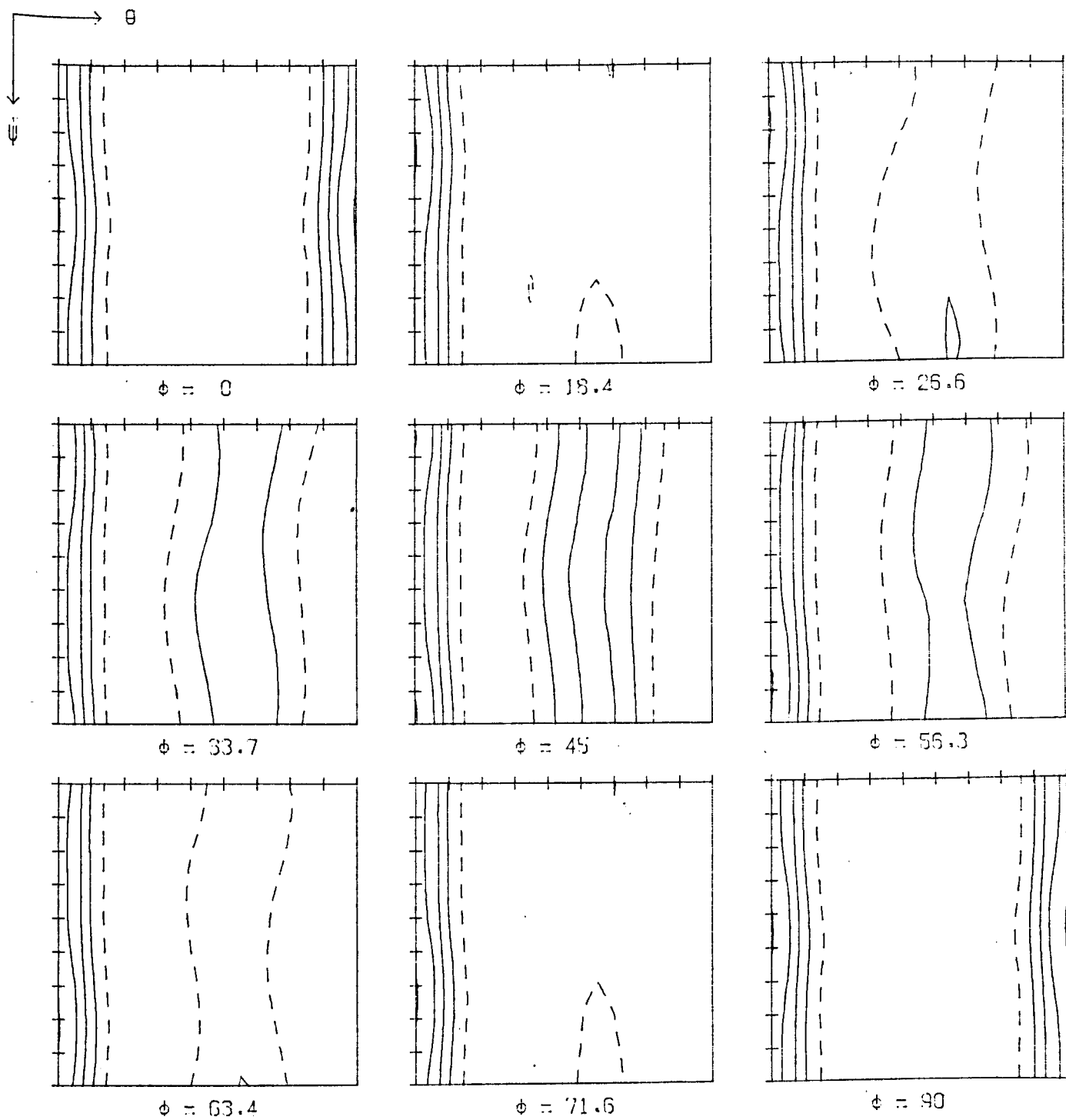


Figure 54 C.o.d.f. plot of B3500. Contour interval 0.2x random. Max. Fn. Ht. 5.lx .Severity 0.90.

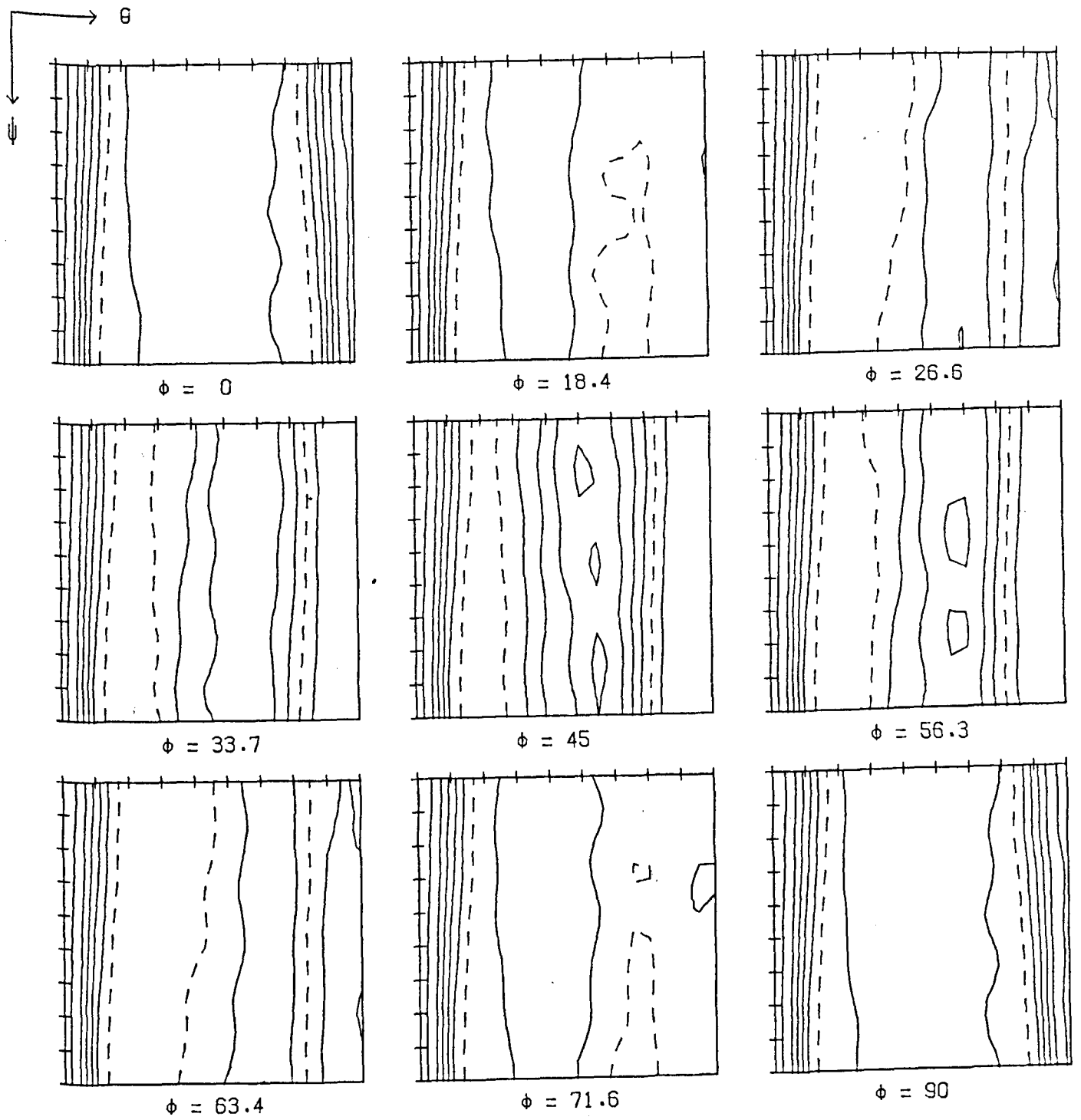


Figure 55 C.o.d.f. plot of A3500. Contour interval 0.5x random. Max. Fn. Ht. 3.9x. Severity 0.85.

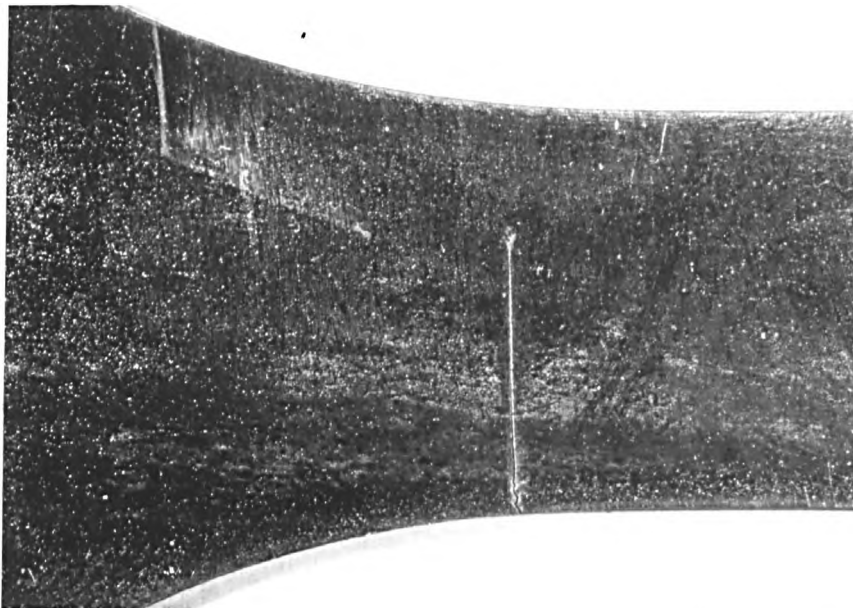
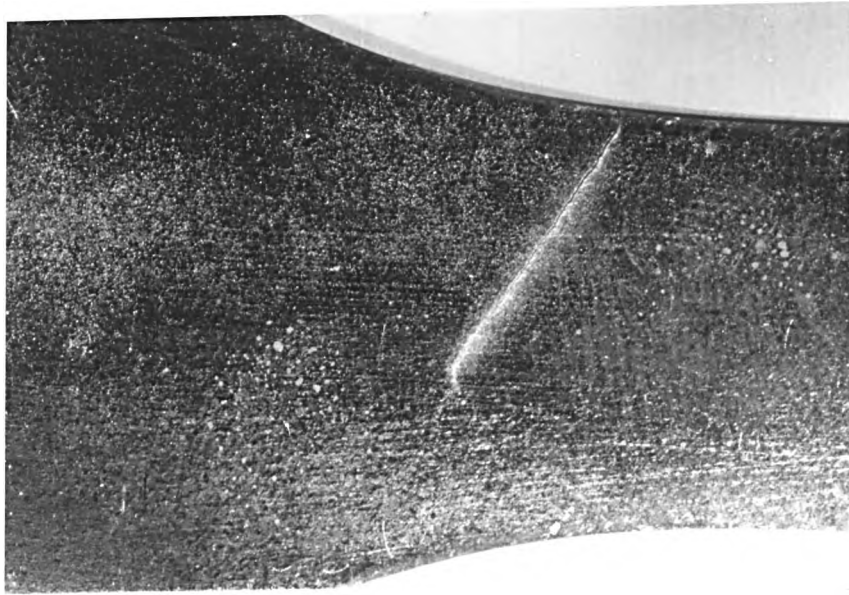


Figure 56 Low magnification optical micrographs.
a) Crack orientation in a 45 specimen of MBCUB
b) Crack orientation in a 90 specimen of MBCUB

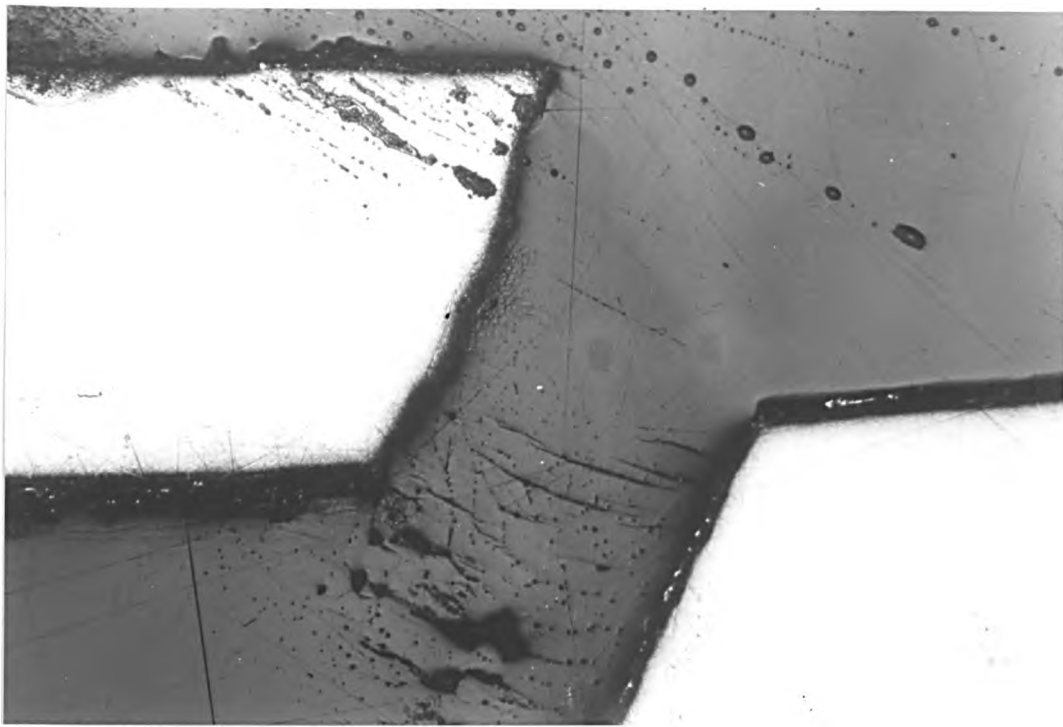


Figure 57 Low magnification optical micrograph of through-thickness section of 45 specimen of MBCUB.

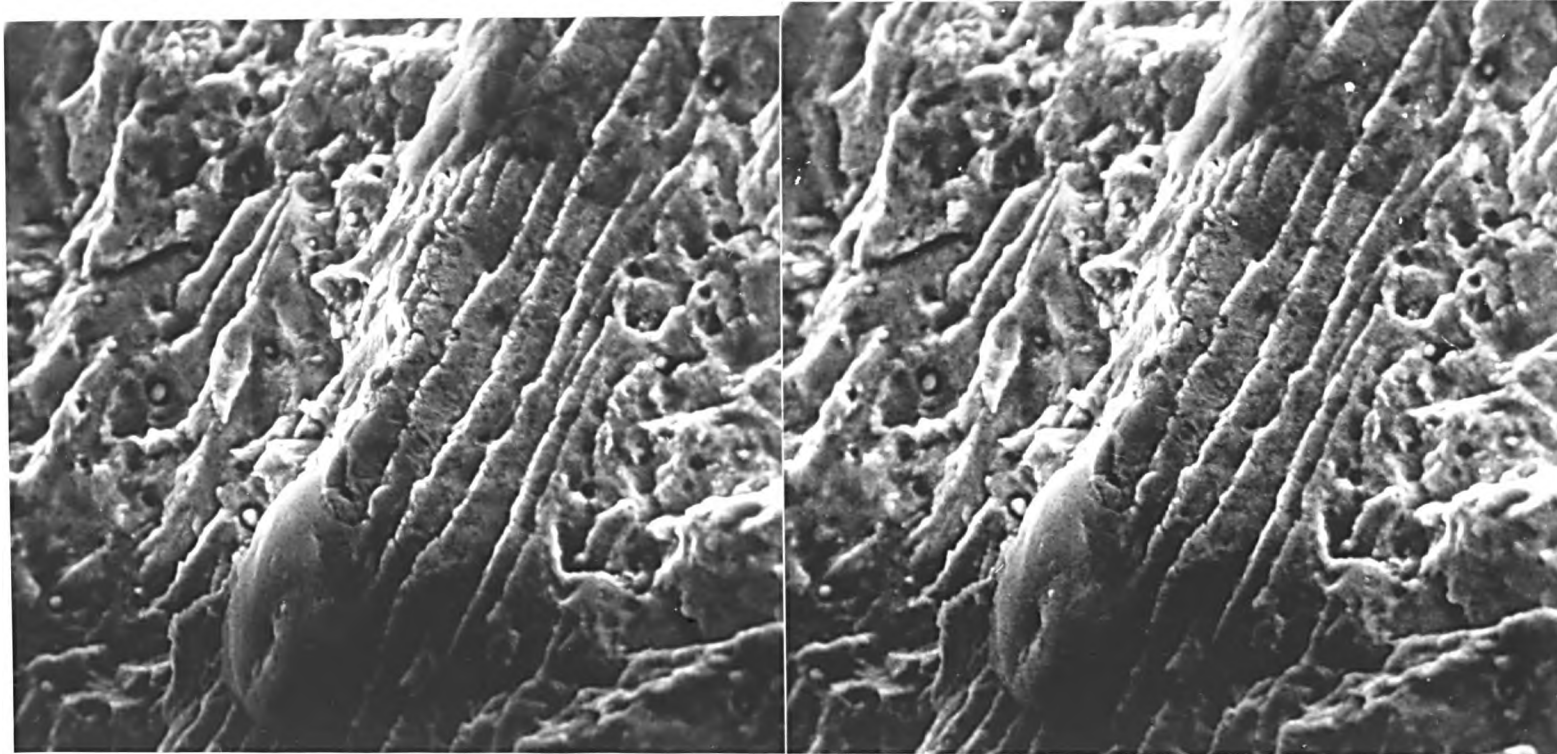


Figure 58 Stereopair SEM micrograph of fatigue fracture surface of a 45 specimen of MBCUB.

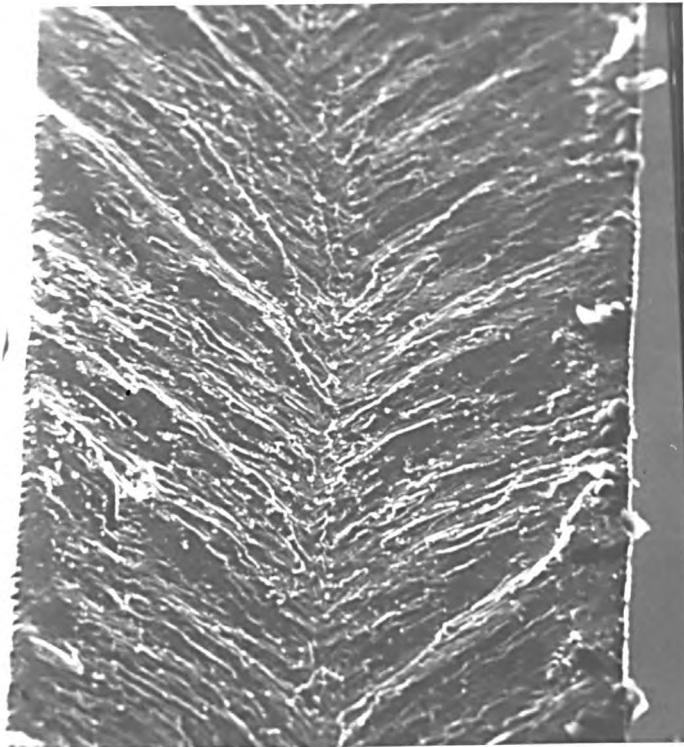


Figure 59 SEM micrograph of typical fatigue fracture surface in a 90 specimen of MBCUB. Magnification 200x.

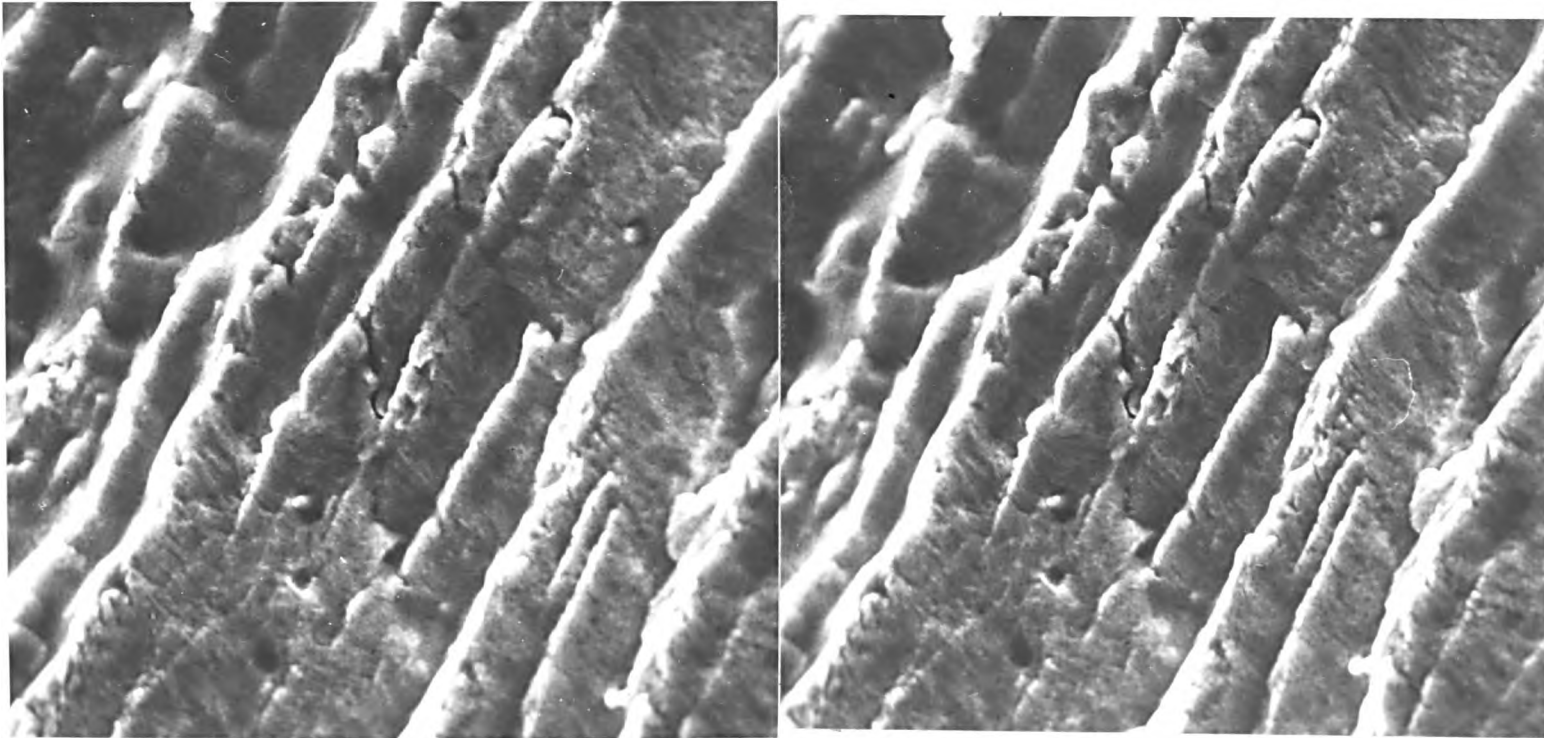


Figure 60 Stereopair SEM micrograph of 'chevron' markings showing crack propagation on two different planes. Magnification 200x.

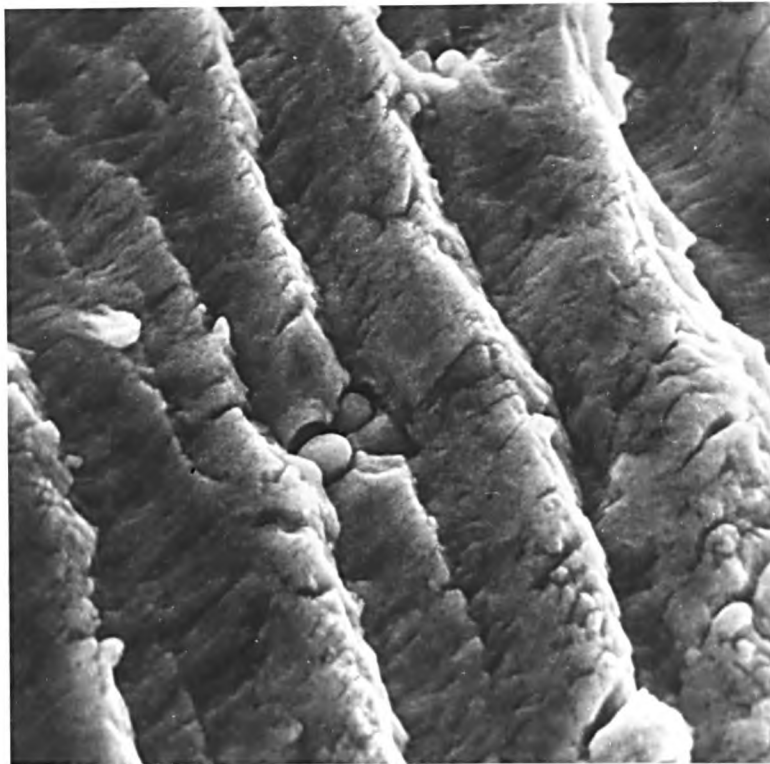


Figure 61 SEM micrograph showing that striations are continuous across 'chevron' markings. Magnification 1000x.

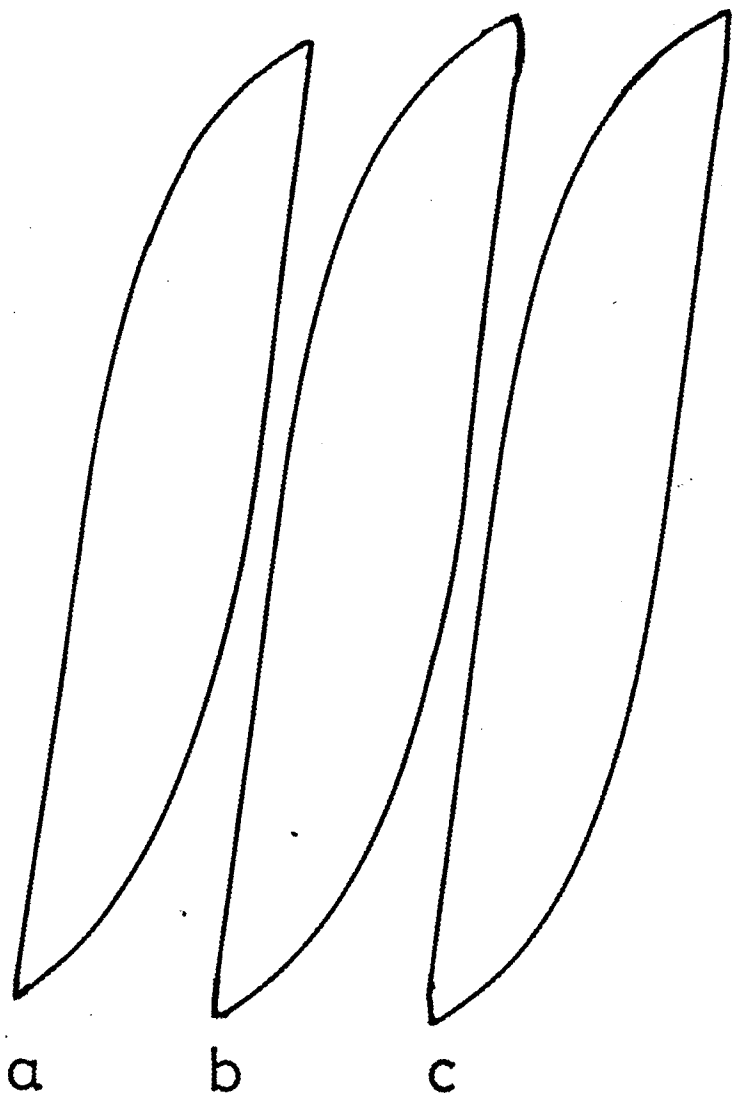
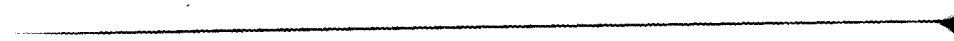


Figure 62 The effect of waveform and frequency on the shape of the stress-strain hysteresis loop. (a) Sine-wave, 0.1Hz. (b) Sine-wave, 1Hz. (c) Triangular-wave, 0.1Hz.



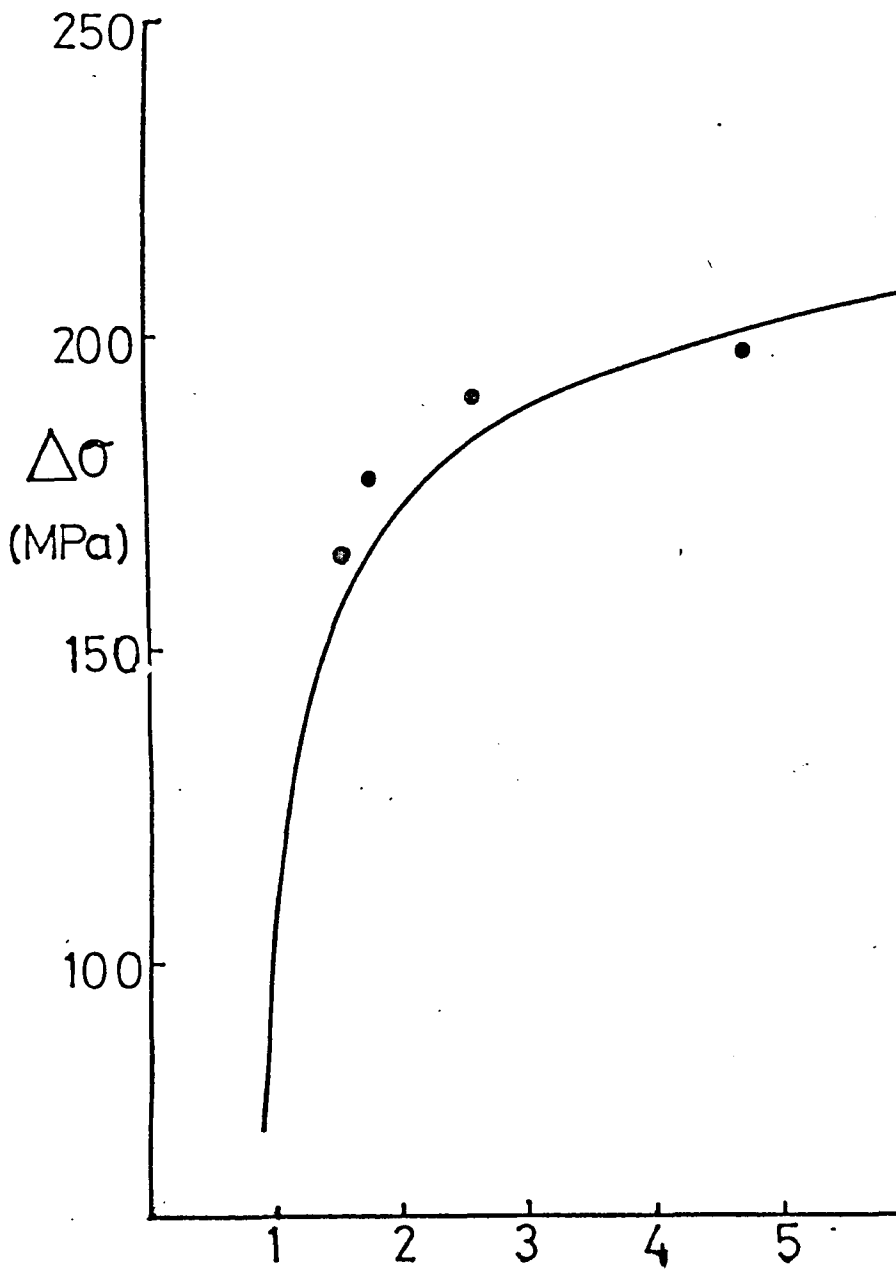
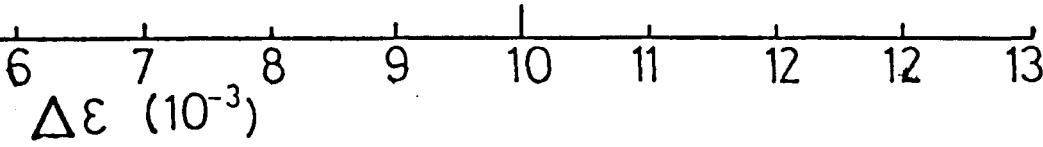




Figure 63 Cyclic stress-strain
curve for I8045



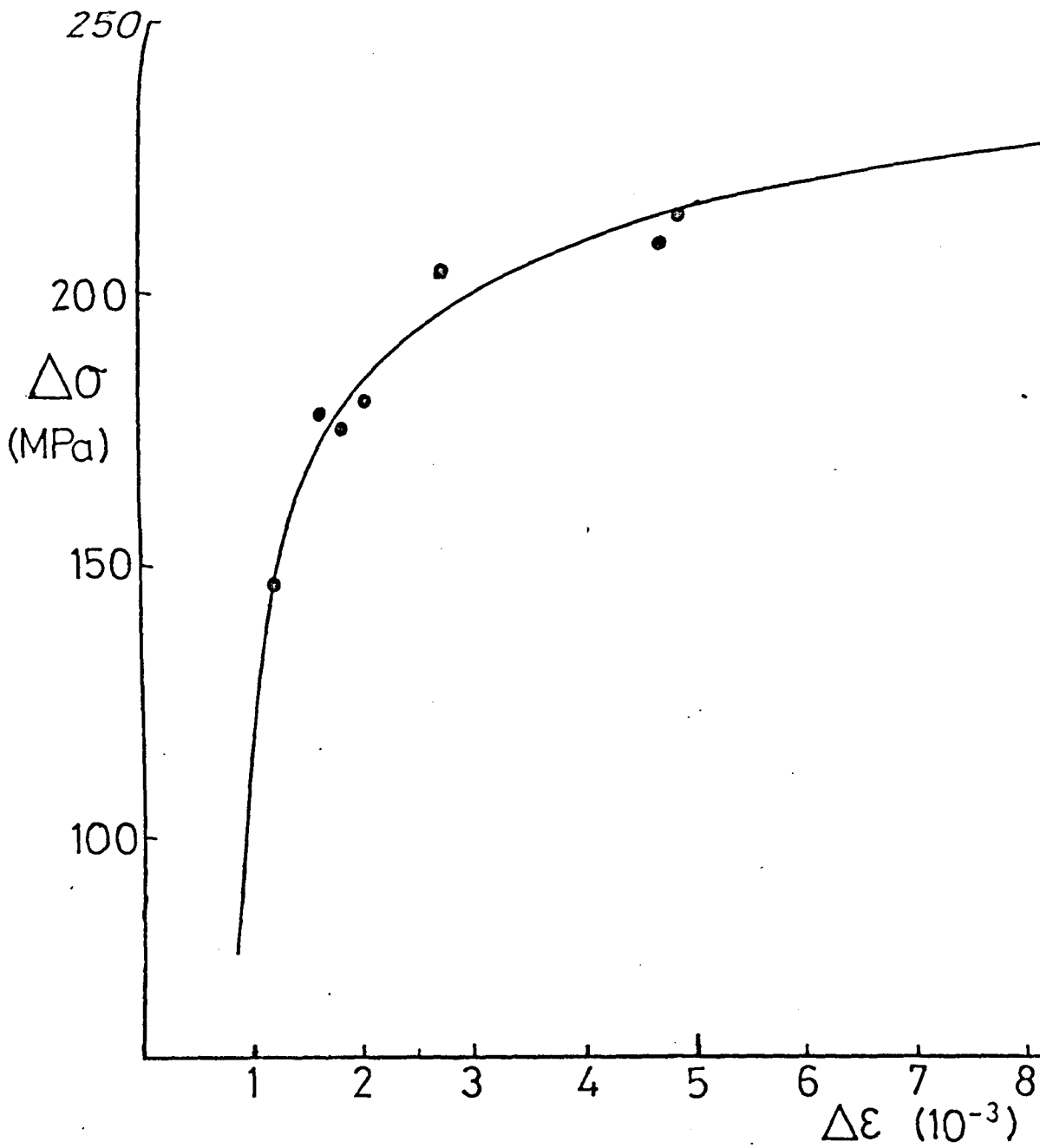
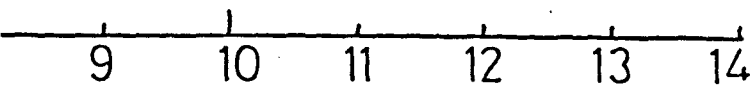
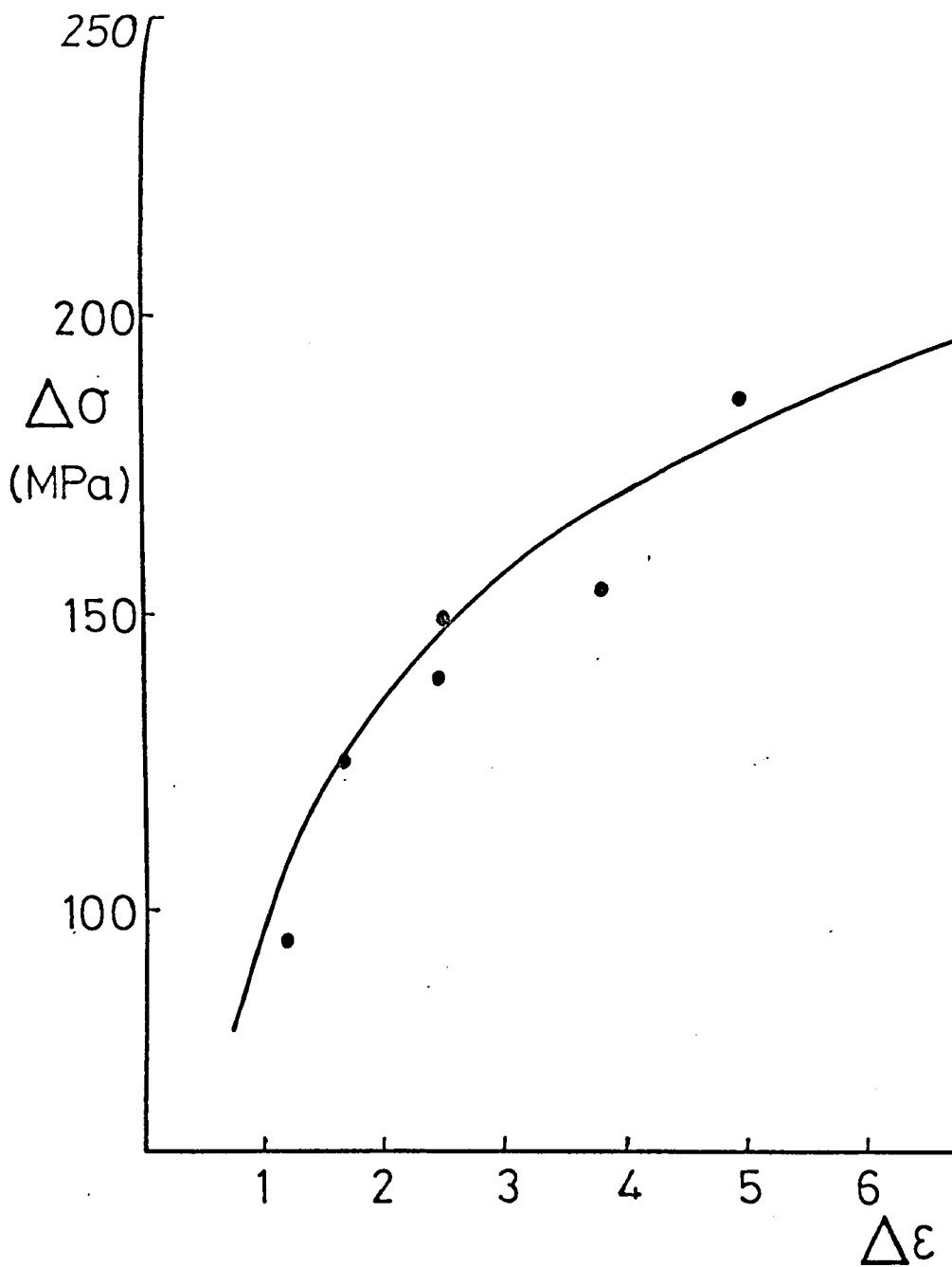




Figure 64 Cyclic stress-strain curve
for I8090.





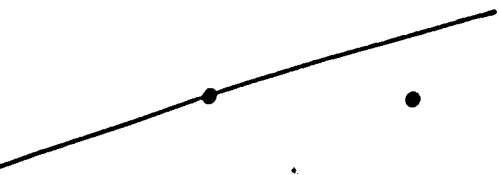
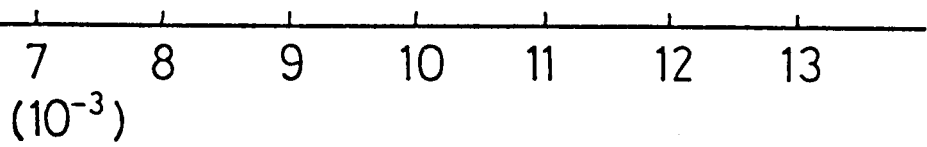
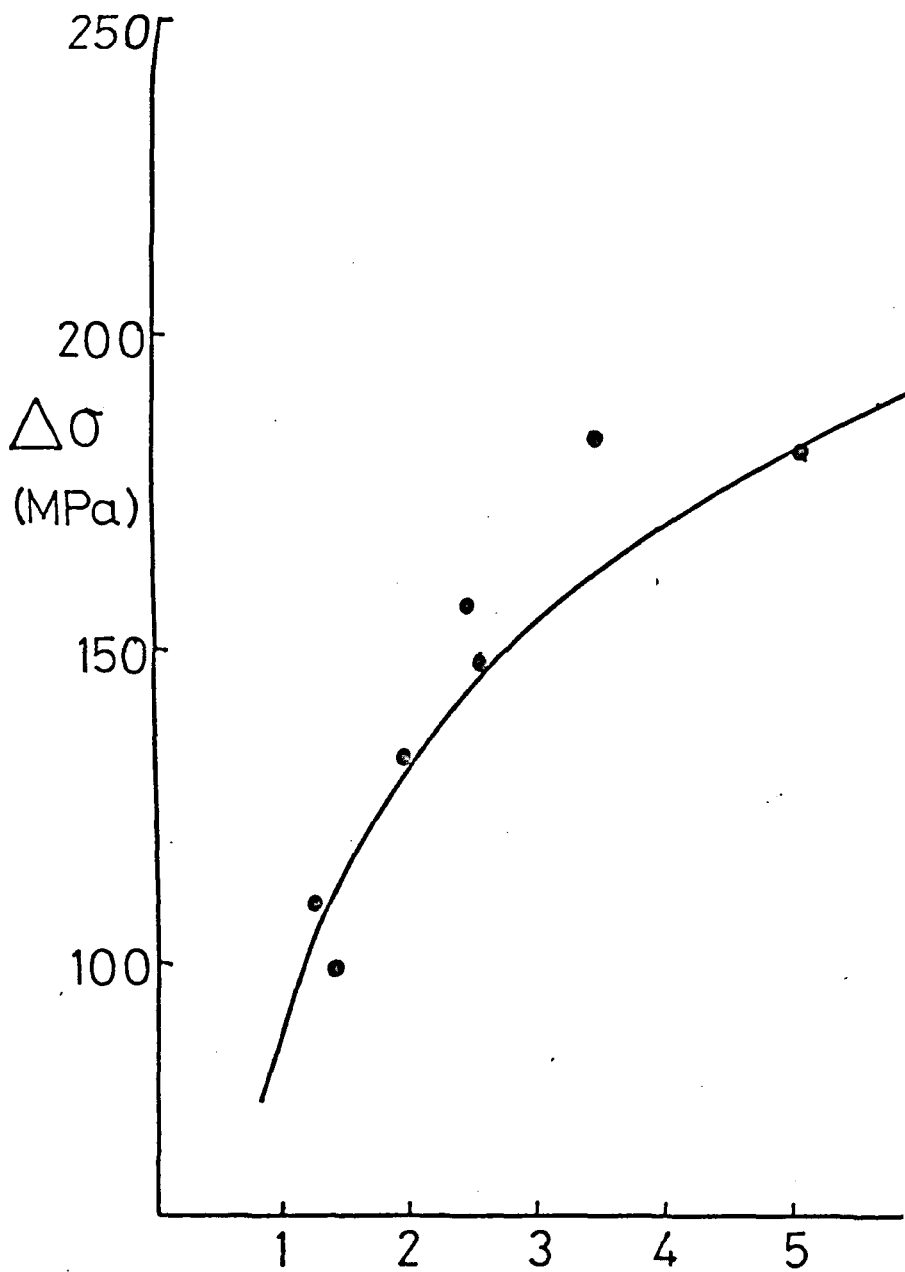


Figure 65 Cyclic stress-strain curve
for G8545.





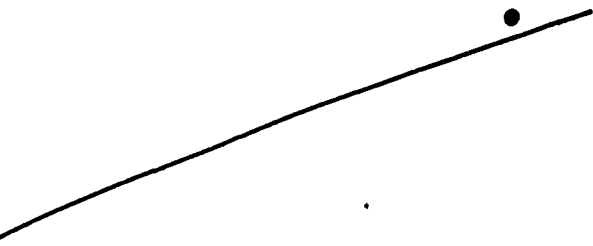
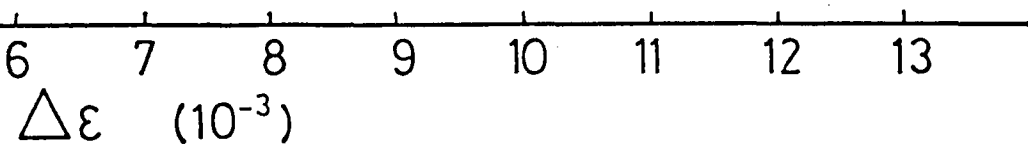


Figure 66 Cyclic stress-strain curve
for G8590.



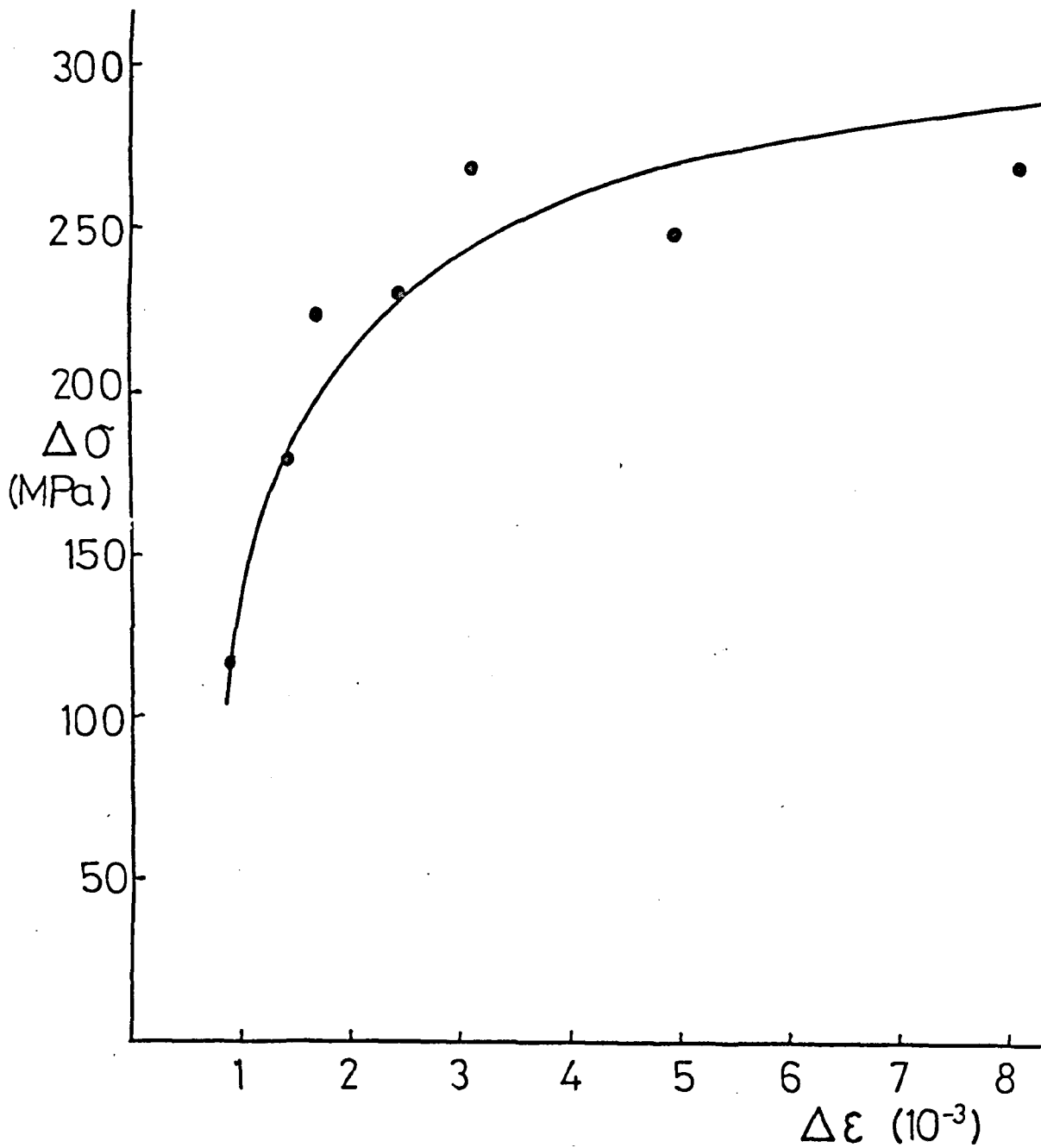
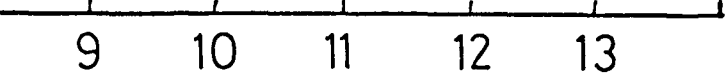




Figure 67 Cyclic stress-strain curve
for FAREN.



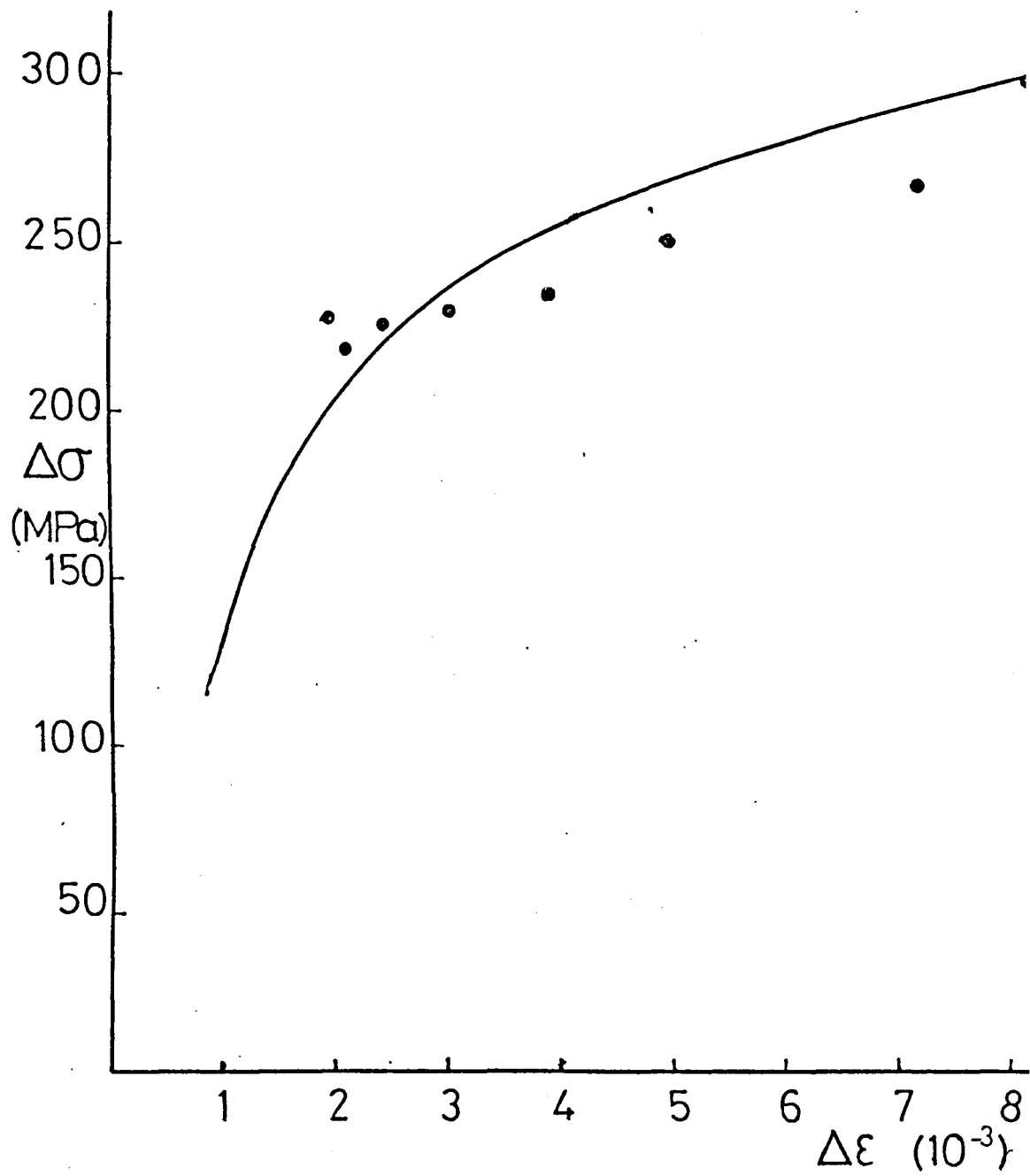
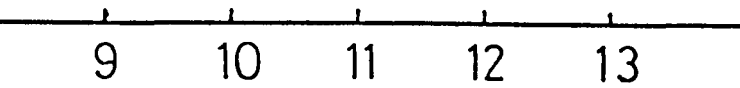




Figure 68 Cyclic stress-strain curve
for FBREN.



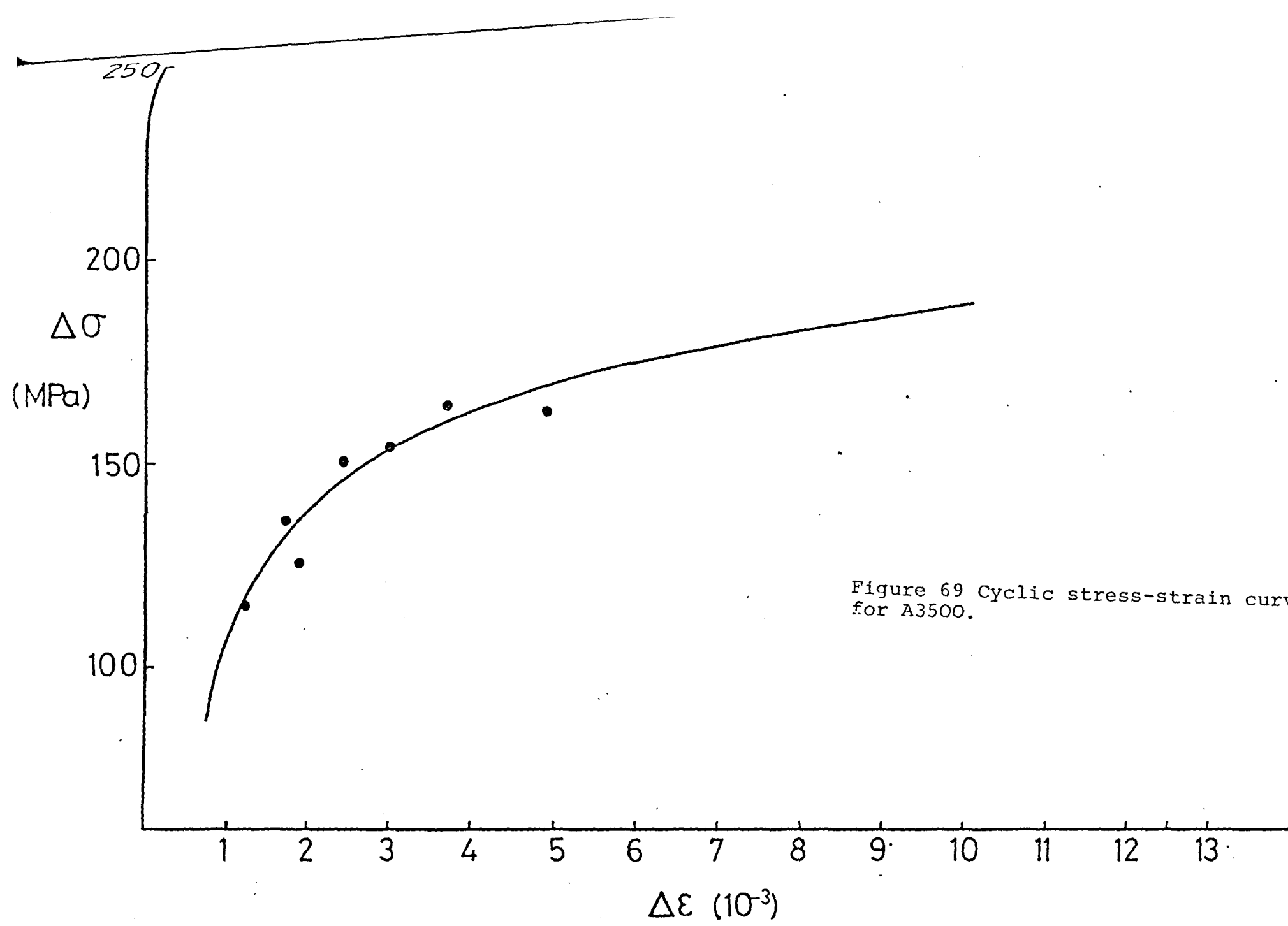
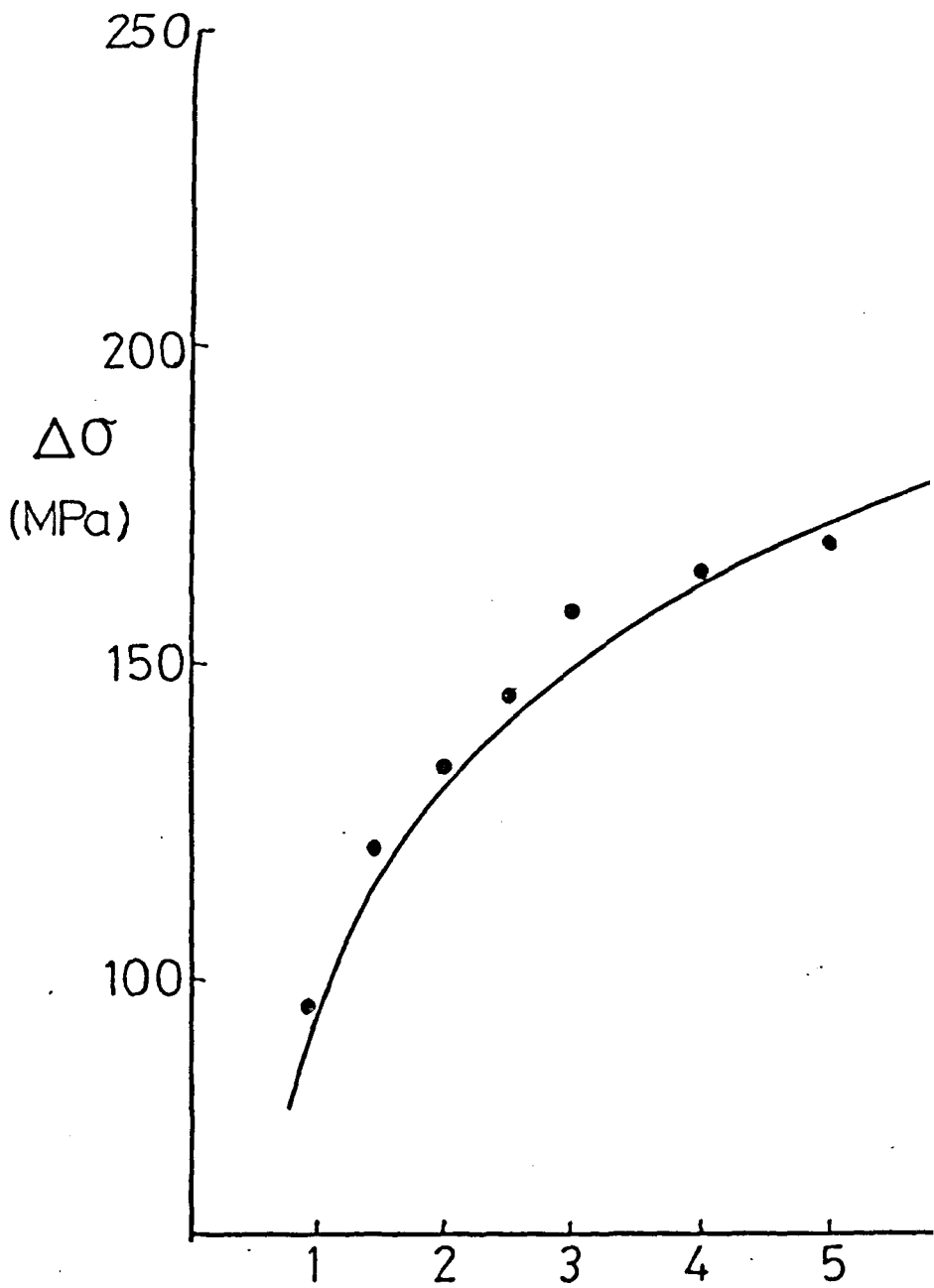


Figure 69 Cyclic stress-strain curve for A3500.



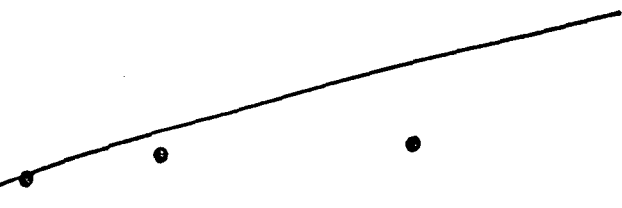
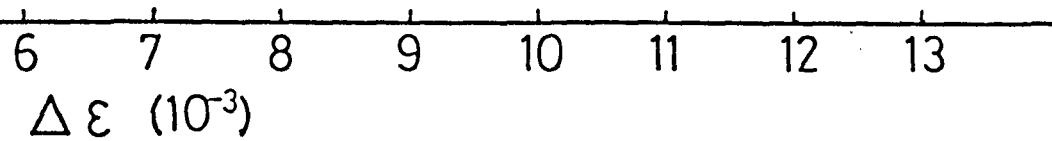


Figure 70 Cyclic stress-strain curve
for B3500.



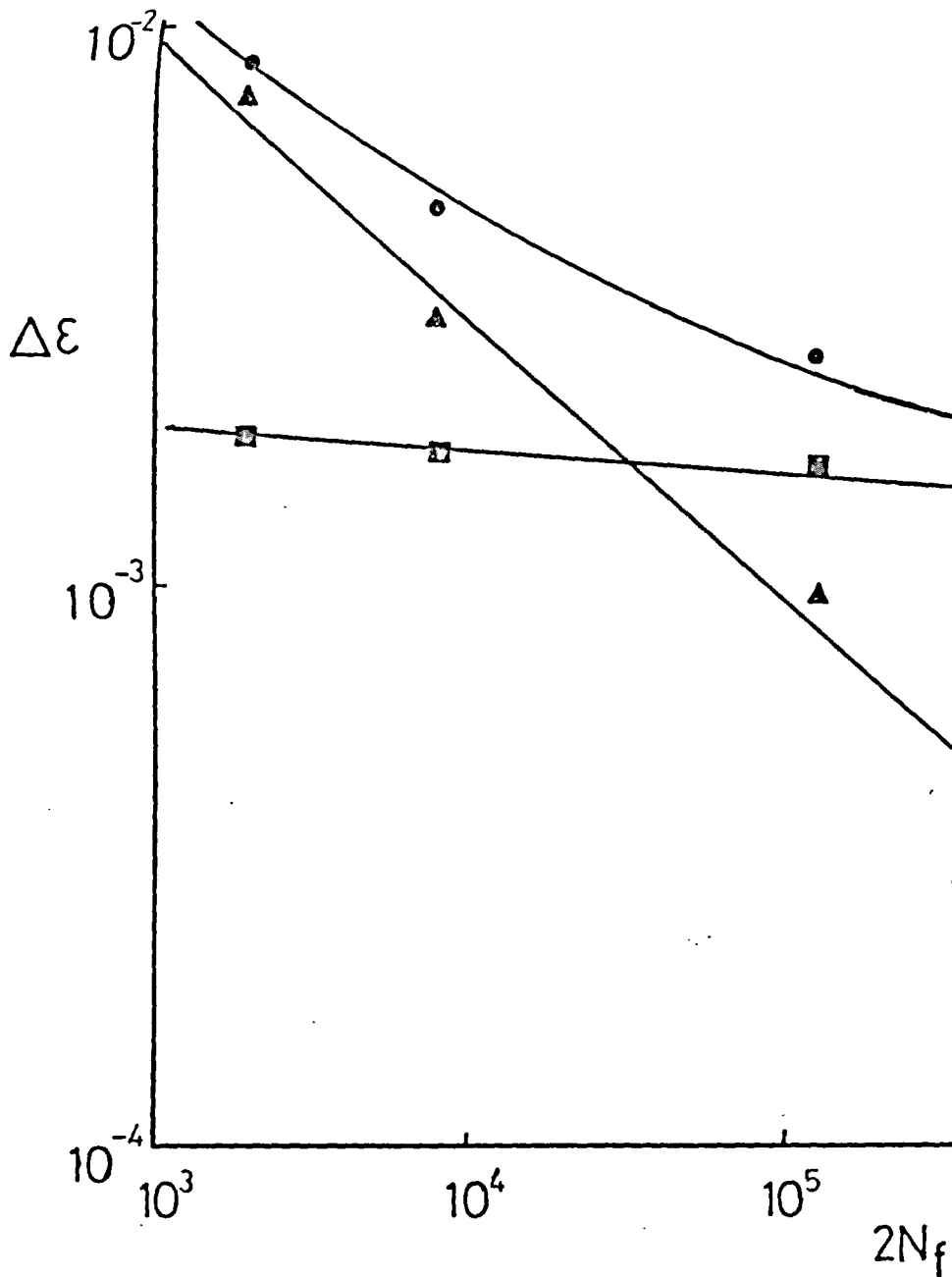
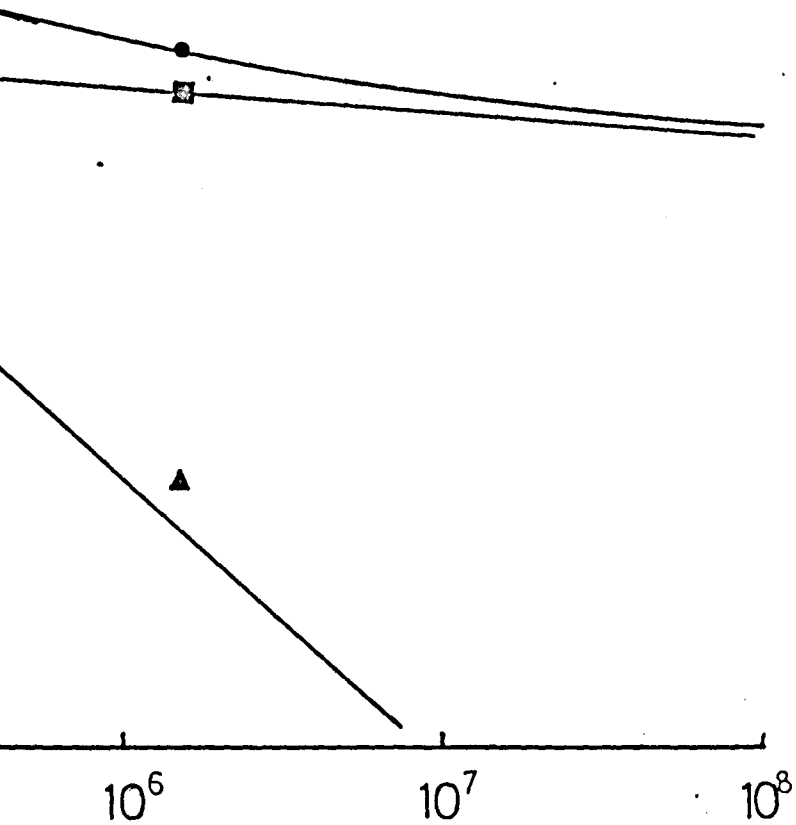


Figure 71 Strain-life curves for I8045
Total● Plastic▲ Elastic■



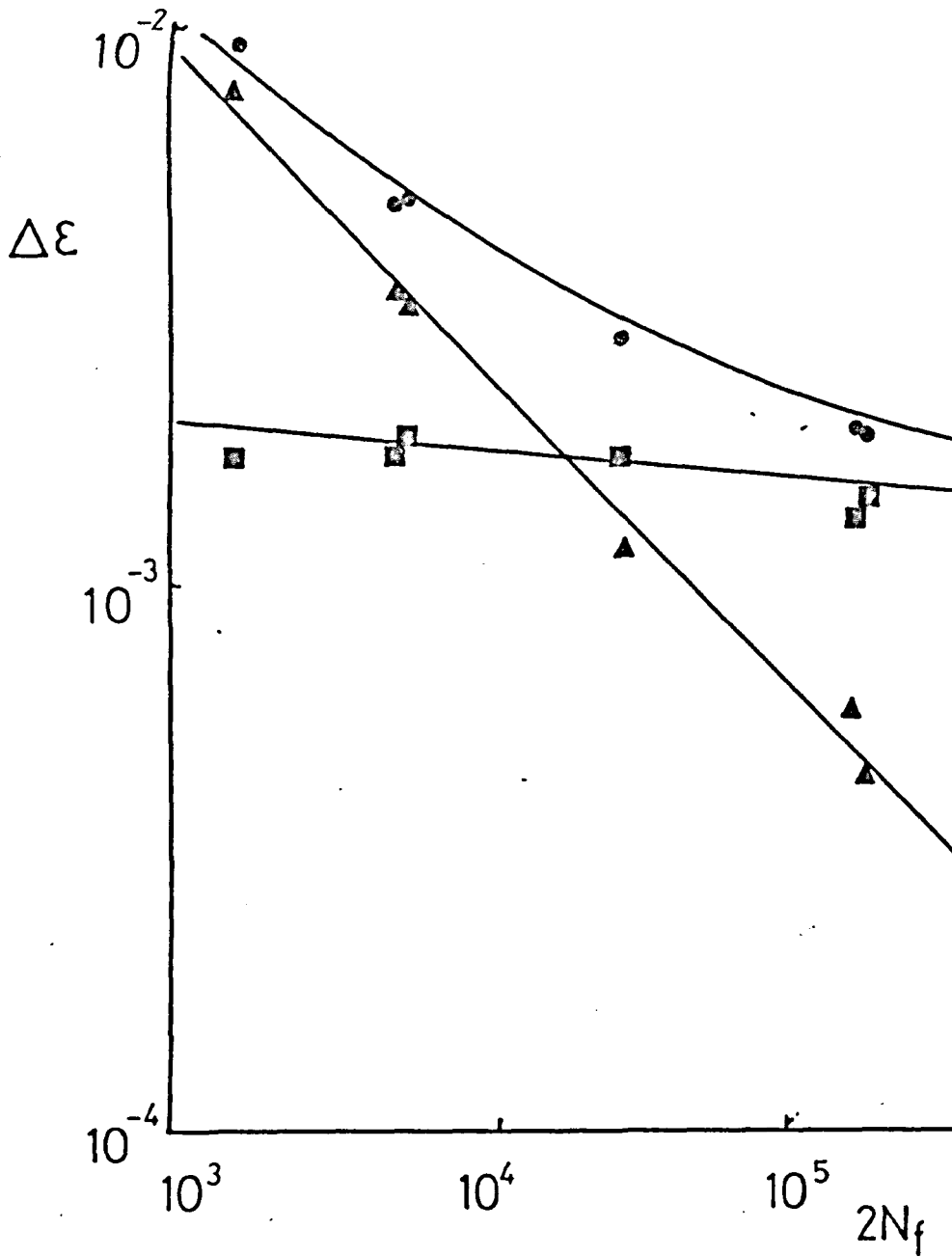
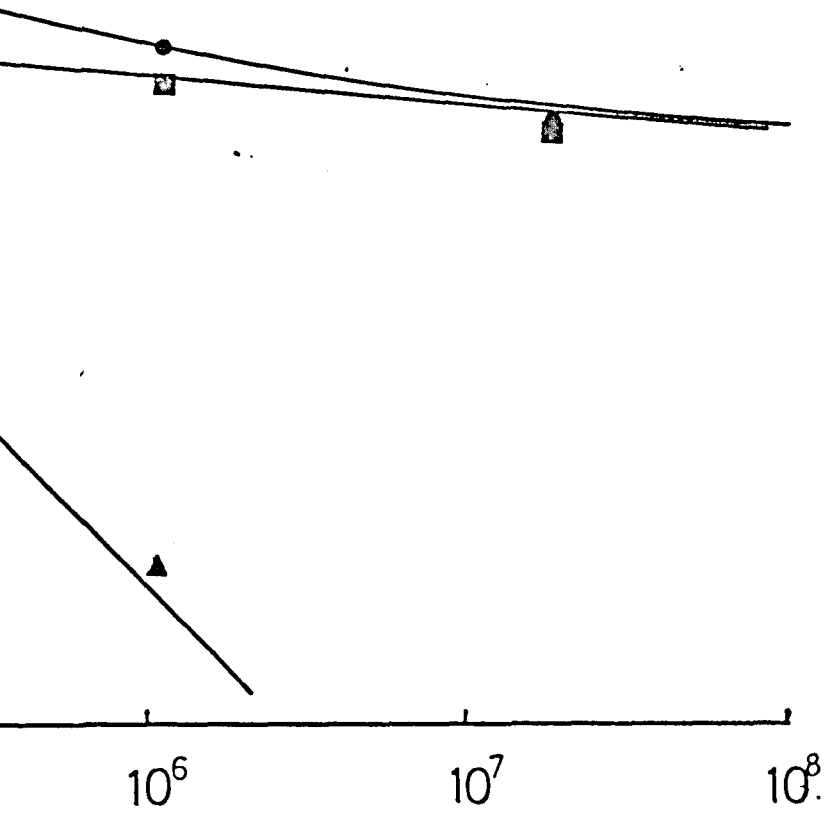


Figure 72 Strain-life curves for I8000 and I8090
Total● Plastic▲ Elastic■

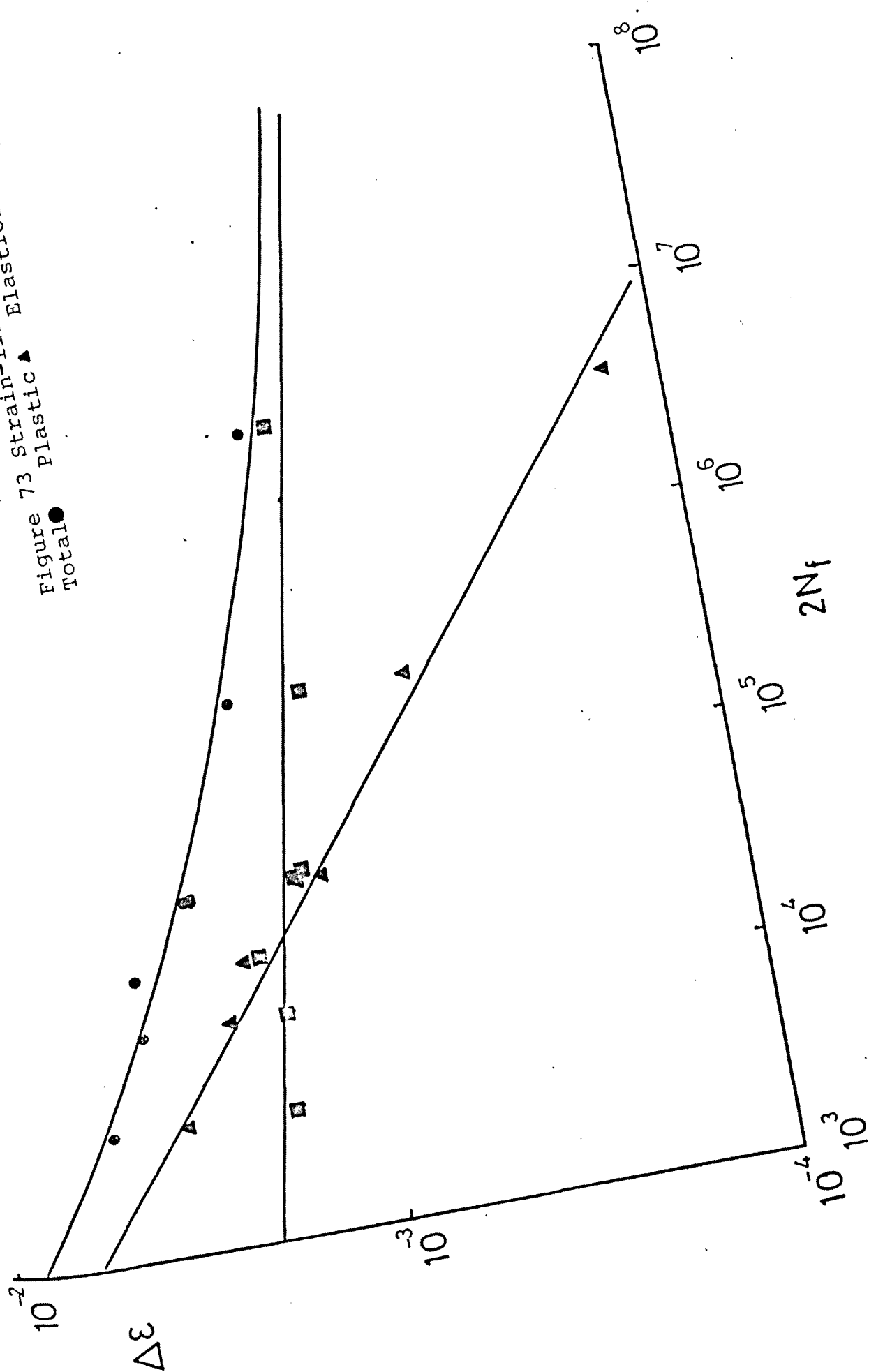


G8545

Figure 73 Strain-life curves for

Plastic \blacktriangle Elastic \blacksquare

Total \bullet



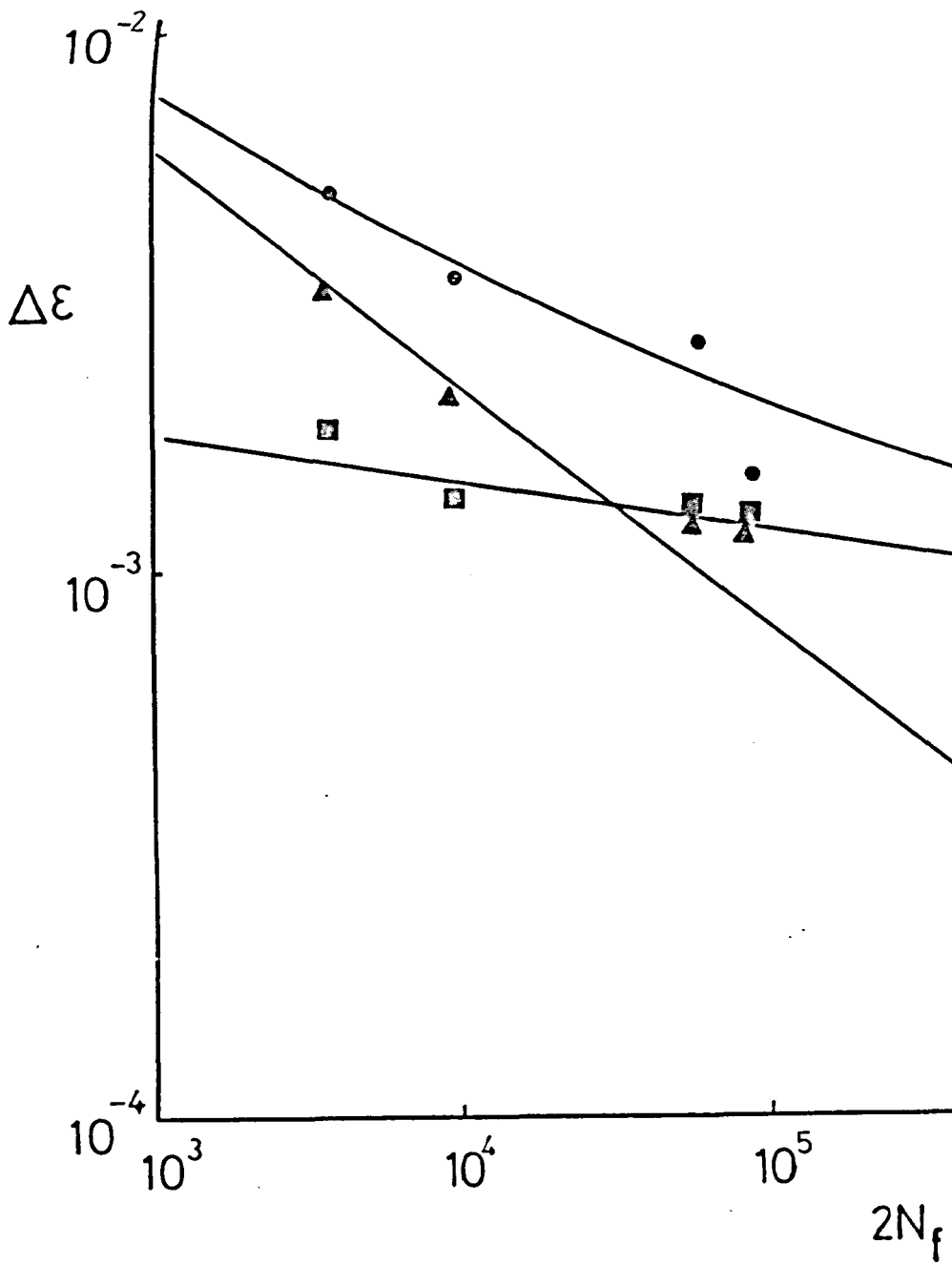
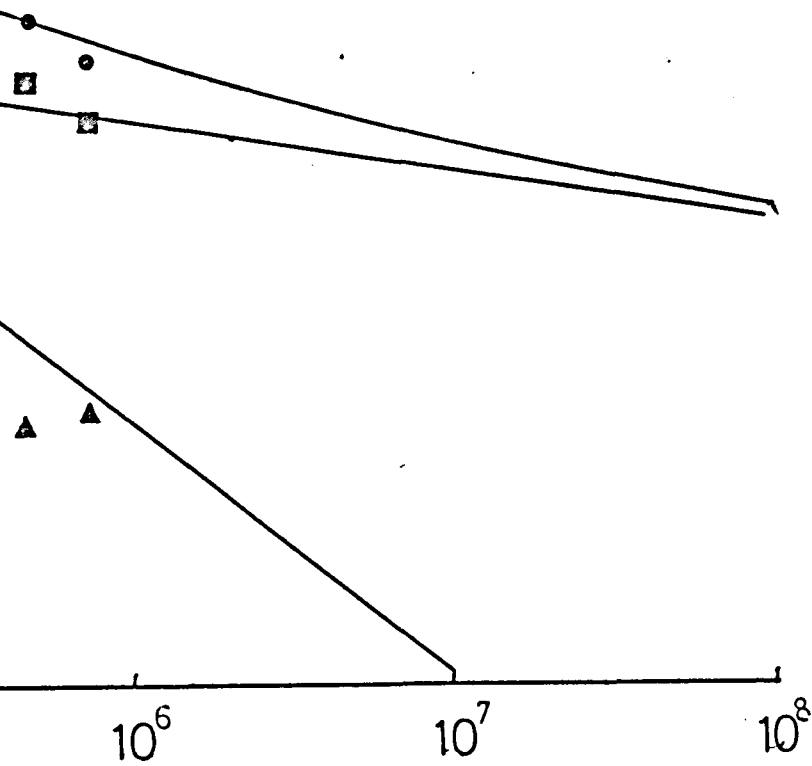


Figure 74 Strain-life curves for G8590
Total● Plastic▲ Elastic■



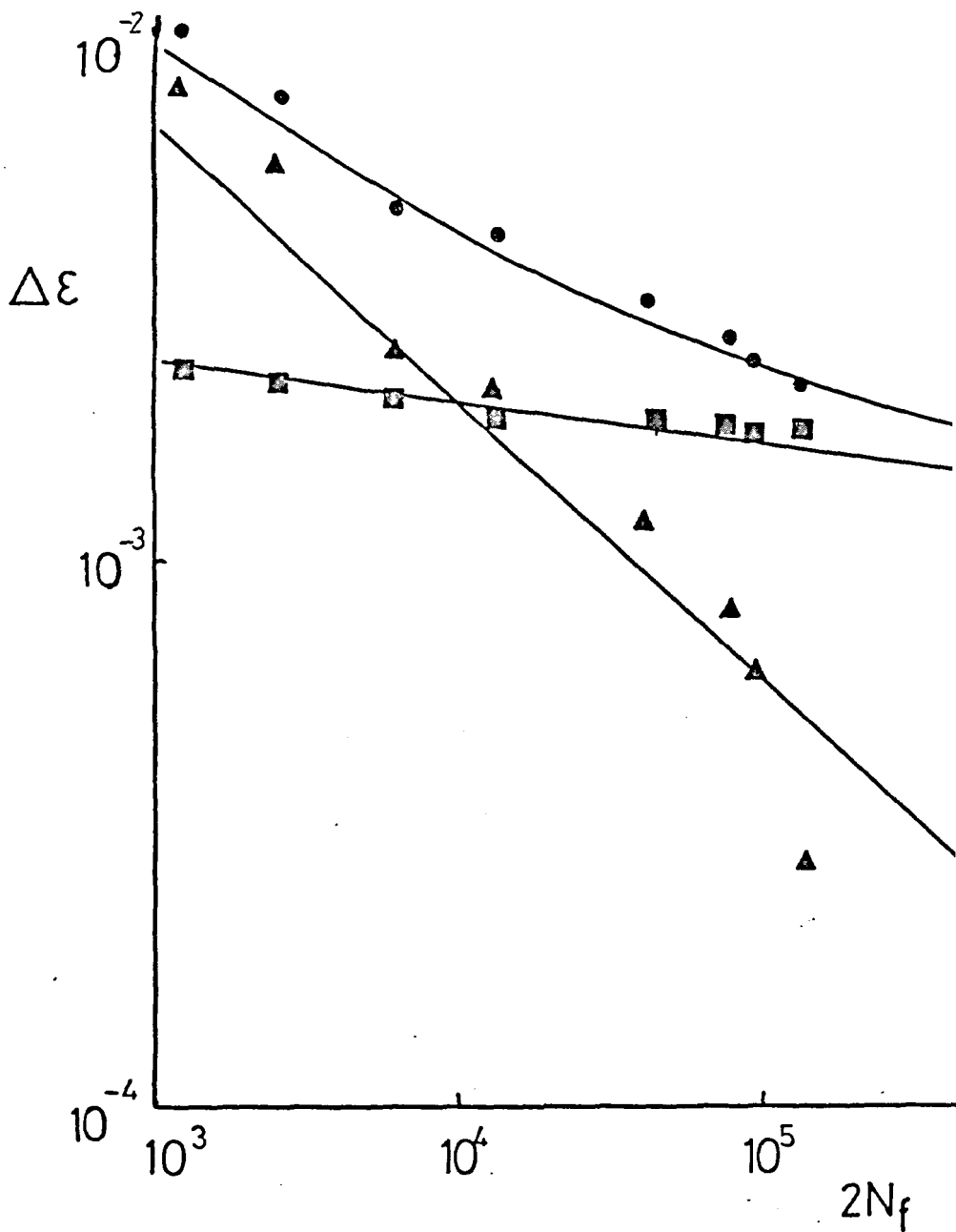
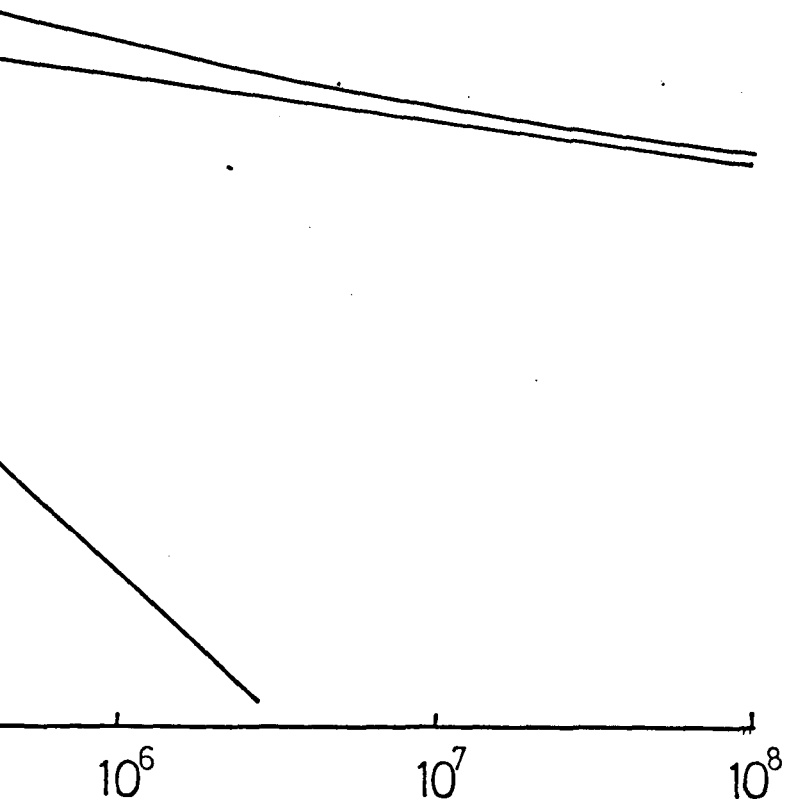


Figure 75 Strain-life curves for FAREN
Total● Elastic■ Plastic▲



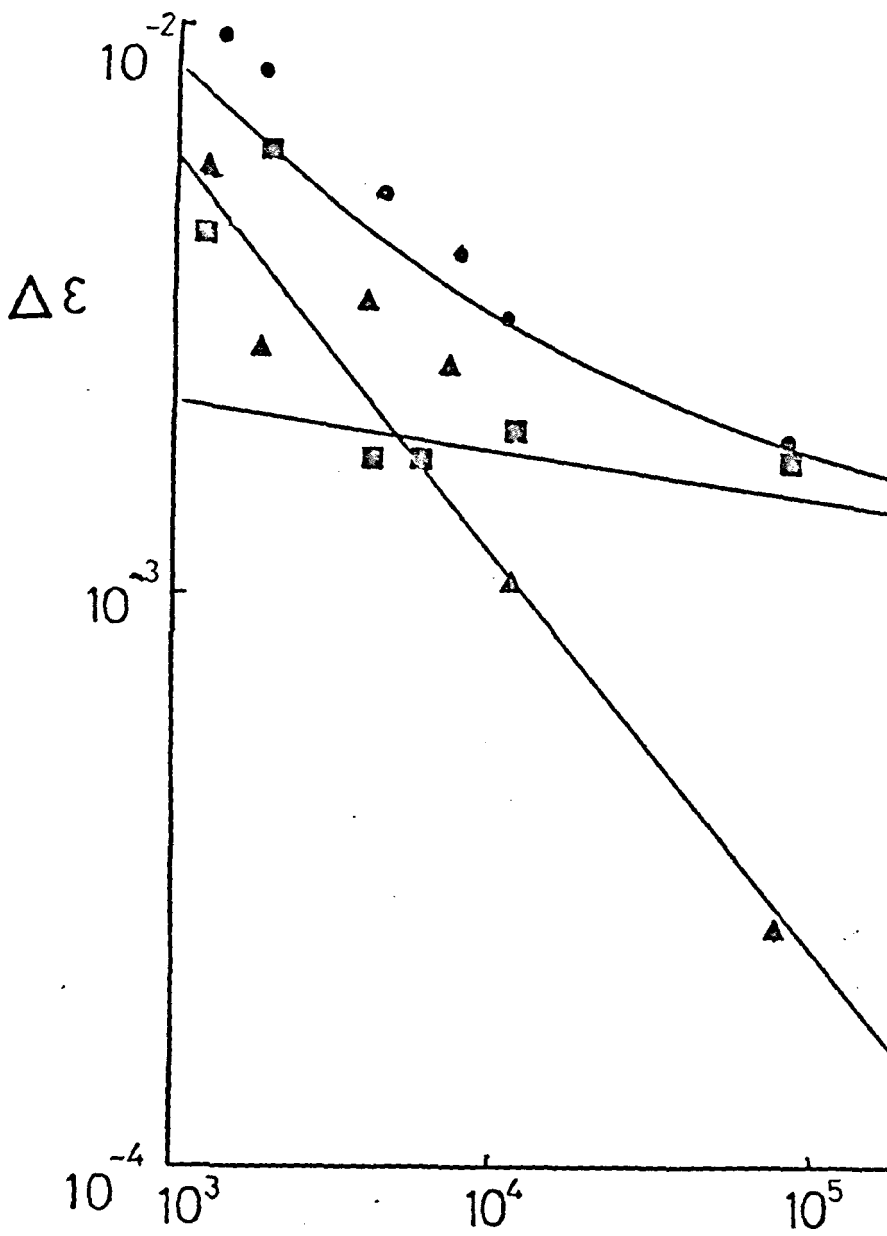
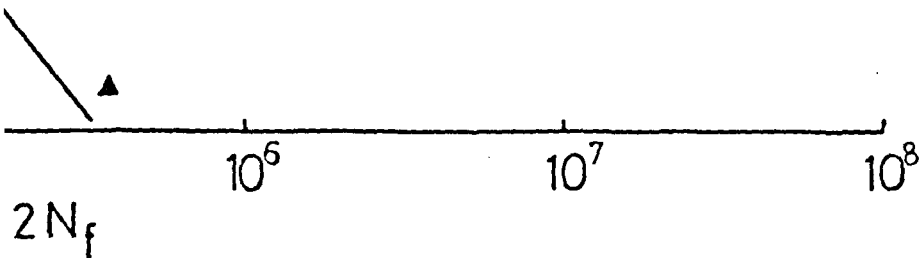
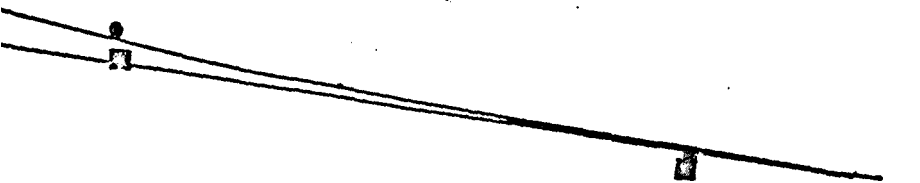


Figure 76 Strain-life curves for FBREN
Total● Plastic▲ Elastic■



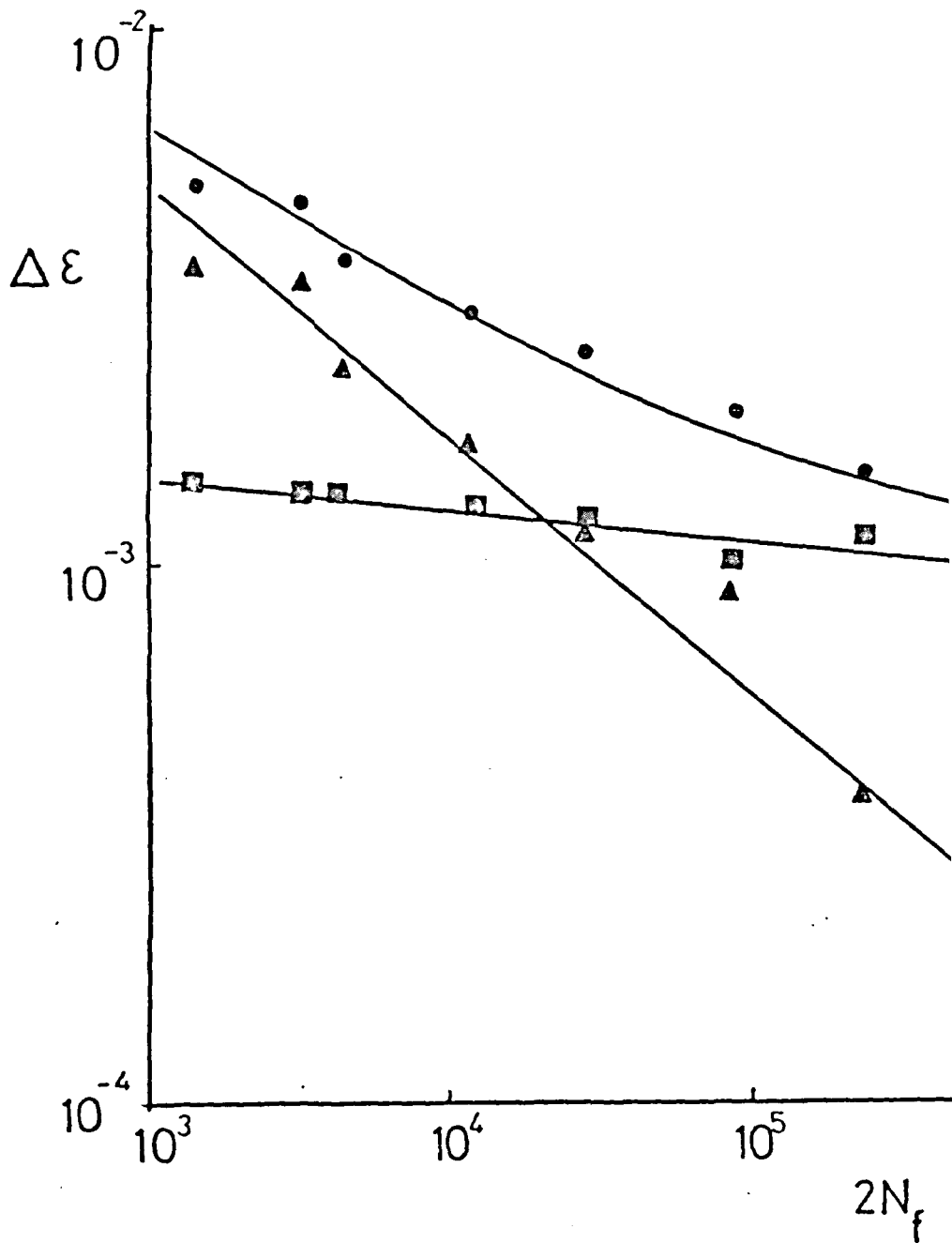
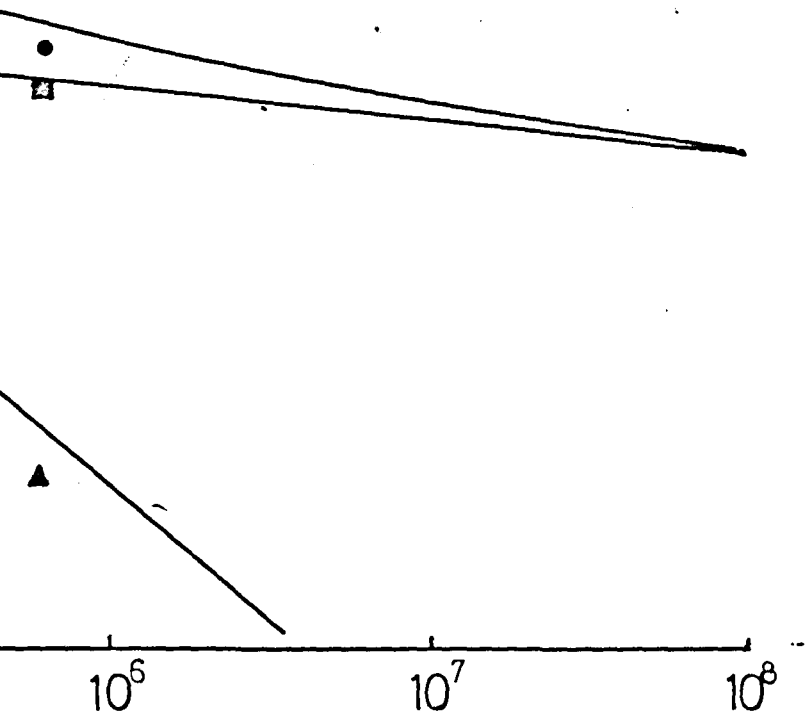


Figure 77 Strain-life curves for A3500
Total ● Plastic ▲ Elastic ■



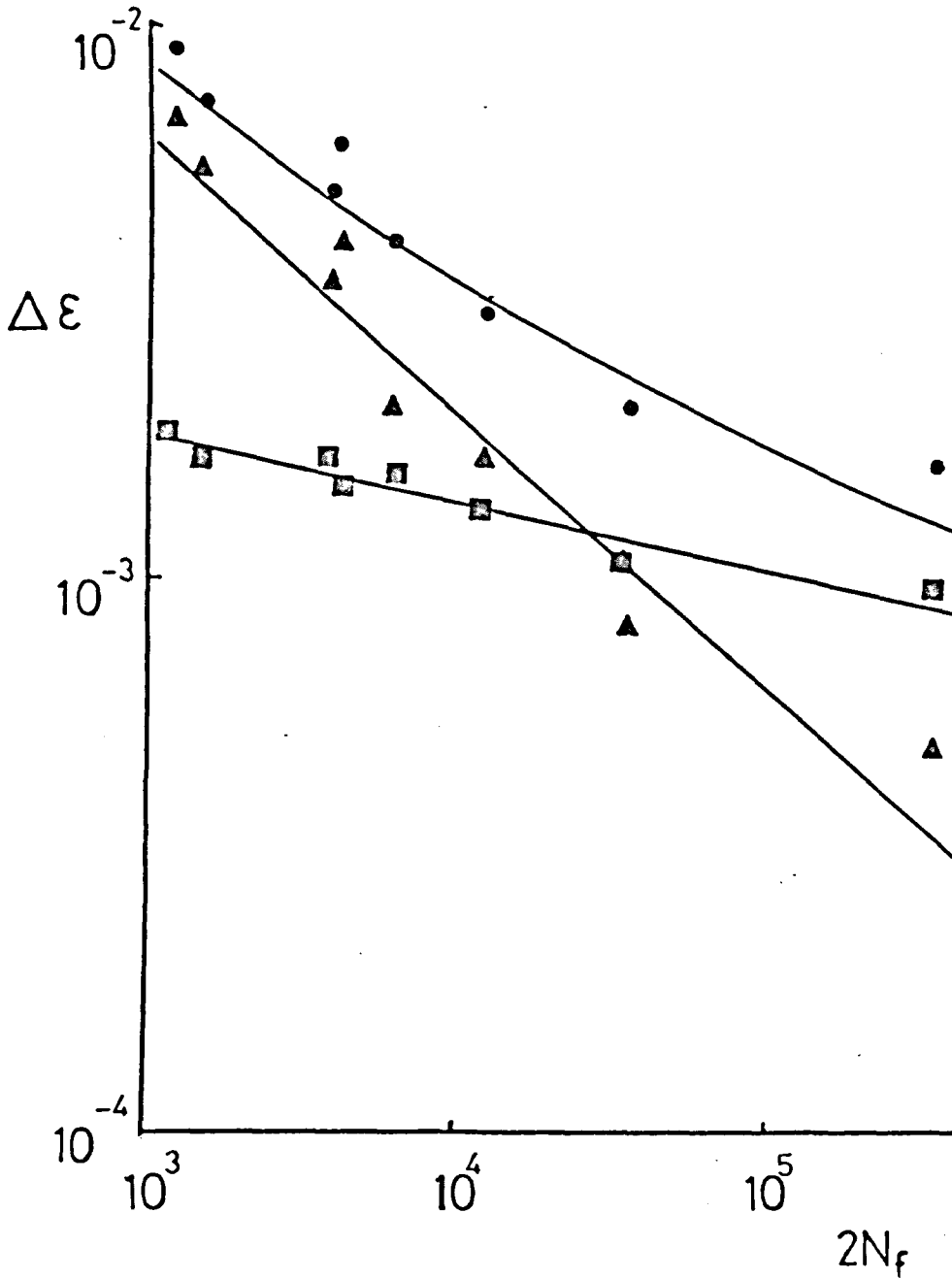
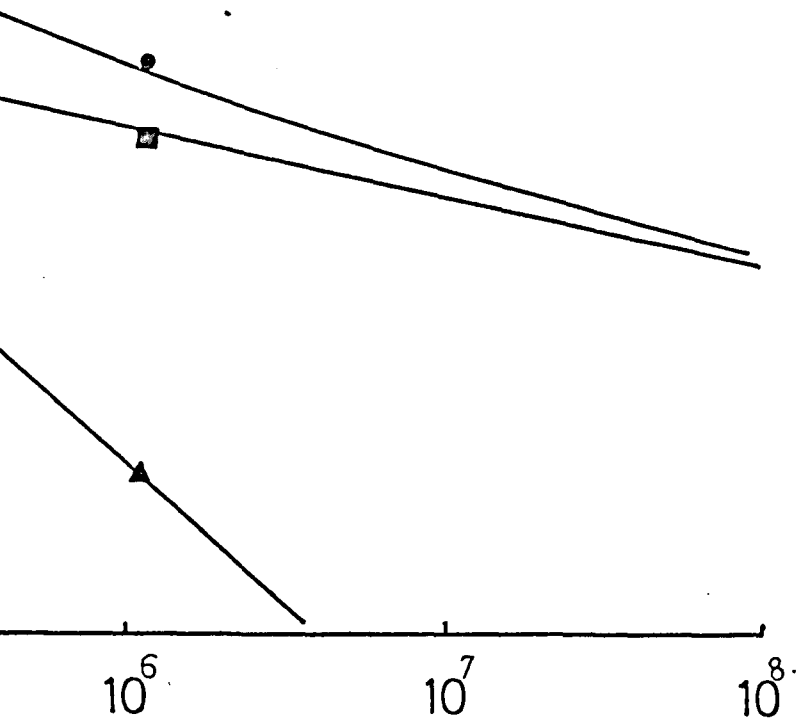


Figure 78 Strain-life curves for B3500
Total ● Plastic ▲ Elastic ■



FATIGUE CORRELATIONS (SPLINE FITTING)

L = 4.0 N = 2

DATA 1

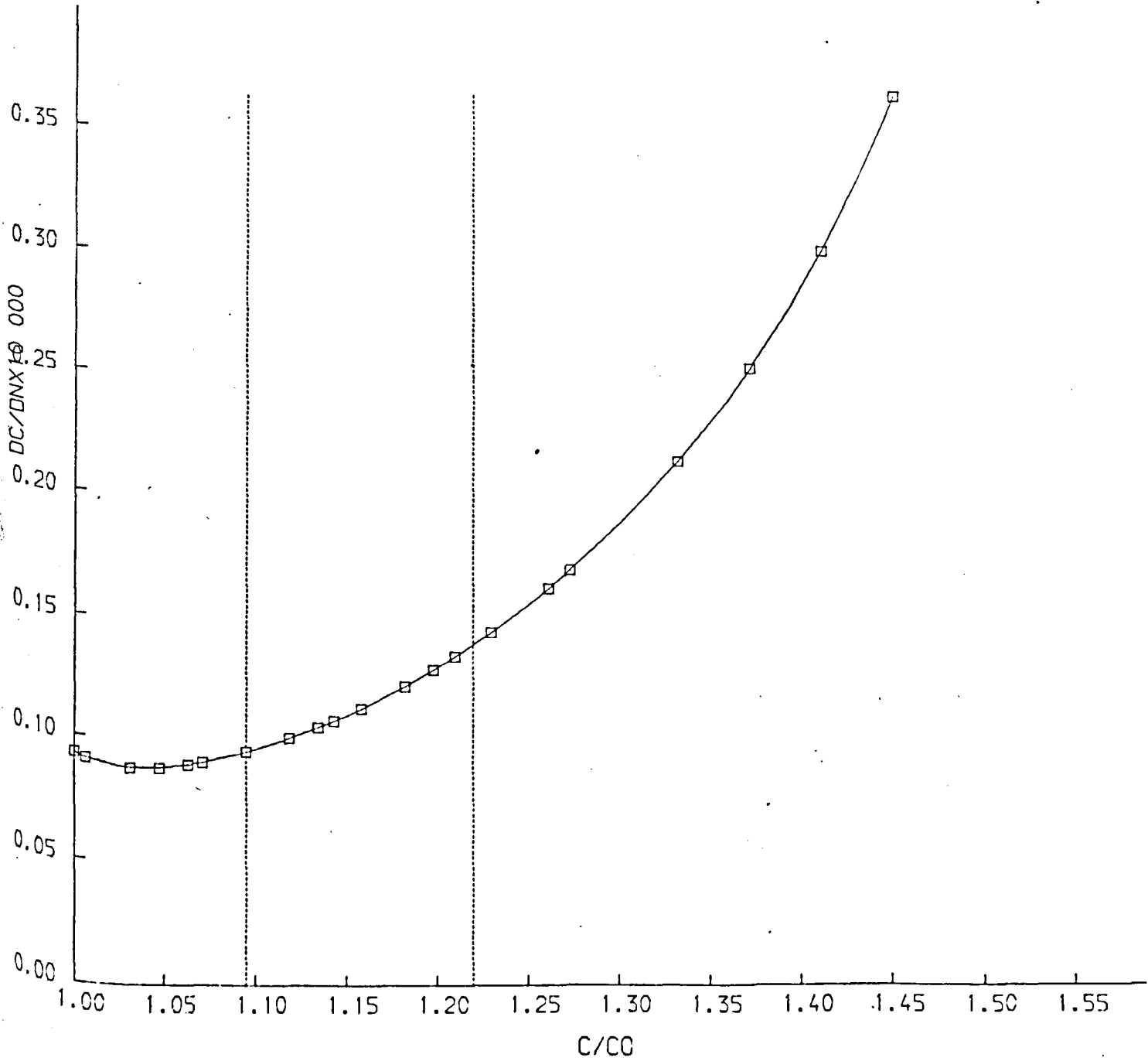


Figure 79 Sample data from crack propagation analysis showing a set of data considered to be well fitted by the computer program.

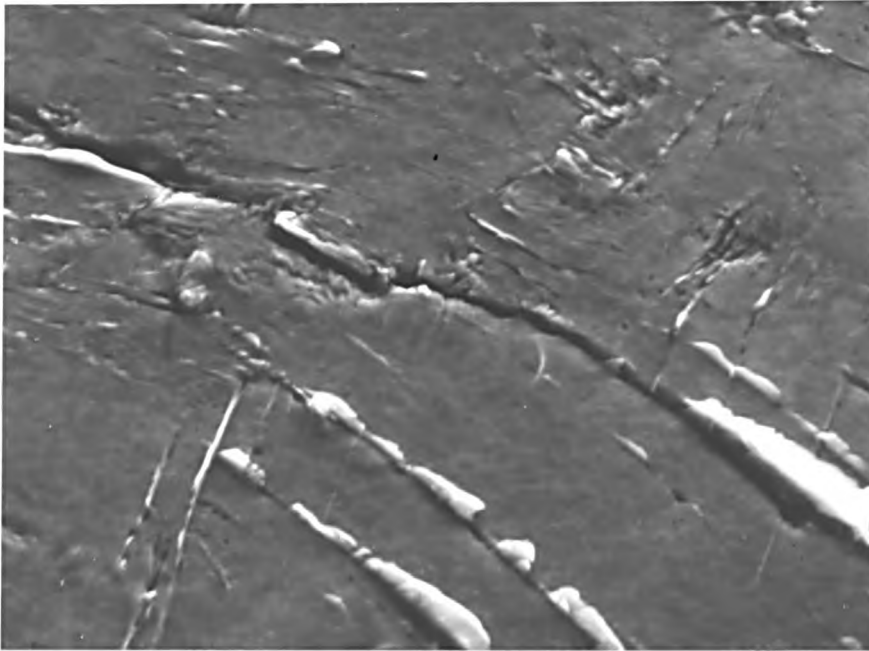


Figure 80 Secondary crack on the smooth side of a cylindrical specimen. SEM micrograph magnification 200x.

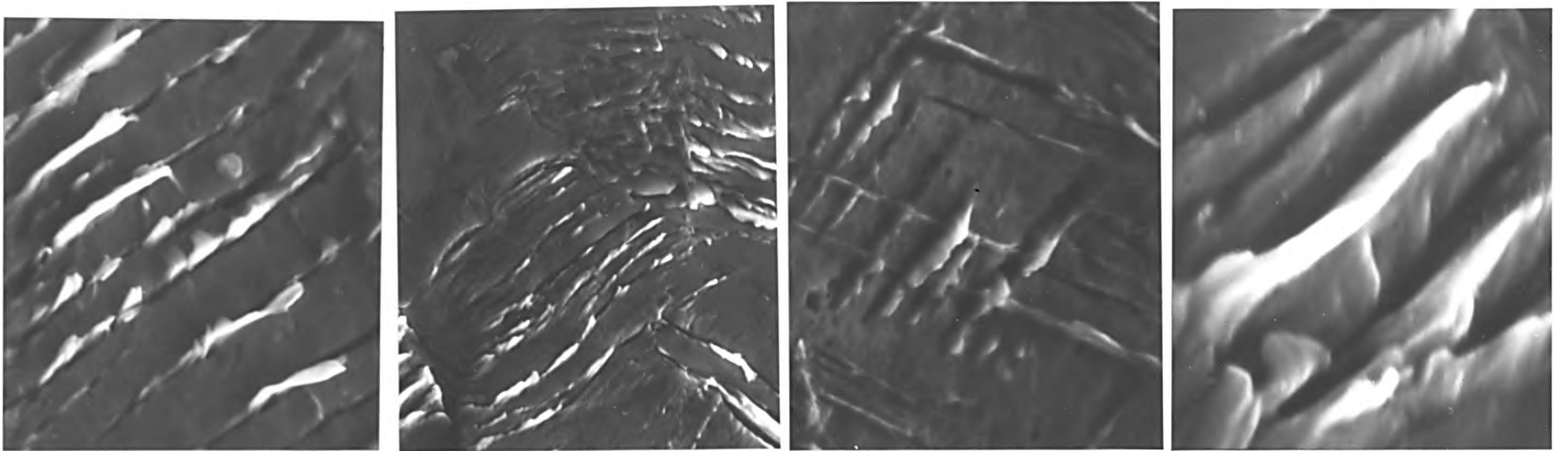


Figure 81 The four different types of surface markings observed on the sides of fatigued copper polycrystals. SEM micrographs, magnification 500x.

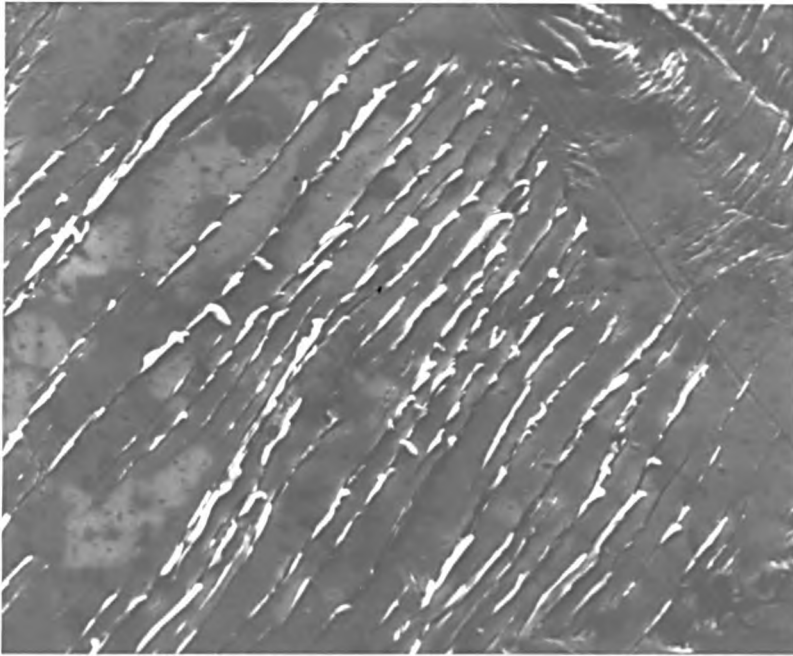


Figure 82 SEM micrograph of grain which displays long, parallel slip markings.magnification 800x.

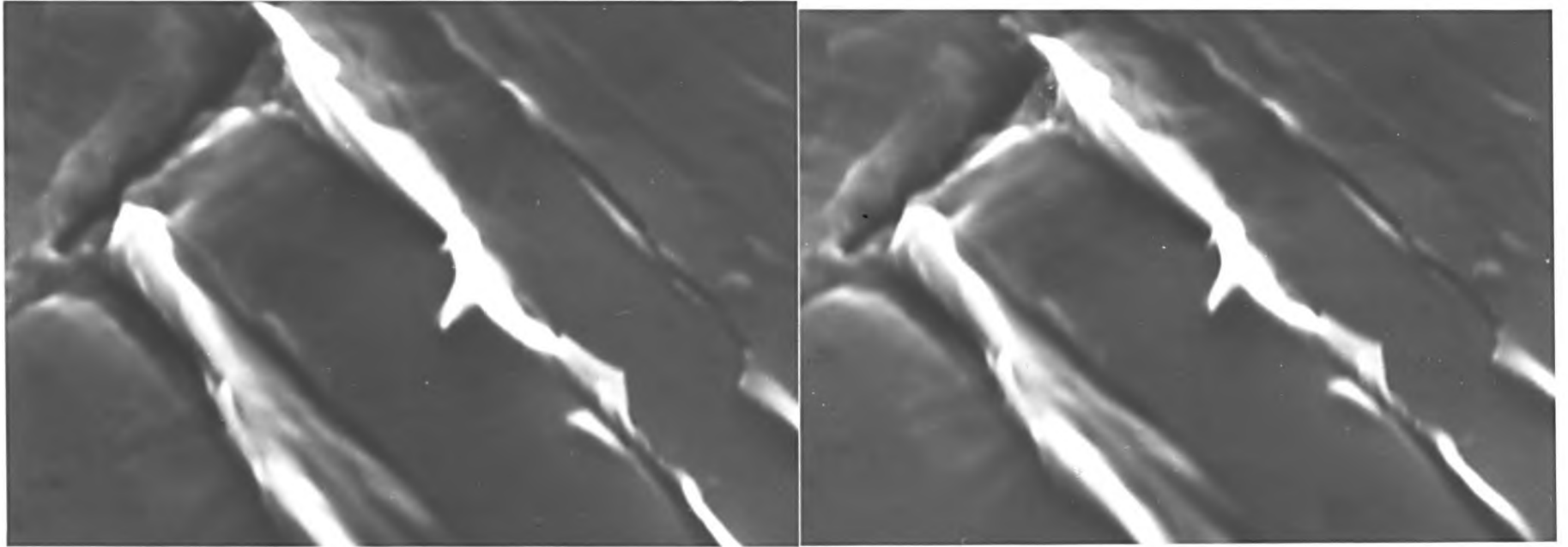


Figure 83 Stereopair SEM micrograph showing the formation of a fatigue crack near a twin-grain boundary intersection. Magnification 10000x.



Figure 84 SEM micrograph of a fatigue fracture. The angular appearance of the surface is due to crack nucleation at two sites. Magnification 15x.

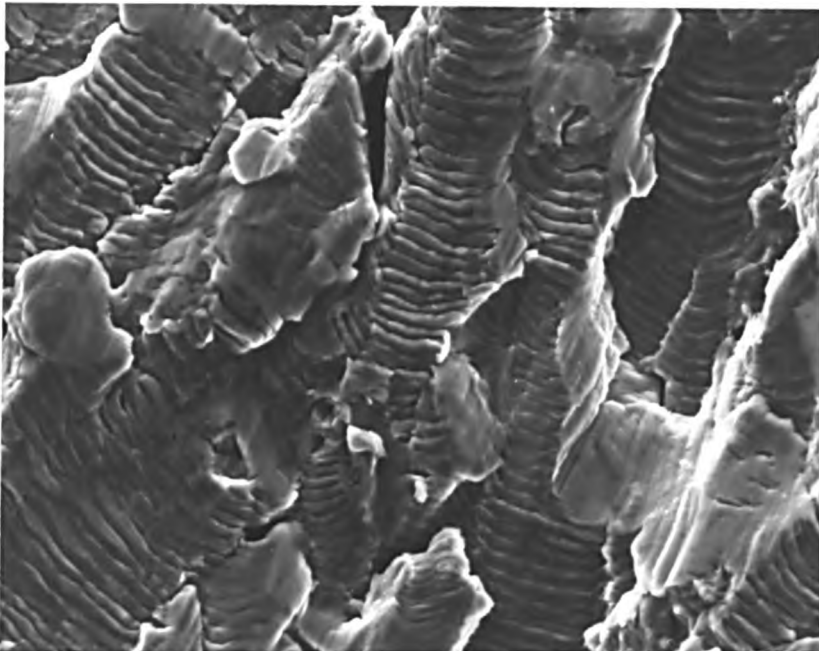


Figure 85 SEM micrograph of fatigue fracture of annealed copper tested in tension-compression. The ductile striations have been preserved in the depressions in the surface. Magnification 500x.

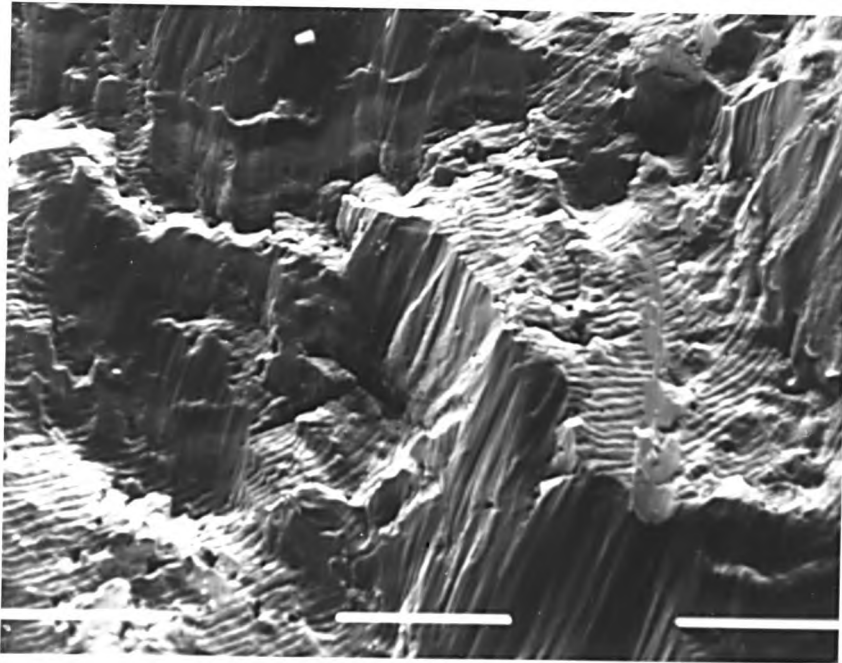


Figure 86 SEM micrograph of the fracture surface of a specimen of I8090 showing the 'ductile' appearance of the surface. Magnification 500x.

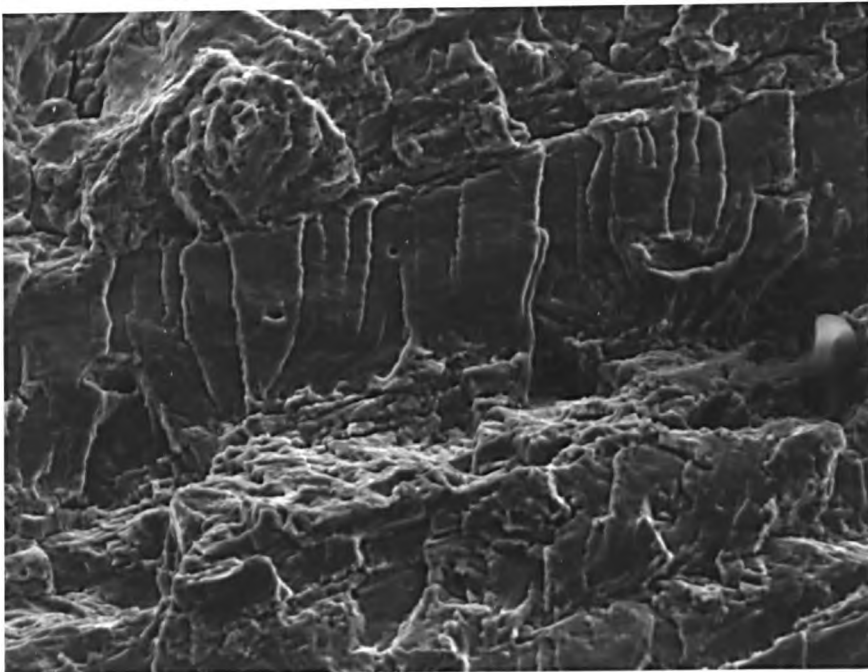


Figure 87 SEM micrograph of the fracture surface of a specimen of I8045 showing 'facets'. Magnification 500x.

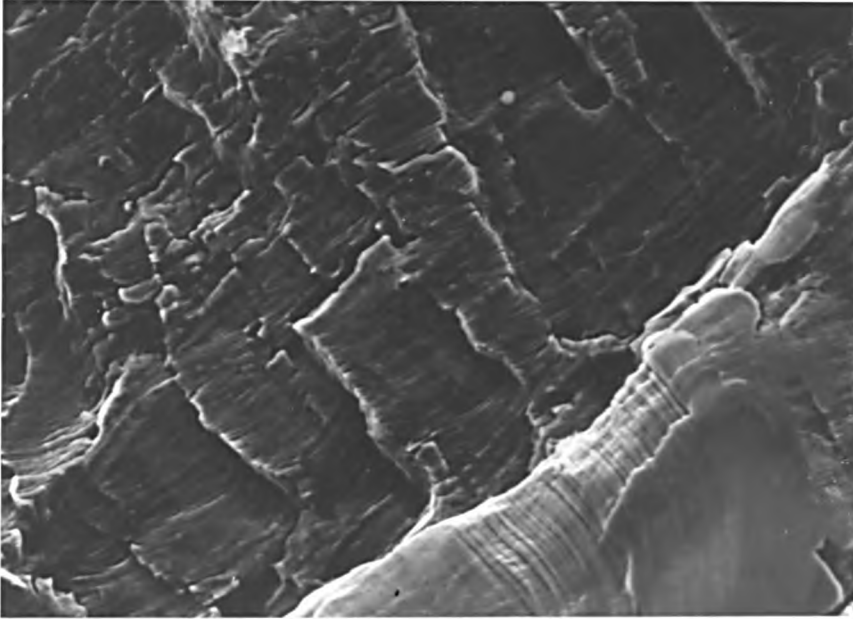


Figure 88 SEM micrograph of the fracture surface of a specimen of I8090 close to site of nucleation. Magnification 150x.

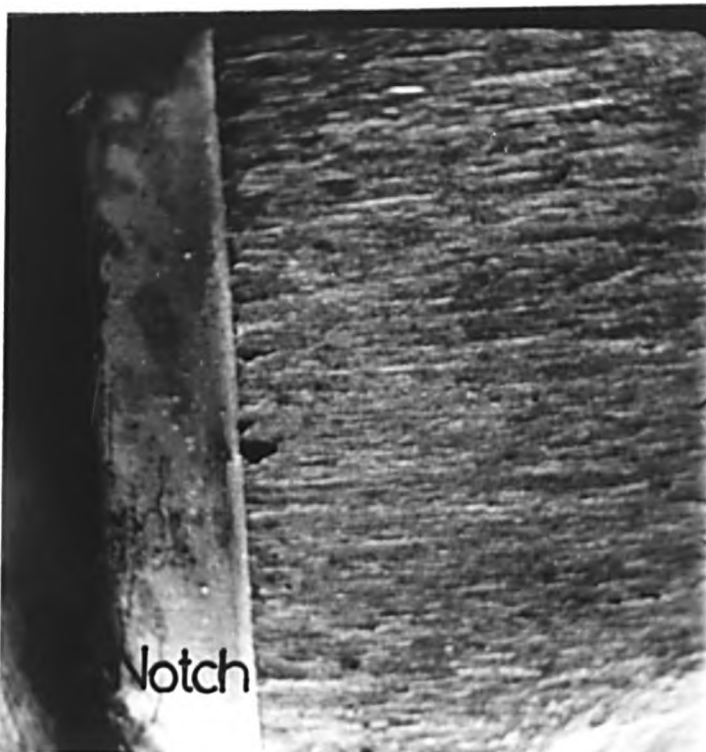


Figure 89 SEM micrograph of the fracture surface of an SEN specimen. Magnification 100x.



Figure 90 SEM micrograph of the fatigue fracture region in a specimen of NUJIG 90 orientation. Magnification 800x.

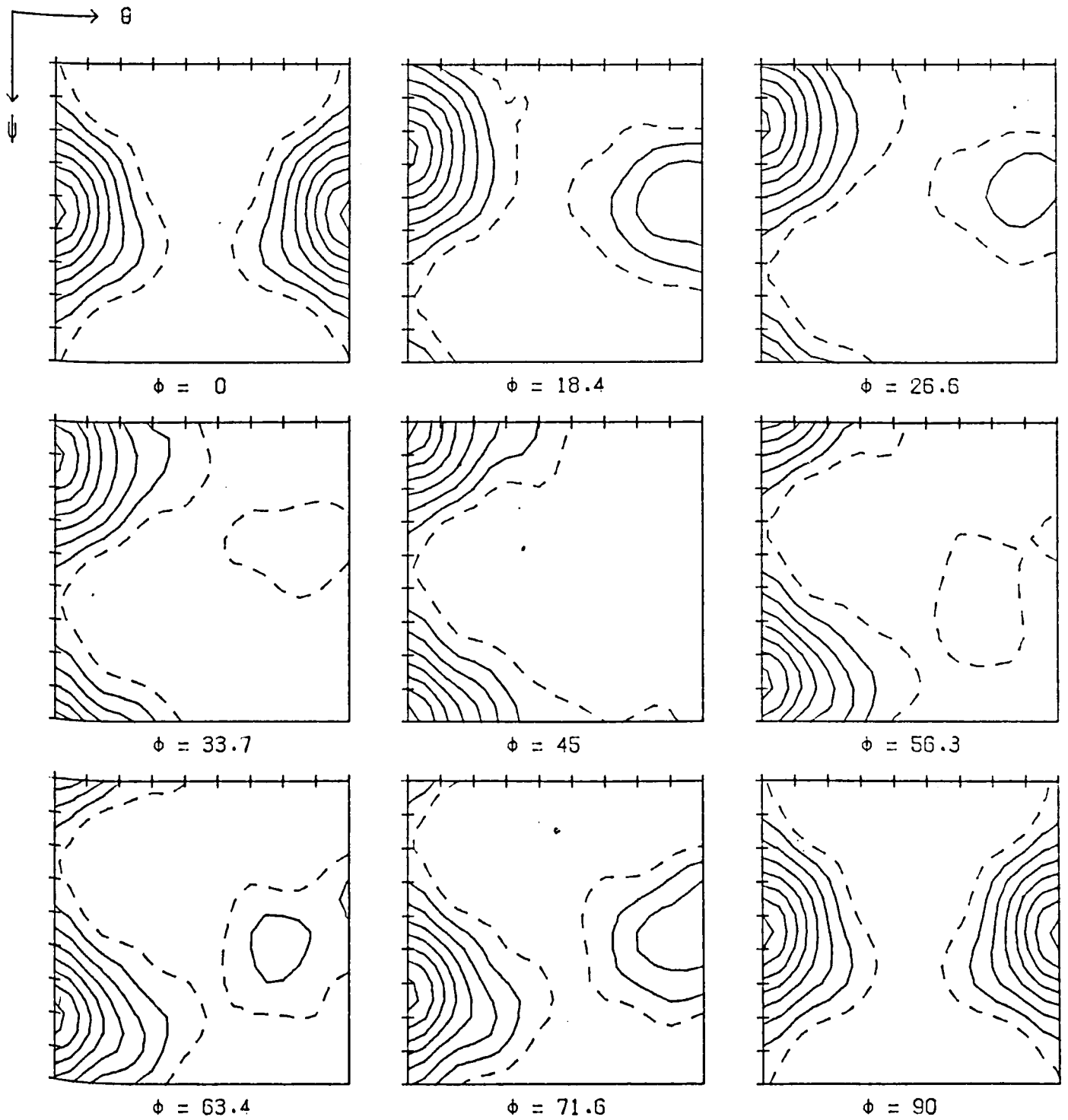


Figure 91 C.o.d.f. plot of material G8545 after
 5300 cycles at $\Delta\epsilon/2 = .0037$. Contour interval
 0.5x random.Max.Fn.Ht. 4.7.Severity 0.68.

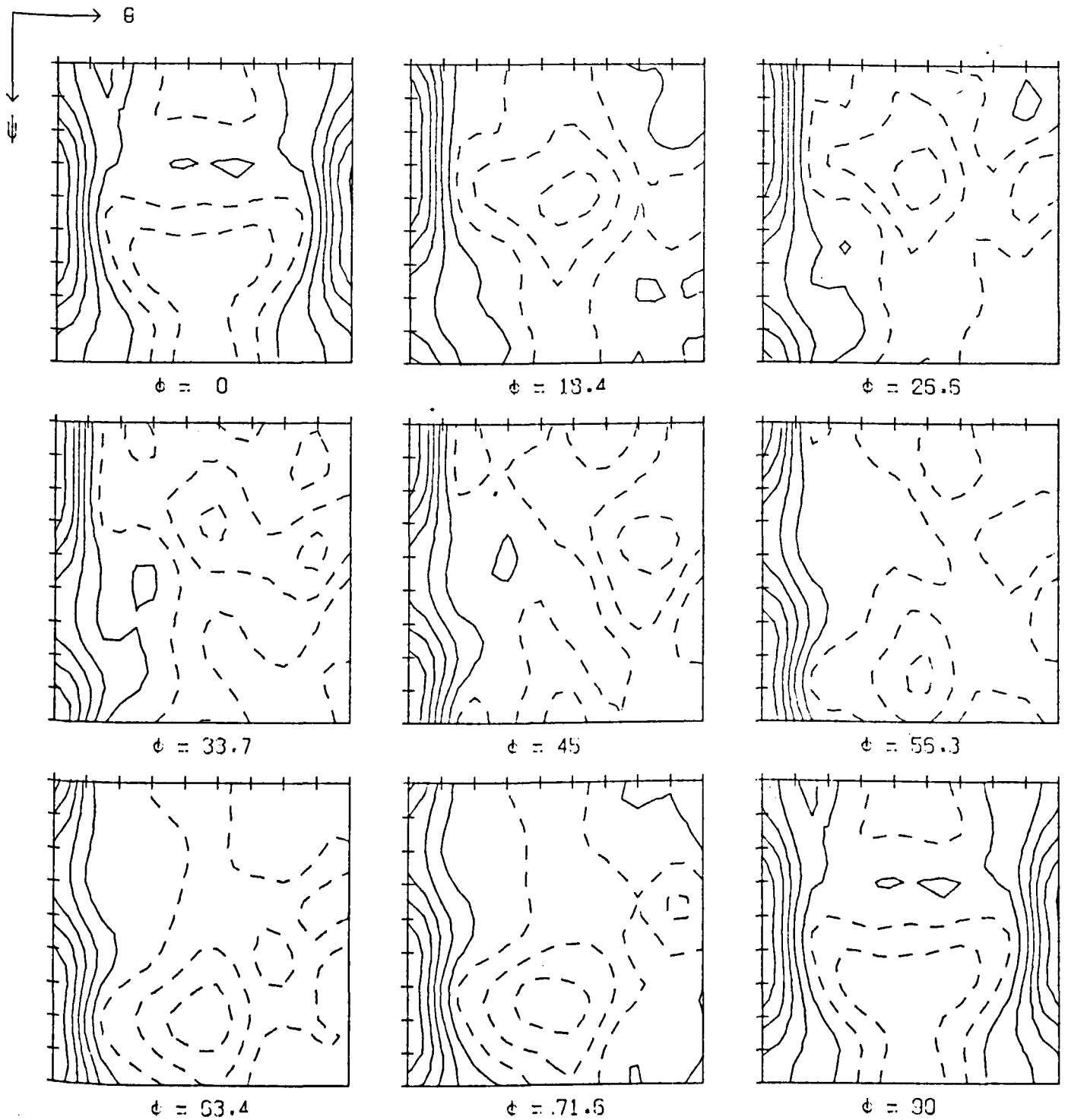
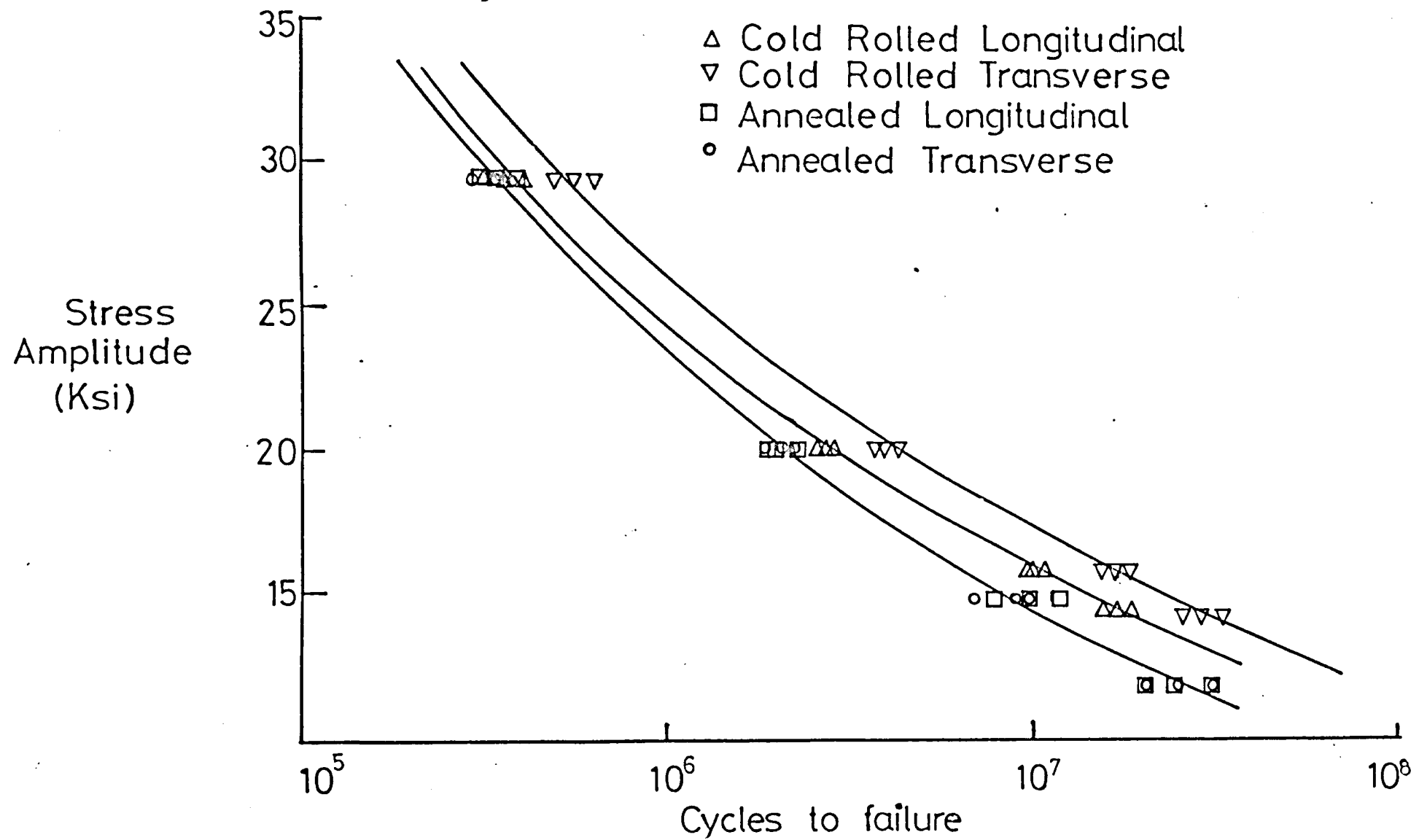
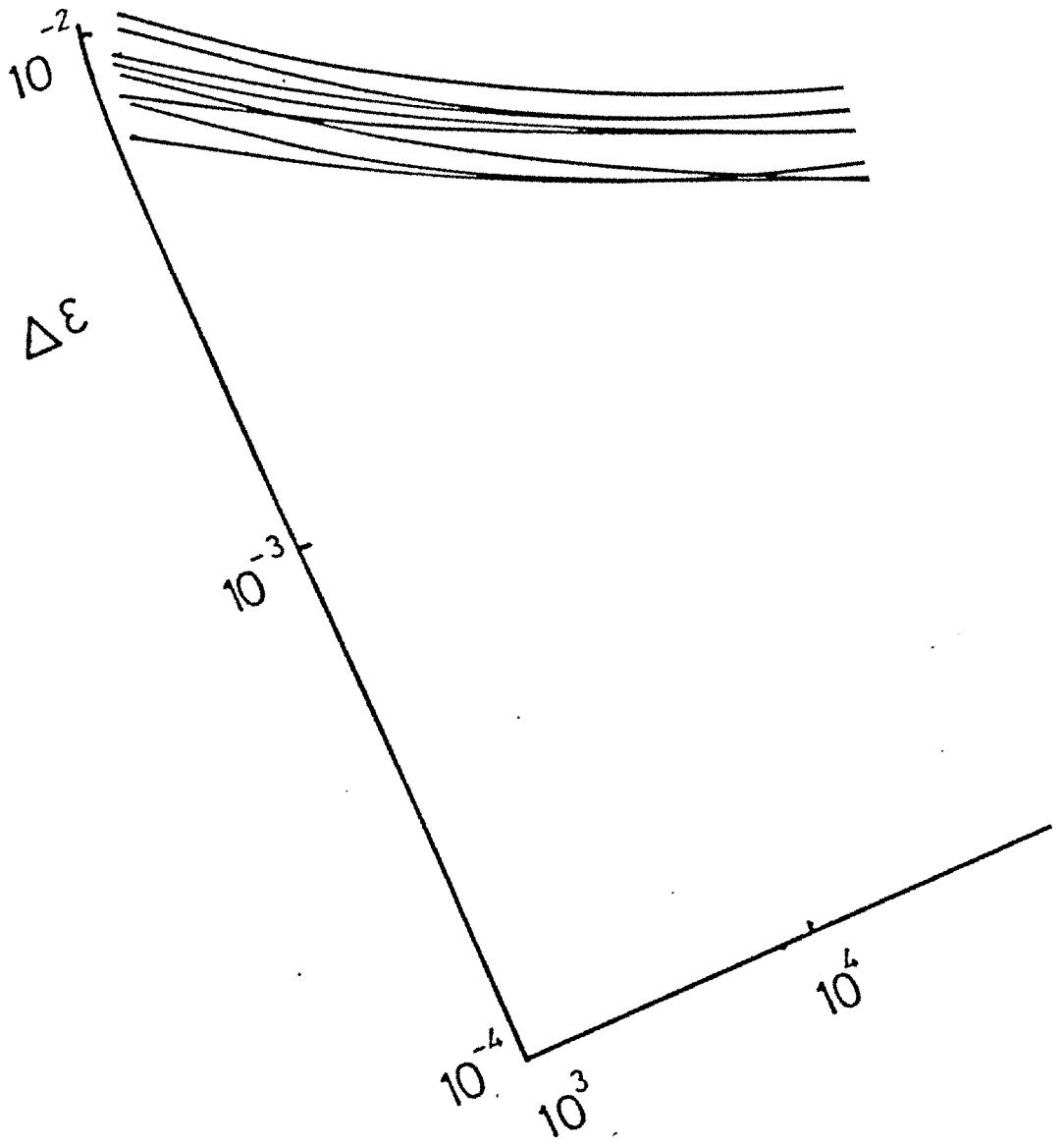


Figure 92 The c.o.d. difference function plot between fig.91 and fig.49. Contour interval 0.5x random. Max.Fn.Ht. 3.1. Severity 0.57

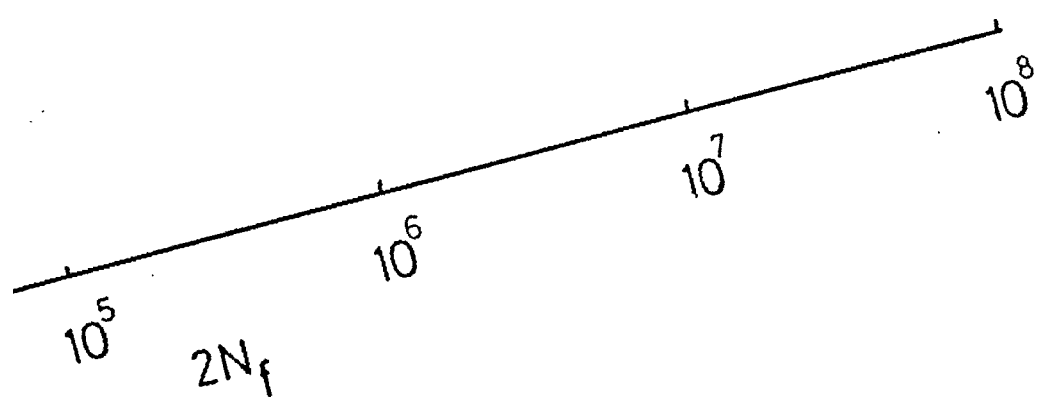
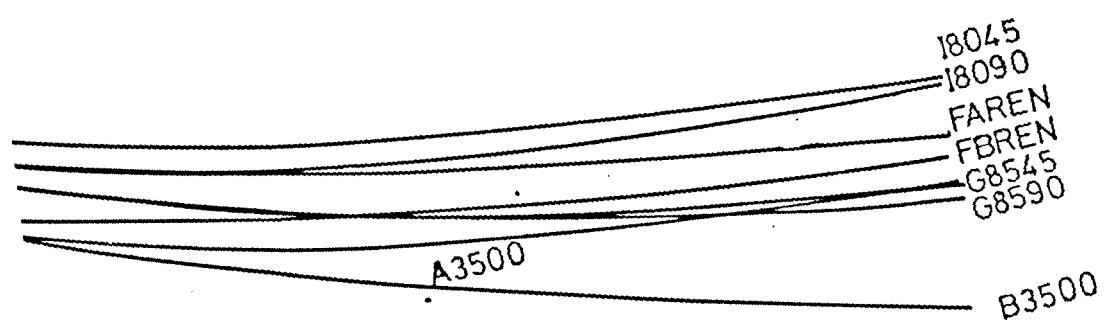
Figure 93 The S/N data of Nair and Le May

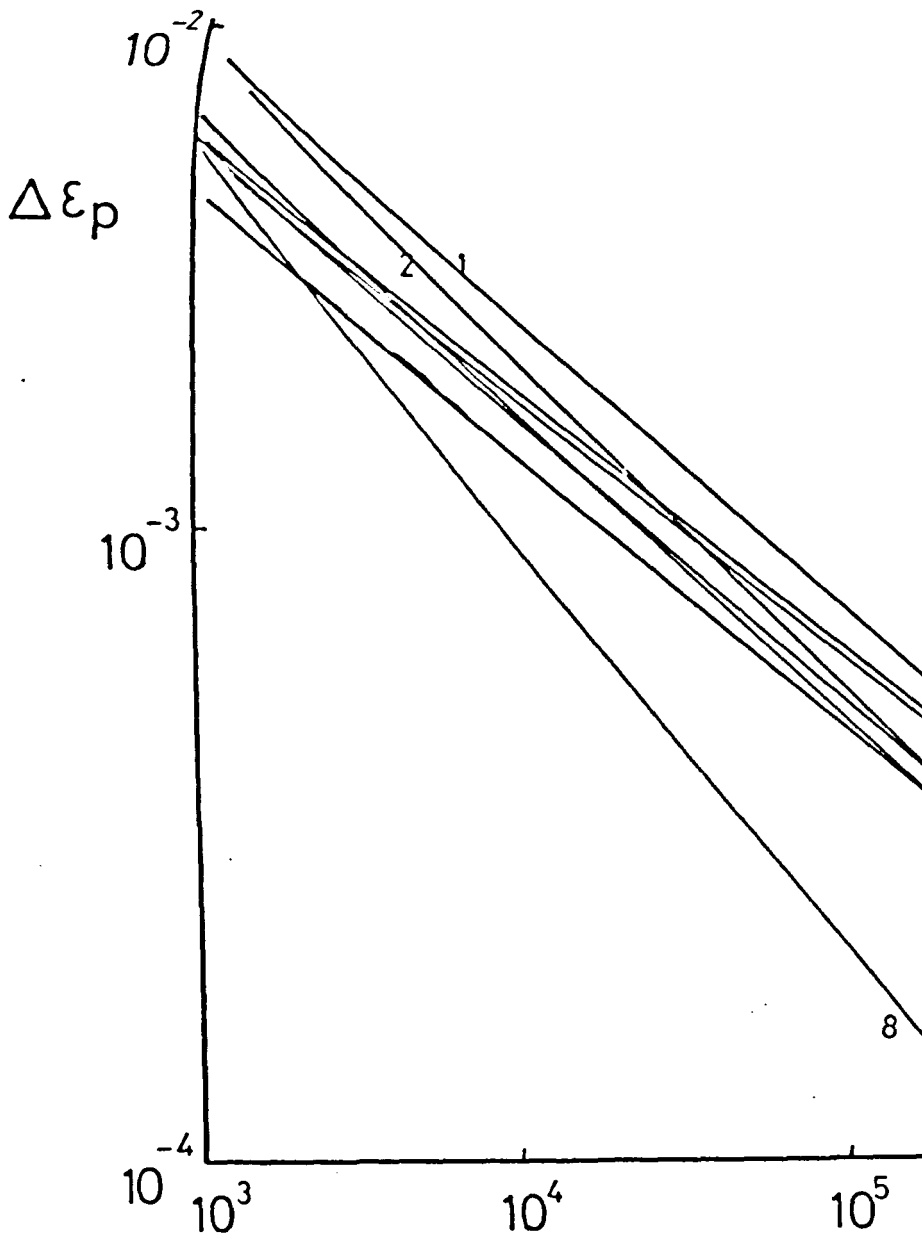


Figure



94 Summary of strain life curves from figs 71-79





- 1 I8045
- 2 I8090
- 3 G8590
- 4 G8545
- 5 B3500
- 6 A3500
- 7 FBREN
- 8 FAREN

Figure 95 Summary of the plastic strain
-life data developed in this investigation.

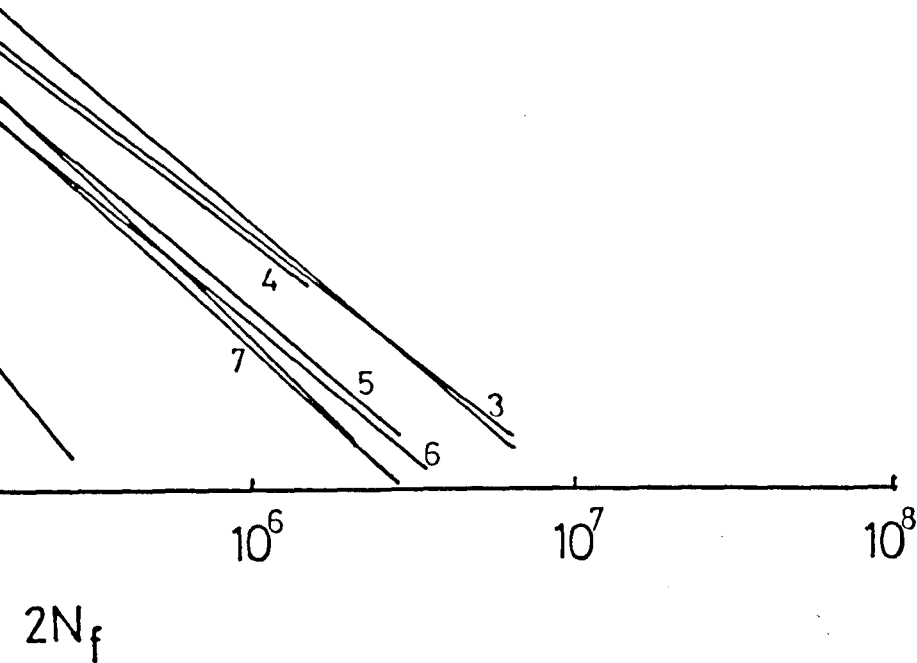
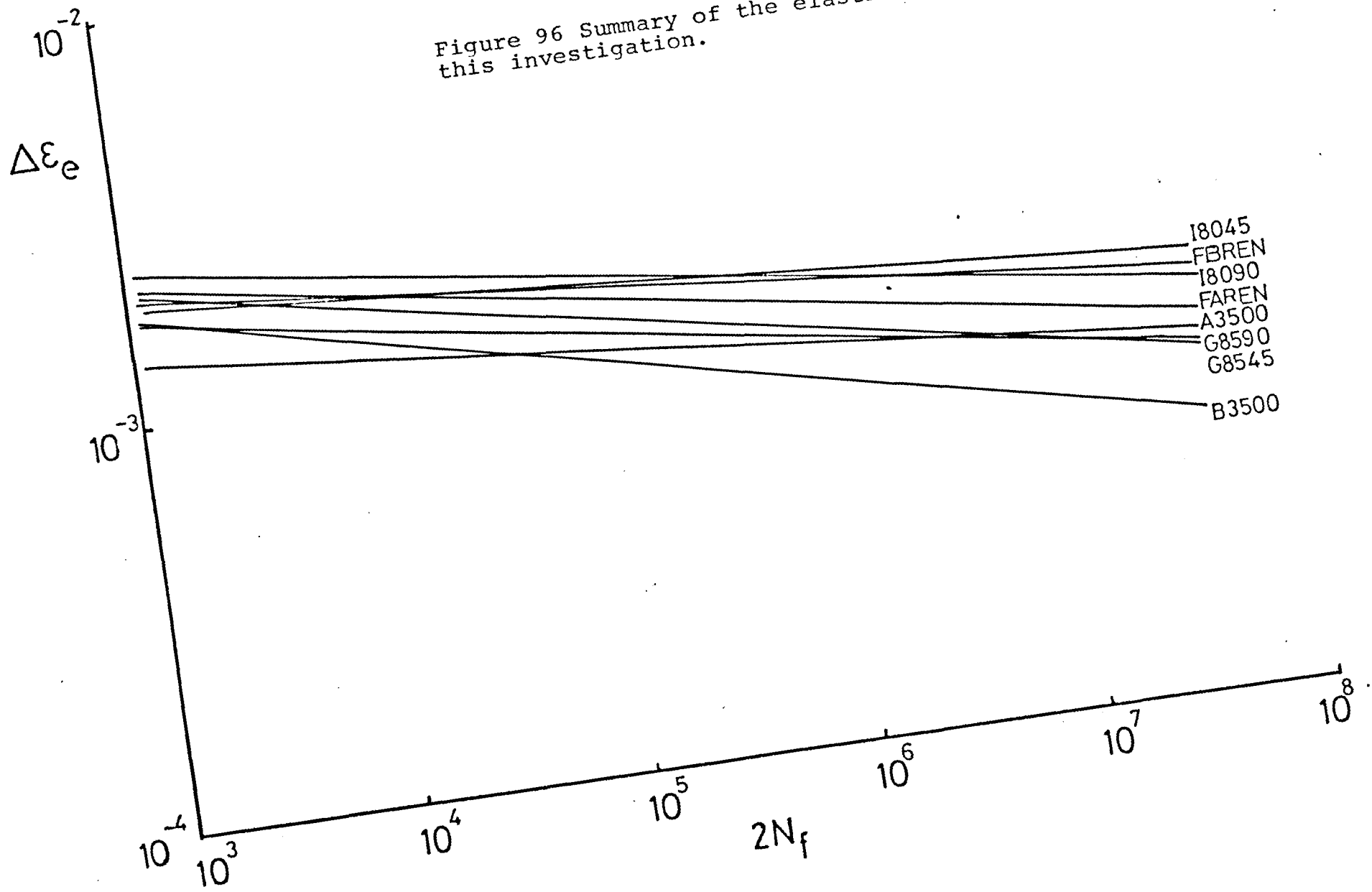


Figure 96 Summary of the elastic strain-life data developed in this investigation.



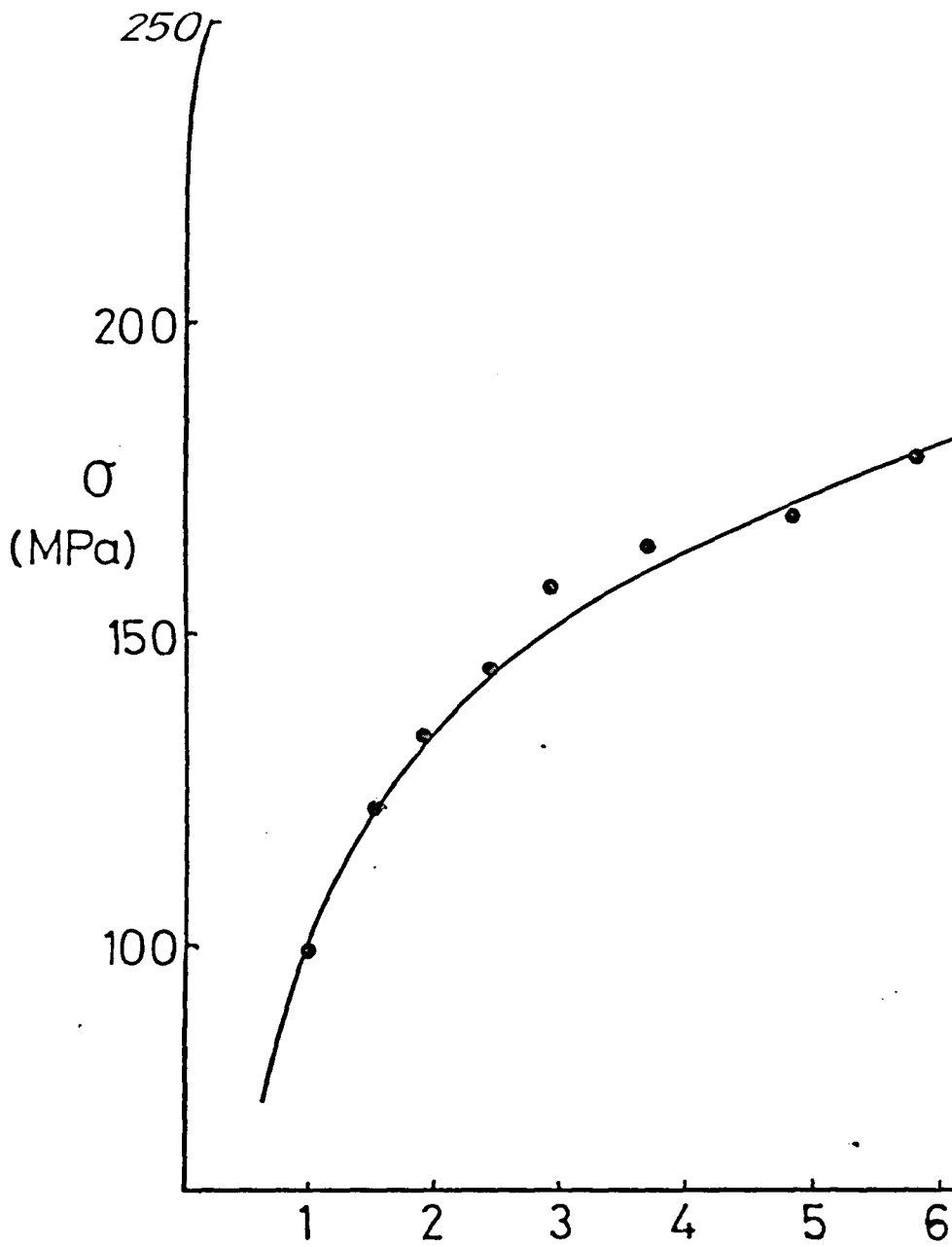
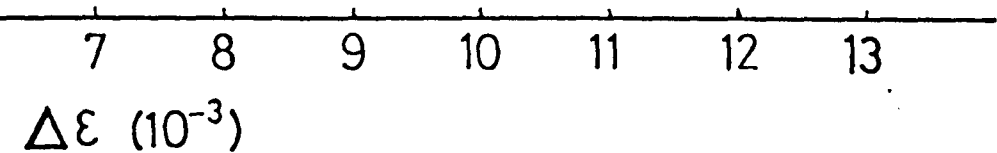




Figure 97 The cyclic stress-strain curve for B35XX.



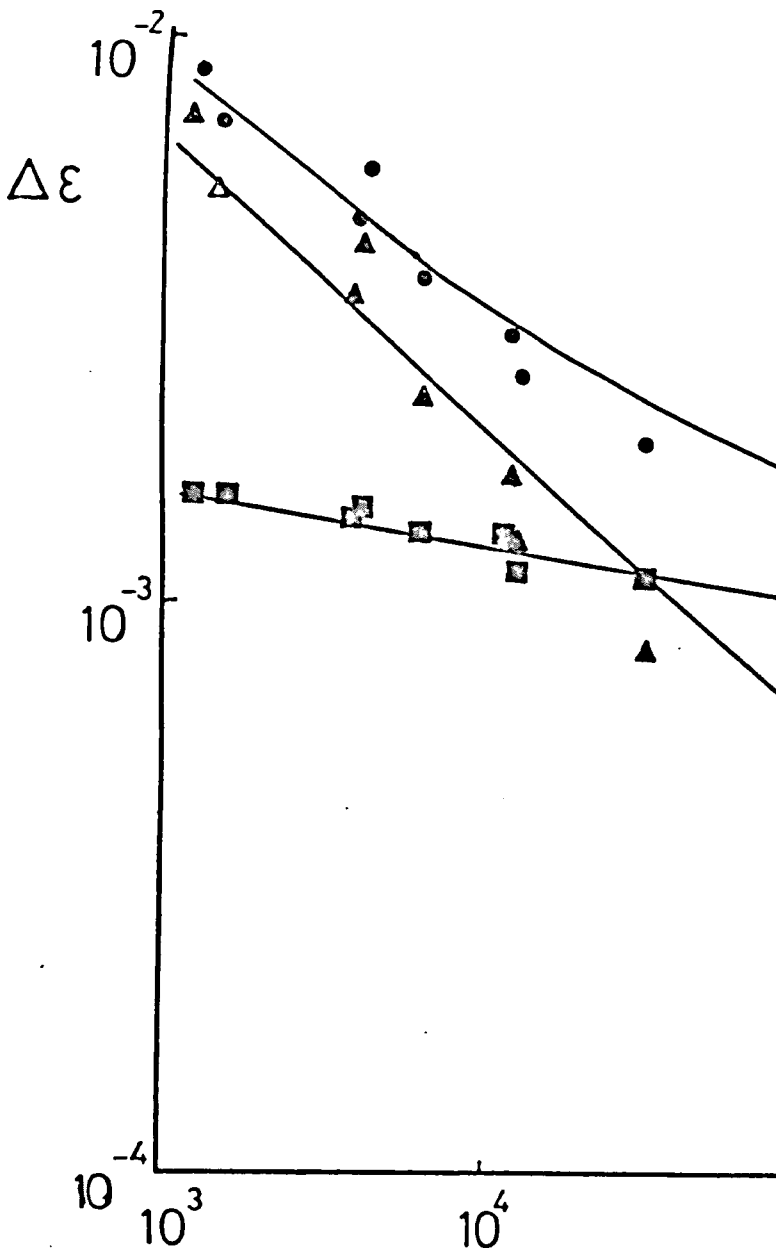
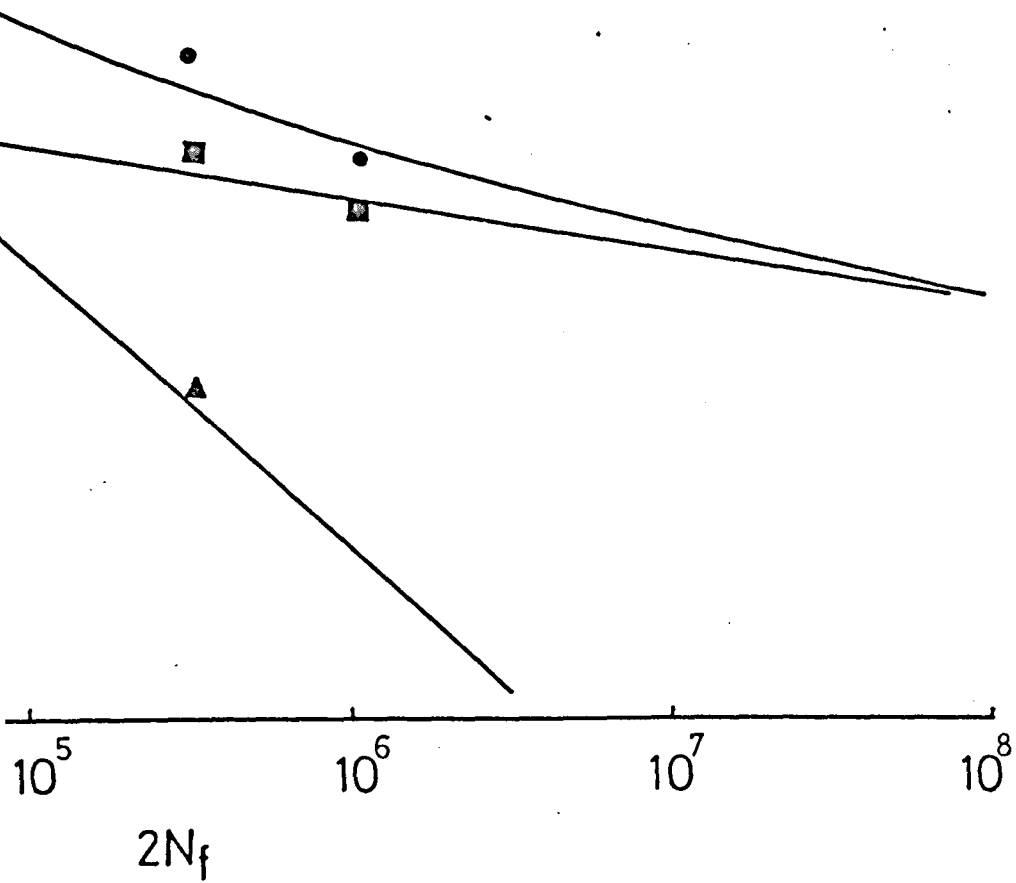


Figure 98 The strain-life curves for B35XX
Total● Plastic▲ Elastic■



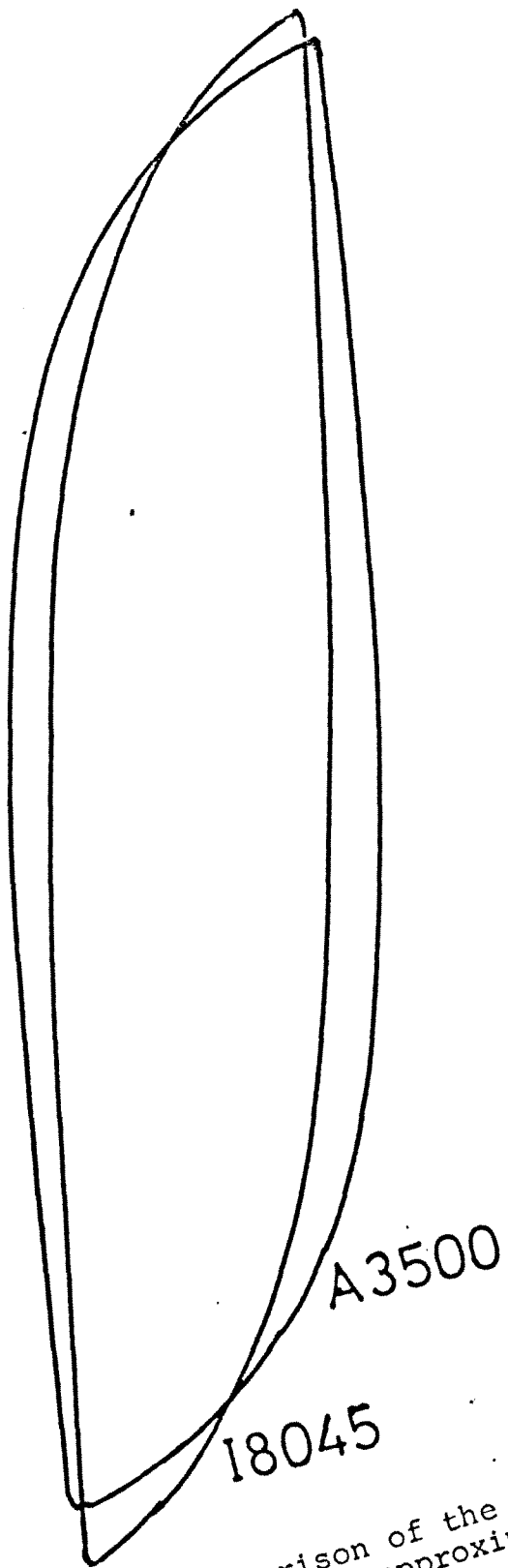


Figure 99 Comparison of the loop shape between specimens cycled at approximately the same strain amplitude.

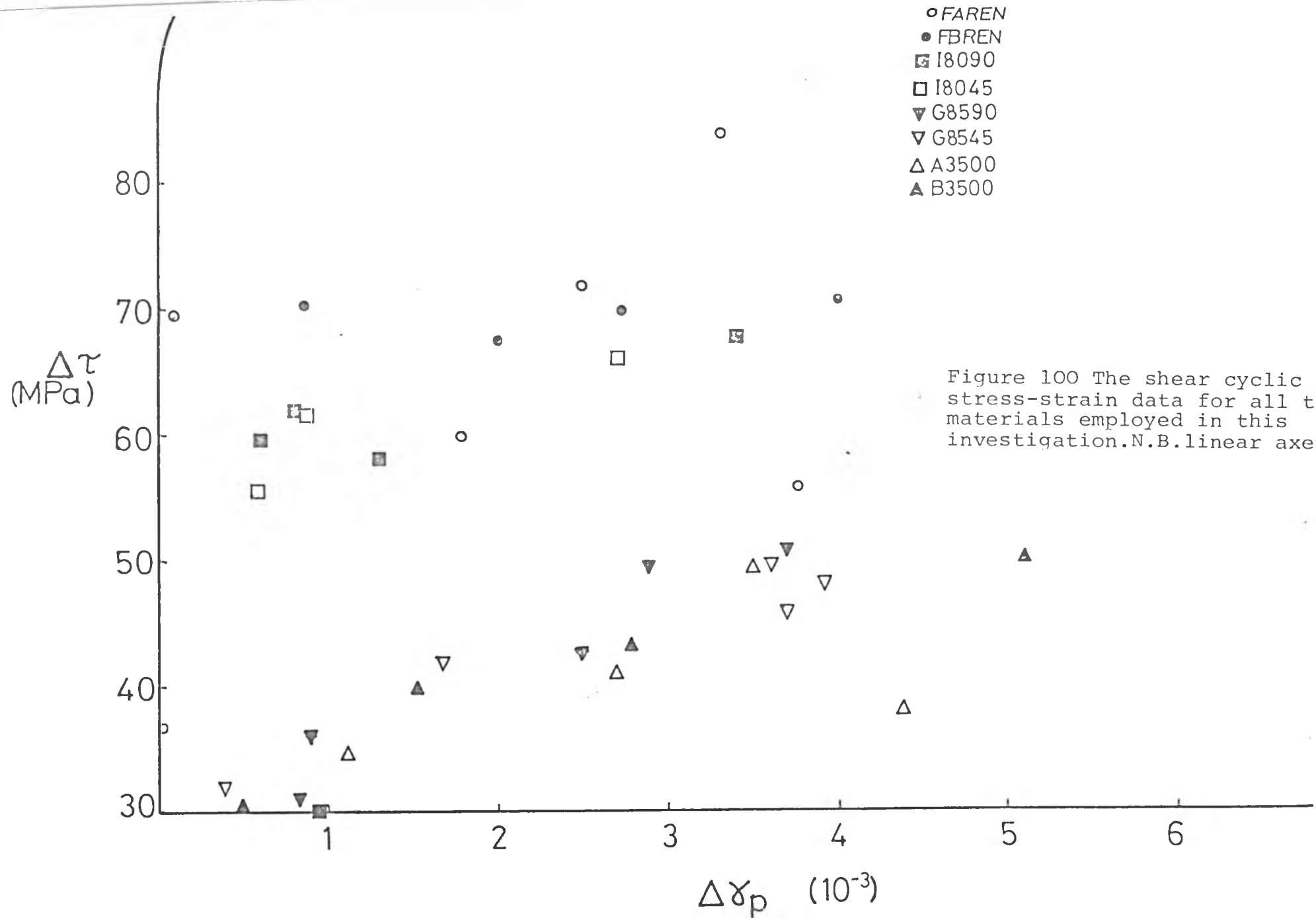
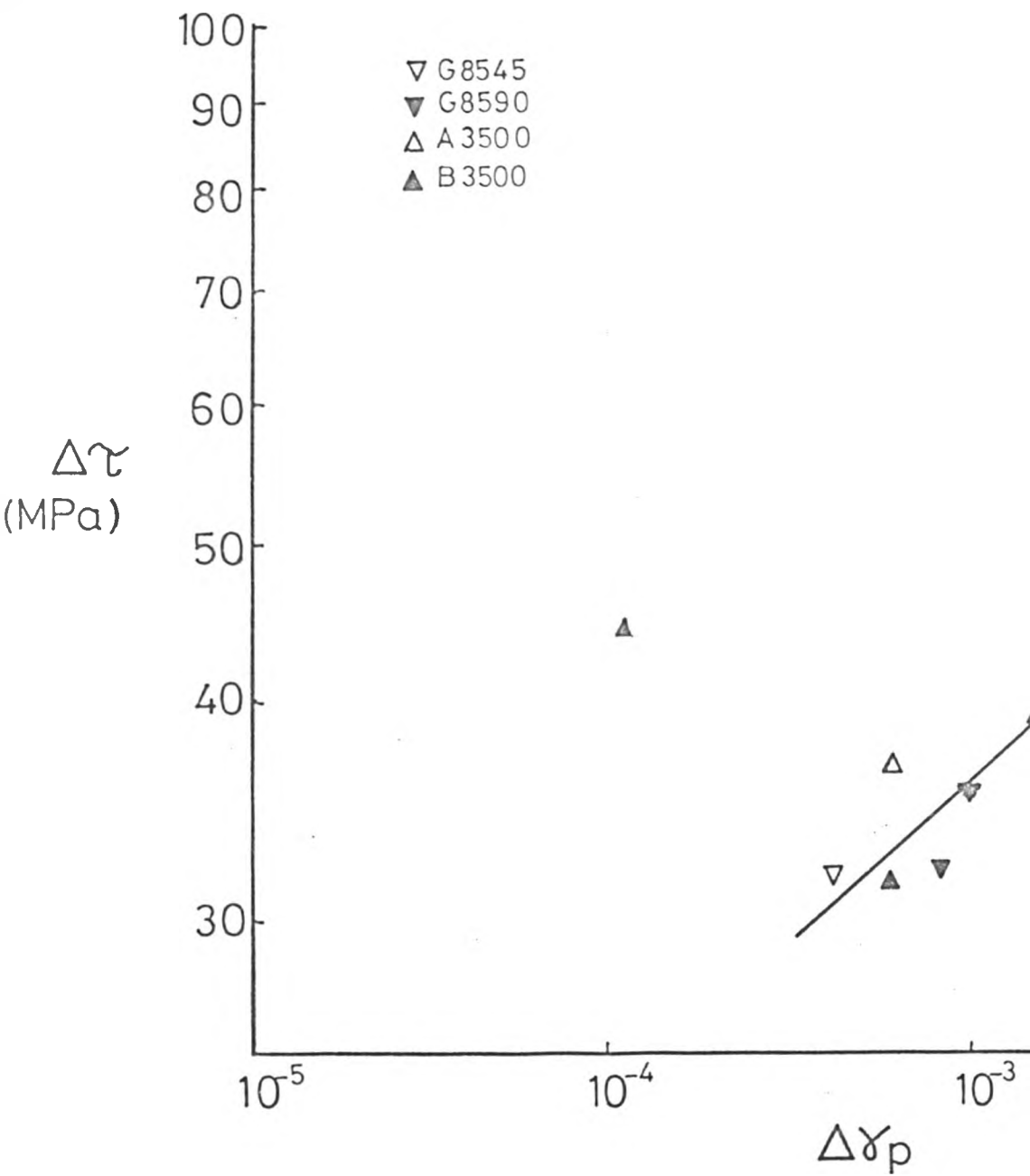
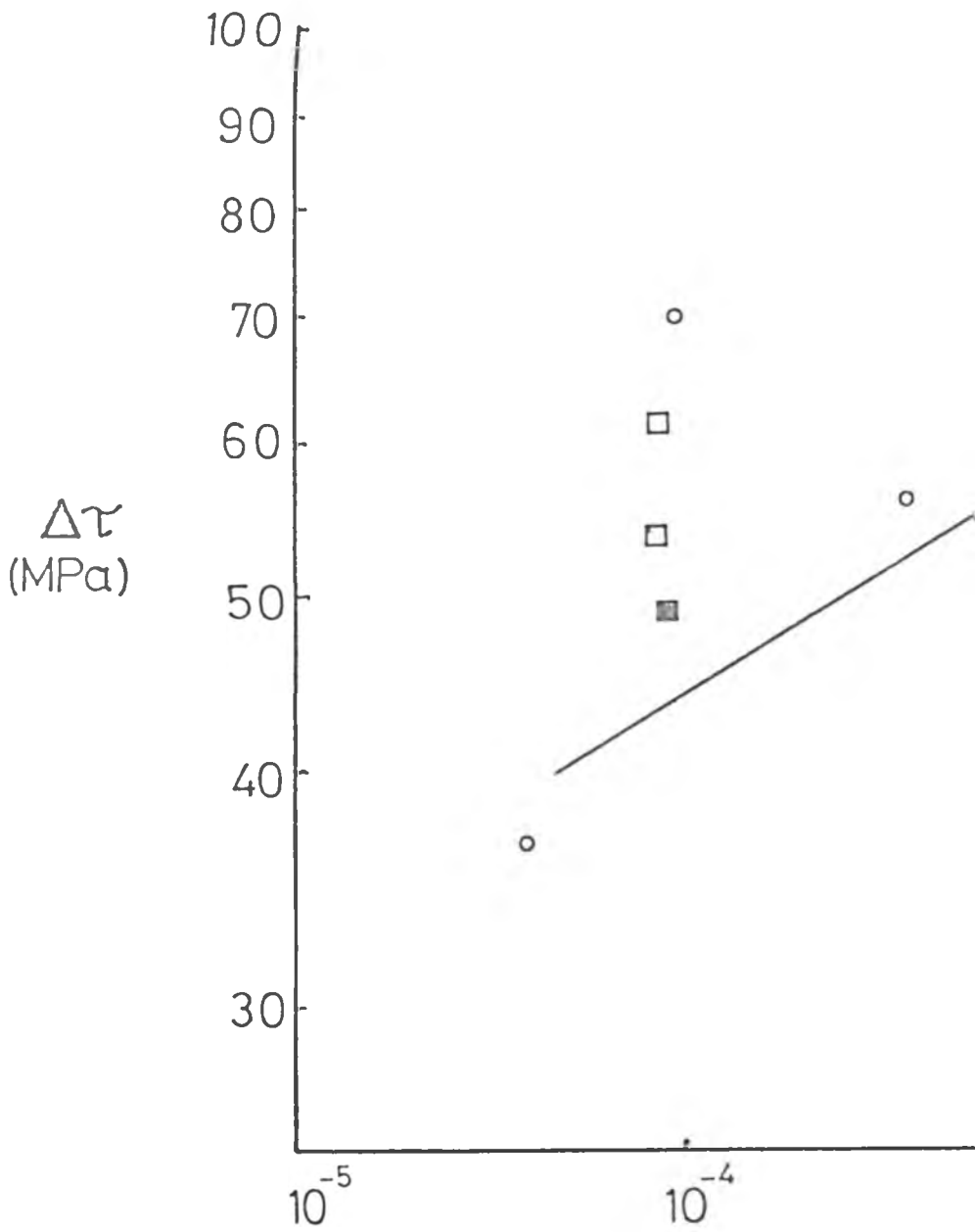


Figure 100 The shear cyclic stress-strain data for all the materials employed in this investigation. N.B. linear axes.





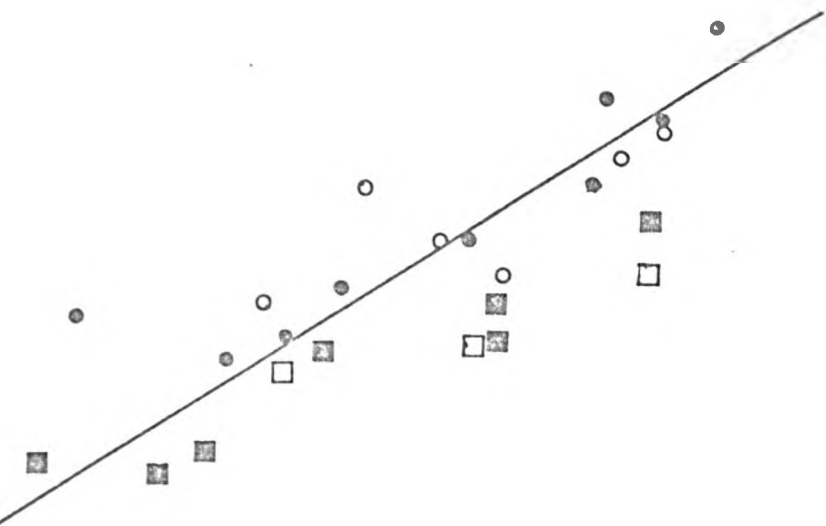
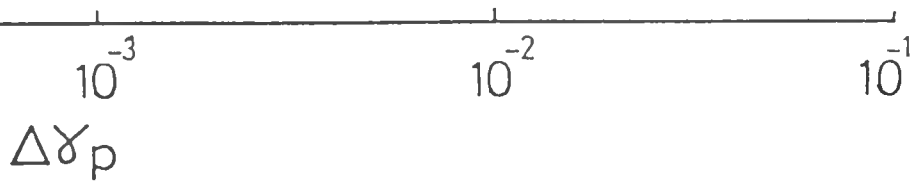


Figure 102 Cyclic shear stress-shear strain data for cold worked materials.

- FAREN
- FBREN
- 18090
- 18045



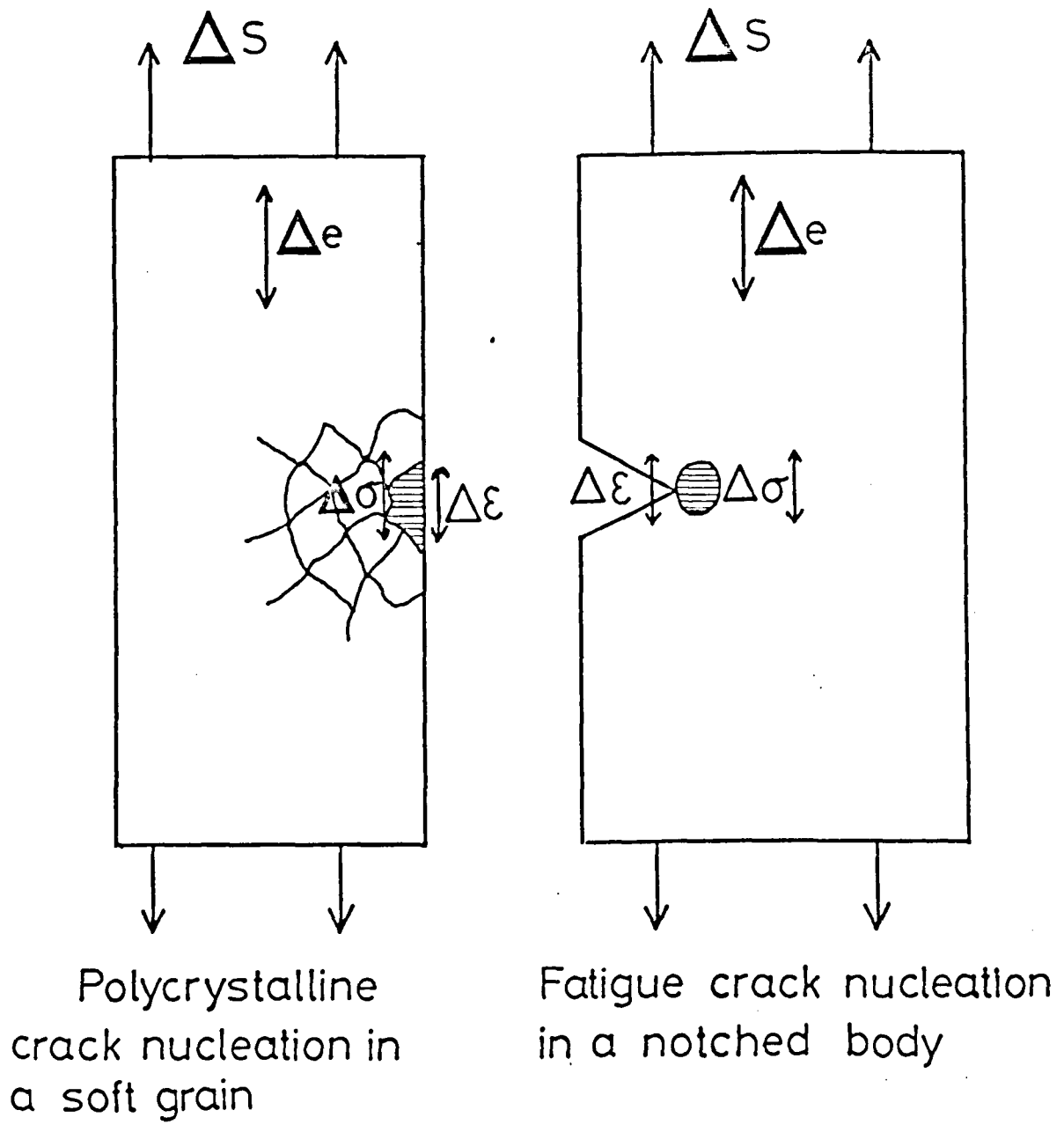
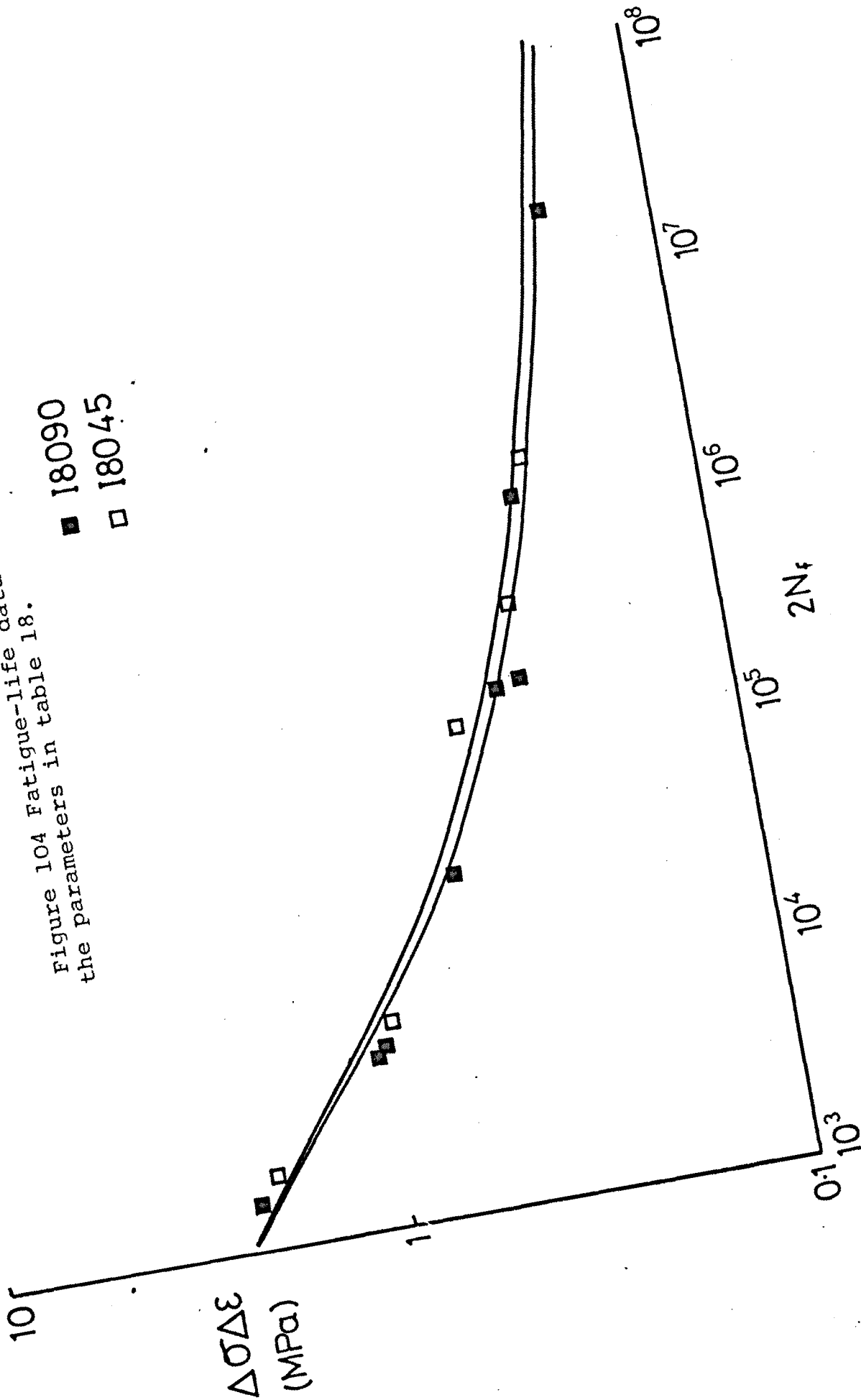


Figure 103 The analogy between a 'soft' grain in a polycrystal and the notch region in a continuum.

Figure 104 Fatigue-life data for III80. Curves calculated from the parameters in table 18.

- 18090
- 18045



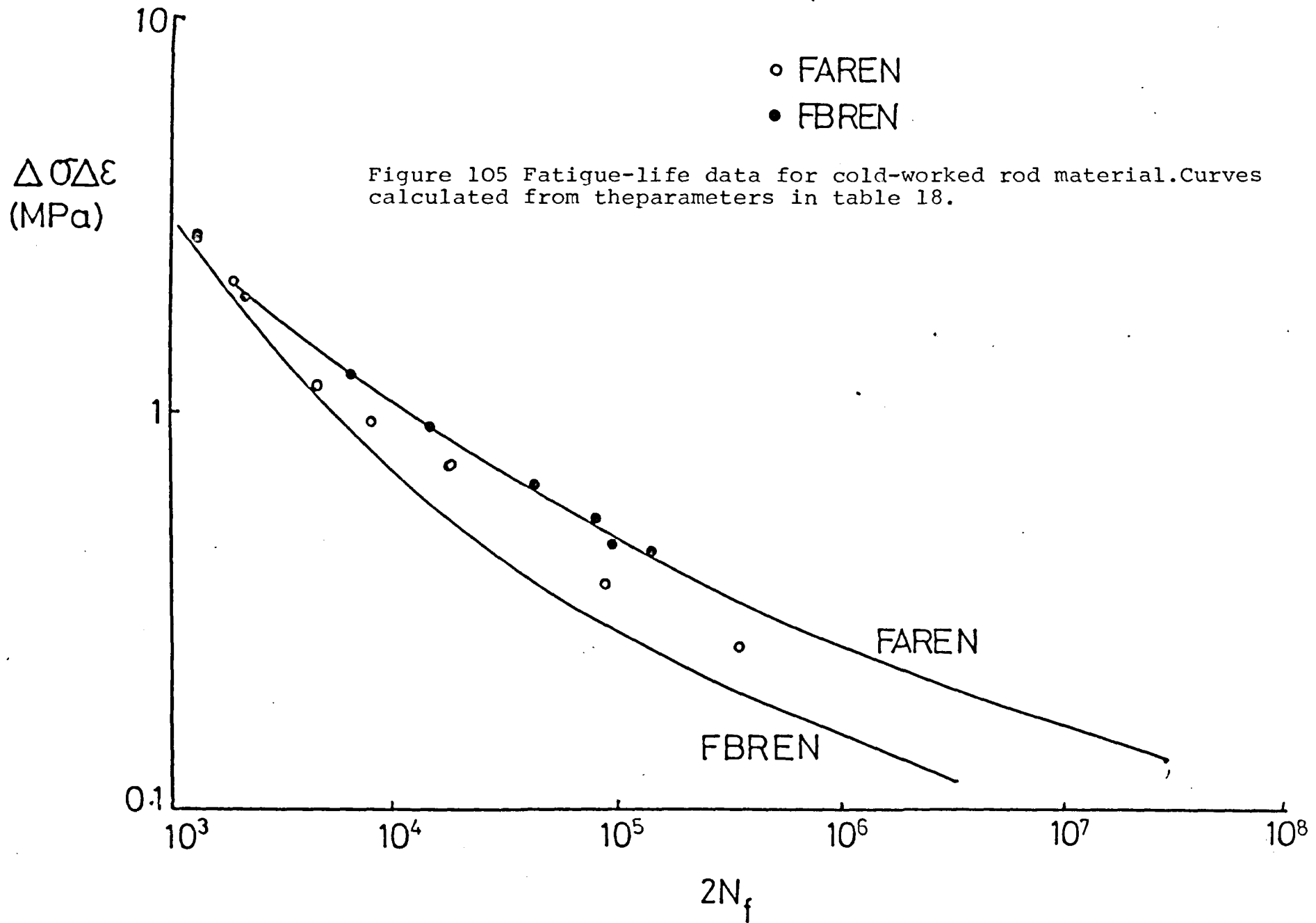


Figure 106 Fatigue-life data for G8585. Curves calculated from the parameters in table 18.

$\Delta\sigma\Delta\varepsilon$
(MPa)

▼ G8590
▽ G8545

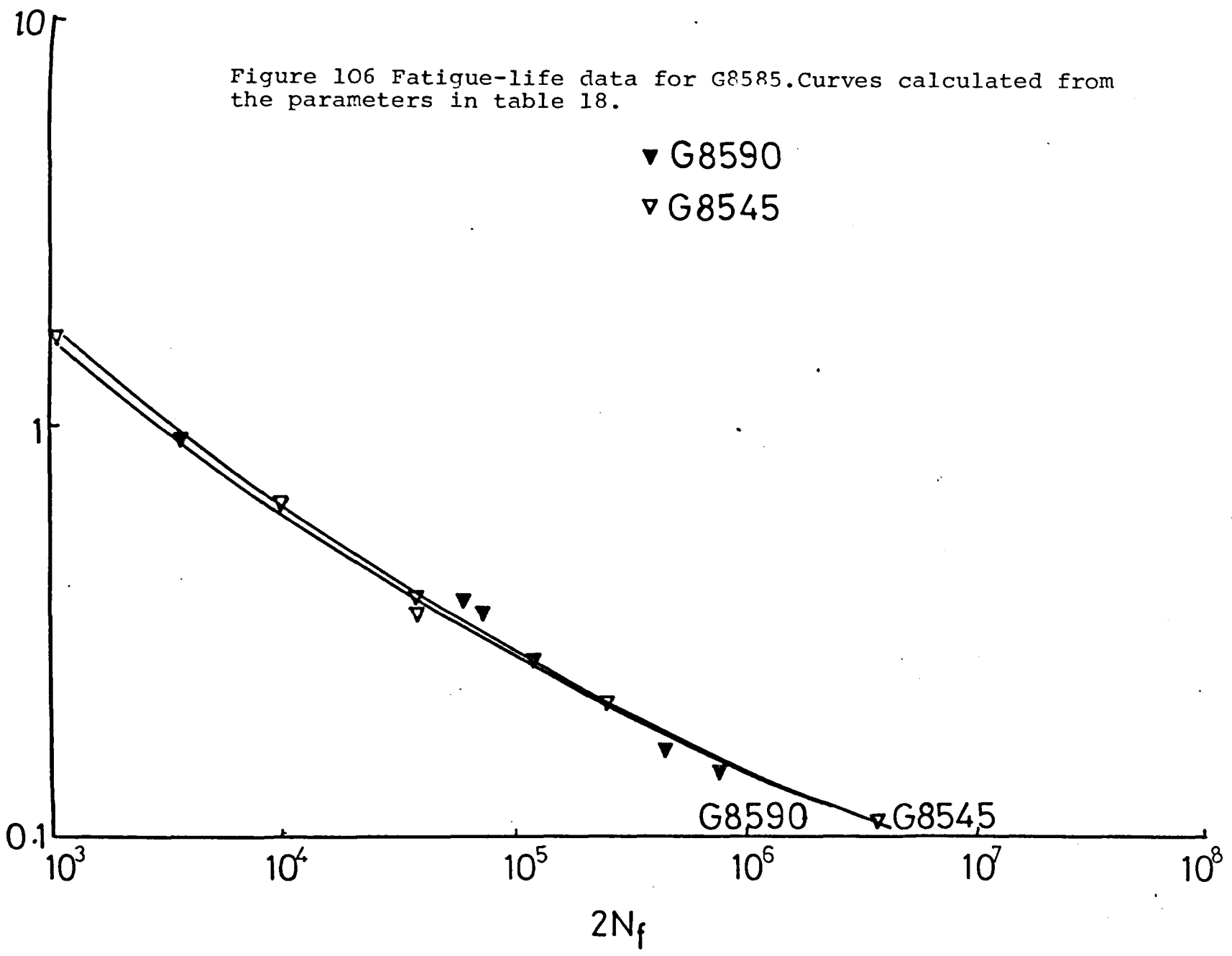
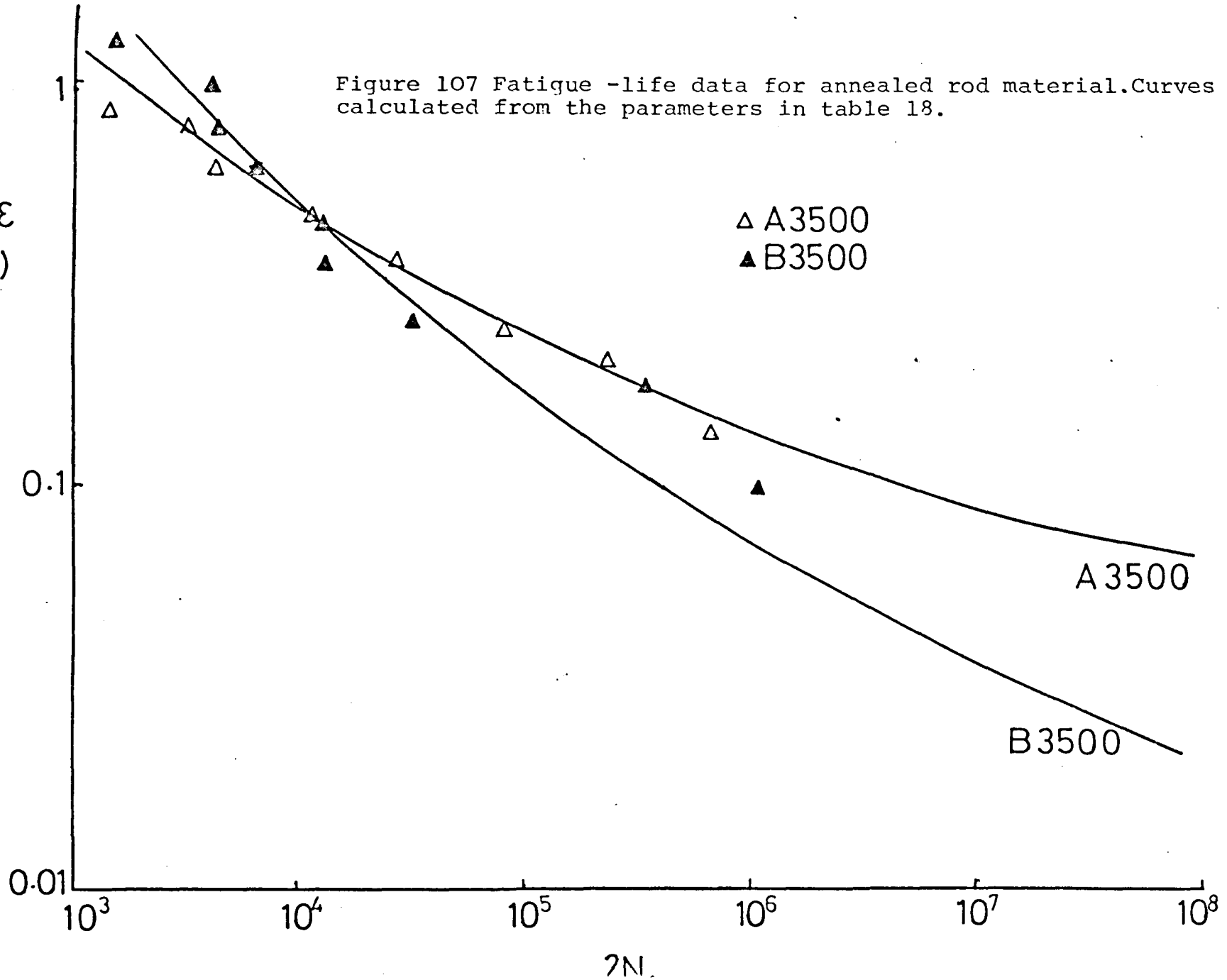


Figure 107 Fatigue -life data for annealed rod material. Curves calculated from the parameters in table 18.

$\Delta\sigma\Delta\varepsilon$
(MPa)



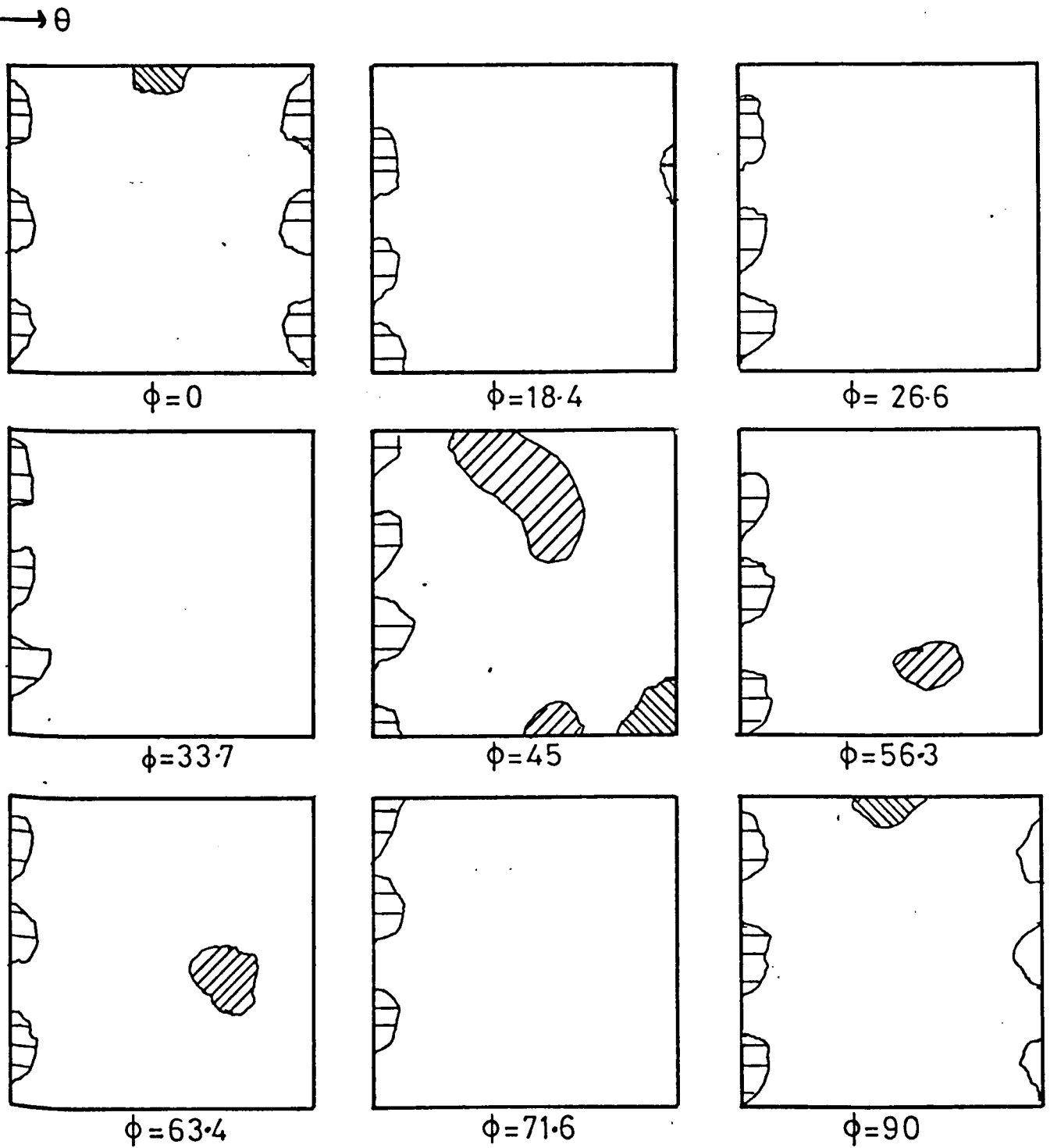


Figure 108 C.o.d.f. plot showing the texture components which have been reported to develop during fatigue.
 — present work, uniaxial. // Inakazu and Yamamoto, low amplitude torsion. \\\\ Witzel, high amplitude torsion.

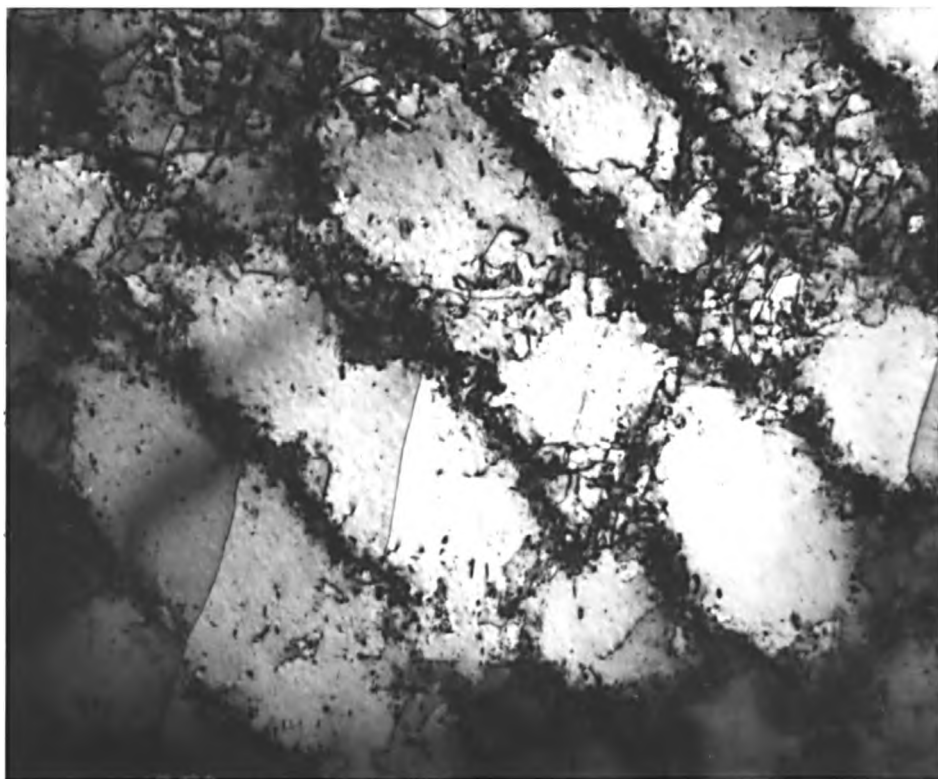


Figure 109 Dislocation cell structure observed after high strain fatigue of a copper-base alloy (ref. 152).

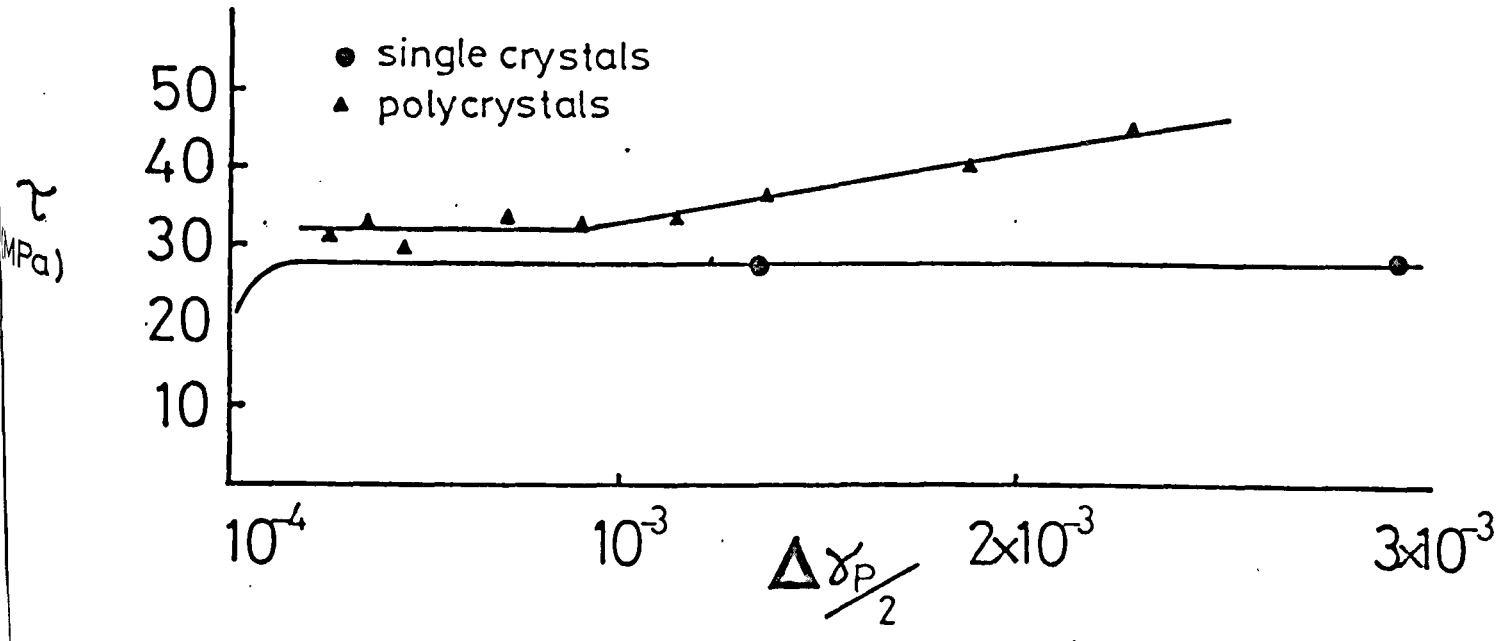


Figure 110 The cyclic shear stress-strain data of Rasmussen and Pedersen (ref.153).The curve for the single crystal data is taken from the work of Mughrabi (ref.24).

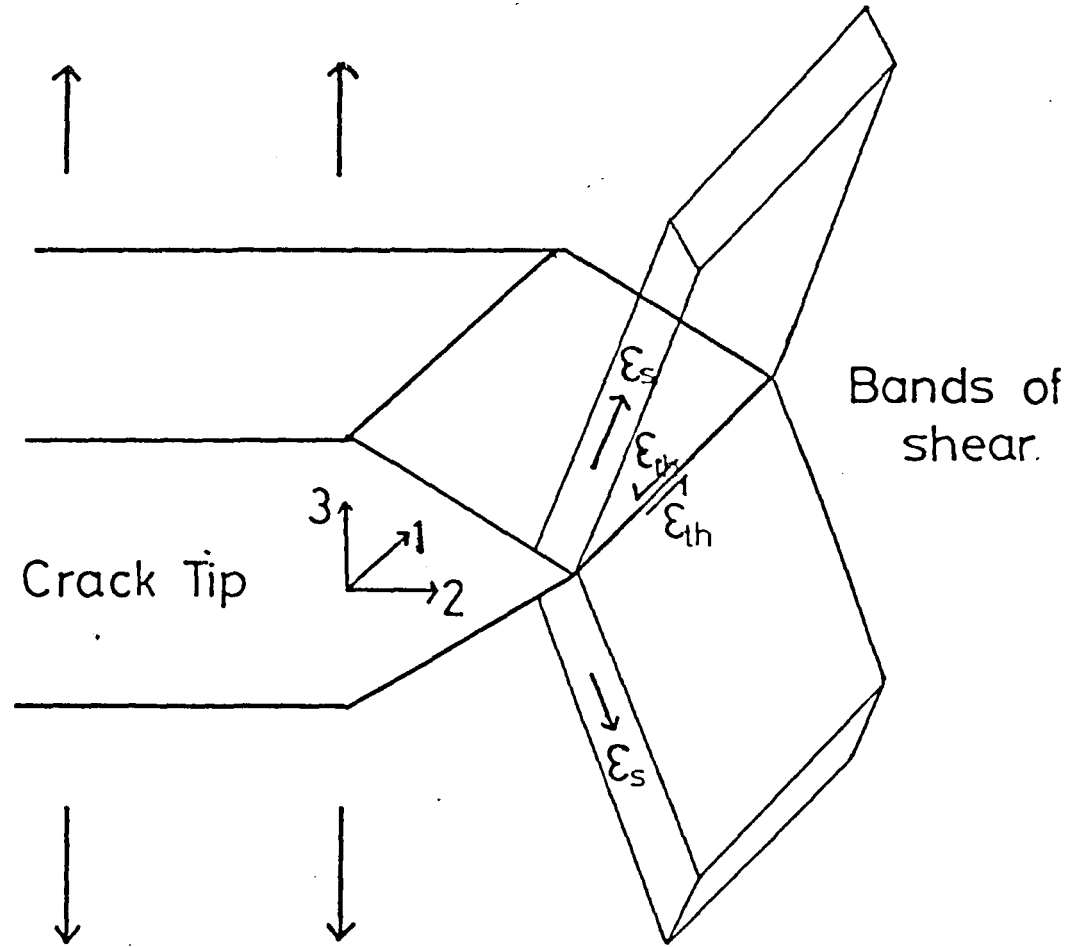


Figure 111 Representation of the ductile propagation of a fatigue crack by the formation of bands of shear at the crack tip.

Auxiliary Figures

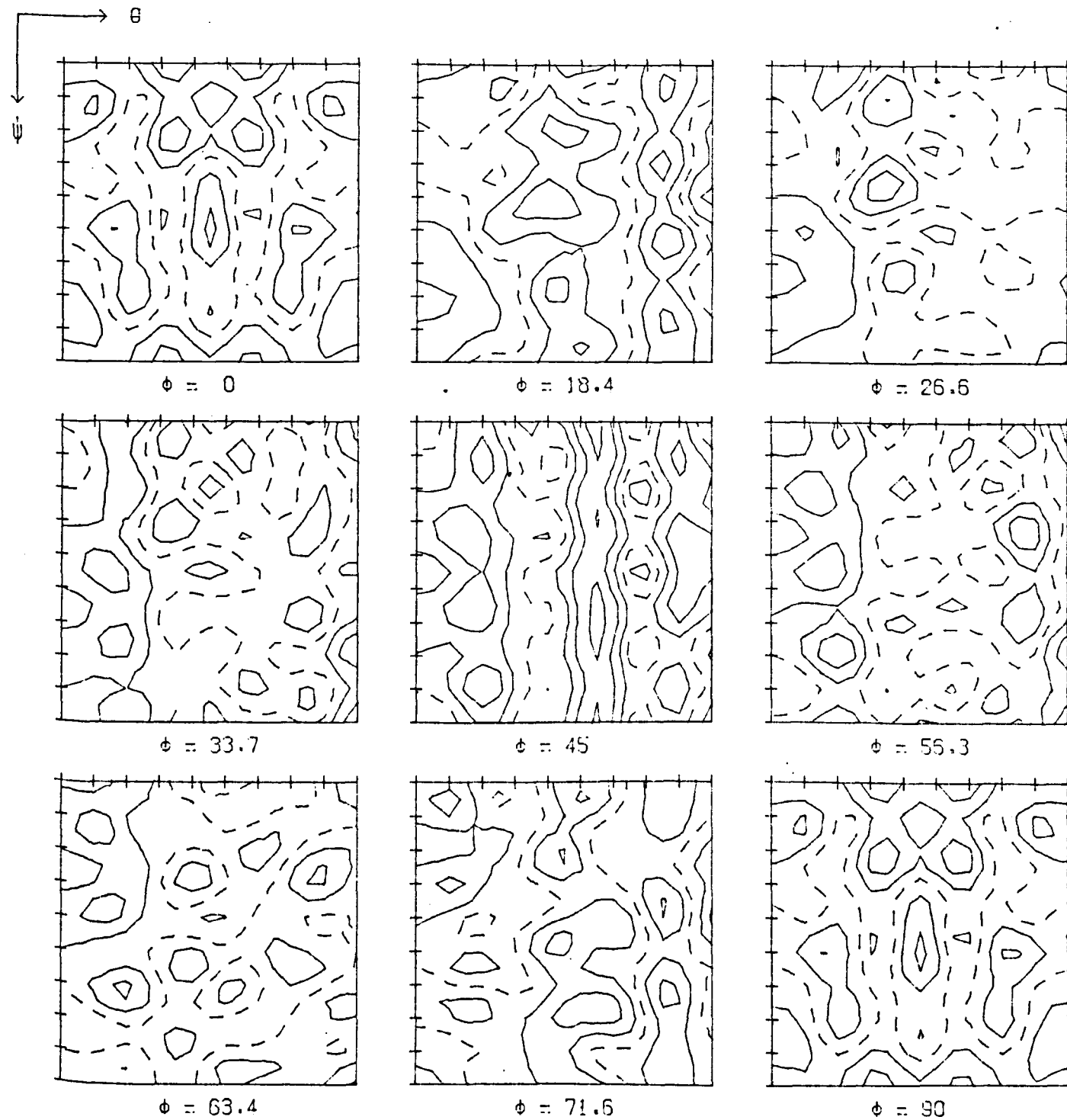


Figure A3-I C.o.d.f. plot of material SAE-4161(Q T).
 Contour interval 0.1. Max. Fn. llt. = 1.3x random, severity = 0.11

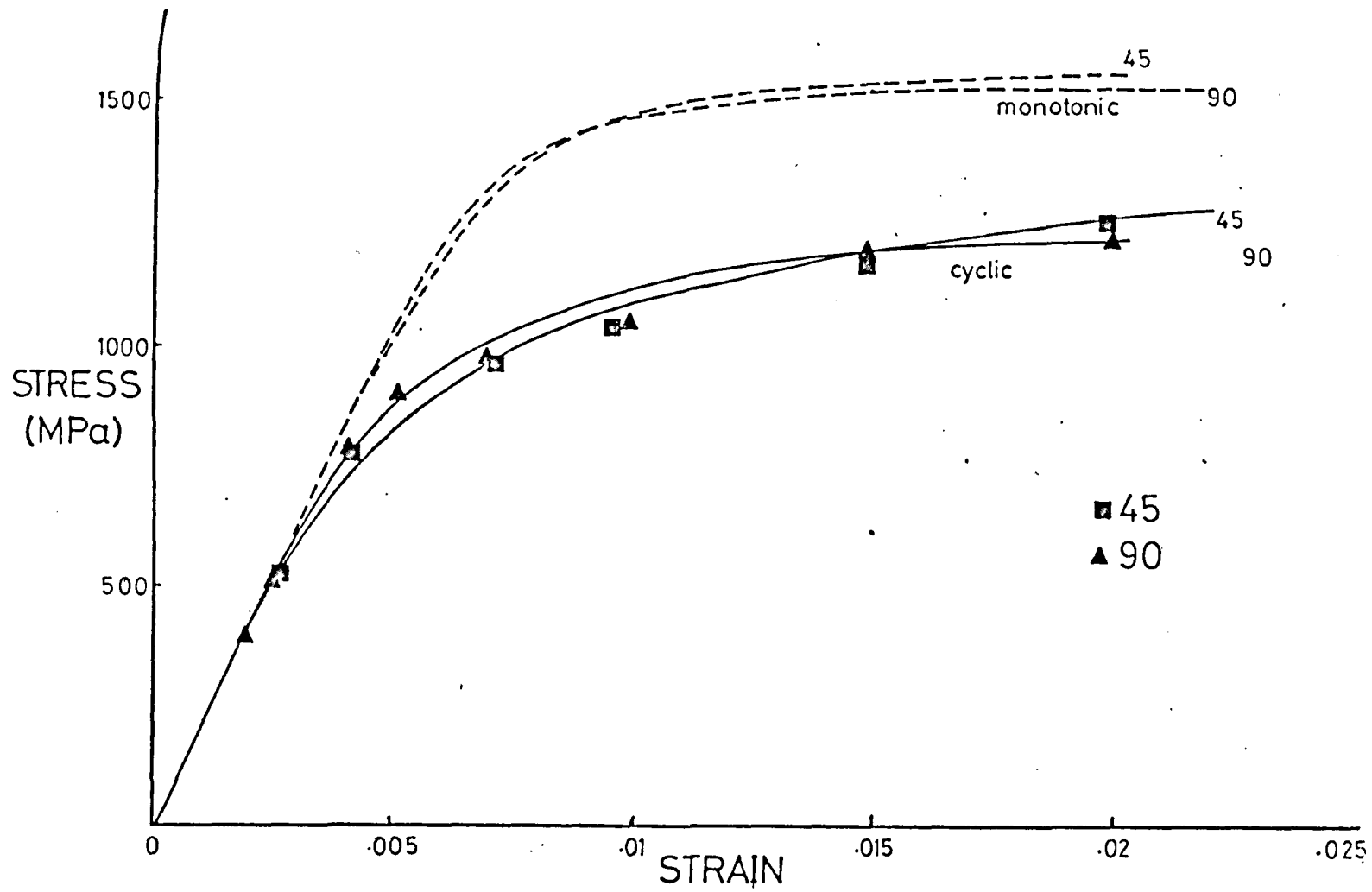


Figure A3-2 Stress-strain curves for SAE-4161(0 T).

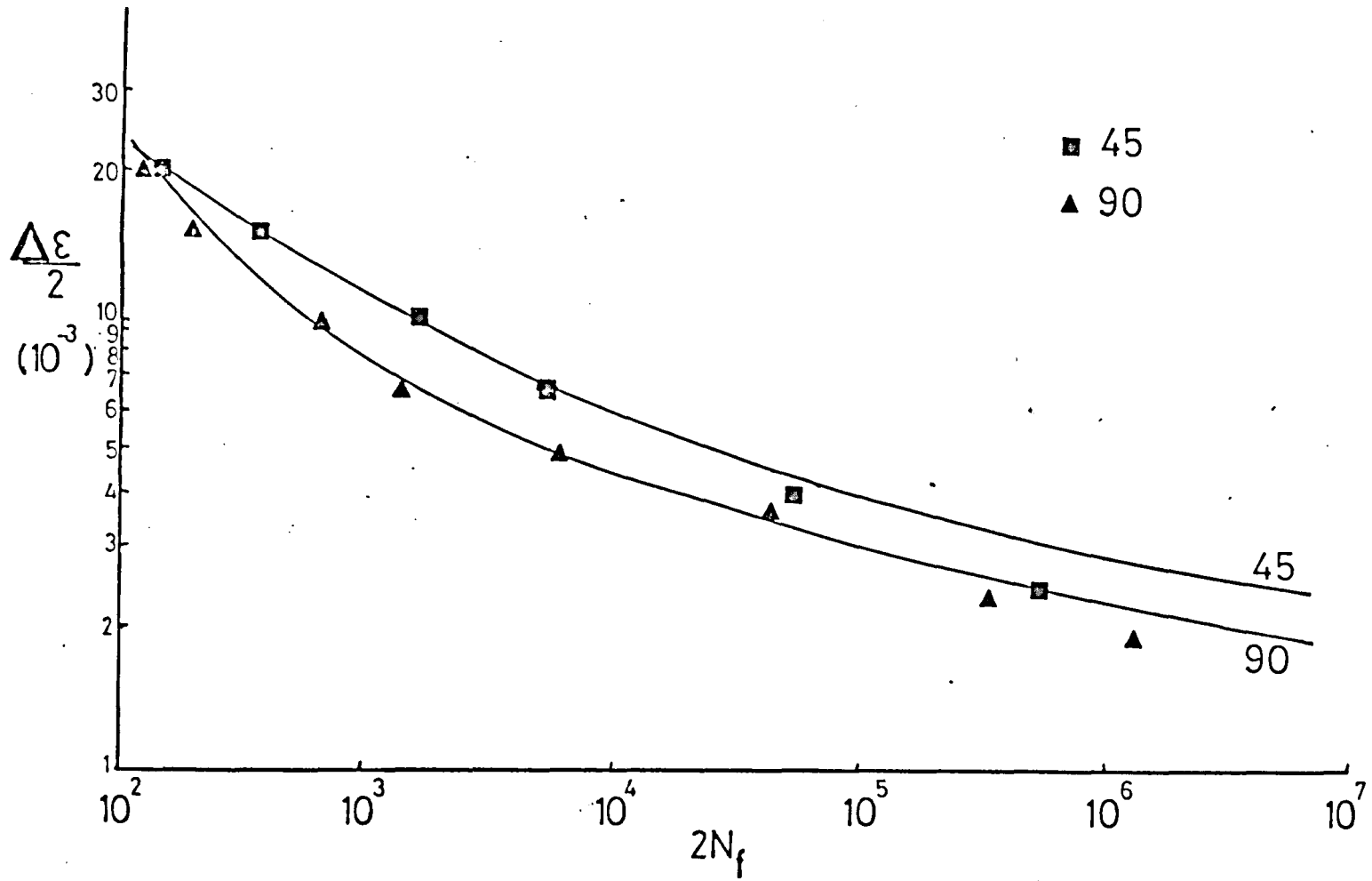


Figure A3-3 Strain-life data for SAE-4161(0 T).

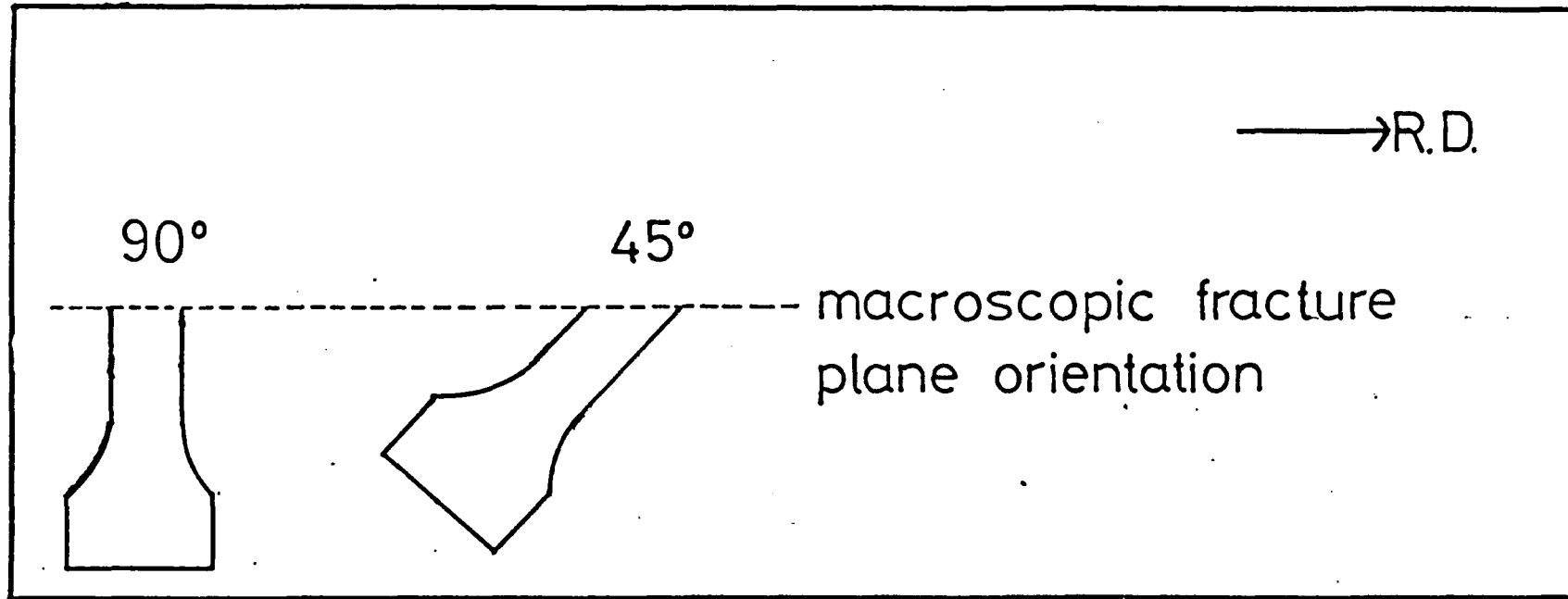


Figure A3-4 Schematic representation of the fracture morphology in SAE-4161(0 T).

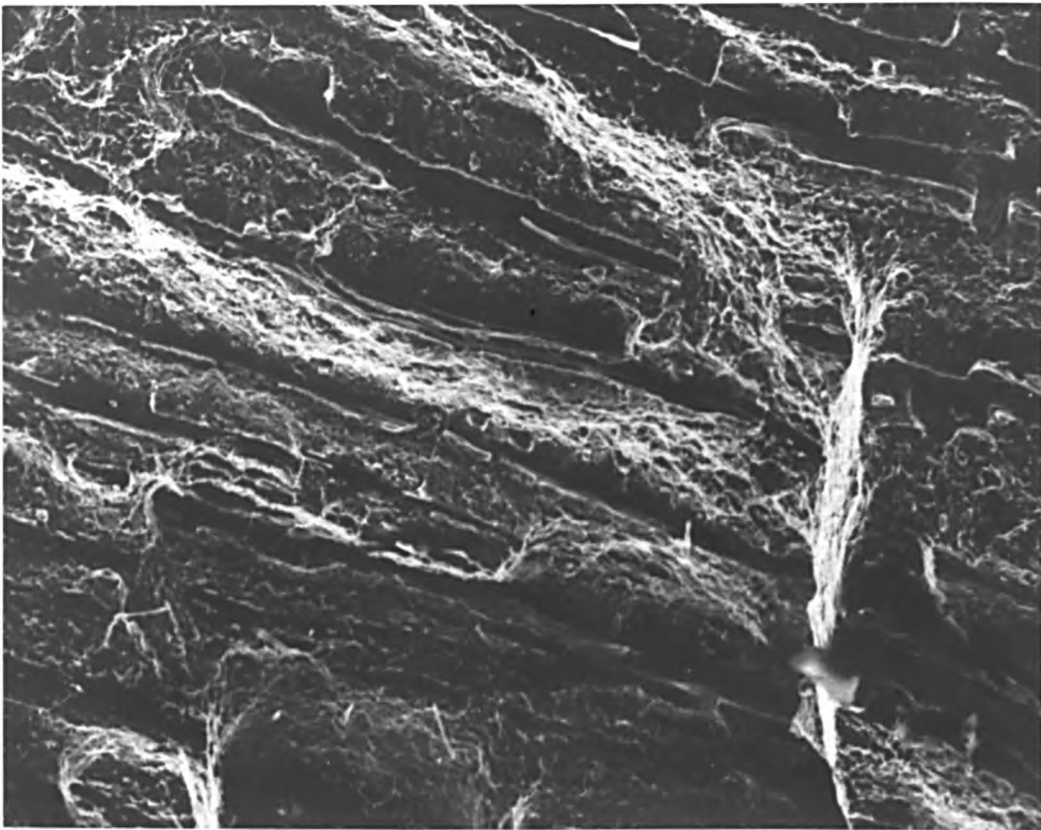
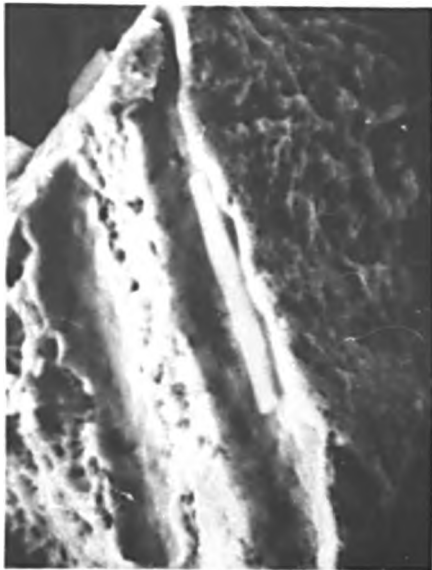
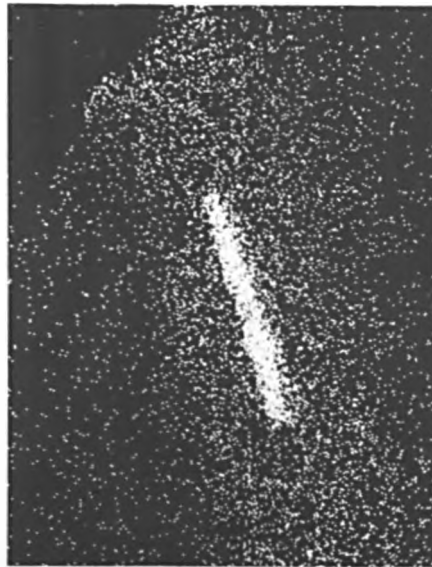


Figure A3-5 Scanning electron micrograph of fracture surface of SAE-4161(O T), showing elongated inclusion. Magnification 900x.

Secondary electrons



X-ray map Mn.



X-ray map Fe.

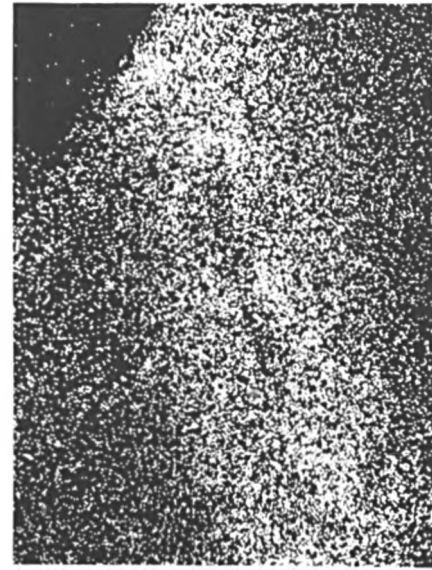


Figure A3-6 SEM fractography of SAE-4161 with X-ray element mapping

Material Codes

- MBCUB Thin sheet, cube texture, 0, 45 and 90 specimens used for constant load amplitude tests.
- III180 Thick plate, shear texture, 0, 45 and 90 orientations used for strain-life tests as I8000, I8045, and I8090. Cold rolled.
- G8585 Thick plate, retained shear texture, 45 and 90 orientations used for strain-life tests as G8545 and G8590. Annealed.
- NUJIG Thick plate, shear texture, 45 and 90 orientations used for crack propagation tests. Cold rolled.
- CROCP Thick plate, shear texture, 45 and 90 orientations used for crack propagation tests. Cold rolled.
- FAREN Fibre textured rod, cold drawn from cast A.
- FBREN Fibre textured rod, cold drawn from cast B.
- A3500 Fibre textured rod, FAREN+3 hours at 770K
- B3500 Fibre textured rod, FBREN+ 3 hours at 770K.